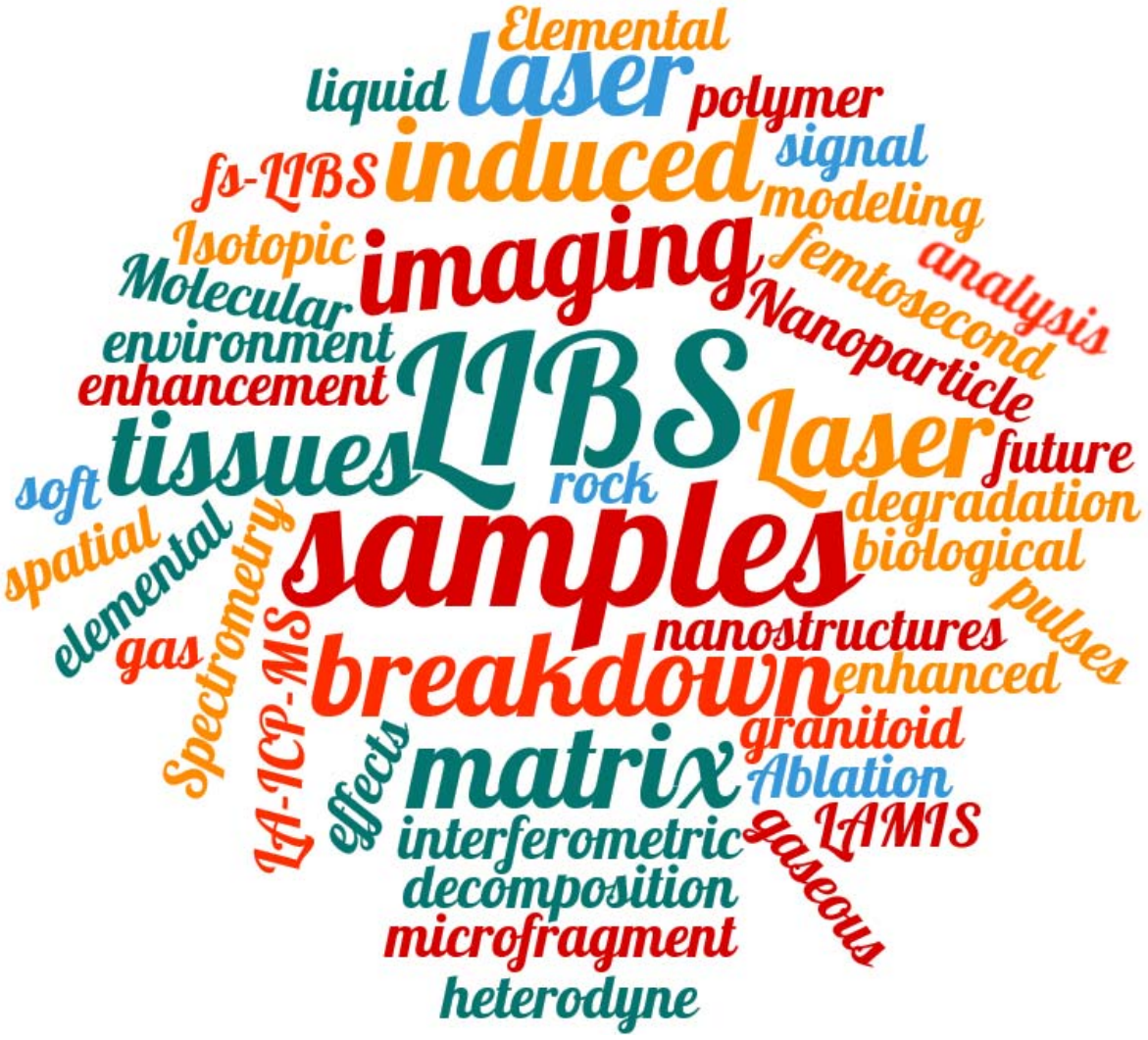

INTERNATIONAL WORKSHOP ON LIBS

December 1-2, 2020 – Szeged, Hungary

December 1-2, 2020 - Szeged, Hungary

INTERNATIONAL WORKSHOP ON LASER-INDUCED BREAKDOWN SPECTROSCOPY

PROCEEDINGS

ISBN 978-963-306-765-9

Organizers:

Department of Inorganic and Analytical Chemistry,
University of Szeged, Hungary

Spectrochemical Working Committee
of the Hungarian Academy of Sciences

ELI-ALPS Research Institute, Szeged, Hungary

Ultrafast physical processes in atoms, molecules, nanostructures and biological systems, EFOP 3.6.2-16-2017-00005 project

Editors:

Gábor Galbács

Albert Kéri

2020

PREFACE

This workshop was originally conceptualized as a one-day meeting, with the support of several scientific organizations, but especially from a consortial research project being conducted at the University of Szeged (Ultrafast physical processes in atoms, molecules, nanostructures and biological systems, EFOP 3.6.2-16-2017-00005). The intention behind the meeting was that it would facilitate the sharing of new scientific results in the LIBS field and could boost the building of new cooperative projects between laser ablation/spectroscopy research groups operating in Hungary and worldwide. We also have a shiny, new, large laser facility (Extreme Light Infrastructure Attosecond Light Pulse Source, ELI-ALPS), which has much to offer for the field of LIBS research in terms of ultra-short, tunable, high repetition rate and high intensity laser pulses. We originally intended to organize a classic workshop, with meeting in person, laboratory visits, fine dining, etc. Unfortunately, due to the covid-19 pandemic, we can now only have an online event (http://www2.sci.u-szeged.hu/libsconf/), which format imposes some limitations.

We are thankful for the support of the international participants, illustrious invited scientists – chemists, physicists and engineers – and we are sure that all participants will have a great time listening to the exciting, altogether 29 presentations from ten countries around the world. We wish everyone excellent health and we hope that this online event, now expanded to two days, will be able to come close to reaching our original, ambitious goals.

This volume contains the papers of all presentations, oral or poster, as well as associated vendor materials.

Prof. Gábor Galbács (University of Szeged), conference-chair
Prof. Sándor Szatmári (University of Szeged), conference co-chair
Prof. Katalin Varjú (ELI-ALPS), conference co-chair
Dr. Albert Kéri (University of Szeged), conference secretary

November 30, 2020.
Szeged, Hungary

SCIENTIFIC PROGRAM

December 1, 2020

(Budapest time, GMT +1)

9:00 - 9:10	Opening address by **Gábor Galbács** (University of Szeged)
9:10 - 9:15	Opening address by **Sándor Szatmári** (University of Szeged)
9:15 - 9:30	Opening address by **Katalin Varjú** (ELI-ALPS, Szeged)
9:30 - 10:10	**Igor B. Gornushkin** (Federal Institute for Materials Research and Testing, Germany): *Laser induced gas breakdown in reactive mixtures containing halides of boron and silicon: diagnostics and modeling*
10:10 - 10:50	**Alessandro De Giacomo** (University of Bari, Italy): *Nanoparticle enhanced laser induced breakdown spectroscopy: fundamentals and perspectives*
10:50 - 11:30	**Pavel Veis** (Comenius University, Slovak Republic): *Why is LIBS the future online analytical technique for plasma-facing materials of thermonuclear reactors?*
11:30 - 13:00	Lunch break
13:00 - 13:40	**Andreas Limbeck** (Vienna University of Technology, Austria): *Assessment of polymer degradation by the combined use of LIBS and LA-ICP-MS*
13:40 - 14:20	**Timur A. Labutin** (Lomonosov Moscow State University, Russia): *Non-analytical applications of laser-induced breakdown spectrometry*
14:20 - 15:00	**Tamás Smausz** (University of Szeged, Hungary): *Study of the fragmentation of solid drug particles during ablation with different pulse length lasers*
15:00 - 15:40	**Pavel Pořízka** (Brno University of Technology, Czech Republic): *Recent advances in the imaging of biological tissues at the Brno University of Technology*
15:40 - 16:00	Coffee break

16:00 - 16:40 **Vincent Motto-Ros** (University of Lyon, France), **Benoit Busser** (Grenoble Alpes University Hospital, France): *Elemental imaging with laser spectroscopy is entering the clinic as a new diagnostic tool*

16:40 - 17:20 **Viktor Chikán** (Kansas State University, USA/ELI-ALPS Research Institute, Hungary): *Characterization of the CN(B) and CH(A) radical formation in plasma generated by femtosecond laser pulses via step-scan FT-UV-VIS spectroscopy*

17:20 - 18:00 **Jhanis Gonzalez** (Lawrence Berkeley National Laboratory/ Applied Spectra Inc., USA): *Laser Ablation Molecular Isotopic Spectrometry (LAMIS) - overview*

18:00 - 18:40 **Vincenzo Palleschi** (University of Pisa, Italy): *About the use of laser-induced breakdown spectroscopy for the determination of fundamental spectroscopic parameters*

18:40 - 18:50 Closing of the oral session

December 2, 2020

(Budapest time, GMT +1)

10:00 - 12:00 **Poster session I.**
Instrumental, theoretical and numerical approaches

Dávid J. Palásti (University of Szeged, Hungary):
Optical and numerical modeling of a spatial heterodyne laser-induced breakdown spectrometer

Lajos P. Villy (University of Szeged, Hungary):
Signal enhancement of gaseous samples in the presence of nanoaerosols generated by a spark discharge

Jelena Petrović (University of Belgrade, Serbia):
Enhancement of the TEA CO_2 LIBS emission using Ag and Ag/Zn nanostructures

Eszter Nagy (University of Szeged, Hungary):
Laser ablation of meloxicam in liquid environment

Jakub Buday (Brno University of Technology, Czech Republic):
Computation of blast wave energy in LIBS using shadowgraphy

Roman Holomb (Uzhhorod National University, Ukraine/Wigner Research Centre for Physics, Hungary):
Reversible laser-assisted structural modification and laser-driven mass transport at the surface of chalcogenide nanolayers

István Rigó (Wigner Research Centre for Physics, Hungary): *Effect of surface roughness on SERS enhancement of patterned gold substrates*

Aurélien Favre (Normandy University, France):
MERLIN, an RT-LTE software supporting the diagnostic application of LIBS to H-isotope measurements

12:00-14:00 Lunch break

14:00 - 16:00 **Poster session II.**
Analytical methodology

Patrick Janovszky (University of Szeged, Hungary):
Identification and Be, Li content assessment of minerals in granitoid rock samples by LIBS

Sára Střítežská (Brno University of Technology, Czech Republic):
Toxicity assessment of photon-upconversion nanoparticles and their bioimaging by using laser-induced breakdown spectroscopy in Brassica oleracea L. plant

Anna Šindelářová (Brno University of Technology, Czech Republic):
Implementation of laser-induced breakdown spectroscopy elemental imaging into the histopathological analysis of soft tissues

Patrick Janovszky (University of Szeged, Hungary):
Investigation of size and exposure time dependent bioaccumulation of silver nanoparticles in plants by LIBS

Nikolai Sushkov (Lomonosov Moscow State University, Russia):
Exploratory analysis of zooplankton spectra using matrix decomposition techniques

Dávid J. Palásti (University of Szeged, Hungary):
LIBS-based approaches for the classification of glass microfragment samples

Daniel Holub (Brno University of Technology, Czech Republic):
Classification of plastics using LIBS and Raman spectroscopy data fusion

Lukas Brunnbauer (Vienna University of Technology, Austria): *Matrix effects in quantitative polymer analysis: a comparison of ns and fs laser systems*

Patrick Janovszky (University of Szeged, Hungary):
Analysis of uranium-bearing materials by laser-induced breakdown spectroscopy

Ádám Bélteki (University of Szeged, Hungary):
On-line and off-line LIBS detection of nanoaerosols generated by electrical discharges

ORAL PRESENTATIONS

LASER INDUCED GAS BREAKDOWN IN REACTIVE MIXTURES CONTAINING HALIDES OF BORON AND SILICON: DIAGNOSTICS AND MODELING

I. B. Gornushkin[1]*, P. G. Sennikov[2]

[1]BAM Federal Institute for Materials Research and Testing,
Richard-Willstatter-street 11, 12489 Berlin, Germany
[2]Institute of Chemistry of High-Purity Substances of RAS,
Tropinin street 49, 603600, Nizhny Novgorod, Russia
**e-mail: igor.gornushkin@bam.de*

1. INTRODUCTION

Plasma-chemical approach is used for synthesis of various gaseous, liquid, and solid substances since 1960th [Vurzel 1970]. Nowadays, the method of plasma enhanced chemical vapor deposition (PECVD) is widely used for production of thin films, protective coatings, carbon-based nanostructures, high purity isotopic materials, biomaterials, and many other products. Plasma for PECVD is typically created in various electrical discharges; e.g. DC and AC glow discharges or discharges operated at audio (10-20 kHz), radio (13.56 MHz), and microwave (2.45 GHz) frequencies. Laser induced plasma (LIP) is rarely used to deposit materials from the gas phase and this work aims at reviving interest to this latter technology and showing its potential.

We run two pilot LIP experiments in reactive gas mixtures. First, LIP is excited in BCl_3 or BF_3 plus H_2 or CH_4 to evaluate the efficiency of deposition of solid boron and boron carbide, materials that are largely used for refractory coatings. Second, we investigate a possibility of synthesis of fluorochlorosilanes SiF_xCl_{4-x} (x = 1, 2, 3) by LIP induced in SiF_4+$SiCl_4$ gas mixtures. Using fluorochlorosilanes with different combinations of F and Cl in the SiF_xCl_y molecule may add flexibility in processes of silicon deposition and etching. The gases used and solid deposits are analyzed by optical emission spectroscopy (OES) and IR and mass spectrometry (MS). We also model the laser induced plasma by performing *static* equilibrium chemistry calculations to see whether desired reaction products are thermodynamically favorable and *dynamic* calculations of the expanding plasma plume to see how and where the products form.

2. EXPERIMENTAL

A sketch of the experimental set-up is shown in **Figure 1**. A Nd:YAG laser (1064 nm, 15 ns pulse width, 800 mJ pulse energy, 5 Hz repetition rate) is focused inside a reactor to create a plasma in the reactive gas mixture. The reactor consists of two coaxial quartz cylinders; it is loaded with gases shown in **Table 1**.

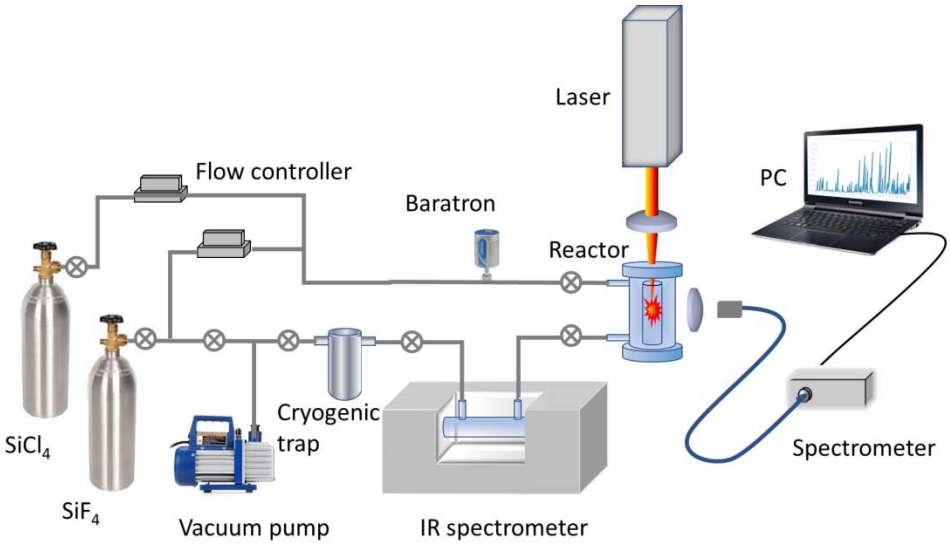

Figure 1. Experimental setup for PECVD with LIP and corresponding diagnostics.

The plasma is analyzed by OES while the gas mixture inside the reactor is analyzed by IR and MS both before and after the laser action. Solid residues that are deposited on the walls of the inner cylinder are studied by the reflectance FTIR.

BCl_3	BF_3	$SiCl_4$
H_2: BCl_3=10:1	H_2: BF_3=3:1	SiF_4
H_2: Ar: BCl_3=10:10:1	H_2: Ar: BF_3=3:4:1	$SiCl_4$: SiF_4=1:2.65
H_2: BCl_3: CH_4=9:1.5:1	H_2: BF_3: CH_4=9:1.5:1	$SiCl_4$: SiF_4=2.65:1

Table 1. Gases used in LIP experiments.

A numerical experiment on the gas mixtures was performed by first calculating the plasma equilibrium composition as a function of its temperature using open source software [CEARUN] and second, calculating plasma dynamic parameters using a hydrodynamic code [Shabanov 2018] and the same open source software embedded in this code.

3. RESULTS AND DISCUSSION

3.1. Halides of boron

The amount of the deposit enough for further analysis is collected with mixture BCl_3+H_2+CH_4. The deposit is identified as boron carbide and carbon (soot) by the reflectance FTIR technique. No deposit except soot (in methane) is observed for mixtures with BF_3. The OES spectra of gas plasma show efficient formation of BH, BX (X=Cl, F), and C_2 (in methane). The IR spectra of the reaction products after the laser action show the presence of the molecules already identified by OES plus precursors (BCl_3, BF_3, CH_4),

radicals ($HBCl_2$), and new derivatives (C_2H_2, B_2H_6). MS analysis confirms the presence of these molecules.

The results of experiment well agree with the predictions of both static and dynamic simulations. The model does not predict formation of solid boron or boron carbide from mixtures of BF_3 with hydrogen or methane, and same is observed in experiment. For mixtures of BCl_3 with the same gases, condensed phases of B, C, and B_4C form that is detected in experiment and predicted by the model. Some results of laboratory and numerical experiments are reproduced in **Figure 2**.

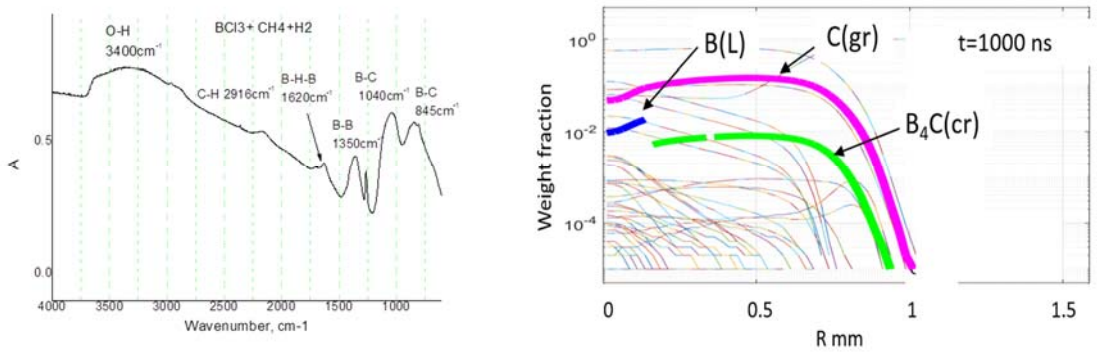

Figure 2. Left panel: IR absorption spectrum of solid deposit from the mixture H_2:BCl_3:CH_4=9:1.5:1. Right panel: dynamic 1D simulation of breakdown in 50% (CH_4+Ar) + 50% (BCl_3+H_2) gas mixture; snapshot of species concentrations at 1 μs of the plasma plume propagation time.

3.2. Halides of silicon

Generation of fluorochlorosilanes in the mixture of SiF_4 and $SiCl_4$ via the reactions $3SiF_4$ + $SiCl_4$ = 4 SiF_3Cl (1160 kJ/mole); SiF_4 + $SiCl_4$ = $2SiF_2Cl_2$ (307 kJ/mole); and SiF_4 + $3SiCl_4$ = $4SiFCl_3$ (71 kJ/mole) is thermodynamically unfavorable due to the positive Gibbs formation energy ΔG_{298} (in parentheses). These reaction products can easily be obtained in LIP after the plasma cools down and formerly dissociated atoms reassemble back into molecules. This is confirmed both experimentally and theoretically. As before, the plasma is analyzed by OES why the reactants and products by IR and MS. Optical emission spectra show the formation of SiCl, SiF, and $SiCl_2$ along with all expected elemental species and their ions. The IR spectra of plasma products reveal strong absorption bands and, hence, efficient formation of sought-after fluorochlorosilanes SiF_2Cl, $SiFCl_2$, $SiFCl_3$, SiF_3Cl, and SiF_2Cl_2 (**Figure 3.**, left panel); the MS measurements convincingly confirm this finding. From IR absorption measurements, a 60% maximum yield of fluorochlorosilanes is estimated for the mixture SiF4:SiCl4=1:1; the dominant specie is SiF_2Cl_2. The same high yield for SiF_2Cl_2 is predicted theoretically based on data generated by ab initio calculations of thermodynamic properties of fluorochlorosilanes. The result of the dynamic simulation for the mixture SiF_4:$SiCl_4$=1:1is exemplarily given in **Figure 3.**, right panel.

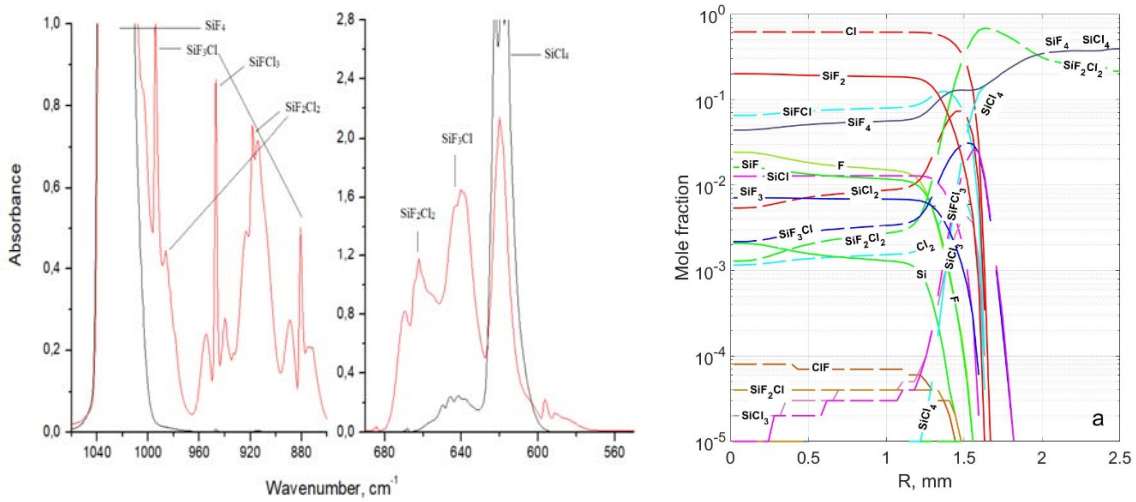

Figure 3. Left panel: IR absorption spectra of mixture $SiCl_4$:SiF_4=1:1 before (black) and after (red) the 40 min laser irradiation. Right panel: dynamic 1D simulation of breakdown in SiF_4: $SiCl_4$ = 1:1 gas mixture; snapshots of the plasma composition after the 5.0μs propagation time.

4. CONCLUSIONS

For the BX_3-containing systems (X=Cl, F), the creation of solid deposits of B, BH_3, and C (in mixtures with methane) is observed by LIP excited in the reactive gas mixtures BX_3+H_2 and BX_3+H_2+CH_4. The dynamic calculations of the expanding plasma plume predict coexisting condensed phases of boron, boron carbide, and graphite in mixtures with BCl_3. The maximum concentration of the condensed species is reached in peripheral plasma zones. Overall, the calculations and experimental results imply that PECVD-LIP can be a promising technique for efficient conversion of gaseous precursors into solid elemental constituents and their compounds.

For the SiX_4-containing systems (X=Cl, F), gaseous fluorochlorosilanes SiF_3Cl, SiF_2Cl_2, $SiFCl_3$ can efficiently be synthesized by LIP induced in SiF4+SiCl4 precursor gas mixtures. It is found that the total yield of fluorochlorosilanes in LIDB plasma comprises 60%, with ~30% of SiF_2Cl_2. The equilibrium chemical model adequately predicts the composition of LIP. The dynamic calculations of the expanding plasma plume also agree with experiment and show that fluorochlorosilanes form in peripheral plasma zone and show high sensitivity toward the mixture stoichiometry and plasma temperature.

5. ACKNOWLEDGEMENTS

The authors thank V. S. Polyakov, A. A. Ermakov, R. A. Kornev, and V. E. Shkrunin for calculations and measurements and Melsytech LTD (D. Stepanov, A. Stepanov, O. Yeremeykin) for technical support. P. S. acknowledges the DAAD/2019 grant 9165134 and RSF grant No 20-13-00035 and Russian Ministry of Education and Science grant

0095-2019-0008. The authors also thank Prof. U. Panne and Dr. K. Rurack for the support of this project.

6. REFERENCES

[Vurzel 1970] F. B. Vurzel, L. S. Polak, *Ind. Eng. Chem.*, 62 (1970) 8.
[CEARUN] https://cearun.grc.*nasa*.gov (accessed on 15 October 2020).
[Shabanov 2018] S. V. Shabanov, I. B. Gornushkin, *Appl. Phys. A*, 124 (2018) 716.

NANOPARTICLE ENHANCED LASER INDUCED BREAKDOWN SPECTROSCOPY: FUNDAMENTALS AND PERSPECTIVES

Vincent Gardette[1], Zita Salaikova[1,2], Elena Vaníčková[2], Marcella Dell'Aglio[3], Alessandro De Giacomo[1,3]*

[1]University of Bari, Department of Chemistry, Via Orabona 4, 70126 Bari-Italy
[2](CEITEC, Brno University of Technology, Purkyňova 656/123, 612 00 Brno, Czech Republic
[3]CNR-NANOTEC c/o University of Bari, Department of Chemistry, Via Orabona 4, 70126 Bari, Italy
**e-mail: alessandro.degiacomo@uniba.it*

1. INTRODUCTION

It has been recently proposed to use metallic nanoparticles for improving the sensitivity and the capabilities of laser ablation analytical techniques, such as LA ICP MS and LIBS (named respectively NE-LA-ICP-MS and NE-LIBS, NE stands for Nanoparticles Enhanced). Metallic NPs allow modulation and enhancement of the incoming laser pulse with the ignition of a surface plasmon resonance (SPR). These enhanced techniques present different advantages: the ablation occurs mainly on the NPs deposited on the surface of the sample which leads to few damages on this one and thus is interesting for numerous domain of applications [Dell'Aglio 2018]. In addition, sensitivity is hugely increased in the case of LIBS allowing the detection of ultra-traces in the range of ppb level [De Giacomo 2013, De Giacomo 2016] whereas, signal from LA-ICP-MS mediated by NPs is also increased, but in a more moderate way, achieving enhancement between 2 to 10 [Mangone 2020]. Mechanisms that relies behind this enhancement are not yet completely understood. In addition, it seems that, mainly, the NPs play a role on the plasma emission in the case of NE-LIBS [De Giacomo 2020], and on laser ablation and elemental fractionating in the case of NE-LA-ICP-MS [Holá 2018], which are two complete different processes.

2. EXPERIMENTAL

NE-LIBS experiments do not need any tuning setup, and in that way, experimental setup is a classical homemade LIBS setup with a pulsed Nd:YAG laser, 6 ns pulse duration, of fundamental wavelength 1064 nm, (Q-SMART 850, Quantel). Laser pulse is focalized on the target using a focal lens of various focal distance depending on the desired spot size and can be replaced by a microscope objective for conducting μ-LIBS experiment. Plasma emission light is collected with a fiber into a spectrometer (TRIAX 500, Andor) coupled with a CCD camera. Additional laser module can be used to change the laser wavelength into the 2nd and 3rd harmonics, respectively 532 and 354 nm, in order to fit perfectly the resonance band of the NPs system.

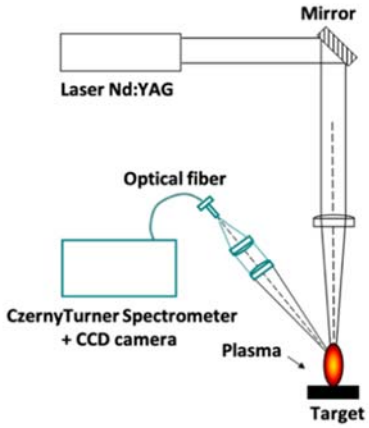

Figure 1. Experimental setup for typical LIBS and NE-LIBS measurement.

Various kind of NPs can be employed, of all different shapes, even if platinum, gold and silver spherical NPs are most commonly used. Sample preparation is quite fast and easy: µL drops of NPs colloidal solution are deposited on the sample surface and gently dried. The NPs size effect will be discussed below. It is important to notice that NE-LIBS effect can only occurs under specific conditions. First, the spot size must be large enough to ablate a large amount of NPs. Secondly, the laser fluence should be relatively low, so the NPs are not destroyed during the ablation. Finally, NPs should not aggregate during the deposition or inside the colloidal solution. This latter point is crucial in order to have a stable and reproducible signal. If all these conditions are fulfilled, NE-LIBS effect can occur and signal enhancement of some orders of magnitude can be reached.

3. RESULTS AND DISCUSSION

3.1. Analytical performance

Briefly, NE-LIBS can achieve a sensitivity close to the ppb level, and an enhancement of some order of magnitude between LIBS and NE-LIBS signal can be observed, especially on metallic target.

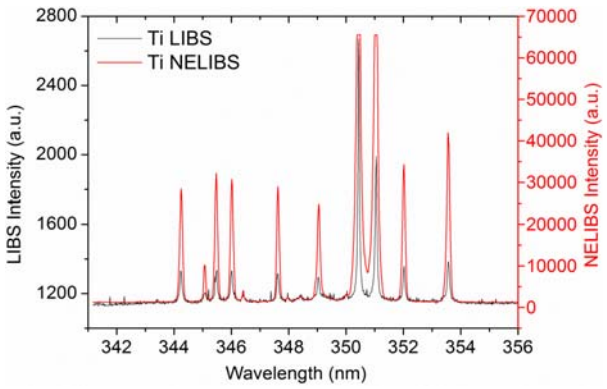

Figure 2. Typical NE-LIBS spectra obtained on a titanium target.

Even if NE-LIBS provides astonishing results on metallic target as shown in Figure 2, it can be used for a wide area of application, as seen in Table 1, including analysis of biological sample, liquids or even crystal and precious sample.

Target	Elements	NPs	Enhancement/LOD
Titanium	Ti	Ag, Au	En > 100
Steel	Fe	Ag	En = 5
Cu-based alloys	Pb, Sn,Mn	Au, Ag, Pt, Cu/CuO	En ~ 50
Al-based alloys	AlO, Ti,Fe	Au	En ~ 10
$CuSO_{4\,(aq)}$	Cu	Au	ppt level in 100 µl
$CuSO_{4\,(aq)}$, $NaF_{\,(aq)}$	Cu, F	Au	En = 3.5 For F LOD ~ 0.1% ppm in 20 µl
$AgNO_{4\,(aq)}$ $PbCl_{2\,(aq)}$, $PbSO_{4(aq)}$	Ag, Pb	Au Au	LOD <ppb in 2 µl En >10
Blood	Pb	Au	LOD ~ 10 ppb in 2 µl
RC Protein solution	Li	Au	En ~ 20
$CuSO_{4\,(aq)}$, $Cr(NO_3)_{2\,(aq)}$ $Pb(NO_3)_{2\,(aq)}$	Cu, Cr, Pb	ultrafine fibers +Au NPs	En ~ 4
Leaf	Fe, Mn, K, Ca, Mo	Au, Ag	En = 5
SiO_2 crystal	Si	Au	En = 30
ZnO pressed pellets of NPs	No plasmonic enhancement	ZnO	2<En<120
Tourmaline	Mn, Fe	Au	En ~ 10

Table 1. Analytical performance of NE-LIBS taken from [Dell'Aglio 2018].

3.2. Understanding the NE-LIBS effect

NPs play a double role during laser-induced plasma experiment: first during the ablation and then on the plasma phase. During the ablation, if the laser wavelength matches the absorption band of the NPs system, plasmonic effects will occur : a coherent and collective oscillation of the NPs system will be created and NPs electrons will be able to move freely between the NPs system and the plasma phase. In addition, NPs will be shielded during the ablation, and the laser pulse will be focused in the space between themselves, leading to multiple ignition point and thus to a more efficient ablation.

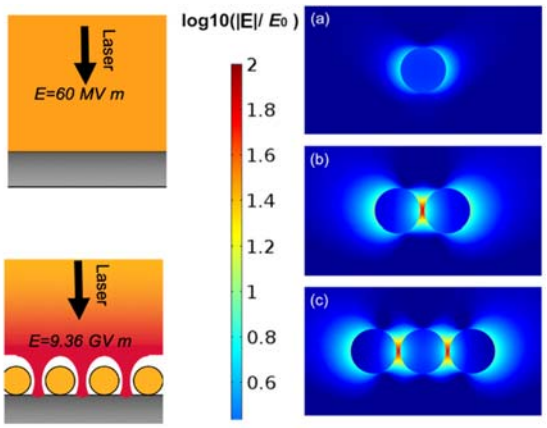

Figure 3. Laser-NPs interaction during laser ablation experiment.

After the laser pulse, NPs will survive the ablation and will be ejected at the top of the plasma. During its expansion, the plasma will slowly take in the NPs and vaporize them. It was shown that the NPs size was not affecting the global enhancement, but rather the temporal evolution of the signal instead.

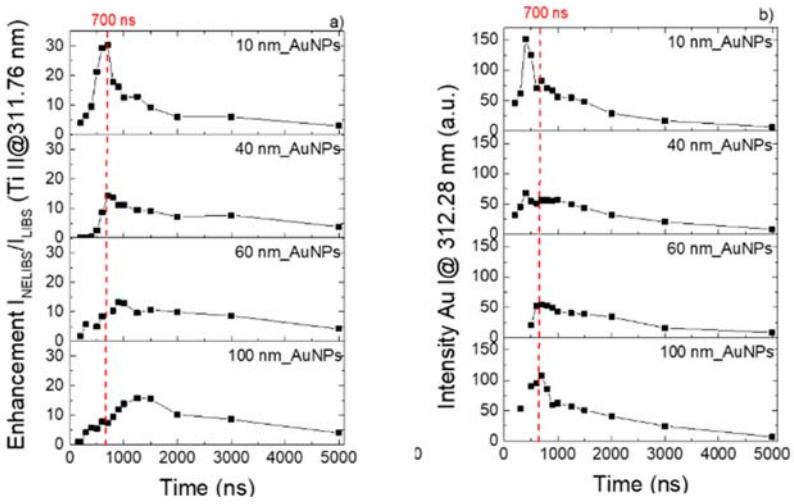

Figure 4. Temporal evolution of signal enhancement and gold (NPs) signal.

Finally, the NPs role on the plasma during its expansion is not yet fully understood. Only a small portion of the ablated mass will take part into the emission processes and it is supposed that the NPs can convert a part of the "sleeping mass" into emissive mass, and thus leading to a higher emission efficiency.

4. CONCLUSIONS

NE-LIBS has shown astonishing capabilities in term of emission efficiency, signal enhancement and sensitivity. NPs can be used for all kind of experiments and their use is not time consuming and no setup tuning is needed. In order to fully optimize the NE-LIBS

effect, there is a crucial need to understand all the fundamental processes which relies behind this enhancement. So far, the NPs are acknowledged to play a role during the ablation and on the plasma phase.

6. REFERENCES

[Dell'Aglio 2018] M. Dell'Aglio, R. Alrifai, A. De Giacomo, *Spectrochim. Acta B*, 148 (2018) 105.

[De Giacomo 2013] A. De Giacomo, R. Gaudiuso, C. Koral, M. Dell'Aglio, O. De Pascale, *Anal. Chem.*, 85 (2013) 10180.

[De Giacomo 2016] A. De Giacomo, C. Koral, G. Valenza, R. Gaudiuso, M. Dellaglio, *Anal. Chem.*, 88 (2016) 5251.

[A. Mangone 2020] A. Mangone, F. Mastrorocco, L. C. Giannossa, R. Comparelli, M. Dell'Aglio, A. De Giacomo, *Spectrochim. Acta B*, 163 (2020) 105731.

[De Giacomo 2020] A. De Giacomo, R. Alrifai, V. Gardette, Z. Salajková M. Dell'Aglio, *Spectrochim. Acta B*, 166 (2020) 105794.

[Holá 2018] M. Holá, Z. Salajková, A. Hrdlička, P. Pořízka, K. Novotný, L. Čelko, P. Šperka, D. Prochazka, J. Novotný, P. Modlitbová, V. Kanický, J. Kaiser, *Anal. Chem.*, 90 (2018) 11820.

WHY IS LIBS THE FUTURE ONLINE ANALYTICAL TECHNIQUE FOR PLASMA-FACING MATERIALS OF THERMONUCLEAR REACTORS?

Pavel Veis[1]*, Vishal Dwivedi[1], Alicia Marín Roldán[1], Gulab Singh Maurya[1], Sahithya Atikukke[1], Matej Veis[1], Matej Pisarčík[1] Milan Držík[2]

[1]Department of Experimental Physics, Comenius University, FMPI, Mlynská dol. F2, 842 48, Bratislava, Slovakia
[2]International Laser Center, Ilkovičova 3, 841 04 Bratislava, Slovakia
**e-mail: veis@fmph.uniba.sk*

1. INTRODUCTION

Currently, a global tendency of reducing carbon footprint is pursued by leading institutions and governments. Unlike other alternatives to fossil fuel burning, such as wind and solar sources, nuclear reactors provide a stable high energy output that can match the ever-rising demand. Even though nuclear fission plants have been well established (a total of 450 power plants in 31 counties), much of the research is being focused to nuclear fusion instead. An advantage over a fission reactor includes heavily reduced operational radioactivity and drastic reduction of radioactive waste. In fusion reactors deuterium and tritium are used as fuels. Deuterium is available in the seawater and tritium can be generated from lithium. For initiating the fusion reaction, a stable and very high temperature plasma is required. These conditions can be only achieved in magnetic confinement devices e.g. torus shaped tokamaks. One of such projects is The International Thermonuclear Experimental Reactor (ITER) that aims to generate fusion energy on a commercial scale in the range of 500 MW.

This research is focused on elemental analysis of plasma-facing components (PFCs) of the aforementioned ITER by means of laser-induced breakdown spectroscopy (LIBS). PFCs of a fusion device face harsh operating environment of high heat, radiation and neutron flux that lead to irreversible mechanical changes of the PFCs surface like cracking, blistering and erosion [Li 2016, Maury 2020, Merca 2011, Hai 2014]. During the high temperature plasma operation in tokamaks (despite of magnetic field confinement), the plasma interaction with walls - especially in the divertor and limiter zones - leads to the erosion of the PFCs. The eroded material migrates away and forms new mixed materials on the surface of the first wall or deposits in the form of flakes and dust in the cooler parts of tokamak.

Certain re-deposited materials exhibit higher fuel retention than original wall material and that is a serious problem for safety in the case of T fuel. In the case of ITER-like wall (tungsten divertor and beryllium principal wall), the re-deposition of Be/W layers together with O impurities leads to the more efficient trapping of D/T fuel than in the case of pure Be/W layers. In ITER, The maximum amount of permitted fuel within the

ITER reactor is up to 1 kg, so the retained T fuel in the first wall must be observed regularly to make sure its reliable operation with a complete fuel cycle [Oelma 2018].

Also due to the re-deposition of the impurities, the visibility of the mirrors and optical windows (essential components for the plasma diagnosis, imaging, and spectroscopy) is decreasing and their spectral transmittance and sensitivity is also changing. Their maintenance and protection is a serious issue for the operation of fusion devices [Mukhi 2009].

The study of material erosion and migration, the formation, release, and re-deposition of the dust are important issues. So, for the reliable and safe operation of the future fusion reactor, it is necessary to measure elemental compositions of all key PFCs periodically, for monitoring of impurities, its deposition pattern, and retained fuel.

The main advantages of laser-induced breakdown spectroscopy (LIBS) are in-situ and standalone analysis, no pre-treatment of the samples. LIBS analysis could be performed under vacuum, low-pressure, or up to atmospheric pressure environments and moreover magnetic field doesn't affect its performance. LIBS can be eventually combined with laser ablation (LA) based technique for the necessary cleaning process of the fusion device first wall [Fanto 2013, Schwe 2009].

2. RESULTS AND DISCUSSION

LIBS has been applied for the depth profile analysis of ITER-relevant materials, time-resolved and space-resolved analysis of PFCs, heating diagnostics of different PFCs, the study of multi-layered and calibrated samples, monitoring the features of the impurity layers deposited on the PFMs, in-situ and real-time diagnostics of the PFCs, etc [Brezi 2017, Maury 2017]. LIBS is an emission spectroscopic technique with the merits e.g., its speed, suitable for almost all kind of the samples, simultaneous multi-elemental analysis, minimal destructive nature (~1 μg material is required), analysis without sample preparation, the ability of contactless or remote analysis/sensing, immune to harsh environments, does not provide any interference itself, etc. Owing to its applicability and versatility, A robotic arm-based LIBS is being considered to monitor different parts of the reactor walls.

2.1. LIBS experimental set-up

Based on requirements in different fields, various LIBS set-ups such as conventional LIBS, back-collection LIBS, double pulse LIBS, etc. is being used for the elemental analysis and depth profile analysis of the samples [Maury 2020].

2.2. Calibration-free (CF) approach

For the CF-LIBS analysis [Ciucc 1999], more spectral lines for neutral and first ionization degree of the same element are necessary, if possible, emitted from different upper levels.

Otherwise, the evaluation of the electron temperature from the Boltzmann plot is doubtful. The transition probabilities for these lines should have good precision, and the spectral peaks should not be too weak, in addition, not to be in interference with other possible lines and not affected by self-absorption. We have performed a quantitative and depth profile analysis of the Be-W-D-based simulated layers (thickness 1.5–2 μm) on the Mo substrates for the H/D content. D content of the samples has been calculated using the CF-LIBS approach ~4.7% ± 2.9%, which is in good agreement with the other spectroscopic techniques for the same samples. We have also characterized Li-based coatings deposited on Ni-Cr based screws obtained after liquid metal experiments from the COMPASS vacuum chamber. After evaluation of plasma parameters using the multi elemental Boltzmann plot (MEBP) for different elements, impurities (e.g. Li, C, B) were quantified and depth profiling of Li content has also been verified.

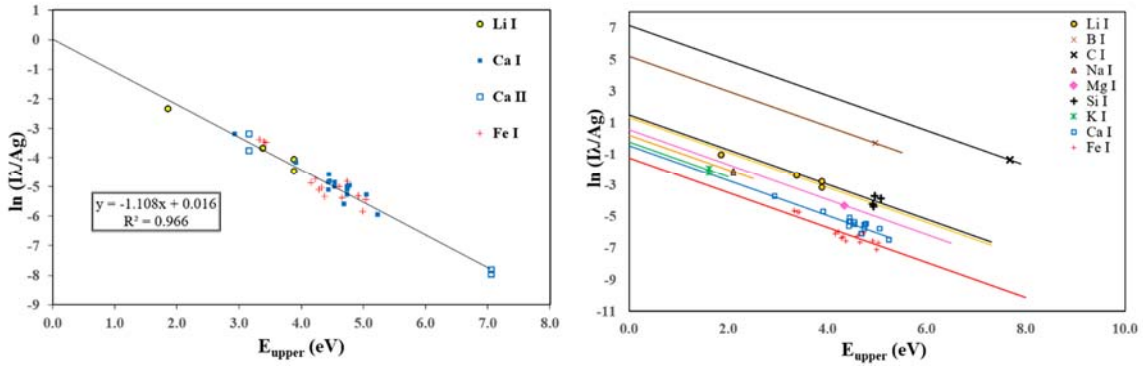

Figure 1. MEBP for the elements Li I, Ca I-II, and Fe I, and Boltzmann plot for Li I, B I, C I, Na I, Mg I, Si I, K I, Ca I, and Fe I spectral lines using the evaluated Te from the MEBP (for one of the screws from COMPASS Li campaign) [Veis 2020a].

CF-LIBS approach is also important for the control of impurities and dust pollution in tokamaks or linear fusion devices. Finally, this LIBS based monitoring is important for the knowledge of the pollution level caused by previous specific campaigns (e.g. previous carbon-based first wall, special limiter, or test with liquid metals, etc.). More precise T_e evaluation from W SB plots by enlarging LIBS analysis down to VUV range was recently proposed [Pribu 2016].

2.3. Molecular bands and LAMIS

Emission of molecular bands of diatomic radicals appears significantly later in the decay of laser induce plasmas, at the moment, when atomic lines start to disappear. So, the molecular emission measurements should have to be done separately from the atomic emission measurements. The perspective of the molecular emission spectroscopy in the fusion reactors wall diagnostics is the ability of an efficient isotopic analysis, due to the fact that the molecular lines isotopic shift is several order of magnitude higher than the atomic line isotopic shift. This idea of so-called Laser Ablation Molecular Isotopic

Spectrometry (LAMIS) was proposed in 2011 by Russo et al. [Russo 2011] and a review paper about the LAMIS method was published in [Bolsh 2016].

A possible application in LIBS fusion research is for the efficient quantification of relevant isotopes (e.g. D/H [Sarka 2013, Bolsh 2017], B [Mao 2011], C [Dong 2013], N, etc.) in laser-induced plasma after the conversion to molecular radicals as OH/ OD, BO, C_2, CN and others. For separation of hydrogen isotopes H/D (and in the future also T), the proposed molecular OH/OD (A-X, Δv=+1) transitions at 281 nm and 287 nm respectively have large separation (6 nm) of both isotopes bands [Russo 2011].

2.4. Depth profile analysis

LIBS has been found promising for the depth profile analysis by recording a successive number of LIBS spectra at the same position of the samples (especially of the analysis of thin layers and deposited impurities). Variation of the spectral signal with the number of laser shots represents depth profiling of the sample and provides information about thickness of the sample layer and ablation rate. LIBS depth profile analysis has been applied for different materials from fusion devices (JET, WEST, COMPASS, W7-X etc.). Veis et al. [Veis 2020b, Sucho 2017a] have applied depth profile analysis and quantification of the elements in Be/W(D) and Dwivedi et al. [Dwivedi 2020] have applied the same method for Be-O-C-D mixture samples and found in good agreement with other established technique like SIMS, NRA and TDS for D retention. Depth profile analysis of LiSn alloy by CF-LIBS was proposed in [Sucho 2017b].

Quantitative LIBS elemental and depth profile analysis of prepared mixed fusion relevant layers or post-mortem analysis of samples exposed in linear machines (Magnum-PSI, PSI-2) or tokamaks (JET, WEST, ASDEX, Compass….) were or could be used for validation by several off-line techniques like AAS, ICP-MS, spark discharge AES, NAA, RBS, NRA, TDS, SIMS, XRF and others. Most of the techniques are time-consuming and need special sample preparation, which is a drawback for in-situ, and online experiments.

2.5. Fuel retention and separation of the hydrogen isotope lines

For safety and control purposes of fusion devices, in-situ analysis of fuel retention is very important. In ITER, A remote-LIBS has been considered the most promising technique for the detection of fuel retention in plasma-facing walls and divertor materials regularly. Paris et al. [22, 23] have studied erosion, deposition, and fuel retention in fusion-related materials using LIBS and compared with other postmortem analysis techniques like NRA, RBS, and SIMS.

At high pressure, in laser-induced plasma, H_α (656.3 nm) and D_α (656.1 nm) lines are partly overlapped due to the Stark broadening effect. Large gate delay can reduce this overlapping, but spectral lines are with a low S/N ratio. Suitable conditions for resolving these lines has been optimized. At atmospheric pressure, suitable gate delay was optimized >2 μs, while vacuum conditions provide well-resolved D_α and H_α lines.

3. CONCLUSION

Owing to its inherent advantages (in-situ and standalone analysis, no pre-treatment of the samples, possible combination of laser diagnostics and laser cleaning process), LIBS, LIBS-based techniques are useful to diagnose and/or quantify the fuel retention, the impurities and the depth profiling of coatings and redeposited mixed materials related to the fusion devices.

4. ACKNOWLEDGEMENTS

The authors acknowledge the Scientific Grant Agency of the Slovak Republic (contract number VEGA-1/0903/17) and the Slovak Research and Development Agency (APVV-16-0612) for financial support. GSM would like to acknowledge the National Scholarship Programme of the Slovak Republic to provide research mobility.

5. REFERENCES

[Bolsh 2016] A. A. Bol'shakov, X. Mao, J. J. Gonzalez, R: E. Russo, *J. Anal. At. Spectrom.*, 31 (2016) 119.

[Bolsh 2017] A. A. Bol'shakov, X. Mao, R. E. Russo, *J. Anal. At. Spectrom.*, 32 (2017) 657.

[Brezi 2017] S. Brezinsek, J. W. Coenen, T. Schwarz-Selinger, et al., *Nucl. Fusion*, 57 (2017) 116041.

[Ciucc 1999] A. Ciucci, M. Corsi, V. Palleschi, S. Rastelli, A. Salvetti, E. Tognoni, *Appl. Spectrosc*., 53 (1999) 960.

[Dong 2013] M. Dong, X. Mao, J. Gonzalez, J. Lu, R. E. Russo, *Anal. Chem.*, 85 (2013) 2899.

[Dwivedi 2020] V. Dwivedi, A. Marín-Roldán, J. Karhunen, P. Paris, P. Veis et al., submitted to *Nucl. Mater. Energy*

[Fanto 2013] R. Fantoni, S. Almaviva, L. Caneve, F. Colao, A. M. Popov, G. Maddaluno, *Spectrochim. Acta B*, 87 (2013) 153.

[Hai 2014] R. Hai, P. Liu, D. Wu, H. Ding, J. Wu, G. N. Luo, *Fusion Eng. Des.*, 89 (2014) 2435.

[Li 2016] C. Li, C.-L. Feng, H. Y. Oderji, G.-N. Luo, H.-B. Ding, *Front. Phys.,* 11 (2016) 114214.

[Mao 2011] X. Mao, A. A. Bol'shakov, D. L. Perry, O. Sorkhabi, R. E. Russo, *Spectrochim. Acta B*, 66 (2011) 604.

[Maury 2017] G. S. Maurya, K. Belešová, M. Anguš, J. MišKovičová, M. Suchoňová, P. Veis, *Proceedings of ELITECH '17*, 2017.

[Maury 2020] G. S. Maurya, A. Marín-Roldan, P. Veis, A. K. Pathak, P. Sen, *J. Nucl. Mater.*, 541 (2020) 152417.

[Merca 2011] L. Mercadier, A. Semerok, P. A. Kizub, A. V. Leontyev, J. Hermann, C. Grisolia, P.-Y. Thro, *J. Nucl. Mater.*, 414 (2011) 485.

[Mukhi 2009] E. Mukhin, K. Vukolov, V. Semenov, S. Tolstyakov, M. Kochergin, G. Kurskiev, K. Podushnikova, A. Razdobarin, A. Gorodetsky, R. Zalavutdinov, V. Bukhovets, A. Zakharov, S. Bulovich, V. Veiko, E. Shakshno, *Nucl. Fusion*, 49 (2009) 085032.

[Oelma 2018] J. Oelmann, N. Gierse, C. Li, S. Brezinsek, M. Zlobinski, B. Turan, S. Haas, Ch. Linsmeier, *Spectrochim. Acta B*, 144 (2018) 38.

[Paris 2015] P. Paris, K. Piip, A. Hakola, M. Laan, M. Aints, S. Koivuranta, J. Likonen, A. Lissovski, M. Mayer, R. Neu, V. Rohde, K. Sugiyama, ASDEX Upgrade Team, *Fusion Eng. Des.*, 98-99 (2015) 1349.

[Paris 2017] P. Paris, J. Butikova, M. Laan, M. Aints, A. Hakola, K. Piip, I. Tufail, P. Veis, *Phys. Scr.*, T170 (2017) 014003.

[Pribu 2016] M. Pribula, J. Krištof, M. Suchoňová, M. Horňáčková, J. Plavčan, A. Hakola, P. Veis, *Phys. Scr.*, T167 (2016) 014045.

[Russo 2011] R. E. Russo, A. A. Bol'shakov, X. Mao, C. P. McKay, D. L. Perry, O. Sorkhabi, *Spectrochim Acta B*, 66 (2011) 99.

[Sarka 2013] A. Sarkar X. Mao, G. C.-Y. Chan, R. E. Russo, *Spectrochim. Acta B*, 88 (2013) 46.

[Schwe 2009 B. Schweer, G. Beyene, S. Brezinsek, N. Gierse, A. Huber, F. Irrek, V. Kotov, V. Philipps, U. Samm, M. Zlobinski, *Phys. Scr.*, T138 (2009) 014008.

[Sucho 2017a] M. Suchoňová, P. Veis, J. Karhunen, P. Paris, M. Pribula, K. Piip, M. Laan, C. Porosnicu, C. Lungu, A.Hakola, *Nucl. Mater. Ener.*, 12 (2017) 611.

[Sucho 2017b] M. Suchoňová, J. Krištof, M. Pribula, M. Veis, F. L. Tabarés, P. Veis, *Fusion Eng. Des.*, 117 (2017) 175.

[Veis 2020a] P. Veis, S. Atikkuke, A. M. Roldan, V. Dwivedi, M. Veis, P. Barton, M. Jerab, R. Dejarnac, *Nucl. Mater. Ener.,* 25 (2020) 100809.

[Veis 2020b] P. Veis, A. Marín-Roldán, V. Dwivedi, J. Karhunen, P. Paris, I. Jõgi, C. Porosnicu, C. P. Lungu, V. Nemanic, A. Hakola, *Phys. Scr.*, T171 (2020) 014073.

ASSESSMENT OF POLYMER DEGRADATION BY THE COMBINED USE OF LIBS AND LA-ICP-MS

Andreas Limbeck[1]*, Laura Pagnin[2], Rita Wiesinger[2], Manfred Schreiner[1,2], Lukas Brunnbauer[2]

[1]TU Wien, Institute of Chemical Technologies and Analytics, Getreidemarkt 9/164, 1060 Vienna, Austria
[2] Academy of Fine Arts, Schillerplatz 3, 1090, Vienna, Austria
**e-mail: andreas.limbeck@tuwien.ac.at*

1. INTRODUCTION

Synthetic polymers are nowadays widely used in a variety of applications, ranging from food packaging, construction materials to the housing of electronic devices. In general, the applied synthetic polymers are composed of an organic-carbon-chain polymer and different additives that give the materials the intended chemical and physical properties. Commonly applied additives include plasticizers, antioxidants, antistatic agents, lubricants, flame retardants or inorganic pigments.

During application, polymers are often exposed to harmful environmental conditions, causing changes in their chemical composition. In this context, the negative influences of sunlight but also contact with ambient gases and environmental liquids have to be mentioned. Whereas UV light and oxidative gases are known to promote degradation, corrosive gases or metals dissolved in rain, snow and river or sea-water are susceptible for uptake into the polymer network, resulting in increased concentrations of inorganic constituents in aged materials. All of these possible interactions contribute to unwanted changes in the polymer composition, which finally lead to altered material properties (e.g. bleaching of colors, reduced thermal stability, increased brittleness, etc.). Thus, analysis of synthetic polymers is experiencing growing interest due to increased environmental regulations and the need for sustainable polymer recycling strategies.

Traditional methods for the investigation of polymer degradation are FT-IR and Raman spectroscopy. Furthermore, Pyrolytic-GC-MS, MALDI-ToF–MS, thermogravimetric analysis (TGA) and differential thermal analysis (DTA) are frequently used techniques. Although well established, these techniques cannot provide the entire information required for thorough material analysis. In particular, with the aforementioned techniques sample analysis is limited to bulk investigations or surface near regions only. Additionally, detection of metal content within polymers with a high sensitivity is not feasible. These shortcomings could be circumvented with the use of LIBS and LA-ICP-MS. In the field of polymer analysis, broadband LIBS spectra have already been used for the identification [Sattmann 1998] and classification [Haddad 2014] of different polymer types. Additional benefits of LIBS are the possibility to perform spatially resolved analysis such as depth profile measurements.

In this contribution, we report the use of LIBS for assessment of polymer degradation. Moreover, the uptake of contaminations from the surrounding environment has been determined using LA-ICP-MS. The developed Tandem LA-ICP-MS/LIBS approach for polymer analysis has been applied for two different research tasks:

- Objects of art and cultural heritage are sometimes exposed to harsh environmental conditions. The permanent exposure to humidity, UV-radiation and corrosive gases results in the degradation of valuable artwork. As the fundamentals of the degradation process are still not completely understood, knowledge about durability and aging properties of applied art materials is of particular interest.

- At the end of their life-cycle, polymers often end up in the environment, for example in the form of microplastics which pose a significant threat to various ecosystems. Accordingly, the composition and metal contents of the degraded polymers should be monitored, to better estimate the adverse health effects of microplastics in the environment.

2. EXPERIMENTAL

A LIBS system (Model J200) equipped with a 266 nm Nd: YAG laser by Applied Spectra, Inc. (West Sacramento, California) was used for LIBS analysis. For collection and spectroscopic analysis of the radiation emitted by the laser-induced plasma, an optical fiber system connected to a Czerny-Turner spectrometer with six-channel CCD detection was employed. ICP-MS analysis of the generated aerosol was performed using a Thermo iCAP Qc quadrupole ICP-MS device (ThermoFisher Scientific, Bremen, Germany). Connection of the tandem LA/LIBS system to the mass spectrometer was achieved using PTFE tubing.

Modern paints composed of inorganic pigments and organic binders were prepared by mixing Alkyd Medium 4 (Lukas®, Germany) with 9 inorganic pigments (Kremer Pigmente, Germany). The pigment/binder ratio chosen was 1:3, prepared paint mixtures were cast on glass slides with a wet film thickness of approx. 150 µm. Sample drying was conducted at ambient conditions for 1 week. Accelerated stress tests were performed to cause degradation of the polymers as well as uptake of sulfur within the investigated samples. Therefore, samples were exposed to synthetic air in combination with corrosive gases (SO_2, H_2S and O_3) or UV light in a weathering chamber [Wiesinger 2010].

Degradation of commercial polystyrene thin films obtained from Goodfellow Inc. (Hamburg, Germany) was conducted by sample exposure to UV radiation and the concurrent treatment with oxidizing agents (H_2O_2 and HNO_3). Careful optimization of the process parameters ensured successful and reproducible degradation of the investigated micro-plastics. The degree of sample degradation was determined using FTIR spectroscopy and LIBS analysis. Subsequently sorption experiments with the aged

polystyrene thin films were performed, with the aim to investigate the temporal behavior of trace metal uptake. Aged polymer samples as well as unaged blank samples were exposed for different times to artificial seawater containing defined concentrations of selected trace metals.

3. RESULTS AND DISCUSSION

3.1. Degradation of modern art materials

Aim of this study was to test the feasibility of LIBS for measurement of polymer degradation and to confirm the uptake of sulfur with LA-ICP-MS of modern art materials consisting of a polymeric binder and inorganic pigments. Unlike most currently employed techniques for polymer characterization, these two are not limited to the surface but also enable depth profiling.

Using LIBS in combination with advanced data evaluation procedures, changes in the polymer composition due to weathering with corrosive gases and UV light was observed. Performing depth profiles on various samples exposed to different corrosive conditions, the influence and severity of these conditions on the degradation of the modern art material was assessed.

LA-ICP-MS parameters were optimized for the qualitative measurement of gas permeability into the investigated modern art material. The acquisition of depth profiles was successful. Again, the influence of different corrosive conditions on the sulfur uptake was investigated. These experiments revealed a high variation of the degree of sulfur uptake depending on the aging conditions. Additionally, sulfur uptake was not only observed in surface near regions of the investigated modern art material but also diffusion profiles into the bulk material were observed.

3.2. Artificial micro-plastic samples

FTIR measurements of the aged polystyrene samples revealed significant changes in the main polymer absorbance bands, in particular when compared to unaged reference samples. This outcome could be confirmed with LIBS, showing a significant increase in the intensity of the oxygen emission line at 777 nm, indicating partial oxidation of the polymer samples.

Samples derived from the sorption experiments were analyzed using tandem LA/LIBS-system, particular attention has been paid to determine the distribution of the absorbed metals within the polymer films. Depth profiles reveal that uptake of trace metals did not only occur on the sample surface, even in the underlying bulk material significant differences to the reference samples were observed. Thus, measurement of the sample surface is insufficient for assessment of total metal contents in aged polymer films, instead analysis over the whole film thickness is required. Moreover, the measured

uptake of the toxic trace metal Cd could be directly correlated with the information obtained for degradation and oxidation of the polymer sample.

4. CONCLUSIONS

A Tandem LA/LIBS approach has been successfully employed for assessment of polymer degradation and measurement of gas or metal uptake from ambient environment. In recent studies the occurrence of molecular emission lines in broadband LIBS spectra has been successfully used for identification and classification of polymers, here we demonstrated that measurement of these lines enables also the detection of polymer degradation. Analysis of the generated aerosol with ICP-MS has been shown to provide the sensitivity required for the determination of sample constituents present in traces only, such as corrosive gases used in the weathering experiments with modern art materials or the trace metals used in the sorption experiments performed with aged micro-plastics.

Analysis of aged modern art materials suggest that UV exposure or pretreatment with O_3 significantly influences the polymer permeability for SO_2 and leads to observable degradation of the polymeric binder material. As the capabilities and limitations of LIBS and LA-ICP-MS have been assessed, a multitude of additional experiments would be of interest to retrieve more comprehensive insights into the aging process of the investigated material.

Application of the proposed tandem LA/LIBS procedure for the analysis of aged micro-plastics has been found to be beneficial. This approach provides information about the extent of polymer degradation but also data about the distribution of the metals within the investigated polymer thin films. Thus, current knowledge about the interaction of trace metals with micro-plastics could be improved. In particular it could be shown that increased degradation of micro-plastics results in elevated trace metal uptake. Moreover, metal uptake is not limited to the sample surface only, even for the bulk material enhanced concentration levels were found.

5. ACKNOWLEDGEMENTS

Presented work was financially supported by the Austrian Research Promotion Agency (FFG) under project number 874907.

6. REFERENCES

[Sattmann 1998] R. Sattmann, I. Monch, H. Krause, R. Noll, S. Couris, A. Hatziapostolou, A. Mavromanolakis, C. Fotakis, E. Larrauri, R. Miguel, *Appl. Spectr*., 52 (1998) 456.

[Haddad 2014] J. El Haddad, L. Canioni, B. Bouscquet, *Spectrochim. Acta B*, 101 (2014) 171.

[Wiesinger 2010] R. W. Siesinger, M. Schreiner, C. Kleber, *Appl. Surf. Sci.,* 256 (2010) 2741.

NON-ANALYTICAL APPLICATIONS OF LASER-INDUCED BREAKDOWN SPECTROMETRY

Timur A. Labutin[1]*, Andrey M. Popov[1]

[1]Department of Laser Chemistry, Lomonosov Moscow State University
119234 Moscow, Leninskie gory 1b3, Russia
**e-mail: timurla@laser.chem.msu.ru*

1. INTRODUCTION

In laser-induced breakdown spectrometry (LIBS) a pulsed laser generates a plasma that vaporizes a small amount of a solid, gaseous or liquid sample. The emission spectrum of the excited species in the laser-induced plasma usually used for qualitative or quantitative analysis of the sample. The last 20 years witnessed a sharp growth of the number of publications devoted to the application of LIBS for analytical purposes. Indeed, LIBS started to be used for determining the elemental composition of various samples from molten steels [Noll 2001] to zooplankton [Sushkov 2020]. LIBS instruments were successfully implemented for on-line control of the raw materials [Gaft 2007], steel or sludge during production as well as finished products on the conveyor belt [Legnaioli 2020]. An interesting application of this method is elemental mapping, which was performed for minerals, plant tissues and histological examination of animal organs [Jolivet 2019].

Protocols and instrumentations for analysis of samples located in a harsh environment were designed and developed to perform measurements on the bottom of a sea up to 3000 m deep [Thornton 2015], to examine underwater garbage in the nuclear reactor core [Saeki 2014], and to study the Martian surface by means of the ChemCam and SuperCam [Meslin 2013, Nelson 2020]. Numerous papers are devoted to applications of LIBS for solving analytical problems like biomedical research, pharmaceutical products [Gaudiuso 2018], food [Markiewicz-K. 2017], analysis of aerosols [Diaz 2020], cultural heritage objects [Botto 2019] and so on. Several handheld LIBS instruments appeared on the market in recent years aiming at providing fast sorting of scrap, plastics or geological samples [Senesi 2021]. Thus, LIBS instruments with pulsed solid state ns-lasers became a “work horse” in various analytical applications. Besides this, there are other application areas where the emission of laser-induced plasma can be employed to solve specific, mostly theoretical tasks. We aim to focus on such non-analytical applications, namely the fundamental studies of laser ablation itself, determination of atomic line parameters (mostly Stark broadening parameters) and imitation of radiation from cosmic objects.

2. RESULTS AND DISCUSSION

The model of the evolution of a laser plasma is based on numerical simulation of ongoing processes [Shabanov 2014], relying on data obtained by optical tomography of plasma. Spectra of laser-induced plasma is also used to support the modeling of the processes occurring during laser–solid interaction [Bogaerts 2005]. This model was then applied to study the influence of laser irradiance, pulse duration and wavelength on laser ablation. In case of fs-plasma the competing processes lead to formation of several fractions in plasma plume. The LIBS helps to distinguish three different velocity populations during the plasma expansion: ions with high kinetic energy, neutrals with a velocity comparable to the nanosecond regime, and lastly by nanoscale clusters.

The next possibility is the determination of transition probabilities in the laser-induced plasma. In this case, branching ratios are determined by measuring the relative emission-line intensities for lines arising from the same upper levels in an optically thin laser-produced plasma. Following these relative values of transition probabilities are put on an absolute scale [Ferrero 1997]. Laser-induced plasmas are also quite extensively used for the determination of Stark parameters [Konjević 2002, Popov 2016], relatively easy to work with, have considerable electron number density and allow selecting different working conditions merely by changing temporal parameters of signal acquisition. Generating of a long plasma ("long spark") instead of a spherical plasma can provide the following advantages for Stark parameter measurements: *i)* illumination of the whole available focal plane of spectrograph, thus increasing the vertical dimension of plasma image on the detector 5–7-fold, which leads to an enhancement of signal-to-noise ratio; *ii)* a long spark is more homogeneous than a spherical one, as we demonstrated earlier, resulting in lesser optical thickness and lower experimental errors (<10%). This allowed us to accurately estimate an impact of hyperfine splitting on the profile shapes of the copper lines taking also into account the isotope shifts. We have shown that both effects considerably influence shift and width of Cu I line at 510.554 nm, and shifts of Cu I lines at 515.324 and 521.820 nm. Hyperfine structure and isotope shift additionally broad and shift the profile of the Cu I 510.554 nm line. This observation helps to resolve observed discrepancies between existing theoretical results and experimental data.

Last, we consider the time-evolution of the spectra of laser-induced plasma of high-purity iron in air, which is used to mimic the FeO pseudo-continuum emission. The iron oxide "orange arc" bands are unambiguously detected in persistent meteor trains, meteor wakes, and clouds, as well as in the terrestrial airglow. In contrast to the majority of other astronomically important diatomic molecules, theoretical simulation of the FeO rovibronic spectra is not feasible due to the extremely condensed and strongly perturbed multiplet structure of its excited states. The LIBS spectra were convolved with Gaussian profile with the FWHM equal to 0.38 nm which is provided a good agreement between the observed profiles of the Fe I isolated line at 537.15 nm in LIBS and Benesov meteor spectra. For comparison, the bolide spectrum at 39 km altitude was chosen, since it contains both persistent Fe I lines and FeO peaks. The significant variations of the intensity of the band at 625 nm should be noted. Such strong variations cannot be

explained by changes in the level population due to changes in temperature. At the same time, this can be easily explained if one assumes a significant contribution to the 625 nm band from FeO_2 emissions as the laser plume cools, which is confirmed by the thermodynamic calculations. Although current experiments have been performed in air at atmospheric pressure, they provide high resolution spectra, which are similar to bolide spectra. Moreover, it seems possible to complete a simultaneous fit for both atomic and molecular emissions of meteor spectra in order to avoid errors due to the erroneous exclusion of atomic lines. The environment of FeO airglow emission looks to be quite different from that of meteor events and laser experiments. Considering that the cold FeO molecules in the upper Earth's atmosphere are excited by solar radiation during the day, while FeO molecules produced during bolide events and laser experiments are hot, LIBS experiments seem to be more suitable for modeling FeO emission in meteor spectra at low altitudes.

3. REFERENCES

[Noll 2001] R. Noll, H. Bette, A. Brysch, M. Kraushaar, I. Mönch, L. Peter, V. Sturm, *Spectrochim. Acta B*, 56 (2001) 637.

[Sushkov 2020] N. I. Sushkov, N. V. Lobus, I. V. Seliverstova, T. A. Labutin, *Opt. and Spectrosc.,* 128 (2020) 1343.

[Gaft 2007] M. Gaft, I. Sapir-Sofer, H. Modiano, R. Stana, *Spectrochim. Acta B*, 62 (2007) 1496.

[Legnaioli 2020] S. Legnaioli, B. Campanella, F. Poggialini, S. Pagnotta, M. A. Harith, Z. A. Abdel-Salam, V. Palleschi, *Anal. Methods,* 12 (2020) 1014.

[Jolivet 2019] L. Jolivet, M. Leprince, S. Moncayo, L. Sorbier, C.-P. Lienemann, V. Motto-Ros, *Spectrochim. Acta B*, 151 (2019) 41.

[Thornton 2015] B. Thornton, T. Takahashi, T. Sato, T. Sakka, A. Tamura, A. Matsumoto, T. Nozaki, T. Ohki, K. Ohki, *Deep Sea Res. Part I,* 95 (2015) 20.

[Saeki 2014] M. Saeki, A. Iwanade, C. Ito, I. Wakaida, B. Thornton, T. Sakka, H. Ohba, *J. Nucl. Sci. Technol.*, 51 (2014) 930.

[Meslin 2013] P.-J. Meslin, *Science,* 341 (2013) 6153.

[Nelson 2020] T. Nelson, et al., *2020 IEEE Aerospace Conference*, 1-12, 2020.

[Markiewicz-K. 2017] M. Markiewicz-Keszycka, X. Cama-Moncunill, M. P. Casado-Gavalda, Y. Dixit, R. Cama-Mouncunill, P. J. Cullen, C. Sullivan, *Trends Food Sci. Technol.*, 65 (2017) 80.

[Botto 2019] A. Botto, B. Campanella, S. Legnaioli, M. Lezzerini, G. Lorenzetti, S. Pagnotta, F. Poggialini, V. Palleschi, *J. Anal. At. Spectrom.*, 34 (2019) 81.

[Diaz 2020] D. Diaz, D. W. Hahn, U. Panne: LIBS for aerosol analysis in: Laser-Induced Breakdown Spectroscopy, *Elsevier*, 2020.

[Gaudiuso 2018] R. Gaudiuso, E. Ewusi-Annan, N. Melikechi, X. Sun, B. Liu, L. F. Campesato, T. Merghoub, *Spectrochim. Acta B*, 146 (2018) 106.

[Senesi 2021] G. S. Senesi, R. S: Harmon, R. R: Hark, *Spectrochim. Acta B*, 175 (2021) 106013.

[Shabanov 2014] S. V. Shabanov, I. B. Gornushkin, *Spectrochim. Acta B*, 100 (2014) 147.

[Bogaerts 2005] A. Bogaerts, Z, Chen., *Spectrochim. Acta B*, 60 (2005) 1280.

[Ferrero 1997] F. S. Ferrero, J. Manrique, M. Zwegers, J. Campos, *J. Phys. B,* 30 (1997) 893.

[Konjević 2002] N. Konjević, A. Lesage, J. R. Fuhr, W. L. Wiese, *J. Phys. Chem.*, 31 (2002), 819.

[Popov 2016] A. M. Popov, T. F. Akhmetzhanov, T. A. Labutin, S. M. Zaytsev, N. B. Zorov, N. V. Chekalin, *Spectrochim. Acta B*, 125 (2016) 43.

STUDY OF THE FRAGMENTATION OF SOLID DRUG PARTICLES DURING ABLATION WITH DIFFERENT PULSE LENGTH LASERS

Tamás Smausz[1]*, Eszter Nagy[1], Tamás Gera[1], Zsolt Homik[1], Judit Kopniczky[1], Tibor Ajtai[1], Rita Ambrus[2], Piroska Szabó-Révész[2], Martin Ehrhardt[3], Klaus Zimmer[3], Pierre Lorenz[3], Béla Hopp[1,4]

[1]Department of Optics and Quantum Electronics, University of Szeged, 6720 Szeged, Dóm square 9, Hungary
[2]Institute of Pharmaceutical Technology and Regulatory Affairs, University of Szeged, 6720 Szeged, Eötvös street 6, Hungary
[3]Leibniz-Institut für Oberflächenmodifizierung e. V., Permoserstraße 15, 04318 Leipzig, Germany
[4]Department of Materials Science, Interdisciplinary Excellence Centre, University of Szeged, 6720 Szeged, Dugonics square 13, Hungary
**e-mail: tomi@physx.u-szeged.hu*

1. INTRODUCTION

A large number of pharmaceutical drugs are poorly water-soluble and have relatively low bioavailability, therefore significant efforts have been made to develop methods for improving their solubility and dissolution rate. Due to its high efficiency, the drug particle size reduction is one of the frequently used methods, since the increase of specific surface (surface to volume ratio) leads to enhanced dissolution rate and a higher bioavailability during the administration [Mosharraf 1995, Shegokar 2010]. Besides the different conventional approaches applied for size reduction, such as grinding, wet milling, forming of solid dispersions for which the smallest attainable sizes remain in the micrometer regime, in the last decade several studies aimed the fragmentation of drug particles by means of pulsed laser ablation. While laser ablation in gas or liquid environments has been widely used for nanoparticle production from inorganic target materials, there are much fewer studies on the production of sub-micrometer sized particles of organic or pharmaceutical compounds with this method [Sylvestre 2011, Ding 2014, Hopp 2018, Gera 2020, Ambrus 2020].

In this study we compare the main properties of the particles produced by pulsed laser ablation of three poorly water-soluble nonsteroidal anti-inflammatory drugs (NSAID) (ibuprofen, meloxicam and niflumic acid) tablets when using of various laser types with pulse lengths in nanosecond, picosecond and femtosecond range.

2. EXPERIMENTAL

The target tablets were produced using a hydraulic compactor at 175 MPa pressure from the following commercially available drug powders:

- Ibuprofen (α-Methyl-4-(isobutyl) phenylacetic acid): white color, particle size of 15.3 μm (d(0.5)), 75-77 °C melting point, 157 °C boiling point, 230 to 250 °C decomposition temperature;
- Meloxicam (4-hydroxy-2-methyl-N-(5-methyl-2-thiazolyl)-2H-benzothiazine-3-car-boxamide-1,1-dioxide): yellow color, particle size of 3.78 μm (d(0.5)), 100% crystalline, 254 °C melting/decomposition temperature;
- Niflumic acid (NIF) (2-(3-(trifluoromethyl)-phenyl)-amino)-3-pyridinecarboxylic acid, white color, 18.85 μm (d(0.5)) particle size, 203 °C melting/decomposition temperature.

Irradiation of the targets was performed in ambient pressure using the following lasers:

- nanosecond range, with 1.5–12 J/cm^2 fluence:
  - KrF excimer laser: FWHM= 18 ns, λ= 248 nm, 10 Hz repetition rate
  - Nd:YAG laser: FWHM= 6 ns, λ= 532/1064 nm, 10 Hz repetition rate
- picosecond range, 0.45–4.35 J/cm^2 fluence
  - Nd:YAG laser: FWHM= 20 ps, λ= 355/532/1064 nm, 80 kHz repetition rate
- femtosecond range, 0.7–1.5 J/cm^2 fluence
  - Ti:sapphire: FWHM=135 fs, λ=800 nm, 10 Hz repetition rate

The ablated aerosol particles were transported by continuous air/N2 flow and collected on a filter membrane. The collected particles were analyzed by FTIR spectrometry and scanning electron microscopy (SEM). In some cases the size distribution of the produced aerosol particles was analyzed by Scanning Mobility Particle Sizer (SMPS) and Optical Particle Counter (OPC). For the nanosecond ablation the material removal process was studied with fast photographic method.

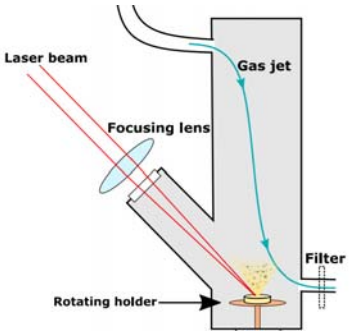

Figure 1. Experimental setup.

3. RESULTS AND DISCUSSION

3.1. Nanosecond ablation

FTIR spectra of the collected particles showed significant chemical decomposition in case of ablation at UV (248 nm) wavelength for all the three compounds, while the spectra maintained their characteristics for visible (532 nm) and NIR (1064 nm) wavelengths for all the fluencies, where notifiable material removal occurred [Gera 2020].

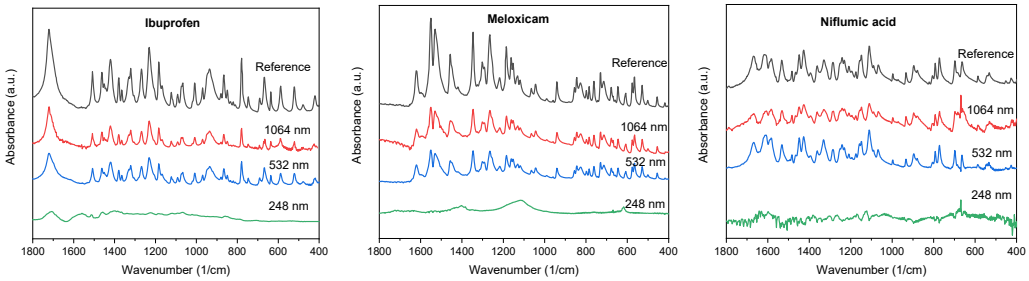

Figure 2. FTIR spectra of the nanosecond ablated drug particles.

SMPS measurements performed with 532 and 1064 nm showed that for a given compound the variation in fluence and wavelength had no strong effect on the size distribution of the particles transported by the gas stream. The smallest particles were detected in case of ibuprofen with modus values well below 100 nm, while the highest modus values with the broadest size distributions were obtained for the meloxicam particles. Practically there were no aerosol particles with sizes above 1 μm in the gas stream as demonstrated by OPC measurements. The number of ablated particles was the highest for meloxicam and the lowest for ibuprofen [Gera 2020].

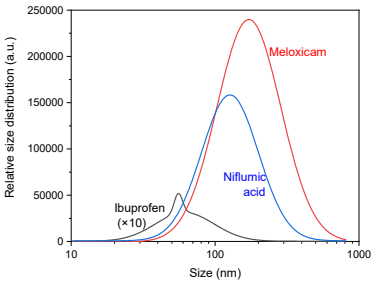

Figure 3. Characteristic SMPS size distributions of the particles ablated at 532 nm.

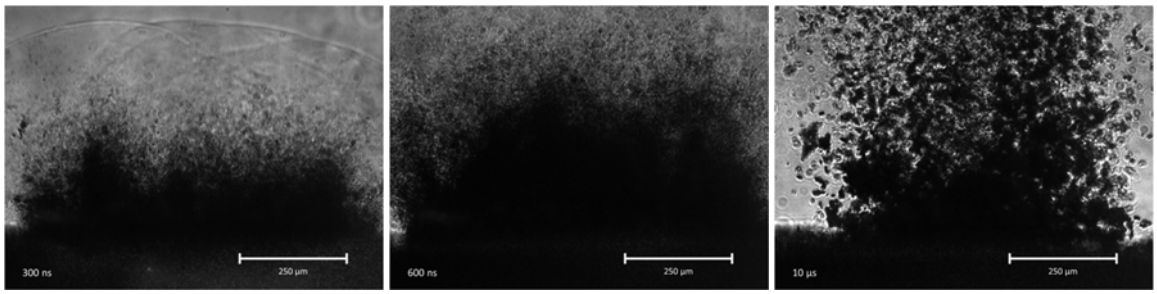

Figure 4. Material ejection when ablating meloxicam at 1064 nm and 9 J/cm^2 fluence.

Fast imaging revealed that the ablation mechanism is the same for all three drugs. The irradiation-generated shock wave is followed by a slightly slower material ejection. This material cloud is initially formed by large number of high speed fine particles (probably of sub-micrometer size) followed by the ejection of larger fragments in the micrometer range that have a lower speed. Particles much larger than those detected by SMPS are also ejected, however, these will probably sediment in the ablation chamber before reaching the gas extraction pipe and thus, the extracted gas stream will contain only smaller aerosol particles.

3.2. Picosecond ablation

In case of meloxicam and NIF the FTIR spectra of particles produced by ablation at 532 and 1064 nm showed good correspondence with that of starting materials, while in case of 355 nm wavelength the spectra were distorted in all the applied fluence range. Contrary to these, in case of ibuprofen measurable amount of ablated material was only obtained at 355 nm and the spectra maintained their characteristics as compared to the reference. The surface of the ibuprofen tablets was melted by the irradiation at all wavelengths, probably caused by the relatively low melting point as compared to the other two drugs.

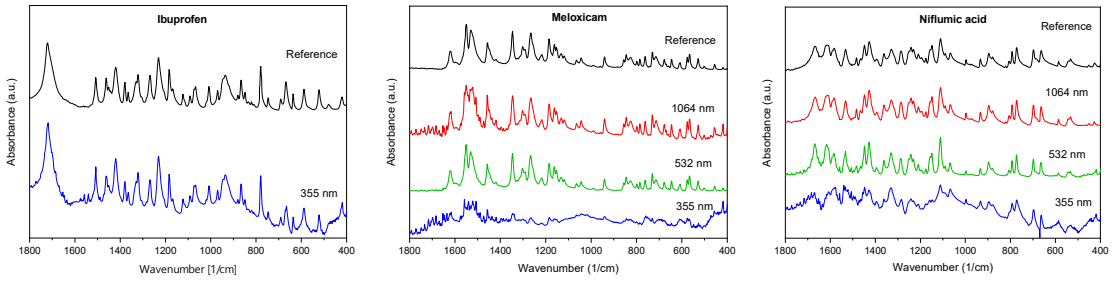

Figure 5. FTIR spectra of drugs ablated with picosecond laser pulses.

In this series of experiments the gas outlet point was places as close to the ablated surface as to extract all the ablated material and to deposit onto a membrane filter. As the SEM images of the deposits demonstrated, in cases of meloxicam and NIF the size of the produced particles ranged from ~100 nm up to 1-2 micrometers, much smaller than the

particle sizes of the original powders. In case of ibuprofen separated particles could not really be distinguished indicating their impact in molten state.

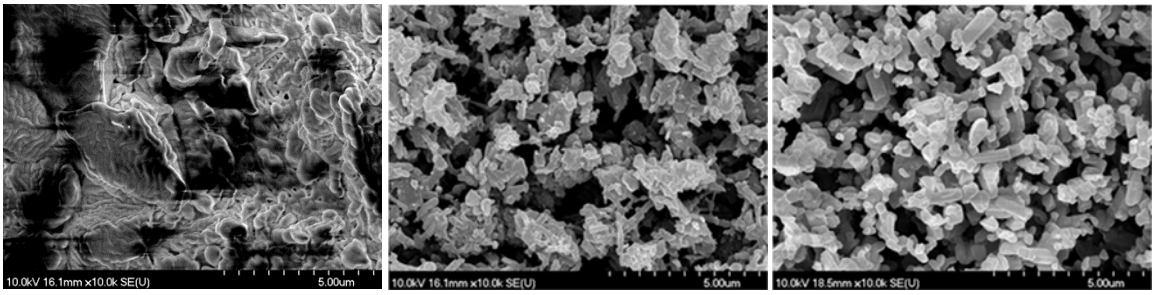

Figure 6. SEM image of ablatum collected after ibuprofen (left, 355 nm), meloxicam (middle, 532 nm) and niflumic acid (right, 532nm) ablation.

3.3. Femtosecond ablation

FTIR measurements of the particles produced by 800 nm femtosecond ablation of meloxicam showed good correspondence with the reference spectra in all the studied fluence range. The morphology of the particles strongly differed from those obtained at longer pulse durations. As shown on SEM images all the particles deposited on the filter membrane show spherical symmetry. Spherical particles in submicrometer size range have smooth surface, while the larger ones (up few micrometers) have surfaces covered with cracks and delaminated layers. The majority of the deposit is formed by spherical nanoparticles below 100 nm aggregated into longer chains.
The particle production by the femtosecond ablation showed much lower efficiency as compared to the nanosecond and picosecond ablation. First trials on NIF and ibuprofen showed similarly low ablation rate, therefore their ablation was not studied in detail.

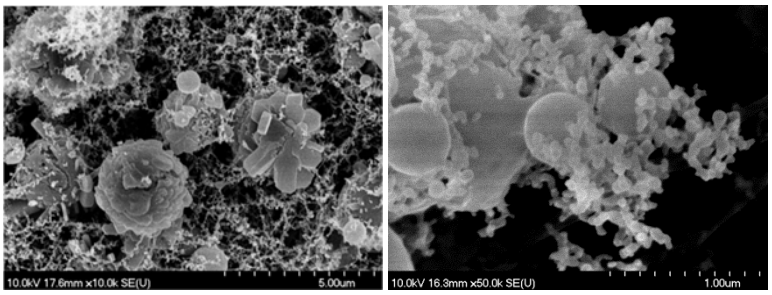

Figure 7. SEM images at different magnifications on ablatum collected from meloxicam.

4. CONCLUSIONS

Laser ablation of pressed drug tablets can be a promising way for fragmentation of poorly water-soluble drug materials and/or producing aerosols. While in the commercially

available powders of the studied compounds most of the mass exists in form of particles in tens of micrometer sizes, the particles generated by laser ablation ranges from about 100 nm to few micrometers. When using nanosecond and picosecond lasers the particles are mostly produced as solid fragments. The efficiency of size reduction is better in case of picosecond laser, as the nanosecond ablation removes from the targets larger material clusters, too, which sediment in bottom of the chamber. As compared to these, the femtosecond laser ablation produces spherical particles and nanoaggregates, while the ablation rate is relatively low.

5. ACKNOWLEDGEMENTS

The project has been supported by the European Union, co-financed by the European Social Fund (EFOP-3.6.2-16-2017-00005); the Ministry of Human Capacities, Hungary grant (TUDFO/47138-1/2019-ITM FIKP program) and the DAAD researcher exchange program (no. 308168). T. Ajtai is indebted for his János Bolyai Research Scholarship of the Hungarian Academy of Sciences.

6. REFERENCES

[Mosharraf 1995] M. Mosharraf, C. Nyström, *Int. J. Pharm.*, 122 (1995) 35.

[Shegokar 2010] R. Shegokar, R. H. Müller, *Int. J. Pharm.*, 399 (2010) 129.

[Sylvestre 2011] J. P. Sylvestre, M.-C. Tang, A. Furtos, G. Leclair, M. Meunier, J.-C. Leroux, *J. Control. Release*, 149 (2011) 273.

[Ding 2014] W. Ding, J.-P. Sylvestre, E. Bouvier, G. Leclair, M. Meunier, *Appl. Phys. A*, 114 (2014) 267.

[Hopp 2018] B. Hopp, E. Nagy, F. Peták, T. Smausz, J. Kopniczky, Cs. Tápai, J. Budai, I. Z. Papp, Á. Kukovecz, R. Ambrus, P. Szabó-Révész, *J. Phys. D. Appl. Phys.*, 51 (2018) 165401.

[Gera 2020] T. Gera, E. Nagy, T. Smausz, J. Budai, T. Ajtai, F. Kun-Szabó, Zs. Homik, J. Kopniczky, Z. Bozóki, P. Szabó-Révész, R. Ambrus, B. Hopp, *Sci. Rep.*, 10 (2020) 15806.

[Ambrus 2020] R. Ambrus, P. Szabó-Révész, T. Kiss, E. Nagy, T. Szűcs, T. Smausz, B. Hopp, *J. Drug Deliv. Sci. Technol.*, 57 (2020) 101727.

RECENT ADVANCES IN THE IMAGING OF BIOLOGICAL TISSUES AT THE BRNO UNIVERSITY OF TECHNOLOGY

Pavel Pořízka[1,2]*, Pavlína Modlitbová[1], Sára Střítežská[1], Anna Šindelářová[1], Jozef Kaiser[1,2]

[1]Central European Institute of Technology (CEITEC) Brno University of Technology, Purkyňova 123, 612 00 Brno, Czech Republic
[2]Faculty of Mechanical Engineering, Brno University of Technology, Technická 2896/2, 616 69, Brno, Czech Republic
**e-mail: pavel.porizka@ceitec.vutbr.cz*

1. INTRODUCTION

Laser-Induced Breakdown Spectroscopy (LIBS) is an optical analytical technique with a multi-element bioimaging capability in various biologic matrices. During the years of LIBS development, the major application field has been in industry. However, during the last two decades, LIBS became a useful imaging tool in different biologic matrices, e.g. bones, tooth, skin, mammals' organs, and in the plant science. In this work, we present an overview of the Brno University of Technology (BUT) Laser Spectroscopy laboratory achievements in biotic sample analysis. The plant bioimaging started in 2007 by pioneering paper [Kaiser 2007] which established the Pb content in sunflower leaves (*Helianthus annuus*) by using the femtosecond laser (Ti:sapphire; 795 nm) with an energy of 0.1 mJ per pulse. The bioimaging of macronutrients, micronutrients, non-essential elements, and even several types of nanoparticles in various plant species and plant tissues were established in several following papers [Kaiser 2007, Galiová 2007, Galiová 2008, Kaiser 2009, Kryštofová 2009, Galiová 2011, Krajcarová 2013, Krajcarová 2017, Modlitbová 2018, Modlitbová 2019, Modlitbová 2020a]. Also, our and other groups bioimaging studies were summarized in two extensive review papers [Kaiser 2012, Modlitbová 2020b].

Our last plant study deals with bioimaging of Cd contained in CdTe Quantum Dots (QD) in *Sinapis alba* (white mustard) plant. The LIBS maps with a lateral resolution of 100 μm were constructed for the whole plants, and maps with a lateral resolution of 25 μm (micro-LIBS arrangement) were used to analyze only the most interesting parts of plants with Cd presence (e.g. root tips or a part crossing the root into the above-ground part) [Modlitbová 2020a].

2. EXPERIMENTAL

LIBS system consisting of a nanosecond laser (CFR 400, Quantel, France; 532 nm, 20 Hz, 10 ns), a Czerny-Turner spectrometer Shamrock (Andor, Great Britain), and an ICCD

detector iStar 734 (Andor, Great Britain). For micro-LIBS system, the extensive changes in the focusing and collecting optics were done.

2.1. Plant LIBS experiments

The apparatus settings were optimized a priori: 0.15 μs of the gate delay, 50 μs of the detection integration time, and 20 mJ of the laser pulse energy. The whole plant area was analyzed in a raster of spots with a 100 μm lateral resolution. The emission line Cd I 508.56 nm was selected based on our previous experience. The line intensity was evaluated as the maximum line intensity after the appropriate background subtraction and after the internal standardization to total emissivity. Intensities of analytical emission lines were then depicted as 2D maps representing the spatial distribution of Cd in plant samples.

2.2. Plant micro-LIBS experiments

The apparatus settings were optimized a priori: 0.4 μs of the gate delay, 50 μs of the detection integration time, and 3.0 mJ of the laser pulse energy. The only several small parts per plant were analyzed (5 × 5 mm) in a raster of spots with a 25 μm lateral resolution. The emission line Cd I 361.05 nm was evaluated because it showed better intensity than the previously used emission line Cd I 508.56 nm. However, the same line intensity was evaluated as for LIBS experiments.

3. RESULTS AND DISCUSSION

The two-dimensional maps of Cd distribution in *S. alba* were obtained using LIBS together with micro-LIBS analyses. LIBS with a lateral resolution of 100 μm was used to assess Cd distribution through the whole plant (**Figure 1.** A), while micro-LIBS with a lateral resolution of 25 μm was used to analyse only the most interesting parts of plants, for example root tips or the part crossing the root into the above-ground part (**Figure 1.** B).

The size of LIBS and micro-LIBS maps was chosen based on the assumed time of analysis. The time of LIBS measurement of an average map of the whole plant with 100 μm lateral resolution was around 45 min (laser pulse frequency 20 Hz). It is not possible to map routinely the whole plant with a resolution of 25 μm due to significantly rising time of measurements (approximately 6 h).

Only a very little number of LIBS studies in a similar lateral resolution dealing with NP distribution in plants has been published until now. Our research group successfully presented three papers dealing with distribution of silver NPs, Cd-based QDs, and photon-upconversion NPs in plants [Krajcarová 2017, Modlitbová 2018, Modlitbová 2019]. Until now, the best lateral resolution was achieved by Krajcarová [Krajcarová 2017], who analyzed silver NPs in cross-sections of *Vicia faba* with lateral resolution 50 μm.

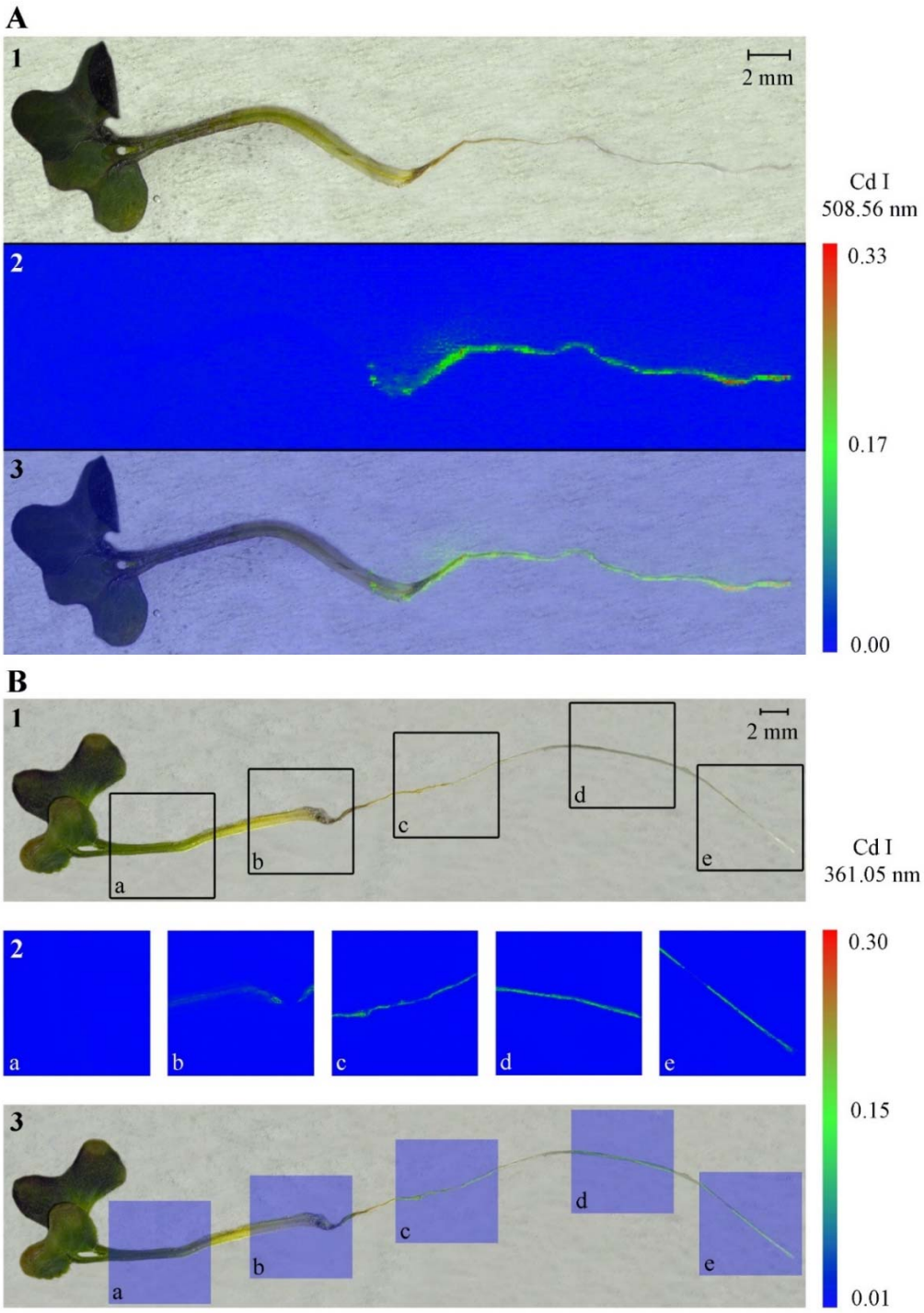

Figure 1. **A)** (1) Photograph of *S. alba* plant exposed to CdTe QDs at the nominal concentration 200 µM Cd before LIBS measurements. (2) LIBS maps constructed for Cd I 508.56 nm. (3) Overlap of the original photograph of the plant with LIBS map. **B)** (1) Photograph of *S. alba* plant exposed to CdTe QDs at the nominal concentration 200 µM Cd before micro-LIBS measurements together with marked spot analyzed by micro-LIBS (a-e). (2) Micro-LIBS maps constructed for Cd I 361.05 nm. (3) Overlap of the original photograph of the plant with micro-LIBS maps. The scale shows the total emissivity of the selected emission lines. [Modlitbová 2020].

4. Conclusions

The LIBS proved to be a relatively fast analysis with a sufficient precision and an acceptable spatial resolution for plant analysis. Also, the great usefulness of LIBS in the fast mapping of relatively large samples was demonstrated in the present case study while micro-LIBS was shown to be suitable for detail investigations of small selected parts of biological samples.

5. ACKNOWLEDGEMENTS

This research has been financially supported by the Ministry of Education, Youth and Sports (MEYS) of the Czech Republic under the project CEITEC 2020 (LQ1601) and the CzechNanoLab Research Infrastructure supported by MEYS CR (no. LM2018110). The authors gratefully acknowledge the financial support by the Czech Grant Agency within the project GACR Junior (no. 20-19526Y). JK acknowledges the support of the Brno University of Technology through grant no. FSI-S-20-6353.

6. REFERENCES

[Kaiser 2007] J. Kaiser, O. Samek, L. Reale, M. Liška, R. Malina, A. Ritucci, A. Poma, A. Tucci, F. Flora, A. Lai, L. Mancini, G. Tromba, F. Zanini, A. Faenov, T. Pikuz, G. Cinque, *Microsc. Res. Tech*., 70 (2007) 147.

[Galiová 2007] M. Galiová, J. Kaiser, K. Novotný, O. Samek, L. Reale, R. Malina, K. Páleníková, M. Liška, V. Čudek, V. Kanický, V. Otruba, A. Poma, A. Tucci, *Spectrochim. Acta B At. Spectrosc*., 62 (2007) 1597.

[Galiová 2008] M. Galiová, J. Kaiser, K. Novotný, J. Novotný, T. Vaculovič, M. Liška, R. Malina, K. Stejskal, V. Adam, R. Kizek, *Appl. Phys. Mater. Sci. Process*, 93 (2008) 917.

[Kaiser 2009] J. Kaiser, M. Galiová, K. Novotný, R. Červenka, L. Reale, J. Novotný, M. Liška, O. Samek, V. Kanický, A. Hrdlička, K. Stejskal, V. Adam, R. Kizek, *Spectrochim. Acta B*, 64 (2009) 67.

[Kryštofová 2009] O. Krystofova, V. Shestivska, M. Galiova, K. Novotny, J. Kaiser, J. Zehnalek, P. Babula, R. Opatrilova, V. Adam, R. Kizek, *Sensors*, 9 (2009) 5040.

[Galiová 2011] M. Galiová, J. Kaiser, K. Novotný, M. Hartl, R. Kizek, P. Babula, *Microsc. Res. Tech*., 74 (2011) 845.

[Kaiser 2012] J. Kaiser, K. Novotný, M.Z. Martin A. Hrdlička, R. Malina, M. Hartl, V. Adam, R. Kizek, *Surf. Sci. Rep*., 67 (2012) 233.

[Krajcarová 2013] L. Krajcarová, K. Novotný, P. Babula, I. Provaznik, P. Kucerova, V. Adam, M. Z. Martin, R. Kizek, J. Kaiser, *Int. J. Electrochem*. *Sci.*, 8 (2013) 4485.

[Krajcarová 2017] L. Krajcarová, K. Novotný, M. Kummerová, J. Dubová, V. Gloser, J. Kaiser, *Talanta*, 173 (2017) 28.

[Modlitbová 2018] P. Modlitbová, K. Novotný, P. Pořízka, J. Klus, P. Lubal, H. Zlámalová-Gargošová, J. Kaiser, *Ecotoxicol. Environ. Saf*., 147 (2018) 334.

[Modlitbová 2019] P. Modlitbová, A. Hlaváček, T. Švestková, P. Pořízka, L. Šimoníková, K. Novotný, J. Kaiser, *Chemosphere*, 225 (2019) 723.

[Modlitbová 2020a] P. Modlitbová, P. Pořízka, S. Střítežská, Š. Zezulka, M. Kummerová, K. Novotný, J. Kaiser, *Chemosphere*, 251 (2020) 126174.

[Modlitbová 2020b] P. Modlitbová, P. Pořízka, J. Kaiser, *Trends Anal. Chem*., 122 (2020) 115729.

ELEMENTAL IMAGING WITH LASER SPECTROSCOPY IS ENTERING THE CLINIC AS A NEW DIAGNOSTIC TOOL

Vincent Motto-Ros[1]*, Benoit Busser[2,3], Marine Leprince[1], Vincent Bonneterre[1], Lucie Sancey[3]

[1]Institut Lumière Matière, UMR5306 Univ. Lyon 1-CNRS, Villeurbanne, France
[2]Grenoble Alpes University Hospital, Grenoble, France
[3]Institute for Advanced Biosciences, IAB INSERM U1209 CNRS UMR5309, Grenoble, France
**e-mail: vincent.motto-ros@univ-lyon1.fr*

1. INTRODUCTION

The physiological and pathological roles of exogenous metals, but also endogenous metallic and organic ions are of major interest for the biomedical community [Austin 2013, Wogelius 2011]. Elemental imaging of biological tissues is currently a technological challenge requiring complex instruments (such as synchrotron) with restricted accesses. We recently developed an all-optical method, fully compatible with standard microscopy systems, for multi-elemental imaging of biological tissues. Our instrument is based on Laser Induced Breakdown Spectroscopy (LIBS) and allows the in situ imaging and quantification of the elements of the periodic table within biological tissues, with ppm-scale sensitivity and lateral resolution at the micrometer scale [Sancey 2014, Gimenez 2016].

In LIBS, the laser-induced plasma generated by focusing laser pulses on the surface of the sample of interest allows a specific optical response to be elicited from the elements constituting the sample. This specific response, resulting from the electronic relaxation of atoms and ions excited by the high plasma temperature, is collected and analyzed using an optical spectrometer. The elemental "signal" (atomic and ionic emission lines) is then extracted from the recorded spectrum, and elemental maps can be obtained in a pixel-by-pixel manner by scanning the sample surface over the region of interest (**Figure 1.**). The implementation of LIBS is simple because a single laser pulse can simultaneously sample the material by laser ablation and excite the vaporized elements by heating the plasma plume. Hence, the acquisition speed for LIBS is mainly governed by the laser frequency rate. The apparent simplicity of the setup endows LIBS with a series of advantages over other elemental imaging methods; these benefits include an all-optical design, operation in ambient atmosphere, and fast acquisition.

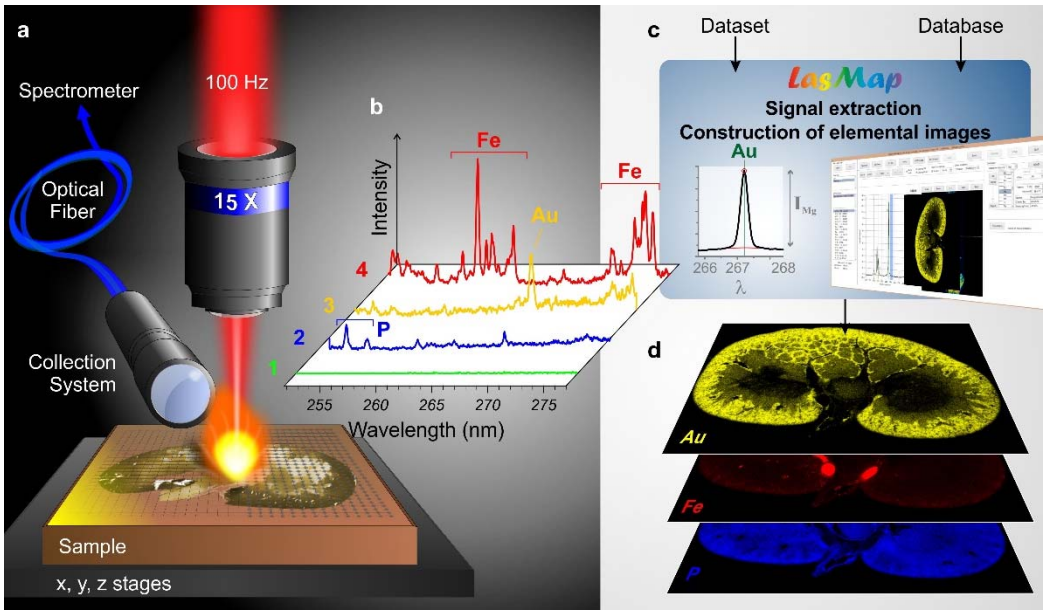

Figure 1. General protocol for LIBS imaging. (a) Schematic view of the LIBS instrument showing the major components: the microscope objective used to focus the laser pulse, the motorized platform supporting the sample and the optical detection system connected to the spectrometer via an optical fiber. (b) Example of single-shot emission spectra recorded in different regions of a rat kidney with the characteristic emission lines of iron (Fe), phosphorous (P), and gold (Au). (c) Methodology for signal extraction and image construction. (d) Example of relative abundance images of Au (yellow), Fe (red) and P (blue) represented in a false color scale.

The proof-of-concept was obtained by studying the bio-distribution of gadolinium or gold-nanoparticles in tumors or organs (kidneys/liver) after i.v. administration in mice [Kunjachan 2015, Sancey 2015, Le Guével 2018]. These experiments helped to describe and understand the kinetics of several metal-based (Gd, Au, Ag, Pt) nanoparticles in vivo. We recently upgraded our instrument to work faster and to image the elements contained in paraffin-embedded samples, which are the most frequent form of archived clinical specimens (surgical resections or biopsies) [Moncayo 2017, Busser 2017]. In the presentation to be held, we will present our latest results relating to the clinical applications of LIBS multi-elemental imaging, most of which constitute novel findings, both for LIBS and medical domains.

2. EXPERIMENTAL

2.1. Experimental setup

The instrumental setup was based on a homemade optical microscope. The LIBS experiment used Nd:YAG laser pulses of 1064 nm, focused onto the sample by a 15x magnification objective (LMM-15X-P01, Thorlabs). The pulse duration was 8 ns, and the repetition rate was 100 Hz. During the experiments, the sample could be translated along

the 3 axes by an XYZ motorized stages. All the measurements were performed at room temperature and under ambient conditions. The light emitted by the plume was collected by two quartz lens – optical fiber systems connected to two different Czerny-Turner spectrometers both equipped with an ICCD camera (Shamrock and iStar, Andor Technology). The simultaneous used of these two spectrometers allows to detect a large number of elements such as Fe, Ca, Na, P, Mg, Zn, Al, Mn, Co, Si, Cr, Ti and Cu.

2.2. Samples

All the studied samples consisted in human biopsies embedded in paraffin. The LIBS results obtained with these specimens of human origin were systematically gathered in elemental pathology reports and subsequently sent back to medical doctors in charge of the patients. The clinicians involved in this research are experts in pulmonology and occupational medicine. They obtained signed informed consent from their patients to perform LIBS imaging analyses with their biopsies. Such a procedure is mandatory, and we believe we are pioneering in the exploration of LIBS imaging as a diagnostic tool, following the standards of clinical research.

3. RESULTS AND DISCUSSION

Because the impact of mineral and metallic particles in lung diseases is probably underestimated, we started to analyze the elemental content of human lung tissues with LIBS. Clinicians selected lung biopsies from patients with various lung diseases with potential occupational/environmental origin. We identified several exogenous elements (including carcinogens) in the lungs of the patients (i.e Be, Ti, Si, Al, Cr), in different lung areas and with very different concentration ranges. Importantly, LIBS produced valuable clinical data for most of the patients and elemental findings were in complete accordance with patients' personal past exposures. Based on these important positive preliminary findings, we initiated the first multicenter retro- and prospective clinical trial aiming at evaluating the feasibility of implementing LIBS imaging as a routine diagnostic test for respiratory diseases (100 patients) [Sancey 2014]. We will present the most relevant results from this ongoing study.

In this presentation we will present some of the most relevant results from this ongoing study with the idea to highlight the potential LIBS-based imaging as a tool useful for pathologists and clinicians in their daily work and management of patients:

1) A large-sized lung specimen (~2 cm^2) with several positive pixels for beryllium (Be). This result was indeed consistent with the diagnosis of chronic beryllium disease, first case to be solved with a space-resolved configuration.
2) A lung biopsy in which more than 4000 pixels were positive for at least one of the following exogenous elements: Si, Al and Ti (**Figure 2.**). This result was in

accordance with the history of environmental and occupational exposures of the patient, suffering from a rare lung disease with no known origin (idiopathic). However, none of the usual elemental techniques used by the clinicians could elucidate the aetiology.

3) A lung specimen with important levels of Si, actually not detected by classical elemental analysis (SEM-EDX). This LIBS finding was the key to convince experts to re-classify the idiopathic disease of the patient as an occupational disease. Additionally, to personal recognition, the patient will therefore benefit from a significant financial compensation.

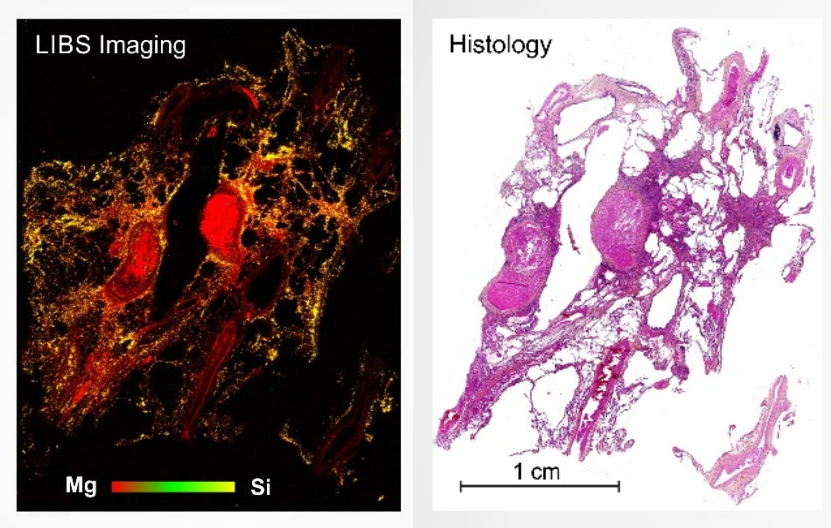

Figure 2. Images of human lung tissue with conventional histological staining (HES, left) and complementary LIBS elemental image (right) representing Magnesium (red) and Silicon (green). These results reveal important levels of Si, Al and Ti (not shown) in the lung tissue from an occupationally exposed patient with idiopathic lung disease.

4. CONCLUSION

This work demonstrates that LIBS allowed the in situ identification of several chemical agents related to patient's exposure (Si, Al, Cr, Zr, etc.), which may help clinicians in assessing the occupational/environmental origin of various lung diseases. As a routine diagnostic tool, LIBS could be indeed an invaluable source of information to help clinicians to better understand the origin and pathogenesis of a number of respiratory diseases.

5. REFERENCES

[Austin 2013] C. Austin, T. M. Smith, A. Bradman, K. Hinde, R. Joannes-Boyau, D. Bishop, D. J. Hare, P. Doble, B. Eskenazi, M. Arora, *Nature*, 498 (2013) 216.

[Wogelius 2011] R. A. Wogelius, P. L. Manning, H. E. Barden, N. P. Edwards, S. M. Webb, W. I. Sellers, K. G. Taylor, P. L. Larson, P. Dodson, H. You, L. Da-qing, U. Bergmann, *Science*, 333 (2011) 1622.

[Sancey 2014] L. Sancey, V. Motto-Ros, B. Busser, S. Kotb, J. M. Benoit, A. Piednoir, F. Lux, O. Tillement, G. Panczer, J. Yu, *Sci. Rep.*, 4 (2014) 6065.

[Gimenez 2016] Y. Gimenez, B. Busser, F. Trichard, A. Kulesza, J. M. Laurent, V. Zaun, F. Lux, J. M. Benoit, G. Panczer, P. Dugourd, O. Tillement, F. Pelascini, L. Sancey, V. Motto-Ros, *Sci. Rep.*, 6 (2016) 29936.

[Kunjachan 2015] S. Kunjachan, A. Detappe, R. Kumar, T. Ireland, L. Cameron, D. E. Biancur, V. Motto-Ros, L. Sancey, S. Sridhar, G. M. Makrigiorgos, R. I. Berbeco, *Nano Letters*, 15 (2015) 7488.

[Sancey 2015] L. Sancey, S. Kotb, C. Truillet, F. Appaix, A. Marais, E. Thomas, B. van der Sanden, J.-P. Klein, B. Laurent, M. Cottier, R. Antoine, P. Dugourd, G. Panczer, F. Lux, P. Perriat, V. Motto-Ros, O. Tillement, *ACS Nano,* 9 (2015) 2477.

[Le guével 2018] X. Le Guével, M. Henry, V. Motto-Ros, E. Longo, M. I. Montañez, F. Pelascini, O. de La Rochefoucauld, P. Zeitoun, J.-L. Coll, V. Josserand, L. Sancey, *Nanoscale*, 10 (2018) 18657.

[Moncayo 2017] S. Moncayo, F. Trichard, B. Busser, M. Sabatier-Vincent, F. Pelascini, N. Pinel, I. Templier, J. Charlesb, L. Sancey, V. Motto-Ros, *Spectrochim. Acta B*, 133 (2017) 40.

[Busser 2017] B. Busser, S. Moncayo, F. Trichard, V. Bonneterre, N. Pinel, F. Pelascini, P. Dugourd, J.-L. Coll, M. d'Incan, J. Charles, V. Motto-Ros, L. Sancey, *Mod. Pathol.*, 31 (2017) 378.

CHARACTERIZATION OF THE CN(B) AND CH(A) RADICAL FORMATION IN PLASMA GENERATED BY FEMTOSECOND LASER PULSES VIA STEP-SCAN FT-UV-VIS SPECTROSCOPY

Viktor Chikán[1,2]*, Krisztina Sárosi[1], Károly Mogyorósi[1]

[1]ELI-ALPS, ELI-HU Non-Profit Ltd., 6728 Szeged, Wolfgang Sandner street 3., Hungary
[2]Dept. of Chemistry, Kansas State University, 213 CBC Building, Manhattan, KS 66506-0401, USA
**email: vchikan@ksu.edu*

1. INTRODUCTION

Laser-induced breakdown spectroscopy (LIBS) is mostly used for simultaneous analysis of multiple elements measuring the atomic emission lines or the emitted light from diatomic radicals in excited states [Rao 2015, Moros 2019]. Typical LIBS measurements apply nanosecond laser pulses [Dong 2011] however, recent publications suggest potential benefits of using femtosecond lasers [Moros 2019, Kotzagianni 2013]. Seven explosive nitropyrazoles were studied by fs-LIBS technique (~40 fs, 800 nm, 1 kHz, ~2.5 mJ pulse energy) [Rao 2015]. Rao et al. studied the atomic emission lines from C, H, O, and N, the molecular emissions of cyanide (CN, violet bands) and diatomic carbon (C_2, Swan bands). Authors collected time-resolved spectral data for the characterization of the plasma dynamics in different atmospheres, such as air, argon and nitrogen. They found a clear decreasing trend in the CN and C_2 decay times with the increasing number of nitro groups. Moros et al. concluded in their review work about the LIBS of organic compounds that the molecular emission from CN and C_2 radicals is stronger with fs-LIBS technique compared with those obtained using nanosecond laser pulses [Moros 2019].

We report a novel approach producing CN(B) and CH(A) radicals from different small organic molecules in gas phase with a high repetition rate femtosecond laser (100 kHz, 1030 nm, ~43 fs, 250 μJ/pulse). The emission spectra can be collected with high temporal and spectral resolution (5 ns and 1 cm^{-1}) with a Fourier transform UV-Vis spectrometer in step-scan measurement mode [Mogyorosi 2020].

2. EXPERIMENTAL

The experiments were performed in a vacuum chamber typically at 5-100 mbar total pressures in argon or nitrogen gas in the presence of organic vapors (bromoform, methanol or acetonitrile) introduced through a bubbler. The HR-1 laser beam at ELI-ALPS with 1030 nm central wavelength, 100 kHz repetition rate, ~43 fs pulse length and 25 W average power was focused into the vacuum chamber with an achromatic lens (f = 10 cm). The intensity in the focal point was estimated to be 1.1×10^{16} W/cm^2. Overview spectra

were monitored with a QEPro spectrometer. The emitted light was also collected with a collimating lens and measured with a Bruker Vertex80 FT-UV-Vis spectrometer with high resolution in step-scan mode (5 ns and 1 cm^{-1}).

3. Results and Discussion

3.1. CN(B) radical formation

The overview emission spectra from acetonitrile in nitrogen and argon are shown in **Figure 1**. The CN violet system ($B^2\Sigma$-$X^2\Sigma$, Δv = 0, -1 and +1; 370-395 nm, 350-365 nm and 410-425 nm, respectively) and the C_2 Swan system ($d^3\Pi_g$-$a^3\Pi_u$, Δv = 0, -1 and +1; 450-480 nm, 500-520 nm and 540-570 nm, respectively) can be observed.

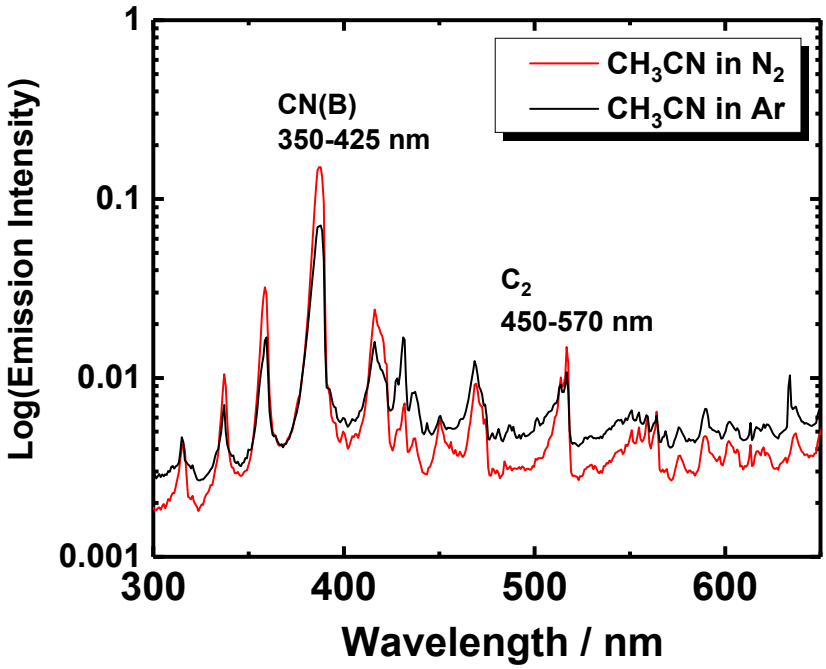

Figure 1. Overview spectra of CN(B) and C_2 radicals generated from acetonitrile.

The highest intensity of CN(B) radicals was observed from bromoform in nitrogen plasma due to the production of reactive carbon atoms and CH radicals. The experimental data obtained with time-resolved Fourier transform spectroscopy were used for the determination of the rotational and vibrational temperatures via fitting (**Figure 2.**) [Western 2017].

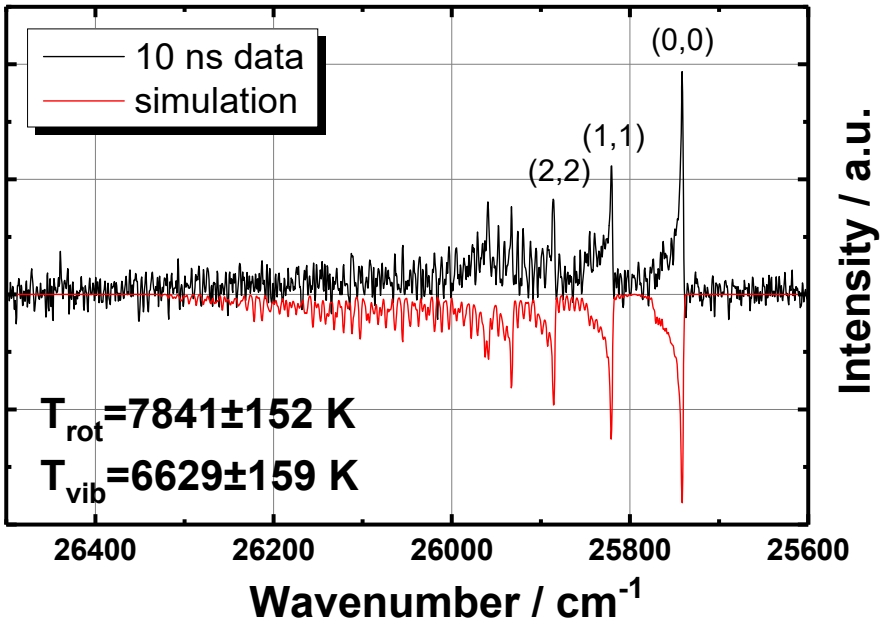

Figure 2. Measured and simulated ro-vibrational spectra of CN from acetonitrile 5 mbar - N_2 95 mbar mixture at 10 ns time point.

The rotational and vibrational temperatures were very high (T_{rot}~6000-8500 K and T_{vib}~4500-8000 K) at about 10 ns for the CN(B) radicals generated from all organic molecules. T_{rot} determined for bromoform and acetonitrile rapidly decreased in all instances within 40 ns. The time-dependent integrated fluorescence signal of the (0,0) band of acetonitrile/Ar (5 mbar/95 mbar) sample is fitted with a mono-exponential curve with a time constant of 87 ns. The CN(B) emission in nitrogen follows a bi-exponential decay. The shorter time constant of this decay (35-40 ns) is close to the natural lifetime of CN(B) emission (~30-90 ns). The longer time constant (130-160 ns) probably belongs to slower chemical reactions involving carbon atoms, C_2 radicals and nitrogen containing species.

3.2. CH(A) radical formation

Based on the overview spectrum of bromoform/Ar (5 mbar/5 mbar) plasma, the formation of CH(A) radicals was confirmed by the observation of a peak at 431 nm. The atomic lines of hydrogen (H-alpha, 656.8 nm) and bromine (827.8 nm) were also noticed. In the case of methanol/Ar (5 mbar/5 mbar), the P-, Q- and R-branches are also recognizable in the high-resolution static spectra. The CH(A) formation kinetic curves are shown in **Figure 3**.

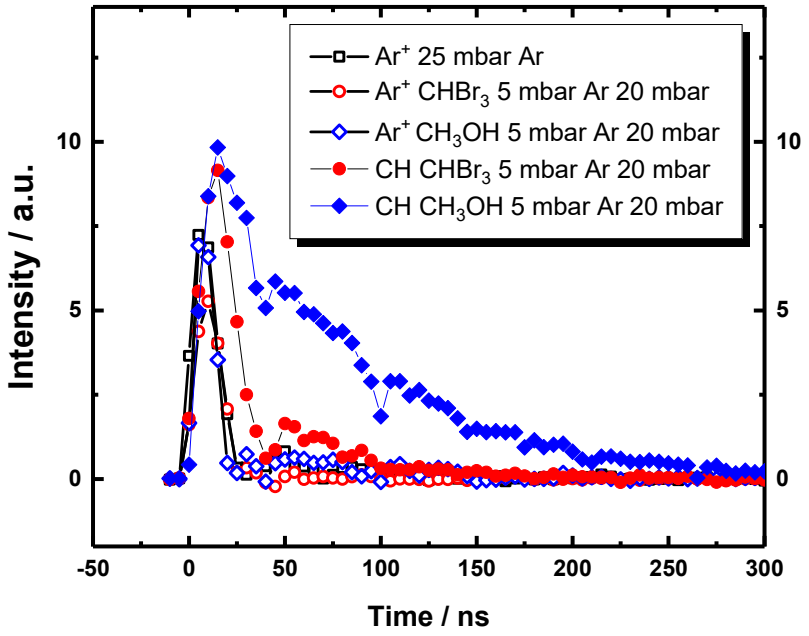

Figure 3. CH(A) formation kinetics in bromoform/argon and methanol/argon mixtures (5 mbar organics/20 mbar argon).

The appearance of the Ar^+ signal occurs in the 5-10 ns time range (that is about the instrument response time). The CH(A) signal formation is similarly fast but the emission decay is different for the bromoform/argon mixture (t = 10.4 (2.2) ns) compared to that of methanol/argon mixture (t_1 = 7.8 (2.2) ns and t_2 = 81.5 (1.7) ns). In the case of methanol, it is likely that the stepwise loss of hydrogen atoms from the CH_3 group results in slower decay of the CH(A) emission.

4. CONCLUSIONS

The step-scan Fourier transform UV-Vis spectroscopy combined with the high repetition rate femtosecond laser (100 kHz, ~43 fs) is an excellent tool for the determination of atomic and molecular composition of samples. The method can be applied for gas, liquid and solid phase samples as well. Due to the localization of the pulse energy of the femtosecond pulse, small quantities can be analyzed with high rate. The main advantage of using femtosecond laser pulses is due to the high starting temperatures (4500-8000 K). This allows the detection of multiple elements and radicals simultaneously, including those which are hardly measurable with the traditional ns-LIBS techniques. It has been demonstrated on model samples that the kinetics of the formation and decomposition of light emitting species can be monitored with high temporal resolution.

5. ACKNOWLEDGEMENTS

The ELI-ALPS project (GINOP-2.3.6-15-2015-00001) is supported by the European Union and co-financed by the European Regional Development Fund, European Social Fund (EFOP-3.6.2-16-2017-00005).

6. REFERENCES

[Rao 2015] E. N. Rao, S. Sunku, S. V. Rao, *Acta Radiol.,* 56 (2015) 1342.

[Moros 2019] J. Moros, J. Laserna, *Appl. Spectrosc.,* 73 (2019) 963.

[Dong 2011] M. Dong, J. Lu, S. Yao, Z. Zhong, J. Li, W. Lu, *Opt. Express,* 19 (2011) 17021.

[Kotzagianni 2013] M. Kotzagianni, S. Couris, *Chem. Phys. Lett.,* 561–562 (2013) 36.

[Mogyorosi 2020] K. Mogyorósi, K. Sárosi, I. Seres, P. Jójart, M. Füle, V. Chikán, *J. Phys. Chem. A,* 124 (2020) 2755.

[Western 2017] C. M. Western, *J. Quant. Spectrosc. Rad. Transf.*, 186 (2017) 221.

LASER ABLATION MOLECULAR ISOTOPIC SPECTROMETRY (LAMIS): AN OVERVIEW

Jhanis Gonzalez[1,2]*, Alexander Bol'Shakov[1], Xianglei Mao[2], Vassilia Zorba[2], Richard E. Russo[1,2]

[1]Applied Spectra Inc., 950 Riverside Parkway #90, West Sacramento, CA 95605, USA
[2]Lawrence Berkeley National Laboratory, 1 Cyclotron Road, Berkeley, CA 94720, USA
**e-mail: jhanis@appliedspectra.com, jgonzalez@lbl.gov*

1. INTRODUCTION

Since the LAMIS introduction in 2011 [Russo 2011], our research team [Russo 2011, Russo 2013, Bol'shakov 2014, Bol'shakov 2015a, Bol'shakov 2015b, Bol'shakov 2017, Dong 2013, Hou 2015, Mao 2011, Mao 2016, Sarkar 2013] and others [Brown 2014, Brown 2016, Choi 2019, Gaft 2020, Hartig 2016, Santos 2020, Yee 2013, Zhu 2019] have focused a great deal of effort on developing this novel laser ablation-based approach to detect isotopic information from the laser-induced plasma. This presentation is meant to give an overview of LAMIS origins and its foundation; we discuss some experimental considerations, review some case studies and advances, quantification approaches, and LAMIS's future.

Laser ablation is commonly used as a direct and rapid sampling technique to measure optical emission or mass spectra for the elemental and isotopic analysis of a sample. Laser Ablation Molecular Isotopic Spectrometry (LAMIS)[Russo 2011] is a similar technique that explores optical spectra of transient molecules produced in ablation plumes in air or buffer gases for rapid isotopic analysis directly on the samples. LAMIS measures molecular emission as the plasma cools when free molecules are formed in the plasma afterglow via several mechanisms, including radiative and three-body association of atoms and recombining ions. The isotopic constituents produce excited isotopologues of dimers, oxides, nitrides, or halides in plasma reactions between atomized matter from the sample and ambient atmosphere.

Isotopologues have isotopic spectral shifts that are considerably larger than those in atomic spectra, and therefore the former can be measured with a general-purpose spectrometer, **Figure 1**. Molecular quantum energy levels, particularly the vibrational and rotational components, strongly depend on the mass difference between isotopes. In contrast, the electronic energy is primarily determined by the Coulomb field but significantly less dependent on nuclei's mass [Russo 2011]. Consequently, molecular transitions involving a change of vibrational and rotational states can exhibit up to several orders of magnitude larger isotopic shifts than atomic transitions, which are purely electronic [Russo 2011]. Larger isotopic shifts significantly relax requirements on the spectral resolution.

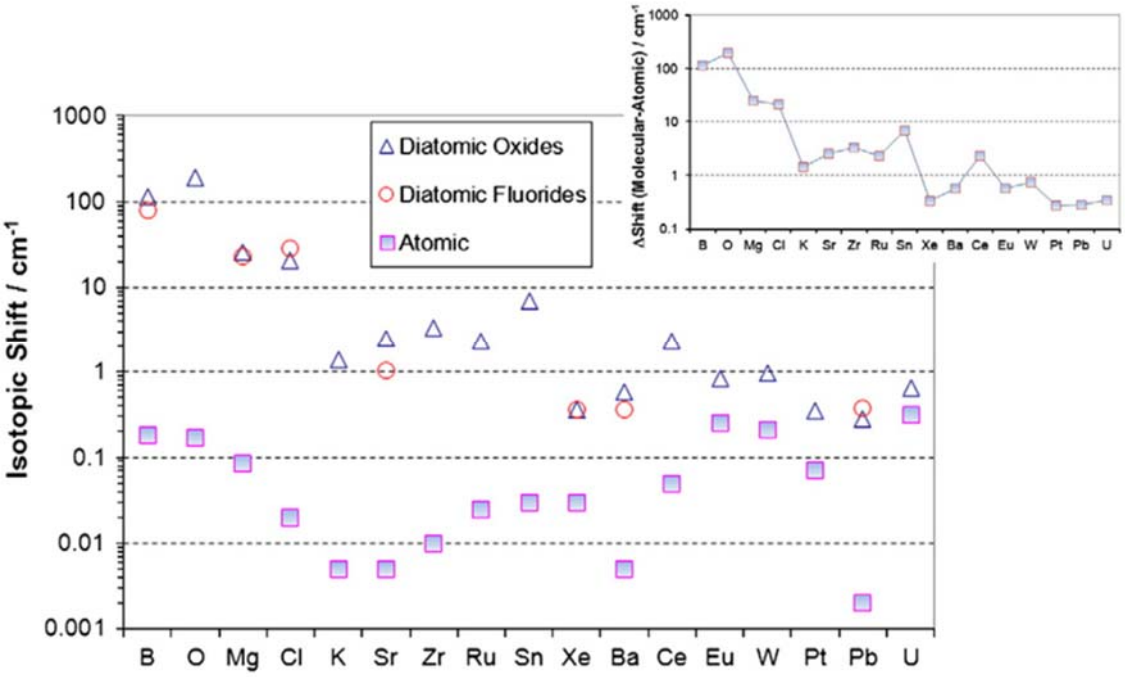

Figure 1. Molecular vs. atomic isotopic shifts for various elements. Molecular shifts were calculated for either the diatomic oxide or fluoride for each element considered in this plot. Isotopic shifts are much larger, up to several orders of magnitude, for molecular species as opposed to atomic species. The inset is a different plot of isotopic shifts. Atomic isotopic shift values were taken from Stern and Snavely.

These concepts will be demonstrated using a few examples of the isotopic systems studied so far, and some of the experimental conditions considerations and data reduction and analysis approaches.

2. EXPERIMENTAL

Both nano- and femtosecond pulsed lasers have been used for LAMIS measurements. Femtosecond ablation yielded significantly stronger molecular emission at a lower background than nanosecond ablation at the same laser power delivered to the sample. The use of a femtosecond laser reduces the analysis's destructiveness due to lower pulse energies applied to the sample relative to nanosecond laser pulses. Double-pulse excitation was found to enhance the sensitivity of LAMIS substantially. Echelle or Czerny-Turner spectrographs fitted with ICCD or EMCCD cameras were generally recognized as suitable for LAMIS. Simultaneously, femtosecond ablation and numerical filtering of spectra enabled LAMIS measurements with a non-gated CCD detector.

Usually, optical emission spectra in LAMIS are measured at longer delays after an ablation pulse than the LIBS delays, **Figure 2**. Accordingly, LIBS and LAMIS's optimal conditions are different but can be achieved with the same instrument. A possibility of combining LIBS and LAMIS for simultaneous elemental and isotopic analysis can enable multiple applications anticipated in the nuclear power industry, medical diagnostics and therapies, forensics, carbon sequestration, geochemistry, agronomy, and many other

studies. Potentially LIBS and LAMIS can be built into a portable device for the elemental and isotopic analysis directly in the field.

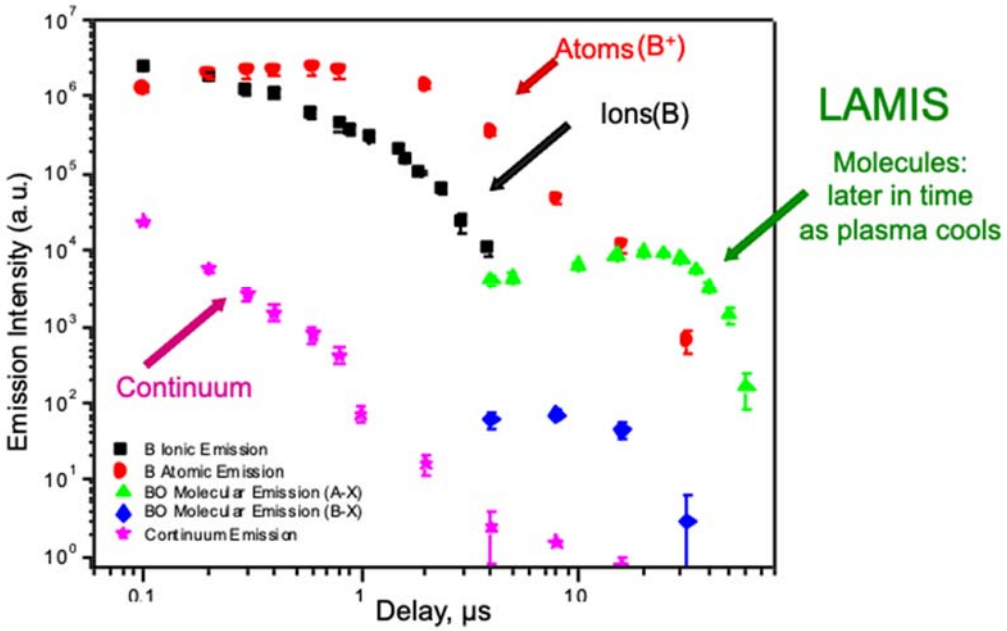

Figure 5. Optical emission signal evolution.

3. RESULTS AND DISCUSSION

These are some of the case studies we will be discussing during the presentation

a. Hydrogen and Deuterium – [Sarkar 2013]

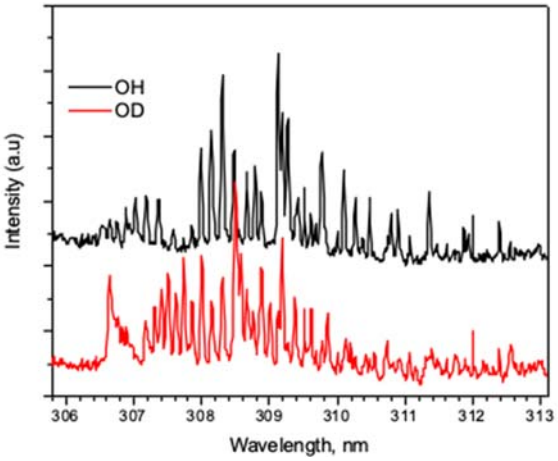

b. Boron - [Yee 2013]

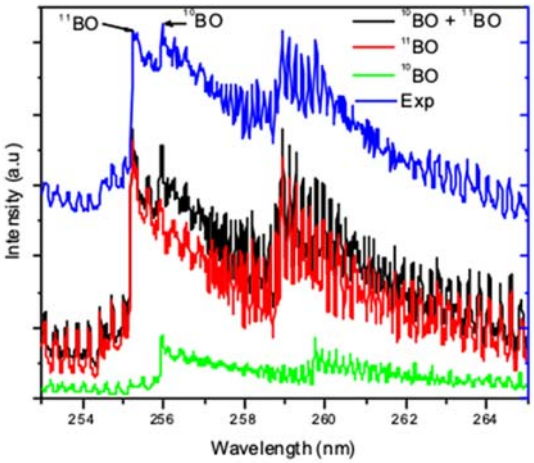

c. Carbon - [Dong 2013]

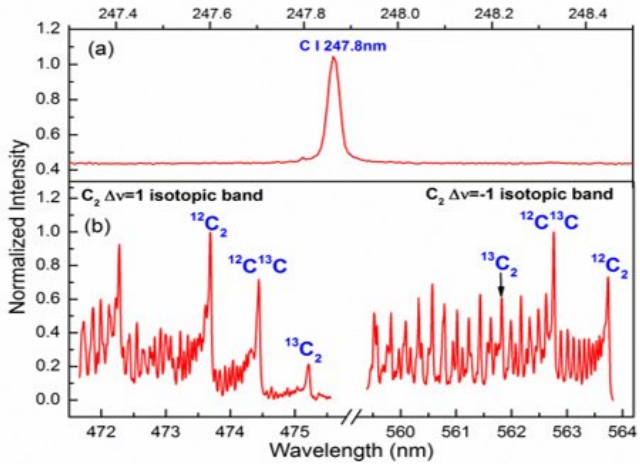

d. Zirconium [Hou 2015]

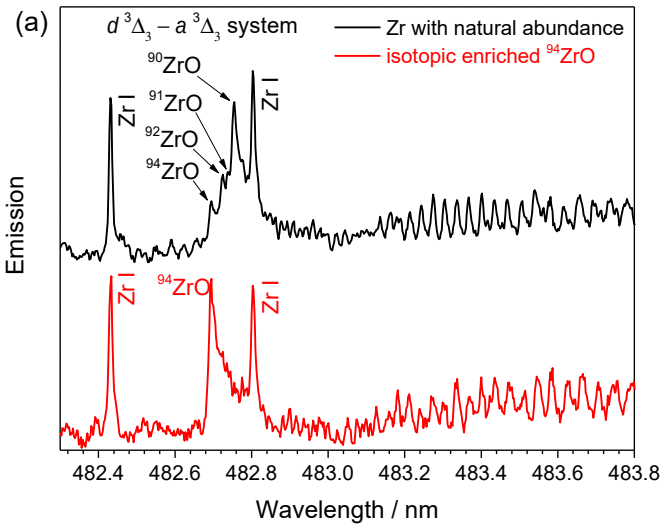

e. Nitrogen, Oxygen, Chlorine, Strontium [Bol'shakov 2014, Mao 2011]

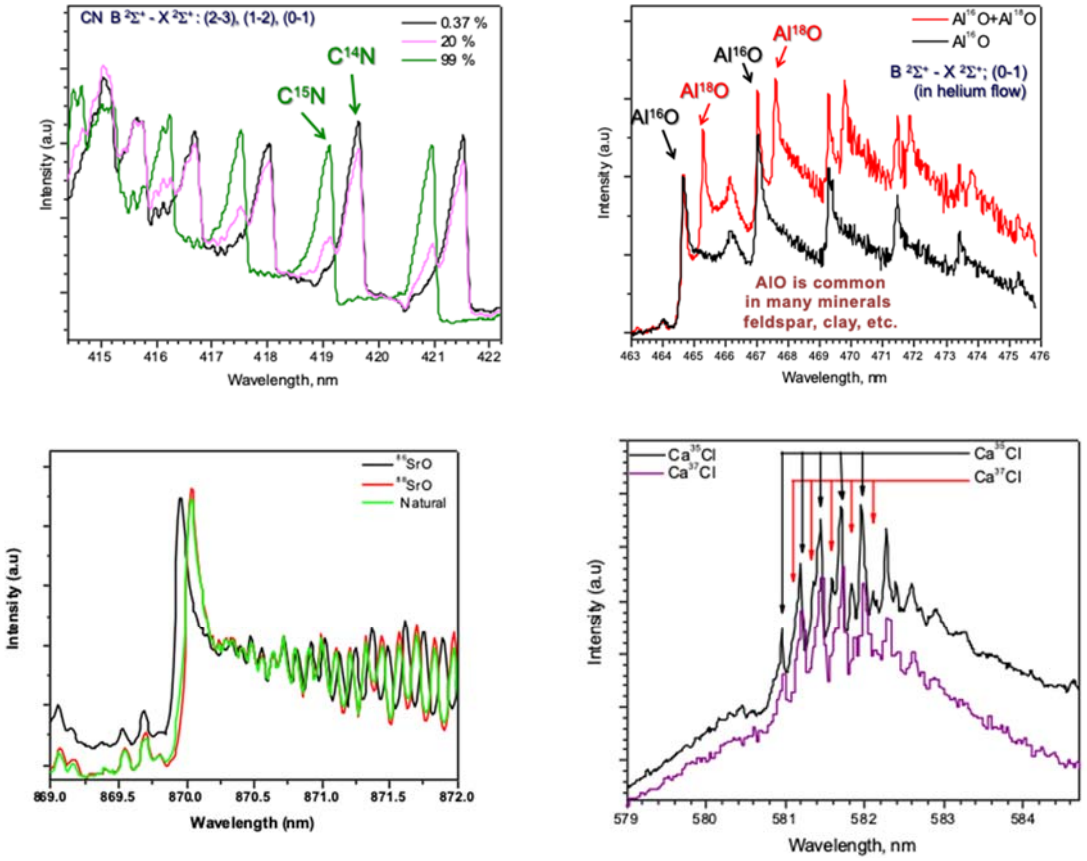

Quantitative calibration of spectral data in LAMIS can be achieved by different means. A common empirical approach involves measuring spectra from a set of known reference samples and building a partial least square regression (PLSR) model to relate them to the nominal abundances of isotopes in the samples. This model is applied to compare the spectra of the analyzed unknown samples to the reference spectra. Quantification is based on proportionality between emission from the plasma-generated isotopologues and the isotopic abundances in the sample. Such calibration alleviates errors caused by possible isotope fractionation in the ablation plumes.

Another quantification approach in LAMIS uses simulated spectra of relevant isotopologues, and a proportional sum of them is fitted to the experimental emission spectra. The isotope ratio is entered as a fitting parameter and is determined from the best fit. This approach does not require isotopic standards but depends on the quality of tabulated molecular parameters and equilibrated and homogeneous plasma assumptions.

4. ACKNOWLEDGMENTS

This work was funded by NASA SBIR program through contract No. NNX14CA03C granted to Applied Spectra, Inc. The work at the Lawrence Berkeley National Laboratory was supported by the Defense Nuclear Nonproliferation Research and Development Office and the Office of Basic Energy Sciences of the US Department of Energy under contract number DE-AC02-05CH11231.

5. REFERENCES

[Russo 2011] R. E. Russo, A. A. Bol'shakov, X. L. Mao, C. P. McKay, D. L. Perry, O. Sorkhabi, *Spectrochim. Acta B*, 66 (2011) 99.

[Russo 2013] R. E. Russo, X. Mao, J. J. Gonzalez, V. Zorba, J. Yoo, *Anal. Chem.*, 85 (2013) 6162.

[Bol'shakov 2014] A. A. Bol'shakov, X. Mao, D. L. Perry, R. E. Russo, *Spectroscopy*, 29 (2014) 30.

[Bol'shakov 2015a] A. A. Bol'shakov, X. Mao, J. J. Gonzalez, R. E. Russo, *J. Anal. At. Spectrom.*, 31 (2015) 119.

[Bol'shakov 2015b] A. A. Bol'shakov, X. Mao, J. Jain, D. L. McIntyre, R. E. Russo, *Spectrochim. Acta B*, 113 (2015) 106.

[Bol'shakov 2017] A. A. Bol'shakov, X. Mao, R. E. Russo, *J. Anal. At. Spectrom.*, 32 (2017) 657.

[Dong 2013] M. Dong, X. L. Mao, J. Gonzalez, J. Lu, R. E. Russo, *At. Spectrosc.*, 85 (2013) 2899.

[Hou 2015] H. Hou, G. C. Y. Chan, X. Mao, V. Zorba, R. Zheng, R. E. Russo, *Anal. Chem.*, 87 (2015) 4788.

[Mao 2011] X. Mao, A. A. Bol'shakov, I. Choi, C. P. McKay, D. L. Perry, O. Sorkhabi, R. E. Russo, *Spectrochim. Acta B*, 66 (2011) 767.

[Mao 2016] X. Mao, G. C. Y. Chan, V. Zorba, R. E. Russo, *Spectrochim. Acta B*, 122 (2016) 75.

[Sarkar 2013] A. Sarkar, X. Mao, G. C. Y. Chan, R. E. Russo, *Spectrochim. Acta B*, 88 (2013) 46.

[Brown 2014] S. Brown, A. Ford, C. C. Akpovo, J. Martinez, L. Johnson, *Spectrochim. Acta B*, 101 (2014) 204.

[Brown 2016] S. Brown, A. Ford, C. A. Akpovo, L. Johnson, *Spectrochim. Acta B*, 122 (2016) 1.

[Choi 2019] S.-U. Choi, S.-C. Han, J.-I. Yun, *Spectrochim. Acta B*, 162 (2019) 105716.

[Gaft 2020] M. Gaft, L. Nagli, I. Gornushkin, Y. Raichlin, *Spectrochim. Acta B*, 173 (2020) 105989.

[Hartig 2016] K. C. Hartig, I. Ghebregziabher, I. Jovanovic: Remote detection of uranium by fs-filamentation laser ablation molecular isotopic

spectrometry, conference paper STh1H.5, *Conference on Lasers and Electro-Optics*, San Jose, CA, USA, 2016.

[Santos 2020] M. S. R. dos Santos, C. Pasquini, *Anal. Bioanal. Chem.*, 412 (2020) 4173.

[Yee 2013] B. Yee, K. C. Hartig, P. Ko, J. McNutt, I. Jovanovic, *Spectrochim. Acta B*, 79–80 (2013) 72.

[Zhu 2019] Z. H. Zhu, J. M. Li, Z. Q. Hao, S. S. Tang, Y. Tang, L. B. Guo, X. Y. Li, X. Y. Zeng, Y. F. Lu, *Opt. Express.*, 27 (2019) 470.

ABOUT THE USE OF LASER-INDUCED BREAKDOWN SPECTROSCOPY FOR THE DETERMINATION OF FUNDAMENTAL SPECTROSCOPIC PARAMETERS

Vincenzo Palleschi*

[1]*Applied and Laser Spectroscopy Laboratory, Institute of Chemistry of Organometallic Compounds, Research Area of Pisa, Via G. Moruzzi, 1 – 56124 Pisa (Italy)*
**e-mail: vincenzo.palleschi@cnr.it*

1. INTRODUCTION

The laser-induced breakdown spectroscopy (LIBS) technique is known as a flexible analytical technique, which has been widely used since more than 40 years in many fields of application, mainly because of its speed, versatility and (apparent) simplicity [Cremers 2013].

In many LIBS applications, the analytical results are often coupled with plasma diagnostics, usually based on simplifying assumptions of thermal equilibrium and plasma homogeneity, for the determination of the main plasma parameters, namely electron temperature and electron number density [Tognoni 2006].

For the determination of those parameters, the knowledge is needed on the fundamental spectroscopic parameters of the emission lines observed in the LIBS spectrum, namely the energies E_k and E_i of the upper and lower levels of the transition, the degeneracies of the levels, g_k and g_i, respectively, the temperature-dependent partition function of the species $U(T)$, the transition probability A_{ki} and the Stark coefficient of the line.

While the first parameters are linked to the intensity of the light emitted in the transition and the number concentration of the emitting species, the latter is only related (in the first approximation) to the shape of the emission line. In fact, in the LTE approximation and for an homogeneous and optically thin plasma, the light intensity emitted at the frequency $(E_k - E_i)/h$, with h = Planck constant, can be expressed through the Boltzmann equation:

$$I_0 = F n^a g_k A_{ki} \frac{e^{-\frac{E_k}{k_B T}}}{U^a(T)} \qquad (1)$$

$$a = \begin{cases} I & \text{for neutral lines} \\ II & \text{for ionized lines} \end{cases}$$

where n^a is the number density of the emitting species, k_B is the Boltzmann constant, T is the plasma temperature and F is a scale factor depending on the efficiency of the experimental apparatus. On the other hand, in the first approximation the Full Width at

Half Maximum (FWHM) $\Delta\lambda_0$ of the emission line can be associated to the electron number density n_e of the plasma using the relation:

$$\Delta\lambda_0 = \omega_s \, n_e \qquad (2)$$

The proportionality between $\Delta\lambda_0$ and n_e through the ω_s coefficient assumes as the only broadening mechanism in the plasma the perturbation on the atomic energy levels given by the electric field of the free electrons in the plasma. This kind of broadening is called *Stark broadening* [Griem 1976], and gives to the LIBS researchers a conceptually simple tool for determining the electron number density from the knowledge of the ω_s parameter and the measure of the FWHM of an emitting line, in the same way as eq.(1) allows the determination of both the number concentration of the emitting species and the plasma temperature through the knowledge of the partition function of the species *U(T)* and E_k, g_k, and A*ki* for at least two emission lines of the same species [Ciucci 1999].

From the knowledge of the spectroscopic parameters of the LIBS lines is thus possible (using eq. (1) and (2) and under some simplifying hypotheses) to obtain the electron temperature and electron number density of the plasma. Several researchers noticed that, if eq. (1) and (2) would give a correct description of the physics of the LIBS plasma, an independent determination of the plasma temperature and electron number density would allow to obtain the spectroscopic parameters (mainly the transition probabilities A_{ki} and the Stark coefficient ω_s, which are the most problematic to measure or to determine theoretically) [Aberkane 2020].

Surprisingly enough, while it is commonly agreed among the plasma physicists and chemists that eq.(1) and (2) (and consequently, the approximation of homogeneous plasma in LTE conditions) describe well the LIBS plasmas in some temporal interval during the plasma evolution, as demonstrated by many results in the literature, the same equations are strongly questioned when they are applied to the determination of the fundamental spectroscopic parameters.

The point which is most criticized is the use of the homogeneous plasma approximation, which is assumed for modelling the plasma by eq. (1) and (2). However, under this objection there is often an underlying concern, typical of the old plasma school, of making the things 'too easy' by the use of LIBS, when the experimental determination of the fundamental spectroscopic parameters typically requires extremely complex strategies when traditional methods are applied.

Two consideration can be done about these concerns. The first is that the measurement of the fundamental spectroscopic parameters of the LIBS emission lines is not easy at all, and requires the same skill and knowledge, if not more, that the traditional methods. The second, quite obvious, is that the results obtained by LIBS can be easily compared with that obtained by traditional methods; when the results coincide, within the experimental errors, few objections can be further raised.

There is another way to demonstrate the feasibility of LIBS for the purpose, which is to simulate numerically some extreme non-ideal plasma conditions and discussing how

these non-ideal conditions reflect on the experimental determination of the fundamental spectroscopic parameters. This is the approach that we have taken, and that we will discuss in this communication.

2. EXPERIMENTAL

The numerical experiment that we will describe assumes a plasma in LTE conditions but takes into full account the possibility that the plasma would not be optically thin at the wavelength of the transition. Moreover, the plasma can be non-homogeneous in both the electron temperature and the electron number density. The plasma emission is simulated through the numerical solution of the radiative transport equation [Rezaei 2020]:

$$\frac{dI(\lambda,x)}{dx} = \varepsilon(\lambda,x) - k(\lambda,x)I(\lambda,x) \quad (3)$$

$\varepsilon(\lambda,x)$ is the contribution of the spontaneous emission:

$$\varepsilon(\lambda,x) = B(\lambda,x)\, k(\lambda,x) \quad (4)$$

and $B(\lambda,x)$ is the Planck black body radiation function. $k(\lambda,x)$ represents the effect of the absorption and stimulated emission:

$$k(\lambda,x) = \frac{\lambda_0^4}{8\pi c} A_{ki} g_k \frac{n_i(x)}{g_i}\left(1 - \frac{n_k(x) g_i}{n_i(x) g_k}\right) L(\lambda,x) \quad (5)$$

n_i is the population of the lower level of the transition, while n_k is the population of the upper level. The population of the levels may vary with the x coordinate within the plasma, because of the possible inhomogeneity of the electron temperature and number density.

The shape of the emission lines is assumed to be described, as usual in LIBS analysis, by the Lorentzian function:

$$L(\lambda) = I_0 \frac{\frac{\Delta\lambda_0}{2\pi}}{(\lambda-\lambda_0)^2 + \left(\frac{\Delta\lambda_0}{2}\right)^2} \quad (6)$$

where I_0 is the line integral intensity and λ_0 is the central wavelength of the line.

The analysis of the simulated spectrum for the determination of the fundamental spectroscopic parameters is then performed as in the case of 'true' experimental data.

In particular, to evaluate the optical thickness of the plasma we used a method developed by our laboratory in Pisa in 2005 [El Sherbini 2005], and largely validated in the following years [Bredice 2007, Safi 2019] which links the self-absorption parameter SA, defined as the ratio between the peak emission of the self-absorbed line over the equivalent peak intensity in the absence of self-absorption, to the measured integral intensity of the line and the line FWHM as:

$$I = I_0\ (SA)^{0.46} \tag{7}$$

$$\Delta\lambda = \Delta\lambda_0\ (SA)^{-0.54} \tag{8}$$

From eq. (5), the parameter SA can be written as

$$SA = \frac{1-e^{-k(\lambda_0)l}}{k(\lambda_0)l} \tag{9}$$

where *l* is the length of the optical path of the radiation in the plasma.

A consequence of eq. (8) is that, from the measurement of $\Delta\lambda$ and the knowledge of SA (from eq. (7), for example) one would be able to estimate $\Delta\lambda_0$ and, from eq. (2), the Stark broadening coefficient ω_s.

3. RESULTS AND DISCUSSION

The main results of the numerical simulation, corresponding to different plasma conditions and various degrees of inhomogeneity, are here summarized in the specific case of the determination of the Stark broadening parameters:

For optically thin plasmas ($k(\lambda_0)l \ll 1$) the effect of plasma inhomogeneity (both electron temperature and number density) on the determination of the Stark coefficient is almost negligible. This is because the determination of the Stark coefficient is experimentally done by comparing the broadening of the line with the one of a suitable (optically thin) reference line of known Stark coefficient. Since also the reference line broadening is affected by the plasma inhomogeneity in the same way, the overall effect on the evaluation of the Stark broadening effect is negligible;

For optically thick plasmas ($k(\lambda_0)l > 1$) the error on the Stark coefficient depends on the degree of inhomogeneity of the plasma. For a homogeneous plasma, eqs. (7) and (8) describe very well the plasma emission up to extreme values $k(\lambda_0)l \sim 20$. The presence of electron temperature and number density inhomogeneities minimally affects the evaluation of the Stark broadening coefficient, unless serious deformations of the lineshape occur (self-reversal). The self-absorption limit for the onset of self-reversal depend on the plasma inhomogeneity; however, self-reversal is easily recognizable in the LIBS emission and its effect decreases with the delay of analysis after the laser pulse. Therefore, the evaluation of the Stark broadening can be usually be performed by carefully selecting the right experimental conditions for minimizing the self-reversal of the line. Moreover, also in the presence of a moderate self-reversal, a meaningful estimation of the Stark broadening coefficient can be obtained, by only fitting the wings of the emission line, which are less affected by the self-absorption.

4. CONCLUSIONS

In this communication are summarized the results of a numerical experiment, aimed to the evaluation of the effect of plasma non-ideality on the experimental determination of the Stark broadening coefficient, one of the spectroscopic fundamental parameters of interest in plasma physics and chemistry.

We have demonstrated that a careful planning and optimization of the experimental conditions allows to obtain almost homogeneous plasmas and that, again under suitable hypotheses, the effect of the inhomogeneity does not affect critically the experimental evaluation of the Stark broadening coefficients.

These results are particularly important, because they allow the researchers to plan a LIBS experiment for the determination of the Stark broadening coefficients of plasma lines of different elements without the need of demonstrating again and again, through complex acquisition and manipulations of the LIBS spectra [Cirisan 2014], that the hypothesis of homogeneous plasma in LTE condition is fulfilled, in the proper time interval, in almost all the conventional LIBS experiments. Most of all, the reliability of the LIBS predictions can be easily checked through a careful analysis of the plasma emission lines, to determine the degree of self-absorption and minimizing its effect on the final results.

6. REFERENCES

[Bredice 2007] F. Bredice, F. O. Borges, H. Sobral, M. Villagran-Muniz, H. O. Di Rocco, G. Cristoforetti, S. Legnaioli, V. Palleschi, A. Salvetti, E. Tognoni, *Spectrochim. Acta B*, 62 (2007) 1237.

[Cirisan 2014] M. Cirisan, M. Cvejić, M. R. Gavrilović, S. Jovićević, N. Konjević, J. Hermann, *J. Quant. Spectrosc. Radiat. Transf.*, 133 (2014) 652.

[Ciucci 1999] A. Ciucci, M. Corsi, V. Palleschi, S. Rastelli, A. Salvetti, E. Tognoni, *Appl. Spectrosc.*, 53 (1999) 960.

[Cremers 2013] D. A. Cremers, L. J. Radziemski: Handbook of Laser-Induced Breakdown Spectroscopy, Second Edition, *John Wiley and Sons* 2013.

[El Sherbini 2005] A. M. El Sherbini, T. M. El Sherbini, H. Hegazy, G. Cristoforetti, S. Legnaioli, V. Palleschi, L. Pardini, A. Salvetti, E. Tognoni, *Spectrochim. Acta B*, 60 (2005) 1573.

[Griem, 1976] H. R. Griem, H. R, *Adv. At. Mol. Phys.*, 11 (1976) 331.

[Aberkane 2020] S. M. Aberkane, A. Safi, A. Botto, B. Campanella, S. Legnaioli, F. Poggialini, S. Raneri, F. Rezaei, V. Palleschi, *Appl. Sci.*, 10 (2020) 4973.

[Rezaei 2020] F. Rezaei, G. Cristoforetti, E. Tognoni, S. Legnaioli, V. Palleschi, A. Safi, *Spectrochim. Acta B*, 169 (2020) 105878.

[Safi 2019] A. Safi, S. H. H. Tavassoli, G. Cristoforetti, E. Tognoni, B. Campanella, S. Legnaioli, S. Pagnotta, F. Poggialini, V. Passeschi, *Anal. Chem.*, 91 (2019) 8595.

[Tognoni 2006] E. Tognoni, V. Palleschi, M. Corsi, G. Cristoforetti, N. Omenetto, I. Gornushkin, B. W. Smith, J. D. Winefordner: From sample to signal in laser-induced breakdown spectroscopy: A complex route to quantitative analysis (Chapter 3) in: Laser Induced Breakdown Spectroscopy (LIBS): Fundamentals and Applications (ed.: A. W. Miziolek, V. Palleschi, I. Schechter), *Cambridge University Press*, 2006.

POSTER PRESENTATIONS

OPTICAL AND NUMERICAL MODELING OF A SPATIAL HETERODYNE LASER-INDUCED BREAKDOWN SPECTROMETER

Dávid J. Palásti[1,2], Miklós Veres[3], Miklós Füle[4,5], Gábor Galbács[1,2]*

[1]Department of Inorganic and Analytical Chemistry, Faculty of Science and Informatics, University of Szeged, 6720 Dóm square 7, Szeged, Hungary
[2]Department of Materials Science, Interdisciplinary Excellence Centre, University of Szeged, Dugonics square 13, 6720 Szeged, Hungary
[3]Department of Applied and Nonlinear Optics, Institute for Solid State Physics and Optics, Wigner Research Centre for Physics, 1121 Konkoly-Thege Miklós way 29-33, Budapest, Hungary
[4]Institute of Physics, Faculty of Engineering, University of Szeged, 6724 Mars square 7, Szeged, Hungary
[5]ELI-HU Non-Profit Ltd., Wolfgang Sandner u. 3., H-6728 Szeged, Hungary
**e-mail: galbx@chem.u-szeged.hu*

1. INTRODUCTION

Spatial heterodyne spectroscopy (SHS) is one the several interferometric spectrometers proposed in the literature. It combines dispersion- and interference-based techniques. Basically it is a version of the Michelson interferometer with no moving parts and diffraction gratings in the place of mirrors. The radiation from a light source is collimated and split between two arms of the interferometer terminated by diffraction gratings. The light dispersed by the gratings recombines at the beamsplitter and produces Fizeau fringes that are recorded by an imaging detector. The wavelength-resolved information is thus converted to a spatially-resolved interferogram, from which the recovery of the spectrum is done by Fourier transformation.

The earliest practical realization of SHS with a useful spectral resolution was presented by Dohi and Suzuki [Dohi 1971], who applied a photographic plate as an imaging detector. Harlender was the first to describe the modern version of the SHS; he used a CCD camera as the detector and also developed algorithms for interferogram processing [Harlender 1991]. For a more detailed description of the SHS principle, please see e.g. [Harlender 1991, Lenzner 2016, Gojani 2019].

Only three full papers were published so far on the combination of SHS with laser-induced breakdown spectroscopy (LIBS). The shared compact and single-shot character make SHS and LIBS a perfect couple in theory. It was Gornushkin et al. who first proposed and tested the SHS-LIBS combination [Gornushkin 2014] as an instrumentation that has potential for sensitive, stand-off quantitative elemental analysis and sample classification applications. Angel et al. successfully demonstrated that the enhanced sensitivity of a miniature LIBS-SHS system is indeed adequate to perform stand-off analysis from a distance of 20 meters using no collection optics [Barnett 2017, Allen 2018].

In our present project, we are in the process of constructing a tunable, optimized SHS setup for LIBS use [Palásti 2019]. Now we present results from optical and numerical

modeling which allow insight into the effect of the most important optical parameters of the setup on the spectroscopy performance.

2. EXPERIMENTAL

The optical model of the double grating SHS arrangement was constructed in Comsol Multiphysics, using the geometrical optics interface and the ray tracing module. A parametric sweep of non-sequential ray tracing was performed using hexapolarly arranged, unpolarized, monochromatic and collimated input light beam consisting of 331 individual rays, with plane wave approximation. Reflective grating parameters were used in the models (150, 300 and 600 mm^{-1} ruled gratings blazing at 500 nm). The plane of the grating surface was vertically aligned (there was no tilt) and the square-shaped detector was always placed at the same distance from the center of the beamsplitter as the gratings. The fundamental experimental variables of the SHS setup were the grating arm lengths (distance of the grating surface from the active plane of the beamsplitter; varied here as 50, 75 and 100 mm), grating rotation angle (around an axis oriented along the *z* direction and placed at the grating surface, measured counterclockwise from the grating to beamsplitter optical axis; here varied between 65 to 90 degrees), input beam wavelength, and input beam diameter. The gratings were used in the first diffraction order and the beam diameter as well as the detector size was kept at 20 mm. A schematic of the Comsol optical model can be seen in **Figure 1**. Lens tubes were added to the setup in order to block stray rays.

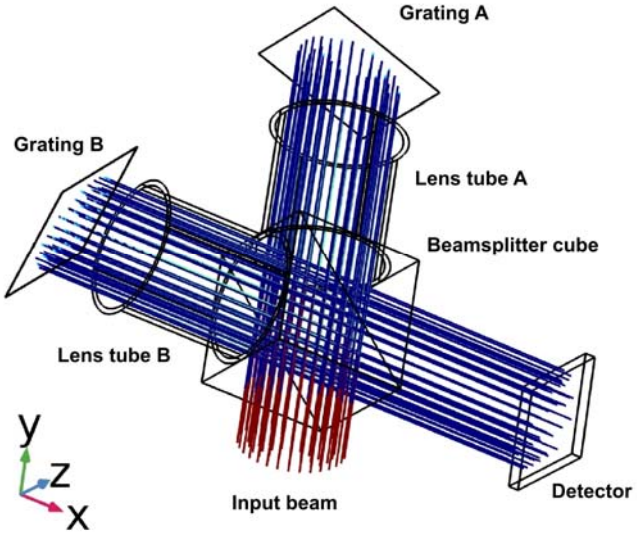

Figure 1. Conceptual ray tracing model of the SHS setup in Comsol.

3. RESULTS AND DISCUSSION

3.1. Spectral coverage and sensitivity

From an analytical point of view, the spectral coverage (SC), and more importantly the free spectral bandpass (FSB), of a spectrometer is crucial, because it directly limits the spectral information that can be collected. In our study, the FSB of the SHS arrangement was estimated by using ray tracing with a parameter sweep for the input beam wavelength (400 to 700 nm) and assessing the range of wavelength in which the first order output at the detector is free from contribution (overlap) from the second order diffraction. The gratings were fixed at their Littrow angle (Θ_L). We defined SC as the wavelength range between the 10% points of the relative sensitivity curve of the setup in the first order (between the maximum and minimum wavelengths for which the relative sensitivity is at least 10%).

It was found that the SC generally becomes consistently narrower with the increase of the grating density and the arm length. The FSB is 100-200 nm and is always significantly narrower than the spectral coverage, except for the 600 mm^{-1} grating, in which case FSB is equal to SC. The center position of FSB decidedly shifts towards shorter wavelengths with the increase of the two control parameters. The FSB is the widest (200 nm) for the 300 mm^{-1} grating, but is not much narrower for the 600 mm^{-1} grating with shorter arm lengths. In general, FSB seems to increase with the arm length for less dense gratings, whereas the trend is reversed for the 600 mm^{-1} grating. These findings indicate that it is generally mandatory to use optical filters in a compact SHS setup, primarily for order-sorting purposes, strategically placed at the input. Please also note that in order to exploit this FSB in LIBS spectroscopy, where a minimum of 100 pm spectral resolution is needed, the use of a megapixel detector is mandatory.

Apart from the transmission and reflectance characteristics of the optical elements used, the sensitivity of the SHS setup is expected to be influenced by the fraction of rays reaching the detector depending on the grating density, rotation angle and grating arm length. The relative sensitivity at the blazing wavelength is maximal at the Littrow angle, as expected. The relative sensitivity decreases rapidly, if the gratings are rotated concertedly; a few degree rotation results in a sensitivity drop of about 50%. Due to the same blazing wavelength, blaze angle (and hence Θ_L) changes linearly with the grating density. The trend is unaffected by the arm length. This indicates that according to the expectations, the highest sensitivity can be achieved if the gratings are fixed at Θ_L.

For geometric reasons, the sensitivity (fraction of rays reaching the detector) also depends on the relative size of the input beam and the detector, as well as the wavelength. This is well illustrated by **Figure 2**. In these ray tracing simulations, we kept the detector size fixed at 20 mm, and varied the other two parameters. As it can be seen, a decrease of the input beam diameter (assuming the same photon flux) increases the relative sensitivity and makes its wavelength-dependence less pronounced. The reason behind this is that a smaller diffracted beam can be better accommodated by the detector than a large beam. At the same time, the decrease of the beam diameter also decreases the spectral coverage. In terms of wavelength, the maximum sensitivity is reached at around

the 500 nm blaze wavelength), as expected. A similar trend was observed for other gratings and arm length values too.

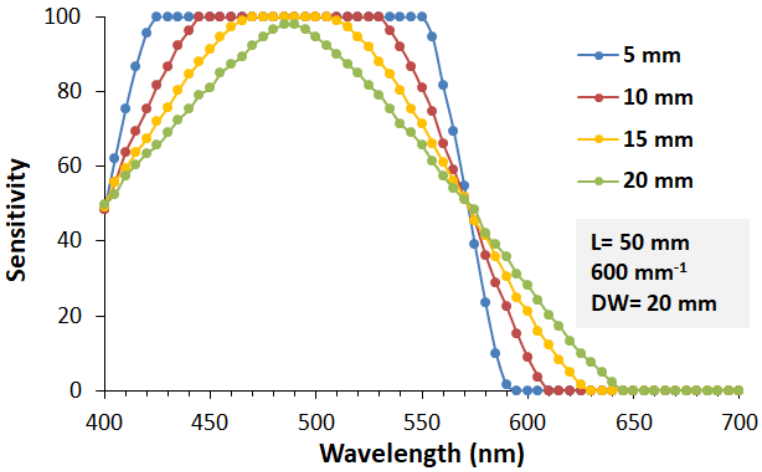

Figure 2. Effect of the wavelength and input beam diameter on the relative sensitivity of the SHS arrangement. The detector size is 20 mm.

A better comparison of the overall sensitivity of setups with different arm lengths and grating densities can be done via the calculation of the total intensity (cumulative fraction of rays) reaching the detector within the FSB. Our calculations clearly showed that the sensitivity is best for the 300 mm^{-1} grating, even if total intensities are normalized with the width of the FSB. It is a somewhat surprising finding, as considering that the blazing wavelength for the gratings used here is 500 nm, and the grating efficiency is known to be greatest around this wavelength, therefore the 600 mm^{-1} grating, for which the FSB is roughly centered around 500 nm, was expected to be optimal from the point of view of sensitivity.

3.2. Time dispersion

Under typical and single-pulse conditions, ns LIBS of a solid sample produces a plasma with a lifetime on the order of some tens of µs. If bulk liquid ns LIBS analysis is performed, the plasma lifetime is roughly an order of magnitude shorter. If a fs laser is used to generate the LIB plasma, then its lifetime is in the ns range. LIBS uses gated detection in order to minimize continuum background radiation, hence the required gating width is often one or two orders of magnitude shorter than the plasma lifetime. The above conditions require a detailed investigation of the time dispersion caused by the SHS arrangement as well as the means of coupling of the plasma light into the interferometer in order to determine the limiting condition and the best possible time resolution of the LIB-SHS system.

First, the time dispersion occurring inside the SHS itself needs to be considered. Dispersion will mainly occur because rays, depending on their relative position within the beam, will reach the detector at different times due the rotation of the gratings. In

addition, different wavelengths will also travel through paths of slightly different length. Ray tracing simulation for all our modeled SHS arrangements indicate that the dispersion within the SHS arrangement is always quite small in our system: it varies between 2.4 and 27.9 ps. As expected, the dispersion scales linearly with the beam diameter, but the effect of wavelength and grating parameters is complex.

The evaluation of the effect of the means of light coupling into the SHS requires detailed analysis. The application of fiber optic light coupling is expected to deteriorate the time resolution of the LIB-SHS system, because chromatic, modal and waveguide dispersion in an optical fiber result in a distortion of the transmitted fast optical pulses. Our calculations revealed that the total dispersion under the experimental conditions used here (gratings, arm length, typical LIBS fiber optic cables, etc.) is between 150 and 342 ps. Clearly, the total dispersion in the optical fiber can be minimized by keeping the fiber length and the NA as small as possible.

It should also be mentioned that dispersion also occurs during the coupling of the plasma emission into the optical fiber and also at the collimation of the light output from the fiber. For the sake of simplicity, let us assume a two-lens light collection arrangement at the fiber input and a single collimation at the output, with identical lenses NA-matched to the fiber. Then the dispersion due to the different path lengths the light travels through the lenses will be proportional to the beam diameter. In total, the calculation gives increasing dispersion values for increasing beam diameters, but these values are only a couple of percents of the total dispersion occurring in the optical fiber.

Overall, it can be stated that the dispersion of pulsed light in the SHS arrangement alone is very small compared to the dispersion that occurs in the optical fiber, if the LIB plasma emission is coupled into the SHS arrangement via a fiber. In this case, the shortest gate width that can be used at the imaging detector is about 0.2-0.4 ns.

4. CONCLUSIONS

We have provided detailed numerical and optical modeling data on the sensitivity, free spectral range and time dispersion characteristics of a dual-grating SHS spectrometer meant for its optimization for LIBS use. It was shown that for high time resolution (e.g. ps) spectroscopy, direct coupling of the light into the spectrometer is advised, but for ns LIBS, fiber optic coupling is completely feasible. The free spectral range was found to be decent (100-200 nm) of the SHS even in a compact size, but to exploit this range for LIBS spectroscopy, where a minimum of 100 pm spectral resolution is needed, the use of a megapixel detector is mandatory.

5. ACKNOWLEDGEMENTS

The financial support received from various sources including the Ministry of Innovation and Technology (through project No. TUDFO/47138-1/2019-ITM FIKP) and the National Research, Development and Innovation Office (through projects No. K_129063, EFOP-3.6.2-16-2017-00005, TKP 2020 Thematic Excellence Program 2020) of Hungary are kindly acknowledged. The project was also supported by the ÚNKP-20-3 – New National Excellence Program of The Ministry for Innovation and Technology from the source of The National Research, Development and Innovation Fund.

6. REFERENCES

[Dohi 1971] T. Dohi, T. Suzuki, *Appl. Opt.*, 10 (1971) 1137.

[Harlender 1991] J. M. Harlander, Spatial heterodyne spectroscopy: interferometric performance at any wavelength without scanning, PhD dissertation, University of Wisconsin (USA), 1991.

[Lenzner 2016] M. Lenzner, J. C. Diels, *Opt. Express*, 24 (2016) 1829.

[Gojani 2019] A. B. Gojani, D. J. Palásti, A. Paul, G. Galbács, I. B. Gornushkin, *Appl. Spectrosc.*, 73 (2019) 1409.

[Gornushkin 2014] I. B. Gornushkin, B. W. Smith, U. Panne, N. Omenetto, *Appl. Spectrosc.*, 68 (2014) 1076.

[Barnett 2017] P. D. Barnett, N. Lamsal, S. M. Angel, *Appl. Spectrosc.*, 71 (2017) 583.

[Allen 2018] A. Allen, S.M. Angel, *Spectrochim. Acta B*, 149 (2018) 91.

[Palásti 2019] D. J. Palásti, L. Himics, T. Váczi, M. Veres, I. B. Gornushkin, G. Galbács, poster presentation #PI_010, *10th Euro-Mediterranean Symposium on LIBS*, Brno, 2019.

SIGNAL ENHANCEMENT OF GASEOUS SAMPLES IN THE PRESENCE OF NANOAEROSOLS GENERATED BY A SPARK DISCHARGE

Lajos P. Villy[1,3], Dávid J. Palásti[2,3], Gábor Skoda[2], Attila Kohut[1,3], Zsolt Geretovszky[1,3], Éva Kovács-Széles[4], Gábor Galbács[2,3]*

[1]Department of Optics and Quantum Electronics, University of Szeged, 6720 Szeged, Dóm square 9, Hungary
[2]Department of Inorganic and Analytical Chemistry, University of Szeged, 6720 Szeged, Dóm square 7, Hungary
[3]Department of Materials Science, Interdisciplinary Excellence Centre, University of Szeged, 6720 Szeged, Dugonics square 13, Hungary
[4]Nuclear Security Department, Centre for Energy Research, 1121 Budapest, Konkoly-Thege Miklós way 29-33, Hungary
**e-mail: galbx@chem.u-szeged.hu*

1. INTRODUCTION

Nanoparticle enhanced laser-induced breakdown spectroscopy (NE-LIBS), first described by de-Giacomo et al., is becoming a well-established signal enhancing technique in recent years [Dell'Angelo 2018]. Properly sized and distributed metallic nanoparticles (NPs) deposited on the surface of a solid sample proved to provide multiple orders of signal enhancement. In addition to solid samples, liquid samples were also described to be successfully analyzed sensitively by this approach [Palásti 2020]. The signal enhancement effect is generally described as being essentially caused by electron field emission. At the same time, gas samples, which generally have a 10-100 times higher breakdown threshold than solids and liquids, have not yet been attempted to be analyzed by the NE-LIBS approach.

Spark discharge nanoparticle generation is a promising physical technique for nanoparticle manufacturing. Similarly to other physical techniques, this method is able to avoid the use of reagents, precursors, or other chemical components therefore can provide a more environmentally friendly route of NP generation. In spark discharge generators (SDGs), high-voltage and high-current, microsecond-long spark discharges are created between two electrodes in a controlled gas flow at atmospheric pressure. Due to the sparking, the electrode material is eroded and a vapor plume is formed between the electrodes, which is then undergoes nucleation, condensation, coagulation, and aggregation [Tabrizi 2009].

In this study, we investigate the possibility of using the NE-LIBS approach to boost the sensitivity of the measurement of gases via mixing the gas with nanoparticles generated by an SDG.

2. EXPERIMENTAL

The central part of the spark discharge generator system is a vacuum chamber (Pfeiffer Vacuum GmbH.), in which the applied cylindrical, gold electrode (99.9% purity, Kurt J. Lesker Co.) pair was horizontally positioned and axially aligned whit 2.0 mm gap between the two electrodes.

The 5.0 standard litre per minute (slm) argon (99.996% purity, Messer Hungarogáz Ltd.) carrier gas flow, controlled by a mass flow controller (Model GFC16, Aalborg Inc.) was fed in the chamber via the down port (upward pointing "crossflow" with injector nozzle) [Kohut 2018]. All experiments were carried out at near atmospheric pressure, and the created gold NPs were lead through a 900 °C compaction furnace (EHA 12/300B, Carbolite Gero GmbH.). The concentration of the particles was controlled by the spark repetition rate and one or two dilution systems (VKL 10, Palas GmbH.). The size sorting and the number concentration measurement was done by a scanning mobility particle sizer (SMPS) system consisting of an electrostatic classifier (3082, TSI, USA), an ultrafine condensation particle counter (CPC, 3756, TSI, USA), and an aerosol charge neutralizer (Kr-85, NRD, USA).

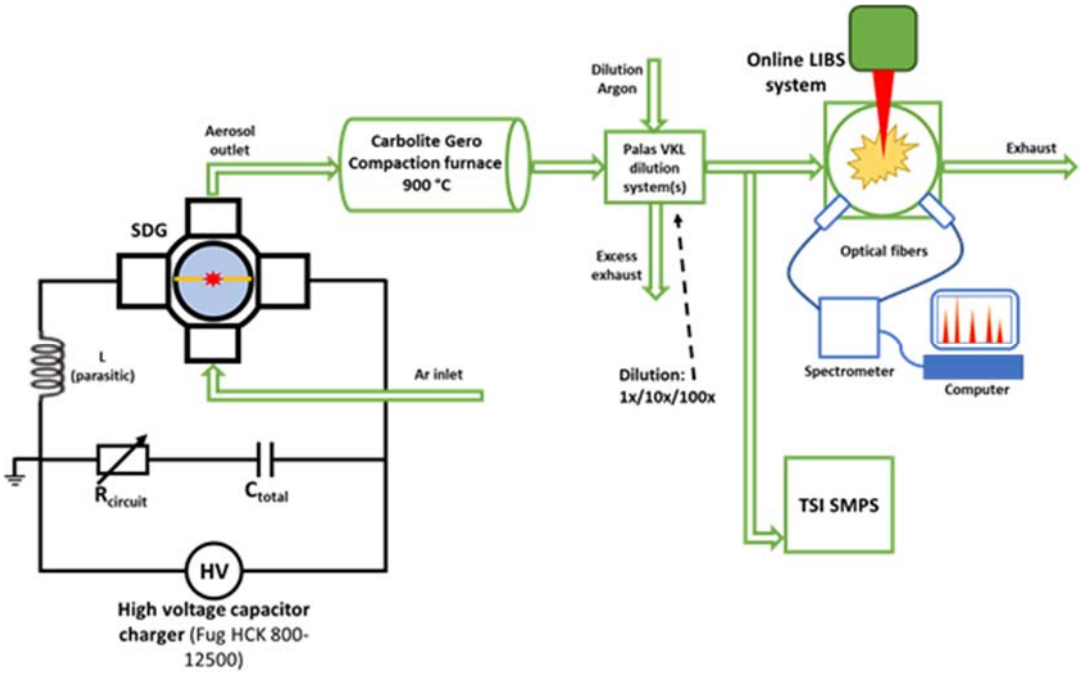

Figure 1. Schematic of the experimental setup.

The LIBS experiments were carried out in a flow-through, small volume measurement chamber constructed in-house for LIBS aerosol measurements [Palásti 2019]. The Nd:YAG laser provided 30 mJ pulses of 4 ns duration at the fundamental 1064 nm wavelength beam, which was focused into the chamber from above through a UV-grade fused silica window. The repetition rate of the plasma generating laser was set to a low value (ca. 0.25 Hz) thereby ensuring that the content of the chamber is completely renewed by the gas flow between laser shots. The LIBS plasma was observed

via two fused silica collimating lenses implemented in two ports located on the sides of the chamber (looking onto the same spot in the chamber in the horizontal direction, with 90° angle between the optical axes of the two lenses). The collected light was coupled into a two-channel fiber-optic CCD spectrometer (AvaSpec-FT2048, Avantes, NL) using optical fibers. The measurement chamber was mounted on a translation stage, which allowed bringing the laser focal spot inside the chamber in front of the light collection lenses.

Gating of the spectral data collection was achieved by the internal electronics of the spectrometer, which was triggered by the laser power supply unit and continuously monitored on a digital storage oscilloscope (TDS1002, Tektronix, USA). The minimum possible gate delay of 1 μs and gate width of 2 ms was set at the spectrometer. The double-channel spectrometer allowed the recording of the plasma emission in the 344–888 nm spectral ranges, with resolutions of 0.09 nm and 0.4 nm, respectively.

3. RESULTS AND DISCUSSION

The averaged spectra of 100 laser shots delivered into a clean argon gas and a gold nanoaerosol stream (in argon) are shown in **Figure 2**. It can be seen that the applied irradiance was not efficient to create a microplasma in the clean gas, but in the presence of nanoparticles it generated an intensive LIBS spectrum. The spectral lines can be assigned to Ar I and Ar II species and none of the intense gold spectral lines were noticeable. This indicates that the presence of Au NPs lowered the breakdown threshold of the argon gas, but their mass concentration was not sufficient to produce a gold spectrum of observable intensity. The Ar signal enhancement is nearly 5000-fold.

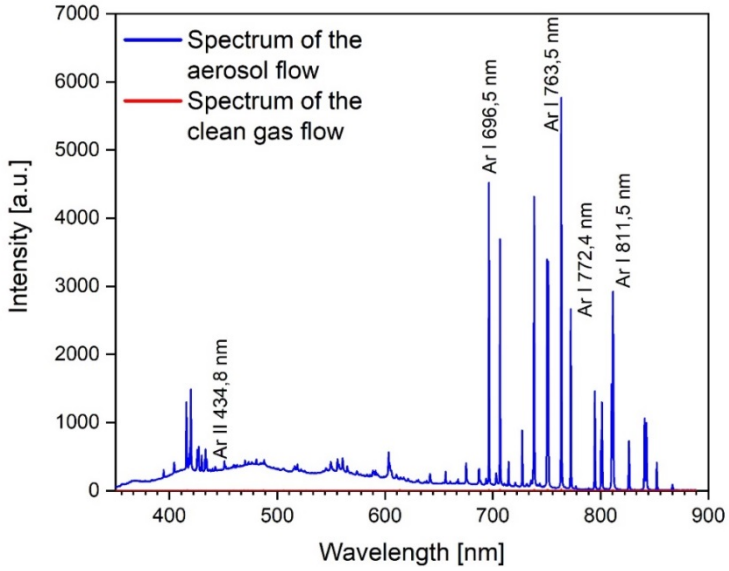

Figure 2. Average spectrum of 100 laser shots delivered into a clean Ar gas flow and an Au NP aerosol stream.

This latter finding is also illustrated on the left side of **Figure 3.**, which shows the monitoring of the net intensity of an Ar I and a Au I line during a 100-shot LIBS measurement session. Although the Ar line intensity may reach high values, but it shows a high variance. Sometimes it cannot even be separated from the background. Since the Ar I 736.5 nm was the most intensive line in our spectra, thus when this line could not be separated from the background, meant that, there was no plasma formation. During our measurements we noticed that if the number concentration of the aerosol was increased, then the frequency of the spectrum producing shots increased, and the shot-to-shot variance decreased at the same time. These trends are probably due to the more or less random distribution of NPs in the gas stream. When their concentration in the blast radius is too low, then no plasma formation is detected. However, a higher NP concentration results in the statistical increase of NPs presence in the blast radius. Due to the significant shot-to-shot variance in the intensities, the accumulation of several spectra is advised, especially if low aerosol concentration is used.

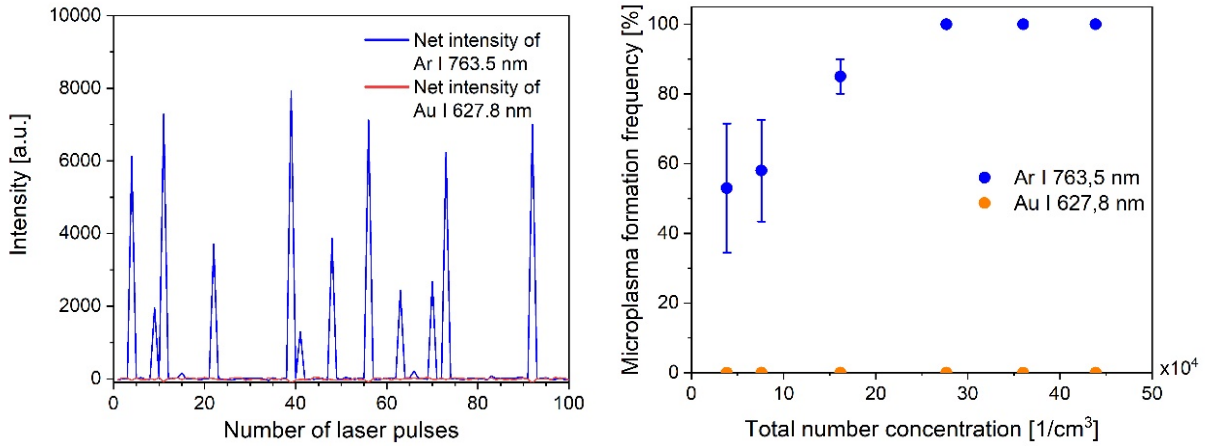

Figure 3. Net intensities of two spectral lines during 100 laser shots on the left, and the plasma formation frequency in the function of the total number concentration of the Au NPs in the aerosol flow on the right.

The effect of the aerosol number concentration and nanoparticle size to the signal enhancing phenomenon was investigated in detail, using similarly sized nanoparticles with different number concentrations and different sized nanoparticles with similar number concentration. Gas line intensities are shown in the **Figure 4.** in the dependence of the Au NP total number concentration. We investigated the effect of number concentration through c.a. two orders of magnitudes (it changed between $3.8 \cdot 10^3$ and $4.4 \cdot 10^5$). In the beginning of our concentration range, the signal grew linearly with the number concentration, but at higher concentrations, the signal started to reach a plato, where no significant change in the intensity of the spectra occurred. Due to instrumental limitations, we were able to investigate the aerosol of only three differently sized NPs, with diameters 20, 25 and 30 nm. Our findings suggest that larger NPs provide larger signal enhancement.

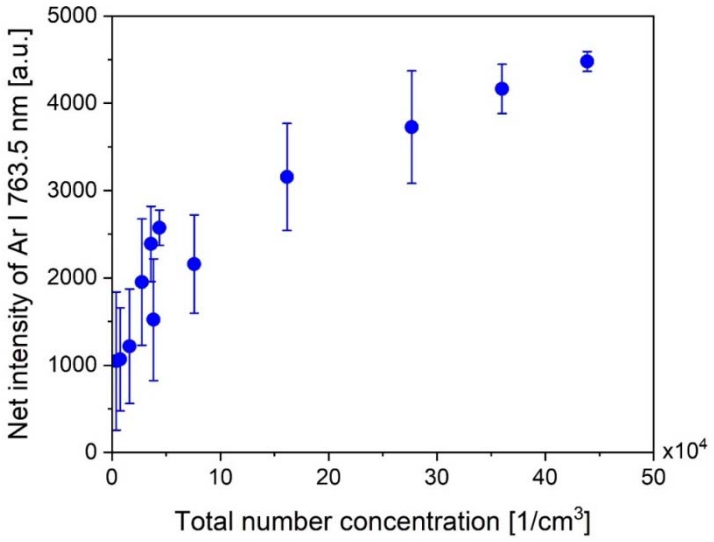

Figure 4. Net intensity of the Ar I 763.5 nm line as the function of the number concentration of Au NPs

Although the signal enhancement phenomenon still needs explanation, but we believe that electron field emission from the NPs causes a decrease in the breakdown threshold for the gas, which helps forming a microplasma. The frequency of plasma formation events seems to be correlated with the NP number concentration up to a level, therefore the use of a ca. $5 \cdot 10^5$ cm^{-3} concentration is advisable for maximizing the signal enhancement.

4. CONCLUSIONS

The mixing of nanoparticles into a gaseous sample is proved to be a potent signal enhancing technique. An approximately 5000-fold signal enhancement was achieved. In our opinion, NELIBS has a great potential for the trace gas analysis. Although at first the need for having an SDG attached to a LIBS system may not seem like a practical analytical setup, but in actuality, reasonably compact and portable SDGs (e.g. Palas model GFG 1000/3000) and LIBS instruments (e.g. Applied Spectra LIBScan 25+) are available on the market, thus their combination is not a far-fetched idea.

5. ACKNOWLEDGEMENTS

The financial support received from various sources including the Ministry of Innovation and Technology (through project No. TUDFO/47138-1/2019-ITM FIKP) and the National Research, Development and Innovation Office (through projects No. K_129063, EFOP-3.6.2-16-2017-00005, TKP 2020 Thematic Excellence Program 2020) of Hungary are kindly acknowledged. The project was also supported by the ÚNKP-20-3 – New National

Excellence Program of The Ministry for Innovation and Technology from the source of The National Research, Development and Innovation Fund.

6. REFERENCES

[Dell'Angelo 2018] M. Dell'Angelo, R. Alrifai, A. De Giacomo, *Spectrochim. Acta B*, 148 (2018) 105.

[Palásti 2020] D. J. Palásti, P. Albrycht, P. Janovszky, K. Paszkowska, Zs. Geretovszky, G. Galbács, *Spectrochim. Acta B*, 166 (2020) 105793.

[Tabrizi 2009] N. S. Tabrizi, M. Ullmann, V. A. Vons, U. Lafont, A. Schmidt-Ott, *J. Nanoparticle Res.*, 11 (2009) 315.

[Kohut 2018] A. Kohut, L. P. Villy, T. Ajtai, Zs. Geretovszky, G. Galbács, *J. Aerosol Sci.*, 118 (2018) 59.

[Palásti 2019] D. J. Palásti, A. Metzinger, T. Ajtai, Z. Bozóki, B. Hopp, É. Kovács-Széles, G. Galbács, *Spectrochim. Acta B*, 153 (2019) 34.

ENHANCEMENT OF THE TEA CO_2 LIBS EMISSION USING Ag AND Ag/Zn NANOSTRUCTURES

Jelena Petrović[1], Marina Radenković[2], Miloš Momčilović[1], Miloš Ognjanović[3], Sanja Zivković[1]*

[1]Department of Physical Chemistry, VINČA Institute of Nuclear Sciences – National Institute of the Republic of Serbia, University of Belgrade, P.O. BOX 522, 11001 Belgrade, Serbia
[2]Faculty of Chemistry, University of Belgrade, P.O. BOX 51, 11158 Belgrade, Serbia
[3]Department of Theoretical Physics and Condensed Matter Physics, VINČA Institute of Nuclear Sciences – National Institute of the Republic of Serbia, University of Belgrade, P.O. BOX 522, 11001 Belgrade, Serbia
**e-mail: sanjaz@vinca.rs*

1. INTRODUCTION

Nanoparticle-Enhanced Laser-Induced Breakdown Spectroscopy (NELIBS) that is firstly introduced by *de Giacomo et al.* has gained much attention due to its capability of improving the spectral intensity and detection sensitivity [De Giacomo 2013]. The presence of nanotechnology in today's scientific world is increasing, as well as their various application. This new approach uses a deposition of nanoparticles on the sample to increase the emission signal of the LIBS plasma. There are various methods of preparation of different types of nanoparticles and different materials of the sample that is analyzed. The possibility of using nanoparticles in different fields increases the need for their production in stable states and environmentally acceptable processes. Several researchers have studied the new approach of NELIBS from both fundamental and application point of view [Palásti 2020, Poggialini 2020].

Enhancement of the LIBS emission signal by deposition of Ag/Zn nanoparticles prepared by laser ablation and silver nanoparticles prepared by chemical synthesis on the surface of the aluminum sample has been investigated. The great potential of the use of nanoparticles in analytical LIBS is shown, by obtained results and the further possible development of this technique is suggested.

2. EXPERIMENTAL

2.1. Synthesis of nanostructures

Silver and bimetallic Ag/Zn nanoparticles were produced by chemical and by the laser ablation method. A pure metal of the Zn sample was placed in a glass and covered with 6 mL of previously synthesized Ag colloidal solution. Laser applied was the picosecond Nd:YAG system, operating at 1064 nm with a 150-ps pulse length, pulse energy 40 mJ pulse energy, and irradiation time of 15 minutes.

For the preparation of silver nanoparticles by the chemical method 1.98×10^{-2} M $NaBH_4$, 3.8×10^{-3} M $AgNO_3$, 0.1 M NaOH, and citric acid were used. A 30 ml 1.98×10^{-2} M $NaBH_4$ was poured into a glass, 0.1 M NaOH was added and the pH of the solution was adjusted to pH 10.5. Then the solution was placed in an ice bath and was stirring for 20 minutes. After that 10 ml of 3.8×10^{-3} M aqueous solution of $AgNO_3$ was added drop-wise into the cooled solution of $NaBH_4$. Stirring was stopped immediately when the solution of $AgNO_3$ was being added. Finally, 0.008 g of citric acid was added into the Ag NPs solution.

The hydrodynamic size distribution of the obtained colloid solution of nanoparticles was analyzed by dynamic light scattering (DLS) technique using a Zetasizer Nano ZS90 (Malvern, UK) with 633-nm He-Ne laser and 90° detection optics. The concentrations of Ag, Zn, and Cu in these solutions were determined by the ICP-OES technique.

2.2. LIBS measurements

LIBS measurements were conducted using a unique developed LIBS system based on pulsed gas TEA CO_2 laser and time-integrated spatially resolved spectroscopy (TISR). In our previous study, we reported that aluminum alloy samples need to be mechanically treated with corundum abrasive paper to increase the absorptivity of applied TEA CO_2 laser wavelength before the LIBS analysis [Zivkovic 2017]. In this study, all aluminum samples were cleaned from the impurities on the sample surface, and after that samples were coated with a thin layer of nanomaterial dispersion droplets and dried at the end.

The plasma was generated by focusing a pulsed TEA CO_2 laser that emits at 10.6 μm on the aluminum target with deposed NPs on the surface at atmospheric pressure. All measurements were taken at the focal point. Applied laser energy was 170 mJ with a repetition rate of 1 Hz and the shot to shot fluctuation of its energy was about 5%. Optical emission from the induced plasma was collected on the entrance slit of a Carl Zeiss PGS2 monochromator by using an achromatic lens with magnification 1:1. LIBS analysis was conducted in time-integrated mode during 5 s using CCD Apogee Alta F1007 camera as a detector. The TISR measurements were performed at the atmospheric pressure in the air. All measurements were carried out in triplicate and obtained spectra present average values of line intensities from 3 different parts of the sample surface.

3. RESULTS AND DISCUSSION

3.1. Characterization of nanostructures

Obtained concentration from ICP-OES analysis for the used nanostructures alongside the size distribution are given in **Table 1**. In both cases, measurement uncertainties were calculated as the standard deviation.

Ag				Ag/Zn			
Size [nm]	**Ag [ppm]**	**Zn [ppm]**	**Cu [ppm]**	**Size [nm]**	**Ag [ppm]**	**Zn [ppm]**	**Cu [ppm]**
1.9 ± 0.7	29.1 ± 0.2	0.8 ± 0.1	< 0.002	574±45	3.5 ± 0.5	35.1 ± 0.1	< 0.002

Table 1. DLS (size) and ICP-OES (composition) results obtained for Ag and bimetallic Ag/Zn dispersions.

3.2 NELIBS analysis of aluminum samples

The LIBS spectra segments of the analyzed sample with a focus on the copper line are shown in **Figure 1**. Each spectrum represents an averaged spectrum from 5 laser pulses while the distance between the focusing lens and a target was constant at 1 mm in front of the target. When the pure sample was analyzed, not even one emission line was detected. At the same time, when the same sample has deposed nanoparticles on it, the emission lines of Ti and Cu from the sample were detected.

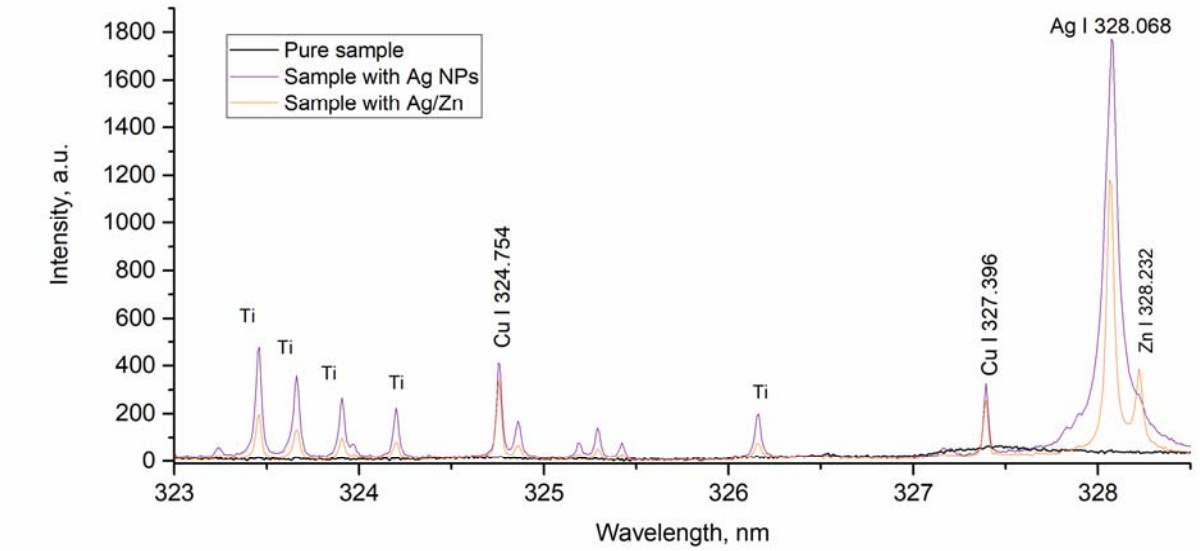

Figure 1. LIBS spectra obtained by analysis of: a) untreated sample; b) sample with Ag nanoparticles; and c) sample with bimetallic dispersion of Ag and Zn.

For determination limits of detection (LOD) of the applied technique, the standard calibration method was chosen. The linear dependency of measured LIBS intensity towards the concentration of Cu in samples was obtained, **Figure 2**. It shows the incensement of a slope when are 2 nm nanoparticles of silver were used, which corresponds to the incensement of method sensitivity. Using a formula LOD = 3σB/b, where σB is the standard deviation of the background surrounding the selected emission line, and *b* is the sensitivity defined as the slope of the calibration curve, we estimated that the limit of detection of Cu by NELIBS was 70 ppm.

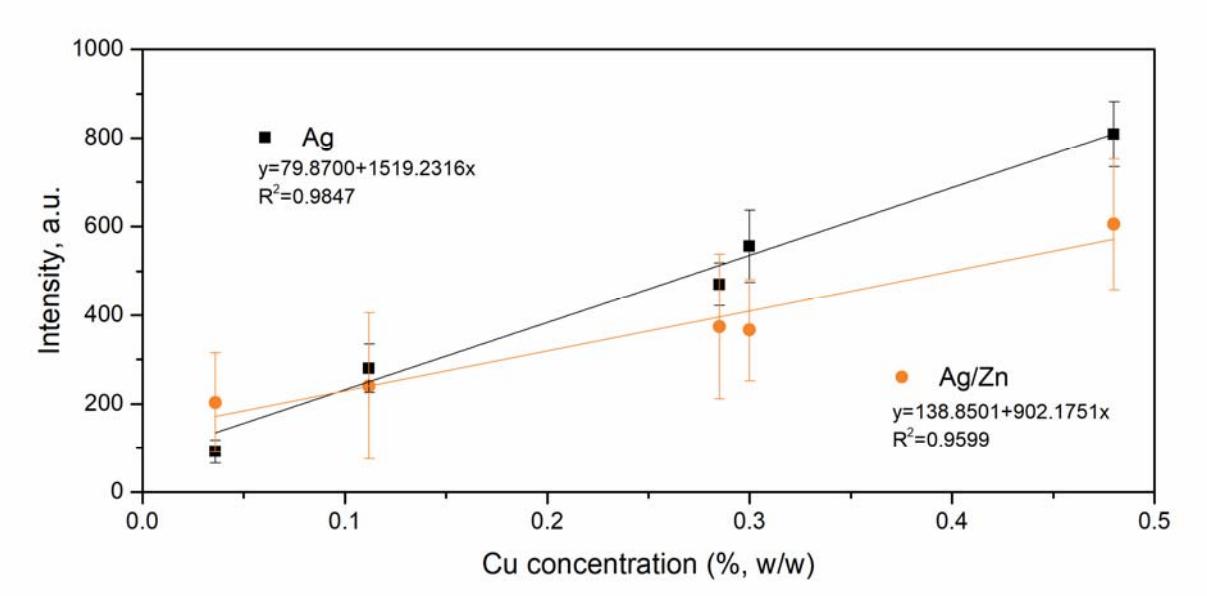

Figure 2. Calibration plots obtained from: a) LIBS analysis of Ag deposed onto Al sample (black); b) LIBS analysis of Ag/Zn deposed onto Al sample (orange).

4. CONCLUSIONS

In our experiment, the influence of nanoparticles application on a signal amplification in the LIBS spectrum was investigated. Nanoparticles were prepared in two ways, by chemical synthesis and laser ablation with Nd:YAG laser. The obtained nanoparticles were deposed to an aluminum target and exposed to TEA CO_2 laser radiation at atmospheric pressure. The recorded spectra show more signals from material with nanoparticles than from clean material. As shown in **Figure 1.**, a better emission signal was acquired using chemically obtained Ag nanoparticles. The developed and improved NELIBS technique for obtaining better emission signals has proven to be compact, easy to use and relatively stable, which can be applied in the analysis of materials.

5. ACKNOWLEDGEMENTS

The research was funded by the Ministry of Education, Science and Technological Development of the Republic of Serbia.

6. REFERENCES

[De Giacomo 2013] A. De Giacomo, R. Gaudiuso, C. Koral, M. Dell'Aglio, O. De Pascale, *Anal. Chem.*, 85 (2013) 10180.

[Palásti 2020] D. Palásti, P. Albrycht, P. Janovszky, K. Paszkowska, Z. Geretovszky, G. Galbács, *Spectrochim. Acta B*, 166 (2020) 105793.

[Poggialini 2020] F. Poggialini, B. Campanella, S. Legnaioli, S. Pagnotta, V. Palleschi, *Spectrochim. Acta B*, 167 (2020) 105845.

[Zivkovic 2017] S. Zivkovic, J. Savovic, M. Trtica, J. Mutic, M. Momcilovic, *J. Alloys Compd. B,* 700 (2017) 175.

LASER ABLATION OF MELOXICAM IN LIQUID ENVIRONMENT

Eszter Nagy[1]*, Zsolt Homik[1], Tamás Smausz[1], Judit Kopniczky[1], Rita Ambrus[2], Piroska Szabó-Révész[2], Béla Hopp[1,3]

[1]Department of Optics and Quantum Electronics, University of Szeged, 6720 Szeged, Dóm square 9, Hungary
[2]Institute of Pharmaceutical Technology and Regulatory Affairs, University of Szeged, 6720 Szeged, Eötvös street 6, Hungary
[3]Department of Materials Science, Interdisciplinary Excellence Centre, University of Szeged, 6720 Szeged, Dugonics square 13, Hungary
**e-mail: nagyeszter.physx@gmail.com*

1. INTRODUCTION

In the development of new pharmaceutical formulation strategies, the need for innovative drug particle size reduction approaches has significantly increased during the past decades. In the US poorly soluble compounds represent 40% of the top 200 marketed oral drugs and 33% of the drugs listed in the US Pharmacopeia. Additionally, 75% of compounds under development and 90% of new chemical entities are poorly soluble [Rodriguez 2015]. A frequently used method to improve the dissolution rate and transport characteristics of these drugs is particle size reduction. Thereby faster absorption and more effective cellular uptake can be achieved [Mosharraf 1995, Rasenack 2003].

Since pulsed laser ablation is a well-established technique for particle generation from both inorganic and organic materials, pharmaceutically relevant investigations became interested in using laser ablation as a particle size reduction technique [Sylvestre 2011, Ding 2014, Hopp 2018, Singh 2020, Gera 2020]. In this systematic study we demonstrate the application of pulsed laser ablation for the fragmentation of drug particles in liquid environment.

2. EXPERIMENTAL

Pulsed laser ablation in liquid (PLAL) was used to generate particles from meloxicam (mx.), a medically relevant poorly water-soluble nonsteroidal anti-inflammatory drug (NSAID). As targets, pastilles were pressed from commercially available meloxicam powder (EGIS Ltd, Budapest, Hungary) by a hydraulic compactor at 175 MPa pressure. To determine the suitable parameter range for ablation, nanosecond (ns) laser pulses of different wavelengths (248 nm, 532 nm and 1064 nm) and fluences (~ 3-13 J/cm^2) were investigated in distilled water environment [Nagy 2019].

To characterize the generated particles several methods were applied. Fourier transform infrared spectroscopy (FTIR) was used for chemical analysis. The size-distribution and morphology of the generated particles were studied by scanning electron microscopy (SEM). The crystallinity was investigated by X-ray powder diffraction (XRPD). Heat induced phase transitions of the PLAL generated particles were detected by differential scanning calorimetry (DSC) [Hopp 2018].

The ablation dynamics were studied using the time-resolved pump-probe shadowgraphy technique. Fast photography took place with a nanosecond time resolution. The ablation process was investigated at three different fluences using 532 nm laser wavelength.

3. RESULTS AND DISCUSSION

3.1. Characterization of the generated particles

The FTIR spectra of PLAL produced particles match the spectra of the original meloxicam powder in the investigated fluence range at all applied wavelengths (***Figure 1.***). The presence of the characteristic peaks indicates that chemically identical meloxicam particles can be generated from a drug pastille by PLAL [Hopp 2018, Nagy 2019].

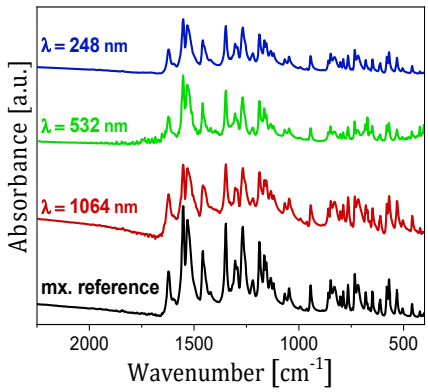

Figure 1. FTIR spectra of PLAL generated meloxicam particles (F= 9.4 J/cm^2) and reference meloxicam (mx.) powder.

SEM images revealed significant reduction in the size of the meloxicam particles as compared to the commercially available reference meloxicam powder. The morphology of the PLAL generated particles resembled broken pieces, scattered crystals, indicating that mechanical effects could have been the most relevant factors during fragmentation (**Figure 2.**) [Hopp 2018, Nagy 2019].

Reference meloxicam powder	248 nm	532 nm	1064 nm
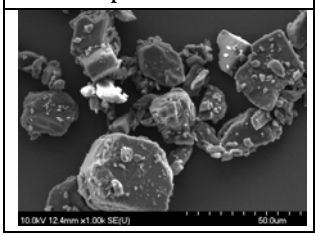	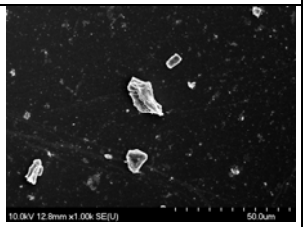	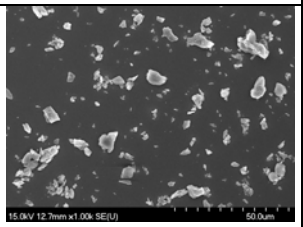	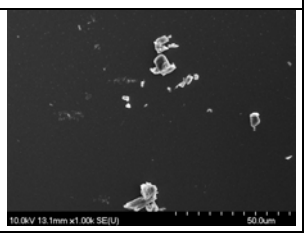

Figure 2. SEM images of the original meloxicam powder particles and of the particles obtained from the meloxicam suspensions produced at different wavelengths (Mag.: 1000x, scale 50.0 μm)

The 532 nm laser wavelength provided the highest ablation yield. Size-distributions were determined using ImageJ® image processing and analysis software [Hopp 2018, Nagy 2019].

In case of the PLAL generated particles XRDP characterization showed slight decrease (~ 7%) in the crystallinity and DSC investigations showed an approximately 20 °C shift to the lower temperatures in the melting point compared to the commercially available meloxicam powder. Both of these measurements indicate that PLAL causes the amorphization of meloxicam to some degree [Hopp 2018].

3.2. Characterization of the ablation process

Based on the time-resolved fast photography observations, three main parts of the ablation process can be distinguished (***Figure 3.***). In the first few hundred nanoseconds the refractive index of the medium changes and numerous small bubbles appear. Evaluating the recorded sequence of pictures, the formation and propagation of the wavefront was constructed. The velocity of the wave propagation was found to be 1480 m/s, which is the velocity of sound in water. This means, that the shockwaves slow down very quickly (after a few 10 ns) and become acoustic waves. The second part, between a few and a few hundred microseconds, is the time period when the formation and pulsation of the cavitation bubble takes place. The third part, a few milliseconds after the laser pulse, is when the cavitation bubble collapses and the ablated particles are released from its interior into the distilled water.

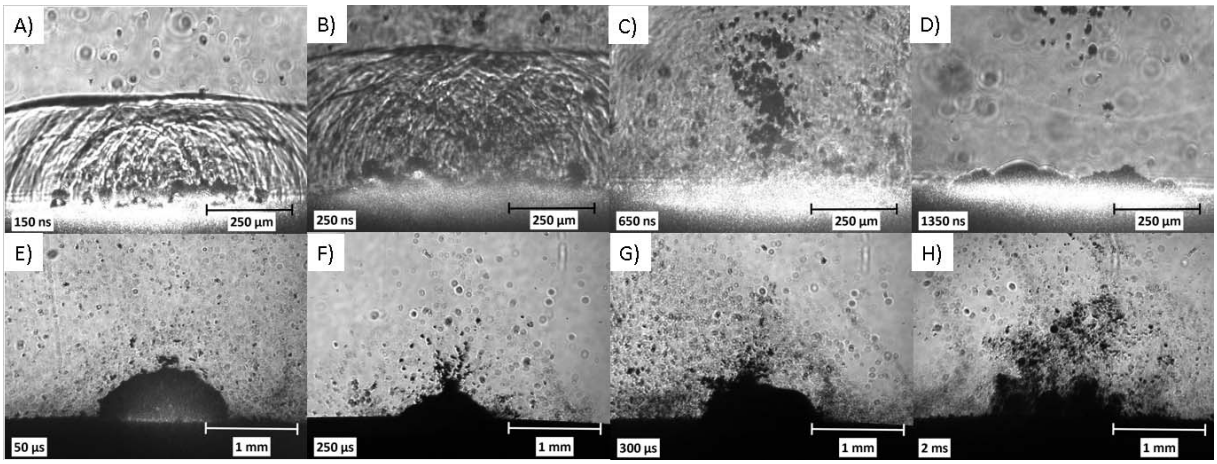

Figure 3. Time-resolved fast photography pictures. The sequence of the pulsed laser ablation (λ=532 nm, F = 6 J/cm^2) of a meloxicam pastille. Ablation process as discussed in the text: part one: A)-C), part two: D)-G) and part three: H).

4. CONCLUSIONS

PLAL proved to be a non-damaging, clean (chemical free) and effective way of generating few micrometre and sub-micrometre sized meloxicam particles. The size of PLAL produced particles was around one-tenth of the average size of the commercially available meloxicam powder particles and comparable with the size of particles produced by conventional techniques (grinding, wet milling). Time-resolved fast photography provided insight into the process of the ablation of the drug pastille.

5. ACKNOWLEDGEMENTS

Supported by the ÚNKP-20-3 - SZTE-549 New National Excellence Program of the Ministry for Innovation and Technology from the source of the National Research, Development and Innovation Fund. This work was supported by the GINOP-2.3.2-15-2016-00036 ('Development and application of multimodal optical nanoscopy methods in life and materials sciences') project and the Ministry of Human Capacities, Hungary grant (TUDFO/47138-1/2019-ITM FIKP program).

6. REFERENCES

[Rodriguez 2015] M. Rodriguez-Aller, D. Guillarme, J.-L. Veuthey, R. Gurny, *J. Drug Deliv. Sci. Technol.*, 30 (2015) 342.

[Mosharraf 1995] M. Mosharraf, C. Nyström, *Int. J. Pharm.,* 122 (1995) 35.

[Rasenack 2003] N. Rasenack, H. Hartenhauer, B. Muller, *Int. J. Pharm.*, 254 (2003) 137.

[Sylvestre 2011] J. P. Sylvestre, M.-C. Tang, A. Furtos, G. Leclair, M. Meunier, J.-C. Leroux, *J. Control. Release,* 149 (2011) 273.

[Ding 2014] W. Ding, J. P. Sylvestre, E. Bouvier, G. Leclair, M. Meunier, *Appl. Phys. A Mater. Sci. Process.*, 114 (2014) 267.

[Hopp 2018] B. Hopp, E. Nagy, F. Peták, T. Smausz, J. Kopniczky, Cs. Tápai, J. Budai, I. Z. Papp, Á. Kukovecz, R. Ambrus, P. Szabó-Révész, *J. Phys. D. Appl. Phys.*, 51 (2018) 165401.

[Singh 2020] A. Singh, H. L. Kutscher, J. C. Bulmahn, S. D. Mahajan, G. S. He, P. N. Prasad, *Nanomed. Nanotechnol.*, 25 (2020) 102172.

[Gera 2020] T. Gera, E. Nagy, T. Smausz, J. Budai, T. Ajtai, F. Kun-Szabó, Zs. Homik, J. Kopniczky, Z. Bozóki, P. Szabó-Révész, R. Ambrus, B. Hopp, *Sci. Rep.*, 10 (2020) 15806.

[Nagy 2019] E. Nagy, F. Peták, T. Szucs, T. Smausz, J. Kopniczky, R. Ambrus, P. Szabó-Révész, B. Hopp, Conference Paper*, CLEO/Europe-EQEC,* Munich, Germany*,* 2019.

COMPUTATION OF BLAST WAVE ENERGY IN LIBS USING SHADOWGRAPHY

Jakub Buday[1]*, David Prochazka[1,2], Pavel Pořízka[1,2], Jozef Kaiser[1,2]

[1] Faculty of Mechanical Engineering, Brno University of Technology, Technická 2896/2, Brno, Czech Republic
[2] CEITEC BUT, Central European Institute of Technology, Brno University of Technology, Purkyňova 123, 612 00 Brno, Czech Republic
**e-mail: buday@vutbr.cz*

1. INTRODUCTION

Shadowgraphy is an optical method, that can be used to observe non-uniformities in transparent media, such as air or water. In connection with Laser-Induced Breakdown Spectroscopy (LIBS) we can see blast wave, that was created by ablation of a sample.

This method in LIBS can be used for observation of different ablation and expansion mechanism using ns, fs or ps laser pulse [Zeng 2005], impact of the wavelength of the ablation laser [Boueri 2009] or its energy fluence [Rezaei 2014]. It is also possible to use Shadowgraphy to see impact on the behaviour of the blast wave expansion in different ambient gas at certain pressure [Skrodzki 2016], or even for underwater ablation [Sakka 2009].

Several models were created for the blast wave expansion, that can predict its distance from the samples surface, or even initial energy of the blast wave. Examples of these models are Drag, Sedov-Taylor and Jones model [Harilal 2003, Taylor 1950]. In our research we focused on using Sedov-Taylor and Jones model in order to calculate initial energy of the blast wave. This way we can approximately determine amount of energy used for ablation of the materials.

2. EXPERIMENTAL

In our experiments we used four different samples: steel, glass, bronze and soft tissues. Shadowgraphy images were captured for these samples in time interval between 100 ns and 10 μs after the ablation. Window between two consecutive times is 50 ns up to 1500 ns after the ablation, and 100 ns up to 10 μs. Finer time resolution in the earlier stage of the expansion is selected due to the Sedov-Taylor model. For each time after the ablation five laser pulses were shot into one spot, creating five shadowgraphy images. Radius of the blast wave was measured as distance from the centre of the ablation to the outer edge of the blast wave, and then averaged. For another time after the ablation new spot on the sample was selected. This way, shadowgraphy was observed for 7, 13, 19, 25, 32, 36, 44 and 50 mJ of the laser energy.

3. RESULTS AND DISCUSSION

3.1. Sedov-Taylor model

Sedov-Taylor model describes relation between distance of the shock wave from the samples surface *r* in time *t* from the ablation [Zel'dovich 1966]:

$$r = \zeta_0 \frac{E_0^{\frac{1}{\beta+2}}}{\rho_1} t^{\frac{2}{\beta+2}} \approx A\, t^{\frac{2}{5}}, \tag{1}$$

where ζ_0 is a constant approximately equal to unity, E_0 is initial energy of the blast wave, ρ_1 is the mass density of the undisturbed ambient gas, t is time of propagation for the shock wave front after the ablation and β is coefficient related to character of the explosion (β = 1 for planar propagation, β = 2 for cylindrical propagation and β = 3 for spherical propagation).

Example of the shadowgraphy images are displayed in **Figure 1**. By measuring the size of the blast wave, we can observe distance of the blast wave from the centre of the ablation in time. Measured data were used for computation of Sedov-Taylor model from the eq. (*1*), where results are affected by selected time interval.

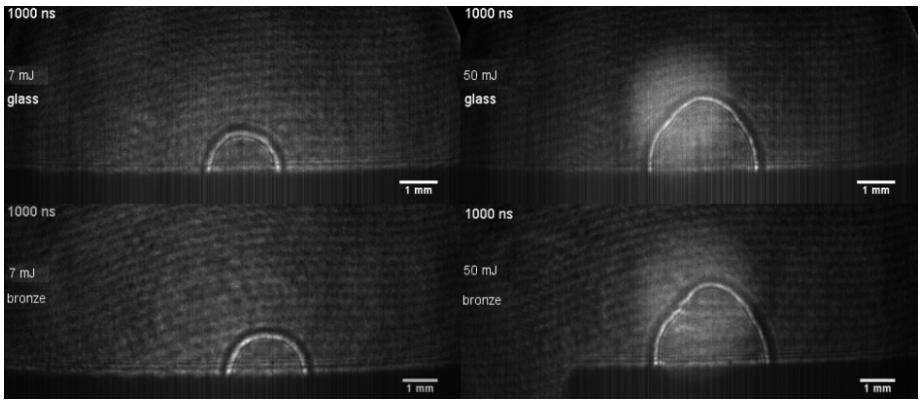

Figure 1. Shadowgraphy for glass and bronze samples ablated with 7 and 50 mJ impulses.

From our data, we can see that Sedov model can provide close representation of the actual data in the earlier stages of the expansion. Since this model is also connected to the initial energy of the blast wave by:

$$E_0 = A^5 * \rho_1 \tag{2}$$

we can use Sedov-Taylor model from the initial stage of the expansion for calculation of this energy. Based on this model, we were able to compute energy conversion coefficient as ratio of laser energy and E_0, as well as difference of these two energies, that represents amount of energy spent on the ablation.

3.2. Jones model

Jones model is also connected with the E_0, therefore we used it for confirmation of our results. This model represents relation between time and blast wave radius as:

$$t = \frac{R_C}{c_0}\left(\frac{2}{5}\right)^{\frac{2}{3}}\left[\left(1+\left(\frac{5}{2}\right)^{\frac{5}{3}}\left(\frac{R}{R_C}\right)^{\frac{5}{2}}\right)^{\frac{5}{2}}-1\right] \tag{3}$$

where c_0 is speed of sound in the ambient gas and R_C is characteristic radius expressed as:

$$R_C = \left(\lambda_S^5 \frac{E_0}{\gamma p_0}\right)^{\frac{1}{3}} \tag{4}$$

where λ_S^5 is a geometry dependent coefficient, E_0 is shock wave energy, γ is the adiabatic index of the ambient gas and p_0 is its pressure. After fitting measured data with Jones model shown in the eq. (3) we can obtain R_c. Knowing rest of the parameters in eq. (4), we can calculate E_0 for each sample. This result was then compared with Sedov's calculation.

4. CONCLUSIONS

In this work we have shown that Sedov-Taylor model can be used for blast wave energy computation. This can also determine energy that was spent for the ablation. From our data it is clear, that this model can be used only in the earlier stages of the blast wave expansion. Moreover, we used Jones model for confirmation of our results. However, this model is a bit more complicated and has a more demanding computation.

5. ACKNOWLEDGEMENTS

This research has been financially supported by the Ministry of Education, Youth and Sports of the Czech Republic under the project CEITEC 2020 (LQ1601). The authors acknowledge the partial support within the project GACR Junior (no. 20-19526Y), application of optical methods FSI-S-20-6353 and RV90200100303 (FV 20-03).

6. REFERENCES

[Zeng 2005] X. Zeng, X. L. Mao, R. Greif, R. E. Russo, *Appl. Phys. A Mater. Sci. Process.*, 80 (2005) 237.

[Boueri 2009] M. Boueri, M. Baudelet, J. Yu, X. Mao, S. S. Mao, R. Russo, *Appl. Surf. Sci.*, 255 (2009) 9566.

[Rezaei 2014] F. Rezaei, S. H. Tavassoli, *J. Anal. At. Spectrom.*, 29 (2014) 2371.

[Skrodzki 2016] P. J. Skrodzki, N. P. Shah, N. Taylor, K. C. Hartig, N. L. LaHaye, B. E. Brumfield, U. Jovanovic, M. C. Philips, S. S. Harilal, *Spectrochim. Acta B*, 125 (2016) 112.

[Sakka 2009] T. Sakka, S. Masai, K. Fukami, Y. H. Ogata, *Spectrochim. Acta B*, 64 (2009) 981.

[Harilal 2003] S. S. Harilal, C. V. Bindhu, M. S. Tillack, F. Najmabadi, A. C. Gaeris, *J. Appl. Phys.*, 93 (2003) 2380.

[Taylor 1950] G. Taylor, L. Series, P. Sciences, *Proc. R. Soc. London. Ser. A. Math. Phys. Sci.*, 201 (1950) 175.

[Zel'dovich 1966] Y. Zel'dovich, Y. Raizer: Physics of Shock Waves and High-Temperature Hydrodynamic Phenomena, *Academic Press*, 1966.

REVERSIBLE LASER-ASSISTED STRUCTURAL MODIFICATION AND LASER-DRIVEN MASS TRANSPORT AT THE SURFACE OF CHALCOGENIDE NANOLAYERS

Roman Holomb[1,2]*, Oleksandr Kondrat[2], Volodimir Mitsa[2], Alexander Mitsa[2], Nataliya Tsud[3], Martin Vondráček[4], Katerina Veltruská[3], Vladimir Matolín[3], Kevin C. Prince[5], Miklós Veres[1]

[1]*Institute for Solid State Physics and Optics, Wigner Research Centre for Physics, 1121 Budapest, Hungary*
[2]*Department of Informative and Operating Systems and Technologies, Uzhhorod National University, 88015 Uzhhorod, Ukraine*
[3]*Charles University, Department of Surface and Plasma Science, 18000 Prague 8, Czech Republic*
[4]*Institute of Physics, Academy of Science of the Czech Republic, Na Slovance 2, CZ-182 21 Prague 8, Czech Republic*
[5]*Sincrotrone Trieste S.C.p.A., 34149 Basovizza, Trieste, Italy*
**e-mail: holomb.roman@wigner.hu*

1. INTRODUCTION

Non-crystalline chalcogenides have been of great interest due to their remarkable structural, electronic, and optical properties and large functionality. In addition to their intrinsic infrared properties, they offer wide possibilities in domains such as information technologies (optical data storage, ultrafast optical transmission and information processing), photolithography, renewable energy technologies (high efficiency solar cells, solid electrolytes), medicine, thermal imaging, sensing and biosensing *etc.* thanks to the advantageous combination of infrared properties, optical activity, structural photosensitivity and high third-order optical non-linearity. Many properties of chalcogenide glasses, including electrical, chemical, optical, and mechanical characteristics and volume changes, show sensitivity to near-bandgap light, where the illumination causes temporary, metastable or permanent changes [Tanaka 1990, Kolobov 2003, Naik 2017]. These phenomena allow the development of numerous applications of chalcogenide glasses and their amorphous thin films. Therefore, special interest is dedicated to light-matter interactions and photo-structural phenomena in various chalcogenide systems. Furthermore, the local structural changes and possibility of selective modifications of the material properties can lead to great advances in modern photonics, nanophotonics and nanofabrication technology. Recent progress in photonics shows that amorphous chalcogenides are among the best candidates as active optical media for ultrafast *all-optical* processing systems [Eggleton 2011].

Here we report the results of *in-situ* investigation of light and thermally induced transformations occurring in As_2S_3 and As_2Se_3 nanolayers by means of high resolution synchrotron radiation photoelectron and surface enhanced Raman spectroscopy combined with DFT molecular orbital energy and Raman spectra calculations.

2. EXPERIMENTAL

The bulk As_2S_3 and As_2Se_3 glasses of optical quality were synthesized by the conventional melt-quenching route in evacuated and sealed quartz ampoules from a mixture of high purity 99.999% As, S and Se precursors. The quality (contamination, homogeneity) of the glasses was verified by X-Ray photoelectron and micro-Raman spectroscopy. The synthesized As_2S_3 and As_2Se_3 bulk glasses were used as precursor materials for the preparation of amorphous As_2S_3 and As_2Se_3 nanolayers by thermal evaporation onto clean silicon substrates [Holomb 2018, Kondrat 2019]. Thermal annealing of the samples was performed at T_g-30 K, where T_g is the glass transition temperature. Super-bandgap lasers operating at 405 and 532 nm were used for *in-situ* irradiation of As_2S_3 and As_2Se_3 nanolayers, respectively.

3. RESULTS AND DISCUSSION

3.1. Laser induced transformations of As_2S_3 nanolayers

The transformations observed in high resolution As 3d core level spectra of As_2S_3 nanolayers during thermal annealing and laser irradiation are shown in **Figure 1.** (left). These changes are related to the short-range order structural changes of nanolayers. Further treatments (thermal annealing and laser irradiation) of As-S nanolayers in cyclic mode indicate that the observed changes are fully reversible. Reversible changes of the atomic composition of As-S nanolayers were also detected (**Figure 1.** A (right)). The systematic As enrichment of the surface of irradiated nanolayers was found to be related with structural re-arrangements of the local structures during molecular transformation of realgar As_4S_4 molecules to their pararealgar form.

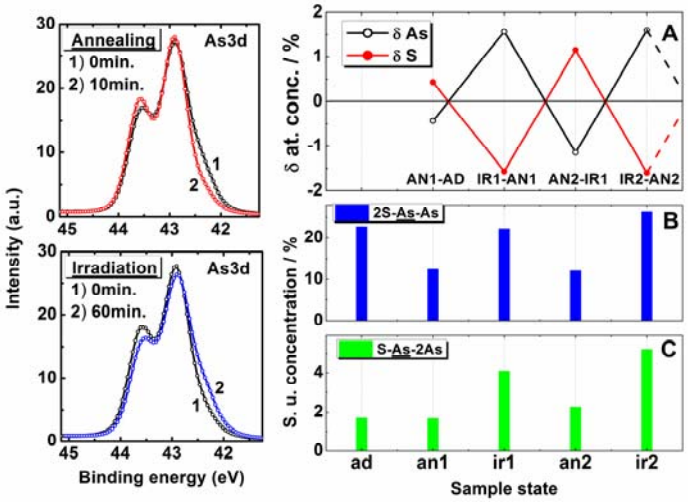

Figure 1. *(Left) Transformation of As 3d (E_{ex} = 150 eV) core level spectra of As_2S_3 nanolayers during thermal annealing (top) and laser irradiation (bottom). (Right) Change of the atomic composition of As-S nanolayers during thermal annealing and laser irradiation cycles (A) and the corresponding alteration of concentrations of local structures (2S-As-As (B) and S-As-2As 3S (C) structural units).*

The results are summarized in **Table 1.** together with the results of DFT calculations of MO energies of different As- and S-centered *s.u.* corresponding to As $3d_{5/2}$ and S $2p_{3/2}$ levels.

Structural unit		Calc. E_{MO}	As-deposited			Annealed			Irradiated		
			E_b	Δ	Pop.	E_b	Δ	Pop.	E_b	Δ	Pop.
i	*As-centered*										
1	As-3S	-42.89	42.9	0.5	75.5	42.9	0.5	85.8	42.9	0.5	73.7
2	2S-As-As	-42.47	42.5	0.5	22.8	42.5	0.5	12.5	42.5	0.5	22.2
3	S-As-2As	-42.07	42.1	0.6	1.7	42.1	0.6	1.7	42.1	0.6	4.1
4	As-3As	-41.67	-	-	-	-	-	-	-	-	-
j	*S-centered*										
1	As-S-As	-155.29	162.0	0.7	94.3	162.0	0.7	96.3	162.0	0.7	100.0
2	As-S-S	-155.86	162.8	0.5	5.7	162.8	0.5	3.7	-	-	-
3	S-S-S	-156.41	-	-	-	-	-	-	-	-	-

Table 1. *MO energies (E_{MO}, eV) corresponding to As $3d_{5/2}$ and S $2p_{3/2}$ core level binding energy of As- and S-centered s.u. calculated using DFT/SVWN5/aug-cc-pVTZ level of theory together with the results of curve fitting of As $3d_{5/2}$ (E_{ex} = 150 eV) and S $2p_{3/2}$ (E_{ex} = 220 eV) spectra of as-deposited, annealed and irradiated As_2S_3 nanolayers (Binding energy (E_b, eV), full width at half maximum (Δ, eV), population (Pop, %).*

3.2. Laser induced transformations of As_2Se_3 nanolayers

Synchrotron photoelectron spectra were also measured for As_2Se_3 nanolayers during their post-fabrication treatments. The Se 3d and As 3d core level spectra of as-deposited, annealed and illuminated As_2Se_3 nanolayers together with the results of curve fitting are shown in **Figure 2**.

The Se 3d core level (**Figure 3. a**) was decomposed into 2 doublets with $3d_{5/2}$ spin-orbit splitting components at binding energy (BE) of ~ 54.8 eV (peak 1) and ~ 55.2 eV (peak 2). According to our calculations, peak 1 originates from the presence of the stoichiometric Se-As_2 s.u. on the surface of nanolayers. DFT calculations showed that substitution of As by Se leads to an energy shift of the Se 3d core level to 55.3 eV for a Se-SeAs s.u. and to 55.7 eV for a Se-Se_2 s.u. Thus, peak 2 indicates the presence of Se-SeAs s.u. in the structure of the nanolayers. The As 3d core level spectra (**Figure 3. d**) of the as-deposited, annealed and illuminated nanolayers, were fitted using three components. These were assigned to arsenic bonded to three selenium atoms (As-Se_3s.u., ~42.9 eV, peak 1), arsenic bonded to two selenium and one arsenic atom (As-Se_2As s.u., ~42.4 eV, peak 2) and arsenic bonded to one selenium and two arsenic atoms (As-SeAs_2s.u., ~42.0 eV, peak 3).

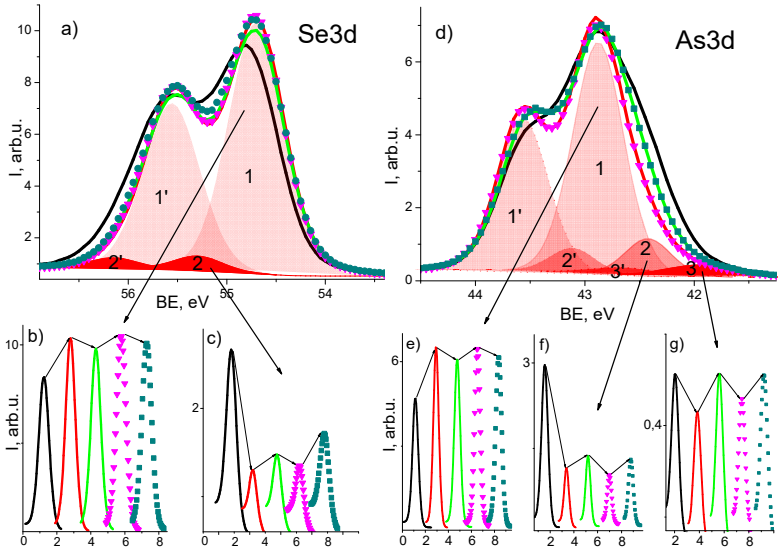

Figure 2. Se 3d (a) and As 3d (d) core level spectra of As_2Se_3 nanolayers: as-deposited (black lines), 1st annealed (red lines), 1st illuminated (green lines), 2nd annealed (pink triangles), and 2nd illuminated (dark green squares), together with results of typical curve fitting. 1 and 1'denote $3d_{5/2}$ and $3d_{3/2}$ components of Se-As_2 s.u. of the Se 3d spectrum (a) and As-Se_3s.u. of As 3d spectrum (d), respectively. 2 and 2' denote $3d_{5/2}$ and $3d_{3/2}$ components of Se-SeAs s.u. of the Se 3d spectrum (a) and As-Se_2As s.u. of As 3d spectrum (d), respectively. 3 and 3'denote $3d_{5/2}$ and $3d_{3/2}$ components of As-$SeAs_2$s.u. of the As 3d spectrum (d), respectively. Lower panels demonstrate the changes of the contributions of Se $3d_{5/2}$ and As $3d_{5/2}$ peak components after the each step of treatment (as-deposited → annealed → illuminated → annealed → illuminated): Se-As_2 (b), Se-SeAs (c), As-Se_3 (e), As-Se_2As (f) and As-$SeAs_2$ (g). For clarity, the position of each component is separated in space with the step of 1.6.

4. CONCLUSIONS

Synchrotron radiation photoelectron spectroscopy investigations were performed on As_2S_3 and As_2Se_3 nanolayers obtained *in-situ* by thermal evaporation from high quality glasses. The composition and local structure of as-deposited, thermally annealed and laser irradiated sample surfaces were analyzed in detail using short- and medium-range order molecular modeling and DFT electronic structure calculations.

Result show that the laser irradiation transforms the local structure of As_2S_3 and As_2Se_3 nanolayers. It is associated with photo-induced transition between different forms of As_4S_4 and As_4Se_4 molecules. The process was found to be fully reversible in thermal annealing and laser irradiation cycles. The mechanism of reversible laser stimulated As-enrichment of the nanolayers is related to selective diffusion and mass transport and consists of molecular transformations related to directional bond breaking and atomic re-arrangements.

5. ACKNOWLEDGEMENTS

R.H. and O.K would like to thank the CERIC-ERIC Consortium for providing access to experimental facilities. CERIC-ERIC consortium and Czech Ministry of Education (LM2015057) are acknowledged for financial support. R.H. and O. K. and V. M. also gratefully acknowledge the support from the Hungarian Academy of Sciences within the Domus Hungarica Scientiarum et Artium Programme.

This work was carried out within the framework of the DB-884 Project of the Ministry of Education and Science of Ukraine and was partially supported by the VEKOP-2.3.2-16-2016-00011 grant, which is co-financed by the European Union and European Social Fund.

6. REFERENCES

[Eggleton 2011] B. J. Eggleton, B. Luther-Davies, K. Richardson, *Nat. Photonics,* 5 (2011) 141.

[Holomb 2018] R. Holomb, O. Kondrat, V. Mitsa, M. Veres, A. Czitrovszky, A. Feher, N. Tsud, M. Vondráček, K. Veltruská, V. Matolín, K. C. Prince, *J. Chem. Phys.*, 149 (2018) 214702.

[Kolobov 2003] A. V. Kolobov, J. Tominaga, *J. Mater. Sci.: Mater. Electron.*, 14 (2003) 677.

[Kondrat 2019] O. B. Kondrat, R. M. Holomb, A. Csik, V. Takáts, M. Veres, A. Fehér, T. Duchon, K. Veltruska, M. Vondráček, N. Tsud, V. Matolin, K. C. Prince, V. M. Mitsa. *Appl. Nanosci.*, 9 (2019) 917.

[Naik 2017] R. Naik, C. Sripan, R. Ganesan, *Opt. Laser Technol.*, 90 (2017) 158.

[Tanaka 1990] K. Tanaka, *Rev. Solid. State Sci.*, 4 (1990) 641.

EFFECT OF SURFACE ROUGHNESS ON SERS ENHANCEMENT OF PATTERNED GOLD SUBSTRATES

István Rigó[1*], Miklós Veres[1], Tamás Váczi[1], Zsolt Zolnai[2], Rebeka Öcsi[2], Péter Fürjes[2]

[1]Institute for Solid State Physics and Optics, Wigner Research Centre for Physics, ELKH, 1121 Budapest, Konkoly-Thege Miklós way 29-33, Hungary
[2]Institute of Technical Physics and Materials Science, Centre for Energy Research, ELKH, 1121 Budapest, Konkoly-Thege Miklós way 29-33, Hungary
**e-mail: rigo.istvan@wigner.hu*

1. INTRODUCTION

Raman spectroscopy is a non-contact, fast, and relatively easy material characterization technique requiring no sample preparation. It is finding many applications in biology, life sciences, and other areas. While Raman scattering is inherently weak (its cross-section can be orders of magnitude smaller than that of fluorescence [Kumar 2012]), the sensitivity of the method can be improved remarkably by implementing surface-enhanced Raman scattering (SERS) [Ryder 2005], where the degree of achievable sensitivity can reach up to attomolar (10^{-18} M) concentrations [Kneipp 1997, Etchegoin 2003]. As a spectroscopic tool, SERS has the potential to combine the sensitivity of fluorescence with the structural information given by Raman spectroscopy.

During SERS the scattering takes place in close vicinity of nanostructured metallic surfaces [Li 2017]. The interaction of the electromagnetic field of photons with the surface plasmons of the metallic nanostructure results in the enhancement of the Raman signal; the gain of which can be several orders of magnitude. A successful SERS experiment requires an appropriate SERS-active agent (in most cases, nanoparticles or substrates) that will provide the required efficiency at a given excitation wavelength.

Periodic arrays of inverse pyramids with characteristic size of a few micrometers were among the first SERS active substrates finding commercial utilization [Stokes 2010]. Recently we found that the insertion of a gold nanoparticle (GNP) into the inverse pyramid remarkably increases the near-field enhancement (NFE) properties of the structure. Our results showed that the near-field intensity distribution depends on the size of the nanoparticle [Rigó 2020].

The NFE of the inverse pyramid array can further be improved by introducing nano-roughness to the gold surface. This can be achieved for example, by laser ablation altering the surface morphology of the array. Some preliminary experiments with a nanosecond laser having high pulse energy have already been performed by our group in this direction. In this work, the effect of the surface treatment on the near-field intensity distribution in inverse pyramids was studied by Finite-difference time-domain (FDTD) calculations and compared with those obtained for the GNP containing system. The

dimensions of the inverse pyramid and the surface roughness were taken from experimental data obtained on real gold coated substrates.

2. MATERIALS AND METHODS

SERS substrates were prepared by lithographic technique. A 2×2 micron base has been designed for the inverse pyramids. After the mask formation anisotropic etching was applied to the surface resulting in voids with sharp edges (inverse pyramids). After that the surface was coated with a 150 nanometers thick layer of gold (**Figure 1.**).

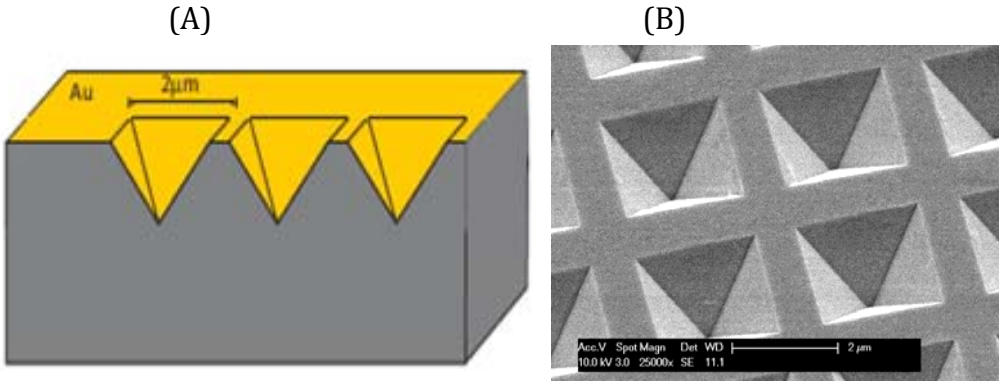

Figure 1. (A) Schematic representation and (B) SEM image of gold coated periodic array of inverse pyramids.

The dimensions of the voids were determined from 3D surface profiles. **Figure 2.** shows a depth profile of the pyramids. It can be seen that due to over-etching the base is 2.9 microns, and the depth of the voids is close to 1.5 microns.

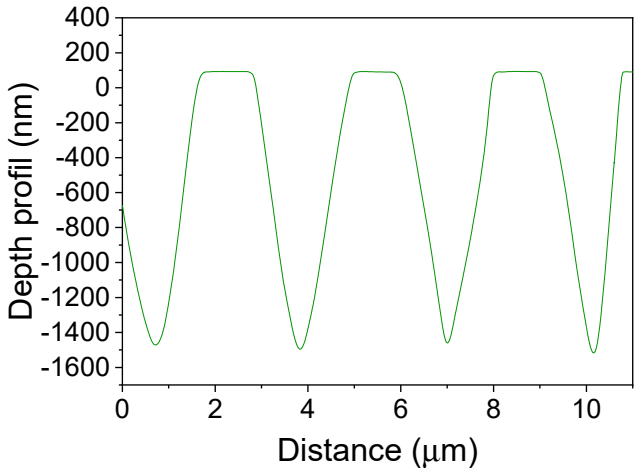

Figure 2. Depth profile of the inverse pyramid array along diagonals.

Near-field intensity distributions of the substrates were studied using the Lumerical FDTD Solutions v.8.15.736 software. Periodic boundary conditions were chosen in the directions parallel to the substrate surface to model the array geometry, together with

perfectly matched layer boundary conditions in the perpendicular direction. The size of the simulation cell was set according to the geometry of the fabricated array structure to 2.9 x 2.9 x 4.6 μm (**Figure 3.**). Silicon was selected as substrate material and a 150 nm gold coating was placed on that. The software's built in material parameter set from CRC Handbook of Chemistry and Physics [Weast 1988] was used for the gold layer and that from the Handbook of Optical Constants of Solids I [Palik 1998], for the silicon substrate. The simulation grid was defined by the built-in auto mesh algorithm with an accuracy level of 3 and 4. The inverse pyramid array was illuminated using a broad band (400–900 nm) plane wave having normal incidence to the array surface and polarization parallel to the base of the pyramid. Near-field profiles were recorded using two monitors placed along the two symmetry planes of the pyramid XZ and YZ plane, being perpendicular, and a third one XY placed above and being parallel to the array surface.

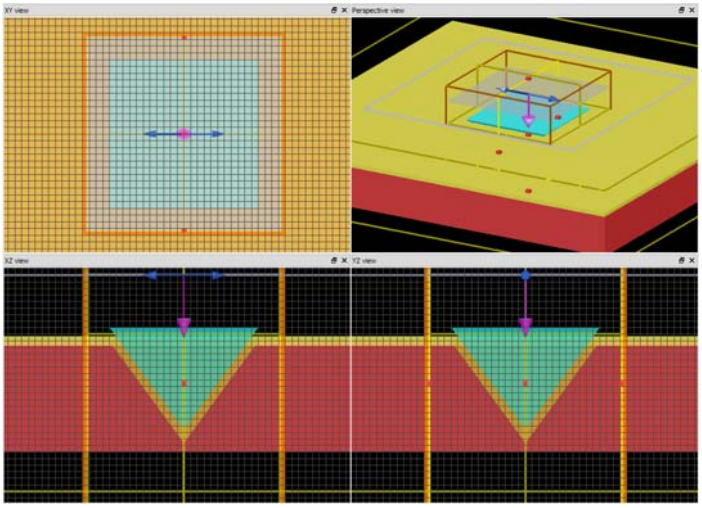

Figure 3. FDTD model geometry used for calculations.

The surface roughness has been introduced into the model by creating a rough surface with given RMS amplitude and correlation length, and 'wrapping' it to create the shape. The roughness was generated by generating a random matrix of values in K-space. A Guassian filter was applied to this matrix, then a Fourier transformation (FT) was used to transform the matrix back to real space. The FT parameters were selected so that the roughness had periodicity in the X and Y directions corresponding to the void model dimensions. This was necessary to avoid seaming during the wrapping of the rough surface.

3. RESULTS AND DISCUSSION

Figure 4. compares the calculated near-field intensity (E) distributions of empty and GNP containing pyramids together with the structure having surface roughness in the two monitor planes placed along two symmetry planes of the model structures. It should be

noted that the intensity distribution maps of different structures are not comparable directly since each map has its own intensity scale, shown by the color bars.

It can be seen that the near-field maximum is localized in the lower half of the empty pyramid. The data obtained for the 50 nm and 100 nm samples are very similar to the empty pyramid, including the near-field intensity distributions and even the magnitudes. For the 100 nm sample local fields of small intensity can also be observed at the bottom of the void, around the gold nanoparticle. The intensity map of the structure with rough surface is differs mainly in the expansion of the region with high intensity compared to the empty, 50 or 100 nm GNP. In addition, it shows the largest values.

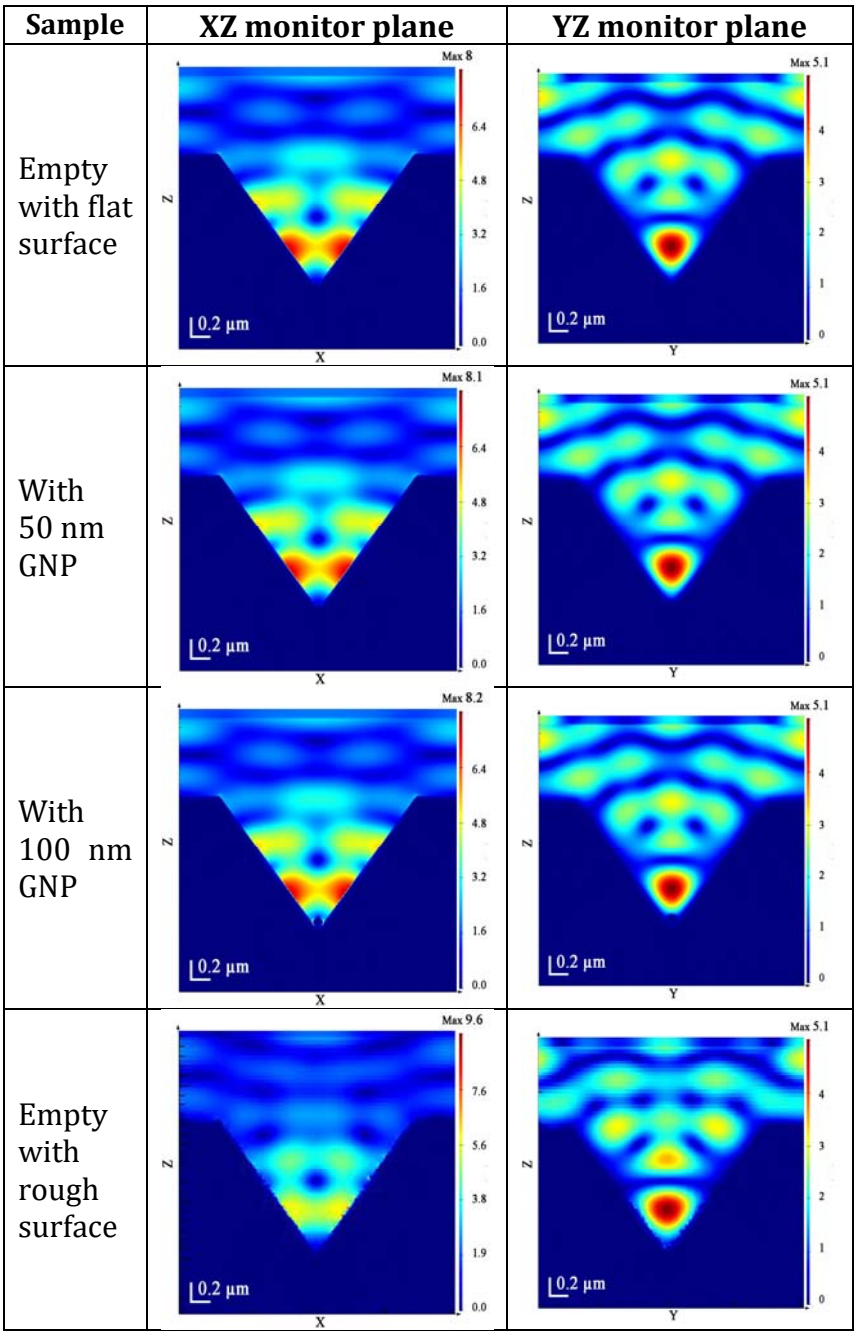

Figure 4. Calculated distributions of near-field intensity (E) inside the empty inverse pyramid with flat and rough surfaces, and that entrapping a 50 and 100 nm gold nanosphere.

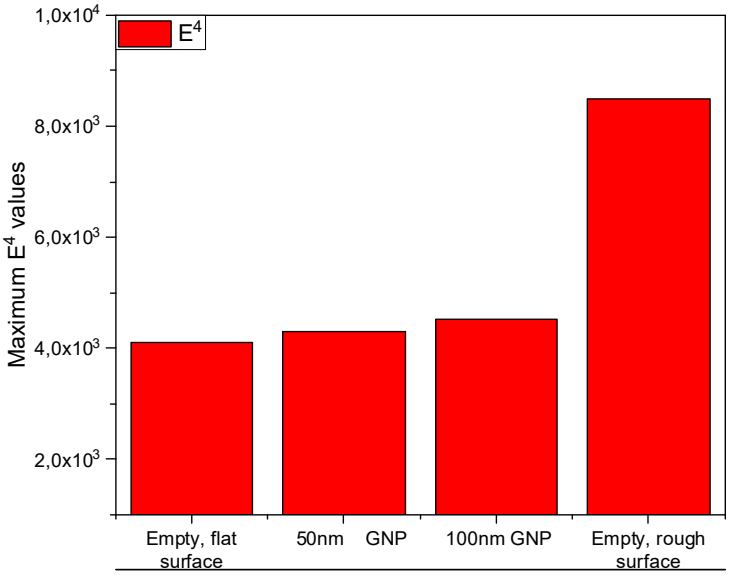

Figure 5. Maximum E^4 values obtained from calculated near-field intensity distributions.

Since surface enhanced Raman scattering and fluorescence scale approximately as E^4 [Pilot 2019], the maximum E^4 values were obtained for the samples with different GNPs and the surfaces (**Figure 5.**). As it can be expected from the intensity distribution maps above, the flat surface empty, 50 nm and 100 nm samples have similar E^4 values around 4-5 x 10^3. However, the empty pyramid with rough surface is close to 10^4.

4. CONCLUSIONS

Near-field intensity distributions were determined by FDTD calculations for micrometer-sized gold coated inverse pyramids with flat and rough surface, and with entrapped 50 nm and 100 nm gold nanoparticles. The maximum E^4 values were also determined. It was found that the addition of gold nanoparticles into the void increases the maximum of near filed intensity, and so the near-field enhancement properties of these structures. However, fabrication of structures with rough surfaces on the nanoscale level is even more efficient. Its theoretical near-field enhancement factor was found to be almost 10^4.

5. ACKNOWLEDGEMENTS

This work was supported by the VEKOP-2.3.2-16-2016-00011 grant, which is co-financed by the European Union and European Social Fund.

6. REFERENCES

[Etchegoin 2003] P. Etchegoin, R. C. Maher, L. F. Cohen, H. Hartigan, *Chem. Phys. Lett.*, 375 (2003) 84.

[Kneipp 1997] K. Kneipp, Y. Wang, H. Kneipp, L. T. Perelman, I. Itzkan, R. R. Dasari, M. S. Feld, *Phys. Rev. Lett.*, 78 (1997) 1667.

[Kumar 2012] C. S. S. R. Kumar: Raman spectroscopy for nanomaterials characterization, *Springer-Verlag,* 2012.

[Li 2017] W. Li, X. Zhao, Z. Yi, A. M. Glushenkov, L. Kong, *Anal. Chim. Acta*, 984 (2017) 41.

[Palik 1998] E. D. Palik: Handbook of Optical Constants of Solids II, *Academic Press,* 1998.

[Pilot 2019] R. Pilot, R. Signorini, C. Durante, L. Orian, M. Bhamidipati, L. Fabris, *Biosensors*, 9 (2019) 57.

[Rigó 2020] I. Rigó, M. Veres, Zs. Pápa, L. Himics, R. Öcsi, O. Hakkel, P. Fürjes, *J. Quant. Spectrosc. Radiat. Transf.*, 253 (2020) 107128.

[Ryder 2005] A. G. Ryder, *Curr. Opin. Chem. Biol.*, 9 (2005) 489.

[Stokes 2010] R. Stokes, D. Graham, U.S. Patent Appl. No.12/475,141, Pub. No.US 2010/0028908 A1, 2010.

[Weast 1988] R. C. Weast, M. J. Astle, W. H. Beyer: CRC Handbook of Chemistry and Physics - 69th Edition, *CRC Press*, 1988.

MERLIN, AN RT-LTE SOFTWARE SUPPORTING THE DIAGNOSTIC APPLICATION OF LIBS TO H-ISOTOPE MEASUREMENTS

Aurélien Favre[1]*, Morgan Lesage[1], Vincent Morel[1], Arnaud Bultel[1], Pascal Boubert[1]

CORIA, UMR CNRS 6614, Normandie Université, 76801 Saint-Étienne du Rouvray, FRANCE
**e-mail: aurelien.favre@coria.fr*

1. INTRODUCTION

Laser-induced plasmas can be used to determine the multi-elemental composition of solid, liquid or gaseous samples. Using a pulsed laser beam focused on the sample, the resulting absorption leads to a temperature increase of several 10,000 K [Morel 2016], therefore to a neutral phase to plasma transition. During the relaxation phase over which the recombination takes place, a continuum then lines radiation is emitted. Its analysis based on Optical Emission Spectroscopy (OES) may lead to the composition of the plasma if fundamental assumptions are fulfilled [Morel 2015]. The most restrictive one is the achievement of the Local Thermodynamic Equilibrium (LTE). The characterization of LTE is therefore one of the key points of this analysis method, also known as Laser-Induced Breakdown Spectroscopy (LIBS) [Mizolek 2006].

A high electron density n_e in the plasma ensures an important collision frequency which permits a satisfactory coupling between electrons and heavy particles. LTE is then achieved which allows a synthetic spectrum computation. The composition is then derived from the comparison between the computed and experimental spectra by an iterative procedure. The reliability of such a determination is directly linked to the quality of experimental data but also to the computational process itself (broadening effect and/or homogeneity).

MERLIN (MultiElemental Radiative equiLibrIum emissioN) has been developed to support OES interpretation and more particularly laser-induced experiments. This software computes equilibrium composition to generate the corresponding emission spectrum of any input mixture through a radiative transfer (RT) calculation. The user has a large set of input possibilities such as choosing input species, enabling different physical broadening effects or even choosing the spectral database used for computation. For this communication, a specific application of MERLIN devoted to LIBS H-isotopes measurements in gaseous, porous and metallic media is presented.

2. DESCRIPTION OF MERLIN

The computation of equilibrium composition is based on a fictitious chemical kinetics (for which the detailed balance principle is assumed). The final result is derived from solving

a coupled system of differential equations obtained from equilibrium laws (mass action, Saha for ionization and Guldberg & Waage for dissociation). The system is bounded by user inputs: ionization degree and species length have to be given. The software automatically requests necessary data (ionization, dissociation potentials and partition function) online. A temperature looped computation enables the obtention of the mixture composition at fixed pressure.

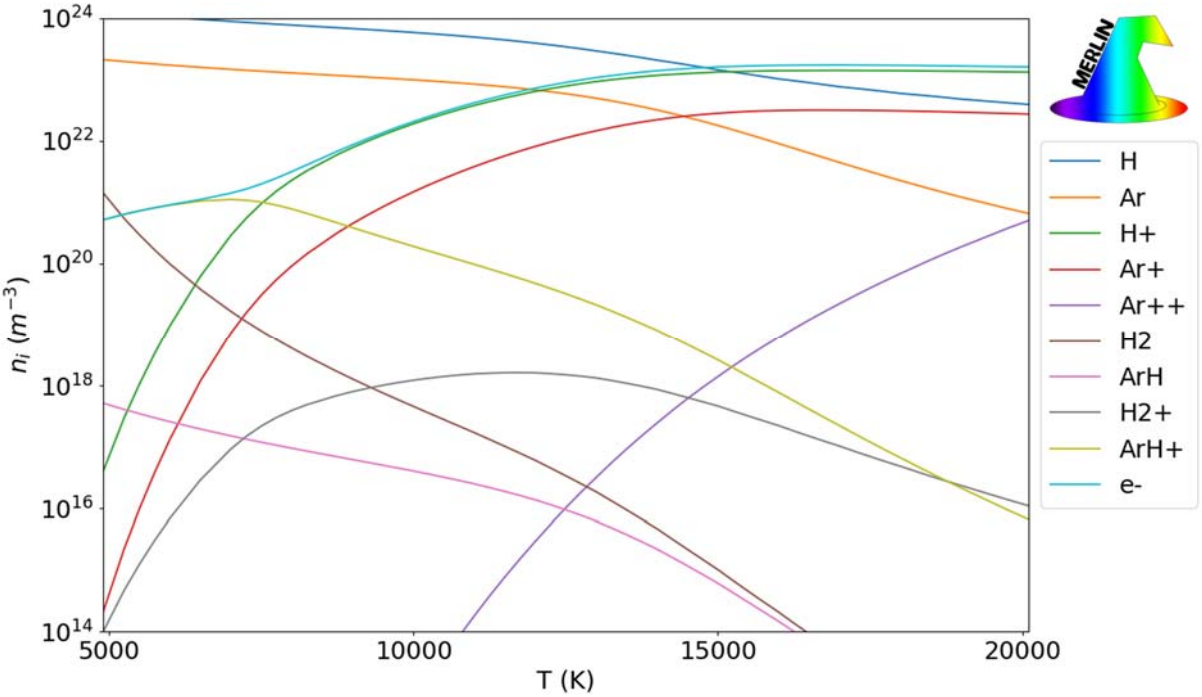

Figure 1. Composition of 0.25Ar - 0.75H_2 (expressed in mole fractions) mixture at equilibrium versus temperature at atmospheric pressure.

An example of this procedure is given for a 0.25Ar - 0.75H_2 mixture in **Figure 1.** [Liu 2009, Stancil 1994, Maltsev 2019, Capitelli 2012]. MERLIN shows a satisfactory agreement with similar published compositions computed by Fauchais *et al.* [Fauchais 1994]. This explains why neutral species remain dominant for T < 12 000 K. Also, for higher temperature the ionization degree increases, which leads to H^+, Ar^+ and Ar^{2+} formation. A competition between ionization and dissociation for H_2^+ is observed through a non-monotonic evolution with temperature.

3. RESULTS AND DISCUSSION

Nowadays research and environmental politics agree to say that hydrogen is an element of interest for the future of humankind for many reasons. First, hydrogen isotopes are nuclear fusion reaction fuels which can be considered as tomorrow's energy. Second, it allows a carbon and NOx free combustion. In addition to this, hydrogen is often used for instance in industrial processes such as plasma vapor deposition, ceramic treatment or

even fundamental research studies. We propose here to describe its emission into plasmas obtained from gas, porous substrates or even metallic samples.

Every spectrum presented below have been computed considering no Van Der Waals or Doppler broadenings. Also, the apparatus function has been fixed to a nominal lorentzian distribution with 0.0145 nm as FWHM (Full Width at Half Maximum), which corresponds to our experimental conditions. Concerning the Stark broadening, the FWHM are fixed as follows (respectively Mijatovic *et al.* [Mijatovic 2020], Fantoni *et al.* [Fantoni 2017]):

$$\Delta_{H-Stark}^{Lorentz} = 1.098 \left(\frac{n_e\ (\mathrm{m}^{-3})}{10^{23}} \right)^{0.67965} \mathrm{nm}$$

$$\Delta_{other-Stark}^{Lorentz} = 2\ \omega_S(T)\ \frac{n_e\ (\mathrm{m}^{-3})}{n_{e,ref}}\ \mathrm{nm}$$

$$\omega_S(T) = 4.8767 \times 10^{-4} + 1.6385 \times 10^{-8} T - 1.8473 \times 10^{-13} T^2$$

Of course, this default correlation can reveal unsubstantial compared to published electron impact parameters and it can be mandatory to inject measured values to obtain realistic Stark broadenings. But this communication only aims to claim the purpose of numerical tools to support experimental LIBS measurements.

3.1. Gas mixture: H mole fraction influence in Ar-H_2 mixture

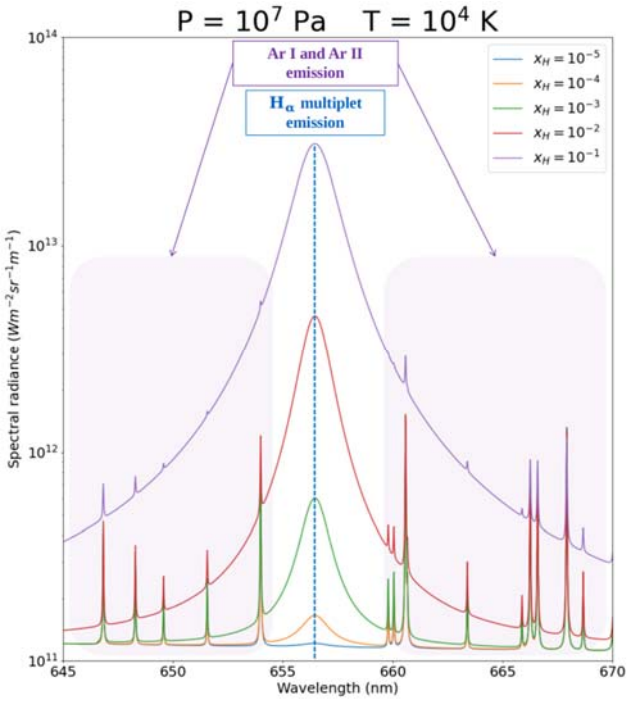

Figure 2. Equilibrium emission spectrum of an Ar - H_2 mixture diluted at X_H mole fraction of hydrogen.

Experimentally, argon is often used as surrounding gas for LIBS experiments because of its spectral data in addition to its high confinement capacity resulting from its atomic mass. As gaseous H-retention, we have chosen to present the emission of an Ar-H_2 mixture with variable H dilution (see **Figure 2.**).

These results are obtained by fixing the plasma pressure at P = 10^7 Pa and the temperature at T = 10^4 K. Namely, H dilution leads to a stronger H_α emission. Diluting also appears to lead to greater n_e values characterized by a strong Stark broadening.

3.2. Porous substrate: temperature influence in zeolite-like structure

Zeolites are crystal lattices which are mainly composed of gaps. This results to a porous material able to capture light species like hydrogen. Several studies are linked to hydrogen retention in those materials which appear to be a reliable solution to hydrogen storage. The LIBS hydrogen probing in such matrices can be used to estimate the capture efficiency. Different computations for a special zeolitic structure have been made at atmospheric pressure (see **Figure 3.**).

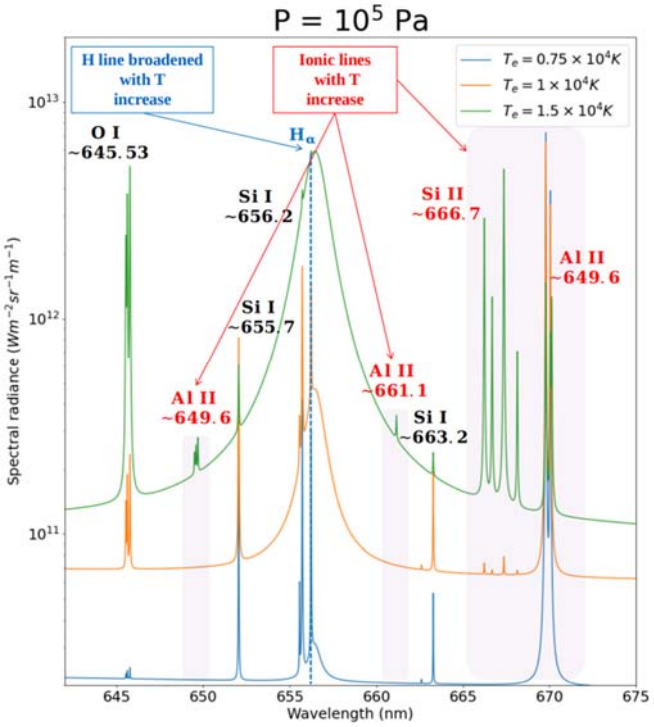

Figure 3. Equilibrium emission spectrum of zeolite-like (0.087H / 0.087Al / 0.217Si / 0.609O) structure versus plasma temperature.

The studied zeolite composition is 0.087H / 0.087Al / 0.217Si / 0.609O without any retention. A temperature increase leads to a higher ionization degree: this is directly observable through the appearance of Al II (around 649.6 nm, 661.1 nm and 649.6 nm) and Si II (around 666.7 nm) lines. In terms of composition, a significative n_H decrease is noticed. In addition, at low temperature, the hydrogen LIBS diagnostic is perturbed by S I

lines around 656.2 nm: probing another Balmer line is therefore requested if the diagnostic is performed in the visible spectral range.

3.3. Metallic samples: H/D mole fraction ratio influence in bulk tungsten

Hydrogen isotopes are used as fuels in nuclear fusion reaction. In a tokamak, a strong magnetic field is used to avoid a contact between the fusion plasma and machine walls (the term «magnetic confinement» is commonly used). The lower part of the tokamak, also named divertor, is more exposed to radiation and high flux density. Divertors are made in tungsten due to its high fusion temperature and its mechanical properties. The LIBS detection of hydrogen and/or deuterium retention in metallic heavy matrix such as tungsten is challenging: since low permeation factor and screening effect due to mass difference increase the limit of detection. We have performed calculations of the resulting emission of a 0.99 W / 0. 01(H-D) plasma with variable light elemental mole ratio (see **Figure 4.**).

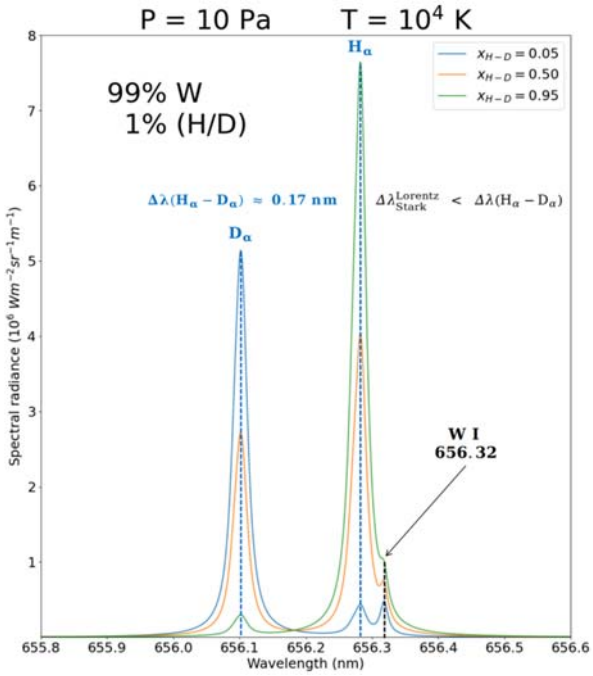

Figure 4. Equilibrium emission spectrum of H/D retention in bulk W (0.99 W / 0. 01(H-D).

A particular attention has to be paid to the spectral scale. In fact, the isotopic shifting of H and D Balmer-α lines is about 0.17 nm. Experimentally, it does not appear to be a limitation as long focal or high gratings spectrometers allow such a resolution with no particular problem. The main issue is residing in broadening which can hardly be as weak as shown on **Figure 4**. Indeed, inner plasma pressure cannot be as low as 10 Pa. Another limitation is due to the perturbation of a W I line emitting at 656.32 nm. In addition to this, a major probing issue is linked to light element concentration profile which is particularly low (the per cent is the order of magnitude) in surface and becomes tinier in a volumic point of view. All of those make the H_α and D_α tricky to detect in a bulk W matrix.

Fortunately, many alternatives can be explored to probe light element in a heavy matrix (VUV H-isotopes Lyman series, stronger H/D concentrations or even implantation in another matrix such as Al with no line around 656.3 nm).

4. CONCLUSIONS

MERLIN has been presented as a relevant tool in support of experimental laser-induced spectral emission data. The software is able to compute a synthetic equilibrium emission spectrum of any kind of mixture from a known spectroscopic setup (apparatus broadening) in known thermodynamic conditions like (P,T) or (n_i, T), with *i* a user chosen mixture species. This is a valuable indicator concerning the power of resolution or even the observability of a probed species in known plasma conditions.

Different applications of H and its isotopes retention have been developed to show the predictive capabilities of the software. Stark broadening for non-H species has been generalized for the simplicity of presentation but must be precised for a fine spectroscopic analysis or a crossed n_e determination. Such a numerical approach allows to observe a competition between apparatus and Stark broadenings when probing near range lines. It is also indicating the necessary conditions to observe ionic emission of a given species.

The upgrade of MERLIN is planned and includes many incoming features to enhance its prediction quality by implementing potential lowerings, resonant and Zeeman broadenings, non-homogeneous emitting media, better molecular emission support or even multi-temperature support.

5. REFERENCES

[Morel 2016] V. Morel B. Pérès, A. Bultel, A. Hideur, C. Grisolia, *Phys. Scr.*, T 167 (2016) 014016.

[Morel 2015] V. Morel, A. Bultel, J. Annaloro, C. Chambrelan, G. Edouard, C. Grisolia, *Spectrochim. Acta B*, 103-104 (2015) 112.

[Mizolek 2006] A. W. Miziolek V. Palleschi, I. Schechter: Laser-induced breakdown spectroscopy, Fundamentals and Applications, *Cambridge University Press*, 2006.

[Liu 2009] J. Liu E. J. Salumbides, U. Hollenstein, J. C. J. Koelemeij, K. S. E. Eikema, W. Ubachs, F. Merkt, *J. Chem. Phys., 130 (2009) 174306*.

[Stancil 1994] P. Stancil, *Astrophys. J., 430 (1994) 360*.

[Maltsev 2019] M. A. Maltsev, I. V. Morozov, E. L. Osina, *TVT,* 57 (2019) 367.

[Capitelli 2012] M. Capitelli G. Colonna, A. D'Angola: Fundamental aspects of plasma chemical physics, *Springer*, 2012.

[Fauchais 1994] M. I. Boulos, P. Fauchais, E. Pfender: Thermal plasmas - Fundamentals and applications, *Springer*, 1994.

[Mijatovic 2020] Z. Mijatovic, S. Djurovic, L. Gavanski, T. Gajo, A. Favre, V. Morel, A. Bultel, *Spectrochim. Acta B*, 166 (2020) 105821.

[Fantoni 2017] R. Fantoni, S. Almaviva, L. Caneve, F. Colao, G. Maddaluno, P. Gasior, M. Kubkowska, *Spectrochim. Acta B*, 129 (2017) 8.

IDENTIFICATION AND BE, LI CONTENT ASSESSMENT OF MINERALS IN GRANITOID ROCK SAMPLES BY LIBS

Patrick Janovszky[1,2], Krisztián Jancsek[3], Dávid J. Palásti[1,2], Judit Kopniczky[4], Béla Hopp[2,4], Tivadar M. Tóth[3], Gábor Galbács[1,2]*

[1]Department of Inorganic and Analytical Chemistry, University of Szeged, Dóm square 7, 6720 Szeged, Hungary
[2]Department of Materials Science, Interdisciplinary Excellence Centre, University of Szeged, Dugonics square 13, 6720 Szeged, Hungary
[3]Department of Mineralogy, Geochemistry and Petrology, University of Szeged, Egyetem street 2., 6720 Szeged, Hungary
[4]Department of Optics and Quantum Electronics, University of Szeged, Dóm square 9, 6720 Szeged, Hungary
** e-mail: galbx@chem.u-szeged.hu*

1. INTRODUCTION

LIBS is a versatile, laser ablation-based atomic emission spectroscopy technique, which allows the fast and direct analysis of solid and liquid (even gaseous) samples with minimum sample preparation, in a non-contact, marginally destructive way [Galbács 2015, Fortes 2013, Hahn 2012]. Its routine configuration already makes trace (ppm level) elemental analysis possible for all elements of the periodic table. One of the most appealing characteristics of LIBS is the possibility of direct solid sample analysis, which makes it of interest also to geologists and mineralogists. LIBS geochemical analysis is generally directed towards one or the other of two primary and related goals: quantitative analysis of the elemental contents of rocks/minerals (e.g. ore prospecting) and identification of the minerals (e.g. mapping of geochemical and mineralogical footprints, provenance analysis). LIBS is being increasingly explored by geologists and the mining and mineral processing industry in the last 10–15 years and is now more and more used for the analysis of geological material (GEOLIBS) [Harmon 2019, Harmon 2013].

2. EXPERIMENTAL

2.1. Instrumentation

LIBS experiments were performed on a J-200 tandem LA/LIBS instrument (Applied Spectra, USA), in the LIBS mode. This instrument is equipped with a 266 nm, 6 ns Nd:YAG laser source and a six-channel CCD spectrometer with a resolution of 0.07 nm. For every laser shot, the full LIBS spectra over the wavelength range of 190 to 1040 nm were recorded in the Axiom data acquisition software, using a 0.5 μs gate delay and 1 ms gate

width. During the experiments, a 40 µm laser spot size was maintained. The pulse energy was generally set at 17.5 mJ and the laser repetition frequency was 10 Hz. The number of repeated measurements in one sampling location (without translation) was ten. The first shots were clean-up shots, so the spectra originating from them were discarded. Measurements were performed at 4-5 sampling points in each mineral grain (sampling was done in a total of 128 locations for biotite, 155 for feldspar, 83 for quartz and 4 for amphibole). LIBS experiments were carried out under argon, continuously rinsing the ablation cell with a gas flow rate of 1 L/min. Argon gas increases the signal intensities and the continuous flow decreases the fallout of ablation debris around at the crater. Contact profilometry measurements were performed on a Veco Dektak 8 Advanced Development Profiler. The tip had a radius of curvature of 2.5 µm and the force applied to the surface during scanning was 30 µN. The horizontal resolution was set to 0.267 µm and 3.175 µm in the x and y scan directions, respectively. The vertical resolution was 40 Å. Optical images of the rock samples were taken with an Olympus BX-43 microscope equipped with an Olympus DP-73 camera, under polarized and transmitted light.

2.2. Samples

Three samples (M1, M2, M3) were prepared from the Mórágy Granite rock for the study. The main mass of the Mórágy Hills belongs to the Eastern Mecsek Mountains of Hungary and consists of monzogranite, with monzonite inclusions crosscut by leucocratic dykes. The rock types of the Mórágy Granite Formation can be divided into four main groups: monzogranite (typical granitoid rocks); hybrid rocks; monzonite (dark in colour and rich in magnesium and iron-bearing minerals) and leucocratic (light) dykes of different compositions. Our studied samples are of the monzogranite type, i.e. a granite variant with 35–65% feldspar. Mórágy Granite contains common rock-forming minerals, quartz, biotite and, to a lesser extent, amphibole.

Two kinds of sample preparation were performed on the studied rock samples: bulk (polished surface) samples were prepared for LIBS measurements, whereas 30 µm thin sections were cut for mineral identification by transmission optical microscopy (in polarized and transmitted light).

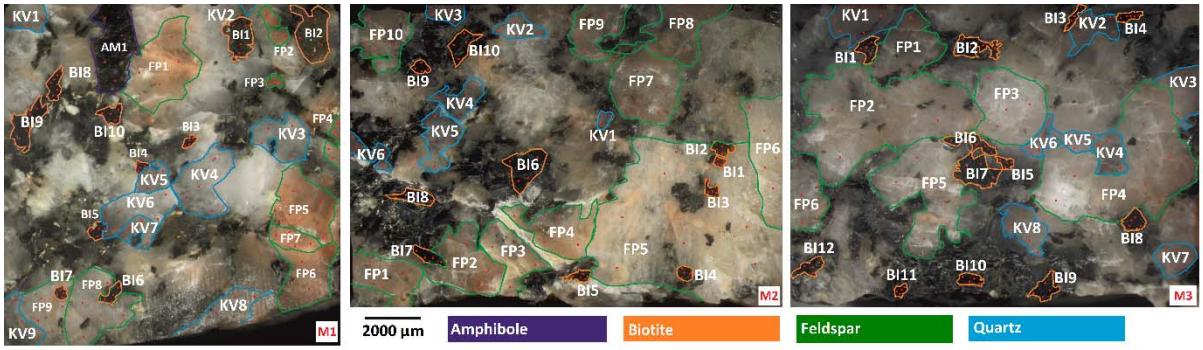

Figure 1. Microscope images of the rock samples M1, M2 and M3 (Mórágy). The four studied mineral types are indicated in the images with abbreviations and borderline colours: AM= amphibole (purple), BI= biotite (orange), FP= feldspar (green), KV= quartz (blue). Individual laser sampling locations are indicated by red dots.

3. RESULTS AND DISCUSSION

3.1. Compositional heterogeneity study of the mineral grains

Most mineral grains in igneous rocks grow during a longer time under various physical (first of all pressure and temperature) circumstances and changing chemical conditions resulting in internal chemical zoning patterns. These changes in chemical composition usually can be detected by different optical methods. Minerals of magmatic rocks, such as the granitoid rocks studied here, are usually zoned.

The extent of heterogeneity of the mineral grains in the samples was first investigated by repeated measurements. Individual LIBS spectra were collected from 10 shots delivered at 4–5 locations within each mineral grain. Spectra within each mineral across locations or depths (intra-mineral variations) were then compared to each other using the linear correlation function. It was generally found that there is a reasonable similarity of spectra, indicated by correlation factors of at least 0.85 in most cases.

3.2. Laser ablation characteristics of the mineral grains

To assess this, we investigated the laser ablation craters in the mineral grains by using contact profilometry. The results indicate that quantitative analysis (or certain discriminative analysis) can only be attempted with reasonable accuracy if matrix-matched calibration or at least crater volume normalization (with a general silicate standard, such as the NIST 6XX glass series) is performed.

3.3. Qualitative discrimination of mineral grains

3.3.1. Classification by using random forests

Random forests (RF) is a multivariate method of classification, which can be considered to be the advanced version of the classification (or decision) tree approach. In the present application, we trained the RF with datasets on M1 and optimized the number of trees as well as the number of nodes. It was found that the out-of-bag error initially steeply decreases with the increase in the number of trees and asymptotically reaches its

minimum at around 50. Simultaneously, the increase of the number of nodes clearly deteriorated the out-of-bag error. RF gave good, well-balanced results.

3.3.2. Classification by using linear discriminant analysis

Linear discriminant analysis (LDA) is a widely employed classification technique. It constructs a linear regression model of the dataset and generates a linear surface in the multi-dimensional variable space that separates the classes. We tested canonical LDA on our uncompressed LIBS data. The overall classification accuracy was good correlated to the result of RF. False classifications can be mostly associated with quartz and feldspar.

3.4. Quantitative assessment of the distribution of selected trace elements

Beryllium is widely used, e.g. in telecommunications infrastructure, advanced medical diagnostics instrumentation, automobile components and aeroplane equipment. Lithium is also a greatly sought-after metal, as it is used in large amounts in batteries, ceramics and glass, lubricating greases and polymer production. Recent years have seen a particularly steep leap in the need for lithium batteries. For these reasons, governments and companies are actively searching for new Li and Be sources, as well as new technologies for economically extracting them. LIBS is a technique which has great potential in this quantitative application, because it is ideal to measure light elements.

3.4.1. Mapping of Be and Li

Step scanning with non-overlapping laser spots (resolution: 40 μm, laser pulse energy: 5 mJ) was employed in this investigation. Spectral intensity-based elemental maps for Be II 313.0 nm and Li I 670.7 nm lines can be seen in **Figure 2.** Here we demonstrate that it is possible to identify the type of mineral that contains most of the targeted trace elements. As Li^{+} has a cation radius rather close to that of Mg^{2+}, in most crystal lattices Li incorporates to the position occupied by Mg. Among the studied phases, biotite and amphibole are the minerals where the Mg↔Li exchange is possible. As there is no exchangeable cation in its structure, not surprisingly, quartz has the least traces of these metals. The distribution of Be and Li among the grains seem to be qualitatively correlated.

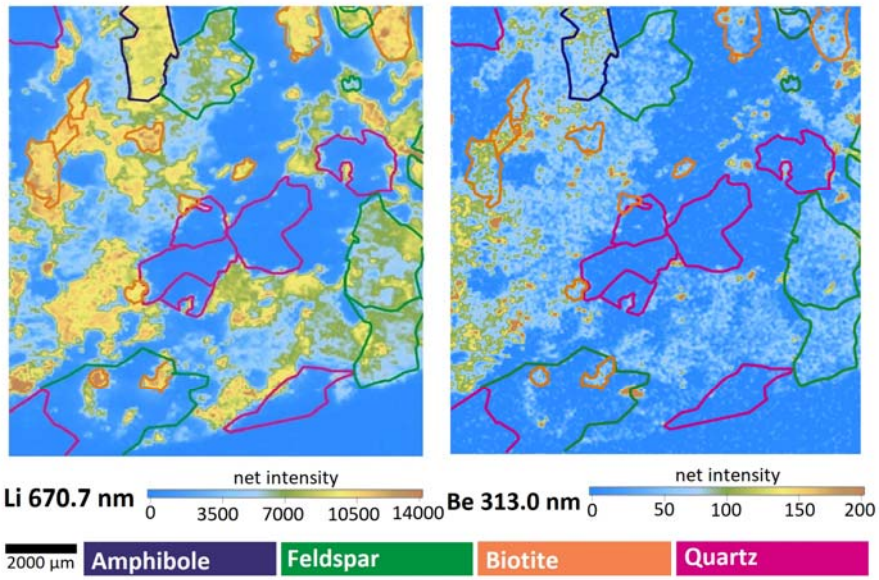

Figure 2. Intensity-based step-scan LIBS elemental maps of the M1 sample. Colors of the contours are indicating the mineral types, as seen in **Figure 1**.

3.4.2. Quantitative estimation of the Be and Li content

We also performed calculations to quantitatively assess the Be and Li content in the mineral grains of samples M1 to M3. Net Intensity data for the Li I 670.7 nm and Be II 313.0 nm spectral lines were converted to concentrations by calibration using matrix-matched standards. The NIST 612 standard was used for quartz calibration based on their similar laser ablation behaviour (similar crater volumes). The results justify the assumption suggested by the intensity-based elemental maps namely that the Li and Be content varies concertedly in all three minerals. The mass of the metals present in the grains naturally changes with the size of the grain. Not surprisingly, quartz contains the smallest amounts of both metals. It is also apparent that feldspar is the best source of Be, whereas biotite is for Li.

4. Conclusions

We have shown that LIBS mapping and spatially resolved local analysis is an efficient and practical approach for the classification of mineral grains (quartz, feldspar, biotite, amphibole) and for prospecting of technologically relevant elements in granitoid rock samples. We have tested three statistical approaches for the classification and it was demonstrated that better than 92% classification accuracy is achievable by using random forests and linear discriminant analysis. Direct classification by assessing the presence of the characteristic elements (decision tree based on indicative spectral lines) is a powerful method but can lead to large failure rates in case of relatively impure minerals, such as quartz.

5. ACKNOWLEDGEMENTS

The financial support received from various sources including the Ministry of Innovation and Technology (through project No. TUDFO/47138-1/2019-ITM FIKP) and the National Research, Development and Innovation Office (through projects No. K_129063, EFOP-3.6.2-16-2017-00005, TKP 2020 Thematic Excellence Program 2020) of Hungary is kindly acknowledged.

6. References

[Galbács 2015] G. Galbács, *Anal. Bioanal. Chem*., 407 (2015) 7537.

[Fortes 2013] F. J. Fortes, J. Moros, P. Lucena, L. M. Cabalin, J. J. Laserna, *Anal. Chem*., 85 (2013) 640.

[Hahn 2012] D.W. Hahn, N. Omenetto, *Appl. Spectrosc*., 66 (2012) 347.

[Harmon 2019] R.S. Harmon, C. J. Lawley, J. Watts, C. L. Harraden, A. M. Somers, R. R. Hark, *Minerals*, 9 (2019) 718.

[Harmon 2013] R.S. Harmon, R.E. Russo, R.R. Hark, *Spectrochim. Acta B.*, 87 (2013) 11.

TOXICITY ASSESSMENT OF PHOTON-UPCONVERSION NANOPARTICLES AND THEIR BIOIMAGING BY USING LASER-INDUCED BREAKDOWN SPECTROSCOPY IN *BRASSICA OLERACEA* L. PLANT

Sára Střítežská[1], Pavlína Modlitbová[1]*, Pavel Pořízka[1,2], Jozef Kaiser[1,2]

[1]Central European Institute of Technology (CEITEC) Brno University of Technology, Purkyňova 123, 612 00 Brno, Czech Republic
[2]Faculty of Mechanical Engineering, Brno University of Technology, Technická 2896/2, 616 69, Brno, Czech Republic
**e-mail: pavlina.modlitbova@ceitec.vutbr.cz*

1. INTRODUCTION

The increasing use of many types of nanoparticles (NPs) in commercial products as well as in many research areas has been found to lead to the NP-accumulation in the environment and within the food chain [Rodrigues 2016]. It poses an additional potential toxic effect on various organism/tissues at the cellular level [Magnuson 2011]. The evaluation of NPs toxicity, bioaccumulation, and translocation in diverse organisms is an extremely challenging task [Modlitbová 2020]. The precise localization of NPs through the plant tissues is of a paramount importance to reveal the relationship between the exact location of NPs and its toxic effect.

In this study, the rare-earth elements-doped photon-upconversion nanoparticles (UCNPs) are studied. They are composed of $NaYF_4$ nanocrystal and doped with Yb^{3+} and Tm^{3+} ions; a carboxylated silica shell is added on the surface to increase the chemical stability and reduce the releasing of free ions [Modlitbová 2019].

Brassica oleracea plant was exposed to the selected contaminants, UCNPs suspension in two nominal concentrations 50 μg UCNPs/mL. After a 72-h exposure, we monitored several macroscopic end-points, and plants were dried, molded, and epoxide-glued onto the glass slides.

The LIBS method was used to determine the permeation of Y, Yb, or Tm through the whole plant. The photon-upconversion laser microscaning was used as a complementary technique confirming the presence of Y, Yb, and Tm in the plants in the form of UCNPs [Sedlmeier 2016].

2. EXPERIMENTAL

2.1. Plant exposure

Seeds of cabbage (*Brassica oleracea* L.) were germinated for 48 hours in Petri dishes with the bottom covered with filtration paper in Milli-Q water. Seedlings with similar size

(approximately 1 cm root length) were selected into the toxicity test. Plants were exposed for 72 hours under the lighting cycle of 15 h light/9 h darkness at room temperature (22 ± 1 °C). The experiment consisted of a control group (Milli-Q water) and UCNPs suspension in nominal concentration 50 μg UCNPs/mL (10 μg Y/mL + 4.4 μg Yb/mL). Each exposure group contained 12 replicates of test plants.

Plants after exposure were washed with milli-Q water, dried and molded at room temperature for seven days and then glued by epoxide onto the glass slide. First the plants were photographed using an optical microscope, then photon up-conversion microscans (only in UCNP-treated plants) and LIBS measurements were performed.

2.2. LIBS measurements

The LIBS Discovery system (CEITEC, Czech Republic) was used for all experiments. Briefly, this set-up consists of a nanosecond laser (CFR 400, Quantel, France; 20 Hz, 532 nm, 10 ns), UV grade collecting optic (F2, SOL instruments, Belarus), an optical fiber (core diameter 400 μm, Thorlabs, US), the Czerny-Turner spectrometer (Shamrock, Andor, UK), and a sCMOS camera (iStar, Andor, UK).

The settings used during the LIBS analysis were optimized in our previous work [Modlitbová 2019] and only slight modifications were made. 1 μs gate delay, 15 μs integration time, 20 mJ pulse energy and 20 Hz repetition rate were used. The lateral resolution was 100 μm based on the crater diameter.

The emission lines found most appropriate for monitoring were Y II 437.49 nm, Yb I 398.80 nm, and Tm I 409.42 nm. After a background subtraction using a moving minimum, the data were imaged in the form of 2D maps.

3. RESULTS AND DISCUSSION

LIBS maps were constructed for selected elements contained in UCNPs, Y (Y II 437.49 nm), Yb (Yb I 398.80 nm), and Tm (Tm I 409.42 nm). These maps were completed by photon-upconversion microscans to confirm the presence of selected elements in the NPs form. The distribution of elements in *B. oleracea* exposed to 50 μg UCNPs/mL is shown in **Figure 1**.

The UCNPs could transfer from the root via the stem into the leaves by vascular bundles [Modlitbová 2019]. However, the main bioaccumulation storage organ was root, as is easily visible on 2D LIBS maps. In the tested concentration of 50 μg UCNPs/mL, UCNPs the found behaviour in plant translocations was: root >> stem > leaves. The detected signal from stem and leaves was negligible.

As visible in **Figure 1.**, the 2D maps of spatial Y, Yb, and Tm distribution obtained by LIBS method showed very similar sensitivity in comparison to photon up-conversion microscans. Moreover, LIBS method could easily detect the NPs without any luminescence, or NPs whose luminescence quench. Also, LIBS offers the bioimaging of selected elements in their ionic form.

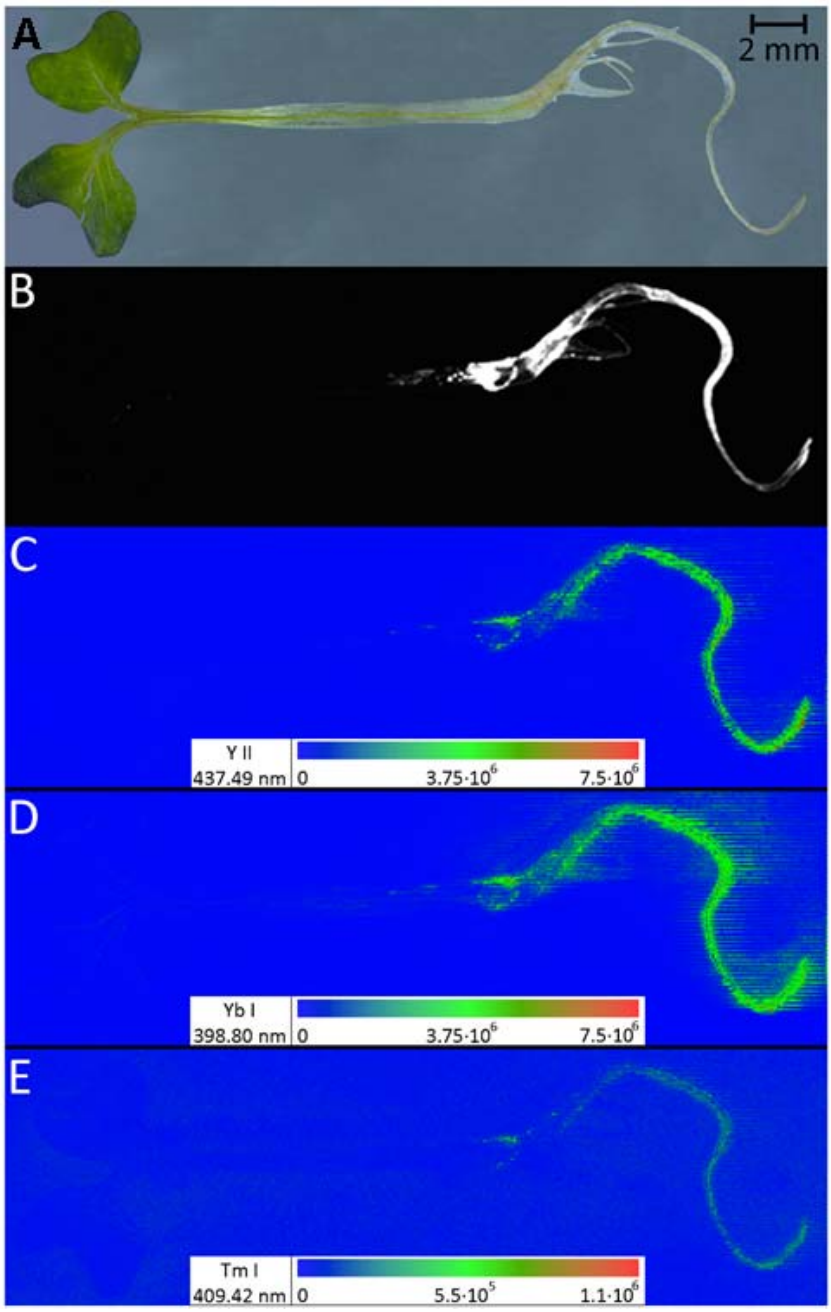

Figure 1. *Brassica oleracea* after 72-h exposure to 50 µg UCNPs/mL suspension, A: photography of plant, B: photon-upconversion microscan of plant, C: 2D LIBS map of spatial yttrium distribution (Y II 437.49 nm), D: 2D LIBS map of spatial ytterbium distribution (Yb I 398.80 nm), E: 2D LIBS map of spatial thulium distribution (Tm I 409.42 nm). The scales show the intensity of emission lines.

4. CONCLUSIONS

As a general conclusion, we can say that it is particularly beneficial to use LIBS for a fast screening in common phytotoxicity tests if information about the site of bioaccumulation, translocation, up-take routes as well as about the contaminants' trophic transfer is needed. All this information is valuable to phytotoxicity research, particularly because it is critically important to understand these processes to protect the quality of global ecosystems. LIBS can predominantly serve as a fast screening method for a large number of samples or as a complementary method providing other details to the complex analysis. Moreover, LIBS could be used in the field conditions to get a preliminary look before the laborious and not trivial sample selection, collection, storing, and transfer for a laboratory analysis.

5. ACKNOWLEDGEMENTS

This research has been financially supported by the Ministry of Education, Youth and Sports of the Czech Republic under the project CEITEC 2020 (LQ1601). This work was carried out with the support of CEITEC Nano Research Infrastructure (MEYS CR, 2016-2019) and CEITEC Nano+project, ID CZ.02.1.01/0.0/0.0/ 16_013/0001728.

6. REFERENCES

[Magnuson 2011] B. A. Magnuson, T. S. Jonaitis, J.W. Card., *J. Food Sci*., 76 (2011) 126.

[Modlitbová 2019] P. Modlitbová, A. Hlaváček, T. Švestková, P. Pořízka, L. Šimoníková, K. Novotný, J. Kaiser, *Chemosphere*, 225 (2019) 723.

[Modlitbová 2020] P. Modlitbová, P. Pořízka, J. Kaiser, *TrAC - Trends Anal. Chem*., 122 (2020) 115729.

[Rodrigues 2016] S. M. Rodrigues, T. Trindade, A. C. Duarte, E. Pereira, G. F. Koopmans, P. F. A. M. Römkens, *TrAC Trends Anal. Chem.,* 75 (2016) 129.

[Sedlmeier 2016] A. Sedlmeier, A. Hlaváček, L. Birner, M. J. Mickert, V. Muhr, T. Hirsch, P. L. A. M. Corstjens, H. J. Tanke, T. Soukka, H. H. Gorris, *Anal. Chem.*, 88 (2016) 1835.

IMPLEMENTATION OF LASER-INDUCED BREAKDOWN SPECTROSCOPY ELEMENTAL IMAGING INTO THE HISTOPATHOLOGICAL ANALYSIS OF SOFT TISSUES

Anna Šindelářová[1]*, Pavlína Modlitbová[1], Pavel Pořízka[1], Lucie Vrlíková[2], Marcela Buchtová[2,3], Jozef Kaiser[1]

[1]Central European Institute of Technology (CEITEC), Brno University of Technology, Technická 3058/10, 616 00 Brno, Czech Republic
[2]Institute of Analytical Chemistry of the Academy of Sciences of the Czech Republic, Veveří 967/97, 602 00 Brno, Czech Republic
[3]Department of Experimental Biology, Faculty of Science, Masaryk University, Kamenice 5, Brno, Czech Republic
**e-mail: anna.sindelarova@ceitec.vutbr.cz*

1. INTRODUCTION

Many reviews already covered the benefits of LIBS utilization in the topic of biological tissue analysis. Overall, the cost efficiency, simplicity, real-time performance and the possibility for large-scale elemental imaging provided by LIBS is vary valuable for histopathological research. In order to be able to detect variations in trace element concentration it is critical to achieve the highest possible analytical sensitivity, achieved through optimization. Even though it is often cited that LIBS does not require sample treatment, but in the case of soft tissues sample preparation can significantly influence the performance of a LIBS system [Jantzi 2016]. We are interested in imaging of the elemental layout in a section of soft tissue, thus we need to treat the sample without affecting the sample matrix. As the formalin fixation and paraffin embedding (FFPE) is routinely used by pathologists, the implementation of paraffin section imaging in LIBS opens a wide range of applications. In this work, we compared two embedding techniques, 10 μm slices of tissue embedded in paraffin on glass slides and tissues in paraffin blocks.

2. EXPERIMENTAL

All measurements were performed using the LIBS Discovery instrument. It was developed at the Central European Institute of Technology, Brno University of Technology (Brno, Czech Republic). The experimental apparatus for LIBS analysis consisted of a Q-switched Nd:YAG laser Quantel CFR Ultra (France; 532 nm, 10 ns, 20 Hz). The laser beam was focused on the sample surface by the triplet lens (Sill Optics, Wendelstein, Germany) with a focal length of 24.5 mm. Plasma emission was collected by wide-angle optics and transferred through an optical fiber to the entrance slit of a Czerny-Turner spectrometer (SR-500i-B2-R, Andor, Northern Ireland) equipped with a grating of 1200 lines per mm

and a 50 μm entrance slit. Plasma emission was obtained using a gated sCMOS detector (iSTAR-sCMOS-18F-E3, Andor, Northern Ireland). The gate width and the gain was set at 50 μs and 4000, respectively. The assignation of spectral lines was cirred out using the National Institute of Standards and Technology (NIST) database [Kramida 2018].

3. RESULTS AND DISCUSSION

3.1. Embedding

The difference between two types of tissue fixation can be seen on **Figure 1**. Here we compare elemental maps of K I 766 nm. No interference is visible in map from tissue in paraffin block as paraffin consists only of C and H. Potassium signal from the tissue clearly differentiates the kidney from the background paraffin. This also applies to Ca, Na, Mg, elements naturally present in the tissue, which from our experience can also be clearly imaged.

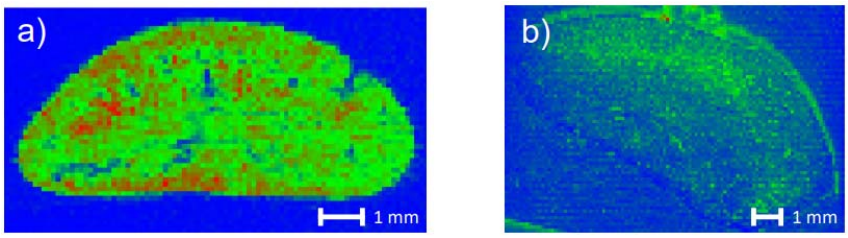

Figure 1. A typical potassium map (K I 766 nm) acquired from a) kidney in a paraffin block; b) kidney slice on a glass slide.

The elemental image of kidney slice on glass slide shows strong interference from elements present in the glass, as glass ablation cannot be totally avoided. Elements, such as Na, Ca, K cannot be properly detected. As previously mentioned, the thickness of kidney slices was 10 μm. Minimalizing the interference from the glass by cutting a thicker slice of tissue wasn't possible as the slices thicker than 10 μm were splitting. Considering preparation, both of these are easy to prepare, although kidney slices on glass slide require a few more steps before they can be used in LIBS analysis. Another benefit of paraffin embedding is that it is possible to cut fresh surface on a microtome after each measurement.

3.2. Optimization approaches

To be able to detect variations in trace elements concentration reaching LIBS limits of detection it is critical to achieve the highest possible analytical sensitivity, which should be provided by a step of optimization. Therefore, we outlined technique of optimization of elemental imaging by detecting element (potassium) present in the matrix in an amount sufficient for detection. The potassium content was 3013 (213) $mg \cdot kg^{-1}$, determined by the ICP-OES method.

We assessed the stability of the elemental signal (**Figure 2.**). Stability was determined as the relative standard deviation (RSD) of repeated measurements [Huang 2013]. The potassium signal in paraffin block is established to be 17%. These measurements were also measured on two separate occasions (red and blue datasets in **Figure 2.**) with the same experimental parameters. From the results, we assume the analysis stable in time and thus repeatable. The elemental image of potassium signal for pulse energy of 10 mJ can be seen in **Figure 3**.

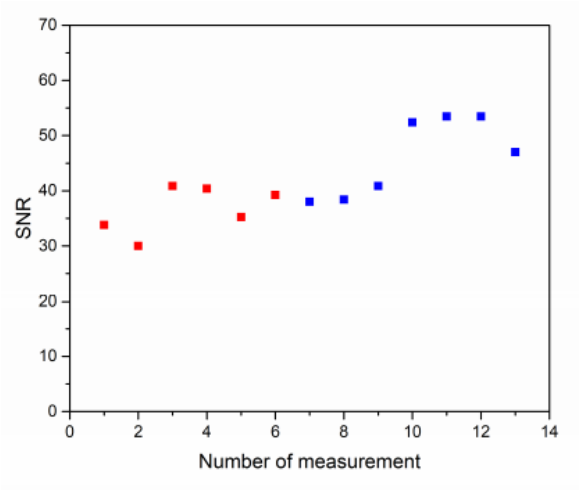

Figure 2. Stability of signal from a) mouse kidney in paraffin block (red – 21.1.2020; blue – 6.2.2020); b) It is not possible to add error lines because SNR is influenced by heterogeneous distribution of analyte concentration, therefore only the average values can be compared.

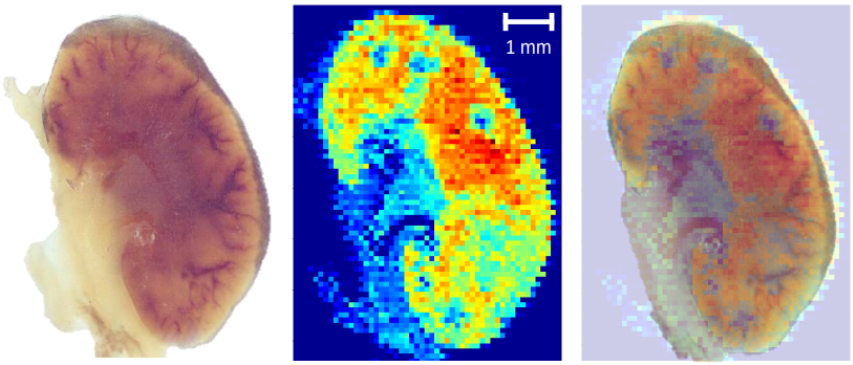

Figure 3. LIBS imaging of potassium (K I 766 nm) as acquired from a kidney sample in a paraffin block for a pulse energy of 10 mJ.

4. CONCLUSIONS

LIBS imaging of elemental distribution can provide valuable insights for the histopathological field of research. In this work, we presented comparison of two embedding techniques and two methodological approaches for the optimization of elemental imaging of soft tissues.

Embedding in paraffin blocks enables to maintain the sample structure and at the same time provides sufficient results in a view of the signal and absence of interference. Considering the stability of signal, our measurements and results from paraffin blocks are stable in time.

5. ACKNOWLEDGEMENTS

This research has been financially supported by the Ministry of Education, Youth and Sports of the Czech Republic under the project CEITEC 2020 (LQ1601). The authors acknowledge the partial support within the projects Action (no. 82p5), GAUK (no. 1193819) and GACR Junior (no. 20-19526Y). We are also very grateful to Ing. Pípalová from Masaryk University in Brno for the help during sample preparation and Mgr. Lucie Šimoníková from Masaryk University in Brno for the help regarding determination of elemental composition in mouse kidneys by ICP-OES.

6. REFERENCES

[Jantzi 2016] S. C. Jantzi, V. Motto-Ros, F. Trichard, Y. Markushin, N. Melikechi, A. De Giacomo, *Spectrochim. Acta B*, 115 (2016) 52.

[Kramida 2018] A. Kramida, Y. Ralchenko, J. Reader, NIST Atomic Spectra Database, version 5.6.1 (https://www.nist.gov/pml/atomic-spectra-database), 2018.

[Huang 2013] L. Huang, M. Yao, Y. Yu, M. Liu, *Appl. Phys. B*, 111 (2013) 45.

INVESTIGATION OF SIZE AND EXPOSURE TIME DEPENDENT BIOACCUMULATION OF SILVER NANOPARTICLES IN PLANTS BY LIBS

Patrick Janovszky[1,2], Sára Střítežská[3], Pavlína Modlitbová[3], Pavel Pořízka[3]*, Jozef Kaiser[3], Gábor Galbács[1,2]

[1]Department of Inorganic and Analytical Chemistry, University of Szeged, Dóm square 7, 6720 Szeged, Hungary
[2]Department of Materials Science, Interdisciplinary Excellence Centre, University of Szeged, Dugonics square 13, 6720 Szeged, Hungary
[3]Central European Institute of Technology (CEITEC) Brno University of Technology, Technická 3058/10, 616 00 Brno, Czech Republic
**e-mail: pavel.porizka@ceitec.vutbr.cz*

1. INTRODUCTION

Environmental and food safety is a very important issue in our world. Since nowadays nanoparticles are produced each year in the amount of thousands of tons for industrial purposes, they easily end up in the environment and can contaminate the food chain too. Thus, fast and reliable measuring tools are needed to monitor the bioaccumulation of NPs.

The aim of the project was to investigate the accumulation of silver nanoparticles in plants. The adverse effects of silver nanoparticles on the environment have been discussed in numerous publications, but no size-dependent bioaccumulation studies of silver nanoparticles in plant samples by LIBS have been performed so far. Earlier studies on animal and human tissues [Peng 2012] have found that smaller nanoparticles are more harmful than larger ones. The toxicity effect and the bioaccumulation of the nanoparticles and cadmium-containing quantum dots on plant samples were measured by LIBS [Modlitbová 2020a, Modlitbová 2020b].

2. EXPERIMENTALS

2.1. Instrumentation

A LIBS Discovery system were used in this study, the measurements were made with the following parameters: the laser pulse energy was set to 20 mJ, the gate delay was 0.75 μs, the number of shots per point was 1, the repetition frequency was 20 Hz and the distance between each measurement point was chosen to be 100 μm, this gave us the 100 μm spatial resolution. The measurements were performed in air. During the measurements the Ag (I) 328.062 nm line was monitored. A Czerny-Turner Shamrock spectrometer equipped with an ICCD detector iStar 734 (both from Andor) was used for measurements.

2.2. Sample preparation

White mustard (*Sinapis alba*) was chosen for the model plants because they germinate relatively quickly in about three days. In the first phase of the experiment, the mustard seeds are placed in a Petri dish lined with filter paper soaked in deionized water. The seeds were placed at a sufficient distance (15 mm) to allow space for growth and germination. The seeds were kept for 3 days at 24 °C in a covered Petri dish.

After the third day, when the germs had grown to a sufficiently large size, the seeds were relocated into Eppendorf tubes containing the nanodispersion (**Figure 1.**). A 10 µmol/L nanodispersion of citrate-stabilized silver nanoparticles of different sizes, 10 and 40 nm, were used. Samples were grown in the nanoparticle solution for 48 and 72 hours, respectively. In the preliminary experiments, 5-5 samples grew for 48 hours in 10 nm and 40 nm particle solution, and 5-5 samples grew in 72 hours also in 10 and 40 nm particle solution and 5 samples grew in 72 hours in deionized water as a control group.

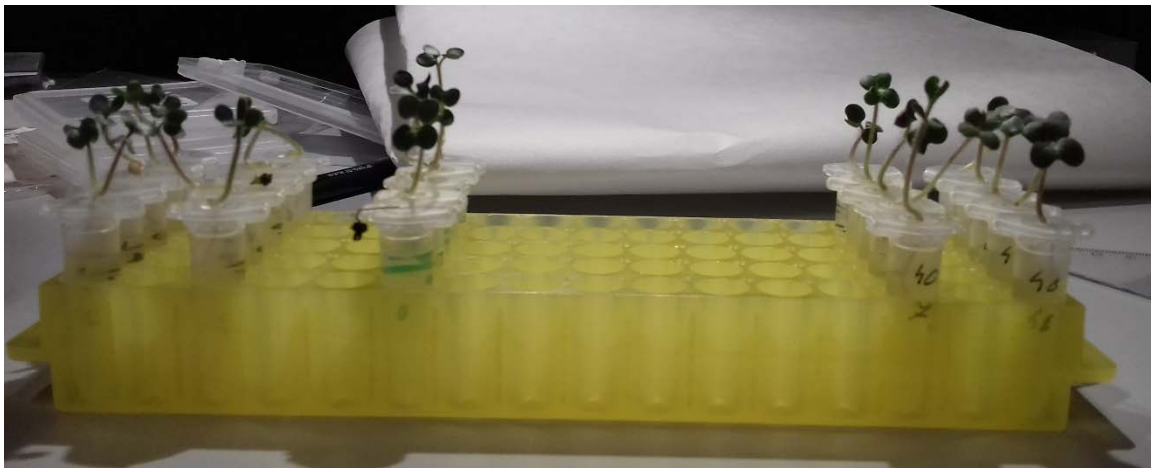

Figure 1. In the post-germination phase, plants were transferred to the Eppendorf tubes containing the nanodispersion, for 48 and 72 hours, respectively.

After each exposure time had elapsed, the samples were carefully removed from the tubes with tweezers due to their extreme fragility, and the roots were rinsed with deionized water to wash away any nanoparticles that were not absorbed but adhered to the root surface. The length of the root, stem, and total length were measured of each plant. Prior to the start of LIBS measurements, the pressed and dried plants were mounted on a glass slide with epoxy resin and allowed to dry for 24 hours.

3. RESULTS AND DISCUSSION

In this research the size and exposure time dependent bioaccumulation of silver nanoparticles were examined. Two, differently sized (10 nm and 40 nm) silver

nanoparticles were used and the exposer times were chosen to 48 and 72 hours. As a control group plants were grown in ultra-pure water for 48 and 72 hours.

3.1 Size-dependent bioaccumulation

In **Figure 2.**, the silver distribution maps can be seen of those plants which were grown in 10 nm and 40 nm silver NPs containing nanodispersions for 48 hours. The colour scale ranges from blue to red, where blue indicates low silver intensity and red indicates high intensity. In **Figure 2. A**, the distribution of 10 nm, in **2. B**, the distribution of 40 nm sized silver nanoparticles is presented. The comparison of these maps reveal that the smaller nanoparticles are present both in the roots and in the plant's stem, but the larger particles are only enriched mostly in the roots of the plant. A possible explanation of this phenomenon is that smaller nanoparticles can easier pass through the intercellular barriers and membrane bilayers of the plant than larger ones.

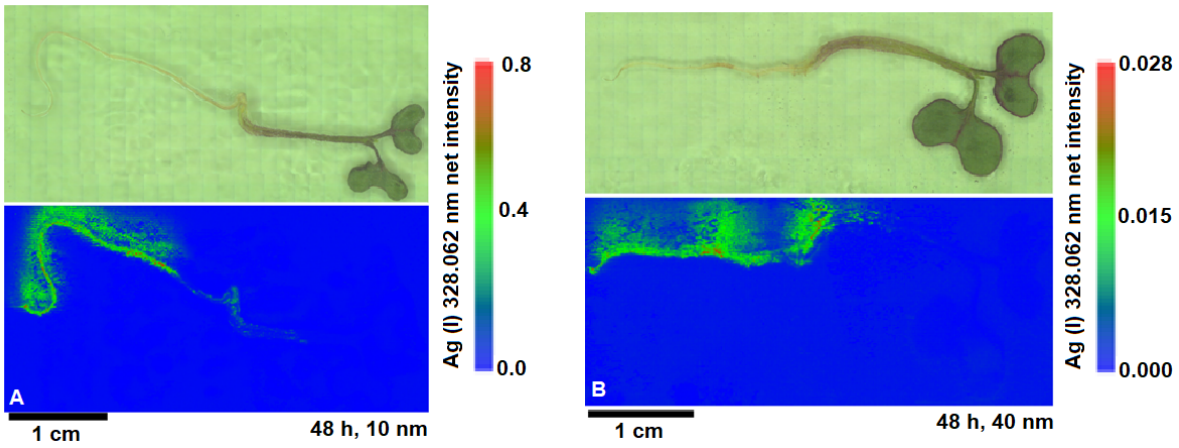

Figure 2. Optical microscopic image (on the top) and LIBS map of Ag (I) 328.062 nm of one of the plants grown in an aqueous dispersion of 10 nm (A) and 40 nm (B) silver nanoparticles for 48 hours.

It is also apparent that the concentration of the silver detected is also different, judged by the signal intensity. In those plants, which were grown in 10 nm NP- containing dispersions, the detected LIBS signals are more than twenty times higher, than in those which were grown in the 40 nm NPs containing nanodispersions. Since the exposition time was the same, this indicates a stronger accumulation of the smaller particles.

3.2 Time-dependent bioaccumulation

Another parameter that influences the accumulation of NPs is the duration of exposition. This effect was tested using two different exposition times: 48 and 72 hours. The result show that detected LIBS signals are twice as high for the 72 hour batch than for the 48

batch. Along with the expectations, this suggests that a longer exposition time produces stronger accumulation.

4. Conclusions

In this research we show that LIBS is a promising tool for this task. We successfully detected silver singes from plant samples grown in silver nanodispersions. Two aspects were examined one was the size dependence, in this part 10 nm and 40 nm sized NPs accumulation was monitored and we found that the smaller nanoparticles are more easily penetrate in the plants compared to the bigger ones. The second influencing factor which was examined was the exposer time. As we thought previously the longer exposer time cause higher NP deposition in the plants.

5. Acknowledgements

The financial support received from various sources including the Ministry of Innovation and Technology (through project No. TUDFO/47138-1/2019-ITM FIKP) and the National Research, Development and Innovation Office (through projects No. K_129063, EFOP-3.6.2-16-2017-00005, TKP 2020 Thematic Excellence Programme 2020) of Hungary is kindly acknowledged. This research has been also financially supported by the Ministry of Education, Youth and Sports (MEYS) of the Czech Republic under the project CEITEC 2020 (LQ1601) and the CzechNanoLab Research Infrastructure supported by MEYS CR (no. LM2018110).

6. References

[Peng 2012] T-H. Kim, M. Kim, H-S. Park, U. S. Shin, M-S. Gong, H-W. Kim, *J. Biomed. Mater. Res.*, 100A (2012) 1033.

[Modlitbová 2020a] P. Modlitbová, P. Pořízka, S. Střítežská, Š. Zezulka, M. Kummerová, K. Novotný, J. Kaiser, *Chemosphere*, 251 (2020) 126174.

[Modlitbová 2020b] P. Modlitbová, P. Pořízka, S. Střítežská, Š. Zezulka, M. Kummerová, K. Novotný, J. Kaiser, *Trends Anal. Chem.,* 122 (2020) 115729.

EXPLORATORY ANALYSIS OF ZOOPLANKTON SPECTRA USING MATRIX DECOMPOSITION TECHNIQUES

Nikolai Sushkov[1]*, Timur Labutin[1], Nikolai Lobus[2], Gábor Galbács[3]

[1]Department of Chemistry, Lomonosov Moscow State University,
119234 Moscow, Leninskie gory 1 str. 3, Russia
[2]Shirshov Institute of Oceanology of the Russian Academy of Sciences,
119997 Moscow, Nakhimovskii pr. 36, Russia
[3]Department of Inorganic and Analytical Chemistry, University of Szeged,
6720 Szeged, Dóm square 7, Hungary
**e-mail: nikolaisushkov@laser.chem.msu.ru*

1. INTRODUCTION

Marine zooplankton communities of high latitudes are often dominated by copepod crustaceans belonging to the order *Calanus* (Fig. 1). They are a link between primary producers (phytoplankton) and higher levels of the food chain, thus making a significant contribution to energy flows in the marine ecosystem. A characteristic feature of calanoid copepods is the so-called winter diapause, which is accompanied by hibernation at a great depth (more than 500 m). In spring, the crustaceans migrate back upwards. The mechanism of buoyancy regulation is not completely clear. It may be based on a change in the density of lipids contained in a special fat bag, depending on the water pressure during vertical migration. Body density can also be regulated through the exchange of heavy ions for lighter ones (e.g. Na^+ for NH_4^+). In addition to ammonium ions, lithium ions can also reduce the density. The Li content in seawater is 28 mmol/l (about 200 mg/l), while in calanoids it can be 2-3 orders of magnitude higher. Accumulation of lithium through the food chain and passive uptake from the environment are considered unlikely. Thus, it should be assumed that there is a physiological mechanism for active accumulation and that lithium has some biological function which is yet to be clarified [Lobus 2016, Freese 2015, Lobus 2018].

Figure 1. *Calanus glacialis* (the scale bar is 2 mm)
[http://www.arcodiv.org/watercolumn/copepod/Calanus_glacialis.html, retrieved Nov. 09, 2020].

The main components of copepod tissues in terms of molecular composition are proteins, fats, and chitin [Freese 2016]. There is also intense coloration due to the presence of carotenoid pigments, whose signals are clearly visible in absorption and/or Raman spectra (e.g. [Zagalsky 1985]). The goal of the present study was to find correlations between atomic and molecular composition of copepod tissues to provide insight into reasons behind lithium accumulation. To this end, analyses by LIBS and Raman spectroscopy were performed.

2. EXPERIMENTAL

Samples. We analyzed 29 zooplankton samples, 14 of which were calanoid copepods. The animals were caught during expeditions in the Arctic seas and in the Black Sea in 2014–2017 (typically from August to October). They were washed with deionized water, dried at 50° C for 12 hours and pelletized under a moderate pressure (d = 8 mm, 20–1000 bar, typically 30 bar).

Equipment. LIBS was performed using the Applied Spectra J200 Tandem LA-LIBS instrument (excitation laser: 266 nm Nd:YAG, 20 mJ/pulse, 10 Hz, spot diameter: 200 μm; acquisition delay: 500 ns). Since the instrument was equipped with a CCD detector, we obtained time-integrated spectra (integration time ~ 3 ms). The spectra covered the entire optical range (186–1049 nm). Resolving power depended on the wavelength range and was typically around 3000.

Raman scattering spectra were recorded using the Thermo Scientific DXR Raman Microscope (780 nm laser, energy 1-14 mW, spot size 1–2 μm) in the range of 45–3500 cm^{-1}. We applied different energies depending on the fluorescent background intensity and resistance of samples to burning. Aperture was selected individually for each sample to attain sufficient signal-to-noise ratio and avoid CCD overflow at the same time. The following apertures were used: 25 and 50 μm slits, and 25 and 50 μm pinholes. Acquisition time ranged from 30 s to 5 min. Spectra were instantaneously fluorescence corrected in the instrument software using a 6th order polynomial function.

Experimental procedures. Due to inhomogeneity of the samples, we distinguished dark, light, and medium coloured spots on the pellet surfaces. For each of the colours, LIBS and Raman spectroscopy were carried out in at least 3 spots of that colour, i.e., a total of at least 18 spots were examined on each pellet by these techniques. In the case of LIBS, typically 10 laser shots per spot were delivered.

2.1. DATA PROCESSING METHODS

a. Data pretreatment. The obtained arrays of emission spectra were filtered for outliers. To this end, several prominent peaks, including analytical lines, were selected. The list typically included peaks at 610.34 (Li I and Ca I), 247.84 (C I), 473.60 (C_2 band head), 568.30 (Na I) and 396.85 (Ca II) nm. Their background corrected heights were checked for outliers using the Grubbs' criterion, which was applied repetitively until there were

no outliers at any peak. This procedure was supervised in a home-made graphical interface, so that results could be corrected if necessary. The remaining spectra were averaged for each of the zooplankton samples, and an array of averaged spectra (29 samples × 12 275 wavelengths, 186–1049 nm) was composed. We performed no background correction for emission spectra.

Raman spectra were first manually background corrected since the automatic correction was not always satisfactory. Then we divided each spectrum by its mean to reduce the effect of different experimental conditions. After that, the spectra were averaged. Dimensions of the resulting matrix were 29 samples × 2801 wavenumbers (450–3150 cm^{-1}).

Bulk composition data (elements from Li to U except non-metals), obtained by ICP-AES and ICP-MS after digestion, were also available.

Data processing was carried out in Origin 8.5, GNU Octave, Microsoft Excel, Wolfram Mathematica 8, and Matlab 2020 software. In order to perform an exploratory analysis of the data, we used various matrix decomposition techniques described below.

b. Principal component analysis (PCA). Decompositions by PCA were a starting point for all further considerations. To determine the optimum number of principal components, we used conventional scree plots of eigenvalues. The same number of components was implied in NMF decompositions (see below).

c. Non-negative matrix factorization (NMF). A detailed discussion of this technique, which may be considered as one of the methods for blind source separation, can be found in [Cichocki 2009]. The approach is a matrix factorization constrained by assumption that resulting components should be non-negative. This helps to obtain physically interpretable components. The problem may be formulated as follows: given a matrix X with m descriptors (rows) and n samples (columns), factorize it into two terms W ($m \times n$) and H ($n \times p$), with $p < \min(m, n)$:

$$X = WH + E$$

Here, the matrix E represents approximation error. Columns of W are called basis vectors, and rows of H are decomposition coefficients. Contrary to other decomposition techniques like PCA, the additive nature of NMF does not allow factors to vanish due to their equal values and opposite signs. The technique has become popular in several areas, such as facial recognition and processing of electroencephalographic data. The drawback of NMF is that the solution is not unique since optimization only leads to a local minimum of cost function. Additionally, the results depend on the initial approximation of W and H. Therefore, it is advisable to perform multiple (10–1000) algorithm runs to obtain a reliable factorization [Buciu 2008, Brunet 2004].

d. ComDim—PCA and ComDim—ICA. The common component and specific weights analysis, also known briefly as ComDim, was first introduced in 1995 [Qannari 2004]. It deals with several blocks of data (e.g., LIBS and Raman data) and seeks to factorize them independently, without concatenation. To this end, the ComDim defines underlying common dimensions relevant to each block and assesses how much each dimension is

relevant to each data block. The measure of the "relevance" is called specific weight, or salience.

If each of N samples is represented by a line in a block of measurements X_k, it is possible to define the W_k matrix as a scalar product $X_k X_k^T$. This matrix is modelled as

$$W_k = Q\Lambda^{(k)}Q^T + E_k$$

Here Q is an orthogonal matrix of dimensions (N, N), which contains the common components in its columns. The matrix $\Lambda^{(k)}$ is a diagonal (N, N) matrix of specific weights; it can be different depending on the block X_k, while Q is the same for all the blocks X_k. Sum of saliences in $\Lambda^{(k)}$ describes to what extent a particular X_k is contributing to Q.

ComDim components are calculated one by one. These steps may be implemented to involve PCA or ICA (independent component analysis). Contrary to PCA, ICA does not assume orthogonality of components, which brings it closer to reality, but at a cost of solution being non-unique. Like NMF, it is a blind source separation technique and seeks to find components as independent as possible by maximizing a certain function which defines the independence [Hyvärinen 1999].

3. RESULTS AND DISCUSSION

3.1. The whole dataset

We have first investigated the whole dataset which contained data about all the 29 samples of crustaceans. We have concatenated LIBS spectra to obtain matrices containing data from dark, medium-coloured, and light spots (29 samples × 36825 predictors). In this fashion, all the available information is used. PCA decomposition of this matrix yielded 5 components (explained variance 99%). One of the obtained loadings contained emission signals of Li, Na, and Mg. Calanoid crustaceans formed a group on the score graphs, which was however not well separated from the other samples. To improve this result, we cut out all resonance lines from the data matrix (like C I 247, Na I 589, K I 769 nm, etc.) to avoid nonlinear signals. Spectral range with wavelengths longer than 947.8 nm was also discarded. There was clearer clustering in score graphs obtained for this shortened matrix than in the previous case.

Same operations were tried with concatenated Raman spectra (8403 predictors). PCA decomposition yielded 5 PCs, but loadings were not easy to interpret, and no clear clustering was observed on score graphs. Discarding wavenumbers greater than 1921 cm^{-1} helped to avoid strong and non-characteristic hydrocarbon chain signals around 3000 cm^{-1} and a large uninformative area between 1921 and 2700 cm^{-1}. Score graphs obtained from the shortened matrix allowed to distinguish crustaceans (incl. *Calanoida*) from other animals (sea snails and arrow worms). However, it was impossible to distinguish calanoids from other crustaceans according to their Raman spectra (in contrast to the LIBS results).

LIBS and Raman spectra can also be concatenated together to give a hybrid dataset. For these data, both PCA and NMF gave 2 "Li-containing" loadings. In the Raman domain, one of them contained signals of amino acids like tryptophan (758 cm^{-1}), and the other one showed carotenoid peaks. Both methods provided reasonably good clustering allowing to distinguish calanoids from other crustaceans and snails, but not from arrow worms (**Figure 2.**).

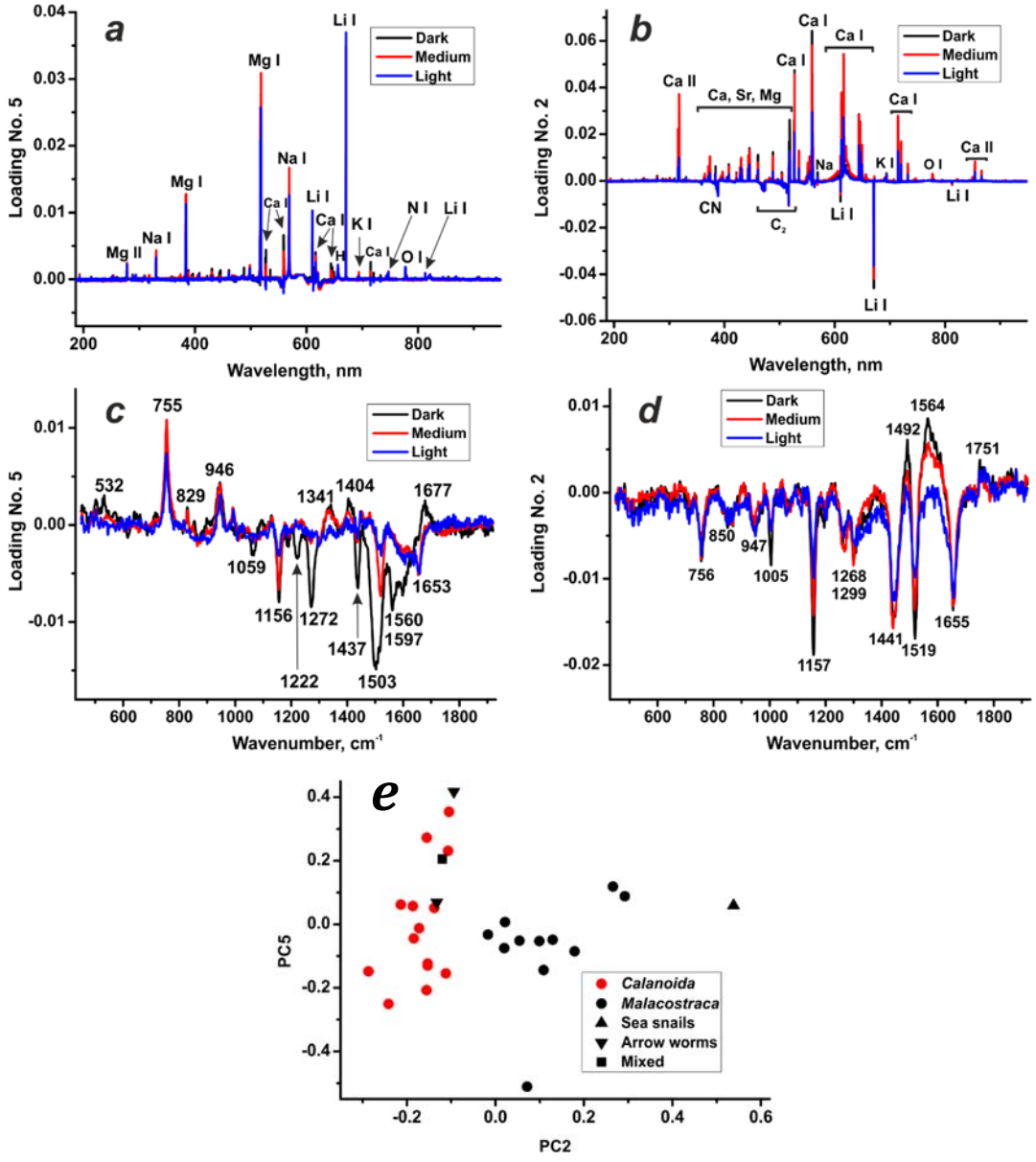

Figure 2. Results of the PCA decomposition of the combined LIBS+Raman dataset (loadings Nos. 2 and 5); a, b: LIBS domain; c, d: Raman domain; e: score graph (PC5 vs. PC2). Calanoid copepods are shown in red.

We also compared performance of ComDim—PCA and ComDim—ICA regarding our data. In both cases there were 6 separate blocks of data, corresponding to 3 spot colours in LIBS and Raman spectra. Spectra were shortened as described above. Although both kinds of ComDim revealed correlation between Li signals, carotenoid and amino acid bands, loadings were easier to interpret in ComDim—ICA. It should be noted that the

correlation with Trp band is stronger in dark and light spots compared to medium-coloured ones. Classification was better in ComDim—PCA.

3.2. *Calanoida* samples only

This section deals with the data subset related to 14 samples belonging to the *Calanoida* order. These spectra were pre-treated as described in the previous section (resonance lines discarded, etc.). PCA and NMF decomposition of the LIBS spectra readily gave a component dominated by Li signals, and on the score graphs, samples showing anomalously high Li content tended to be located separately from other samples. Raman spectra yielded separate loadings corresponding to carotenoids and to amino acids. This trend was more distinct for the PCA than for NMF. The Raman score graphs are less informative than the LIBS-related graphs; classification is apparently driven mainly by the intensity of carotenoid bands.

As for combined LIBS+Raman data, both PCA and NMF mainly underline the correlation between Li signals and carotenoid bands, although bands of amino acid are also present in the relevant loadings. There is reasonably distinct clustering of samples on the score graphs according to their Li content.

ComDim—PCA (**Figure 3.**) again placed Li together with carotenoid pigments and amino acids. It is interesting that ComDim—ICA suggested 2 carotenoid-containing loadings with roughly equal proportions of explained variance. Lithium signals dominated in the loading which contained more tryptophan signal. This may suggest that Li accumulation is more importantly related to amino acids than to pigments.

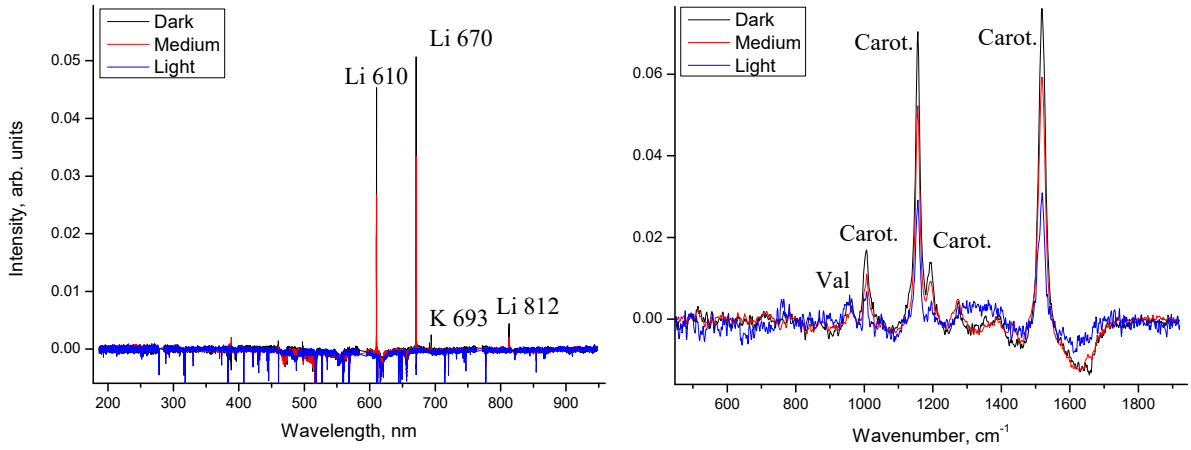

Figure 3. The Li-related common component in ComDim. Left: LIBS data. Right: Raman data. "Carot." = carotenoid compounds, "Val" = valine.

Indeed, there is a distinct pair correlation between Li bulk content (as determined by ICP-MS) and the intensity of Trp peak in Raman spectra (**Figure 4.**). There is no comparable correlation between Li and carotenoid bands.

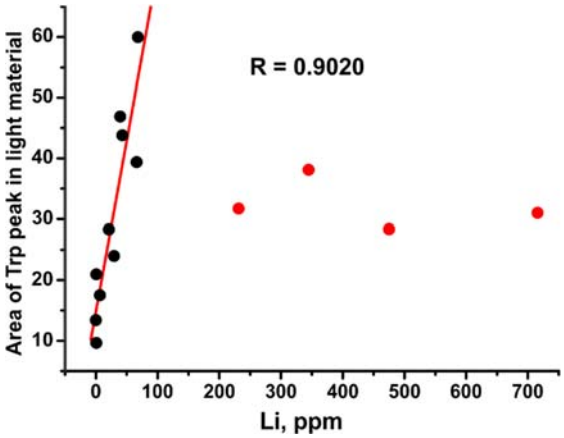

Figure 4. Linear correlation between Li content and Trp band in Raman spectra of calanoid copepods. Samples marked in red are considered anomalous and not included into the regression.

4. CONCLUSIONS

Matrix decomposition techniques used in this study for exploratory analysis of LIBS and Raman spectra revealed correlation between Li content, amino acids, and carotenoid pigments in marine zooplankton. The most interesting correlation is that with tryptophan. Results obtained by PCA, NMF, ComDim—PCA, and ComDim—ICA are generally the same, although PCA-based approaches are often more precise in classification and yield higher explained variance. Discarding resonance emission lines and uninformative regions of LIBS and Raman spectra helped to improve results of matrix decomposition. The most productive way of analysing LIBS and Raman spectra is data fusion, either by simple (low-level) concatenation or by more sophisticated techniques such as ComDim.

5. ACKNOWLEDGEMENTS

ICP-AES and ICP-MS elemental analyses of zooplankton samples were funded by the Russian Science Foundation (research project No. 18-77-00064). The authors are grateful to Á. Bélteki, Dr. A. Kéri, P. Janovszky, D. Palásti, Dr. K. Fintor (University of Szeged) and Dr. R. Rajkó (Universtity of Pécs, Hungary) for their valuable assistance. The financial support received from the National Research, Development and Innovation Office of Hungary through project No. K_129063 is kindly acknowledged. The MATLAB code for performing ComDim was kindly provided by Prof. D. N. Rutledge (AgroParisTech, France).

6. REFERENCES

[Brunet 2004] J.-P. Brunet, P. Tamayo, T. R. Golub, J. P. Mesirov, *Proc. Natl. Acad. Sci.*, 101 (2004) 4164.

[Buciu 2008] I. Buciu, *Int. J. Comput. Commun. Control*, 3 suppl. issue (2008) 67.

[Cichocki 2009] A. Cihocki, R. Zdunek, A. H. Phan, S. Amari: Nonnegative Matrix and Tensor Factorizations: Applications to Exploratory Multi-Way Data Analysis and Blind Source Separation, *Wiley Publishing*, 2009.

[Freese 2015] D. Freese, B. Niehoff, J. E. Soreide, F. J. Sartoris, *Limnol. Oceanogr.*, 60 (2015) 2121.

[Hyvärinen 1999] A. Hyvärinen, *Neural Comput. Surv.*, 2 (1999) 94.

[Lobus 2016] N. V. Lobus, *Oceanology*, 56 (2016) 809.

[Lobus 2018] N. V. Lobus, A. V. Drits, M. V. Flint, *Oceanology*, 58 (2018) 405.

[Qannari 2004] E.M. Qannari, I. Wakeling, H. J. H. MacFie, *Food Qual. Prefer.*, 6 (1995) 309.

[Zagalsky 1985] P. Zagalsky: Invertebrate carotenoproteins (Chapter 9) in: Methods in Enzymology, Steroids and Isoprenoids Part B (ed. by J. H. Law, H. C. Rilling), *Elsevier*, 1985.

LIBS-BASED APPROACHES FOR THE CLASSIFICATION OF GLASS MICROFRAGMENT SAMPLES

Dávid Jenő Palásti[1,2], Anikó Metzinger[3], Judit Kopniczky[2,4], Béla Hopp[2,4], Gábor Galbács[1,2]*

[1]Department of Inorganic and Analytical Chemistry, University of Szeged, 6720 Szeged, Dóm square 7, Hungary
[2]Department of Materials Science, Interdisciplinary Excellence Centre, University of Szeged, Dugonics square 13, 6720 Szeged, Hungary
[2]Department of Physics and Chemistry, Hungarian Institute for Forensic Sciences, 1087 Budapest Mosonyi street 9, Hungary
[4]Department of Optics and Quantum Electronics, University of Szeged, 6720 Szeged, Dóm square 9, Hungary
**e-mail: galbx@chem.u-szeged.hu*

1. INTRODUCTION

Glass is one of the most commonly used materials. Due to its various uses and numerous manufacturers, the elemental composition of glass objects varies at the level of main components and micro contaminations as well. Glass microfragments (<1 mm splinters) are generated in great number during a fracture, thus are commonly found on scenes of car accidents, burglaries, vandalism, assaults and many other, and therefore are often are the subject of forensic investigations. Glass fragments generated by breakage can be trapped by the cloth, shoes or even hair of people present at the crime scene, thus glass fragments frequently link people to each other or to locations [Caddy 2001]. Thus, the analysis of glass samples is important in forensic investigations.

Glass fragment analysis can be done in many ways. Non-destructive methods are preferred, such as refractive index (RI) measurement [Katz 2016], electron microscopy with energy dispersive X-ray spectroscopy (SEM-EDX) [Ramos 2011], micro X-ray fluorescence spectroscopy (μ-XRF), but microprobe methods are utilized as well, such as laser-ablation inductively coupled atomic emission (LA-ICP-AES) or mass spectrometry (LA-ICP-MS) [Trejos 2013]. One promising microprobe method is laser induced breakdown spectroscopy (LIBS), which is a laser ablation based atomic emission spectroscopy technique with many practical features for the forensic analysis. It requires only simple sample preparation and the amount of the consumed sample is in the ng range only. It is sensitive for all elements, the typical detection limits are in the ppm range. LIBS spectra are very feature-rich which produces fingerprint-like spectra that are very characteristic for specific samples. Despite its advantageous properties, LIBS has only rarely been investigated as a possible instrument for forensic glass analysis (e.g. [Barnett 2008, El-Deftar 2014]).

In the current study, we set out to investigate the potential of LIBS for the qualitative discrimination of glass types, also including the investigation of their homogeneity and ablation properties.

2. EXPERIMENTAL

During this investigation, 131 glass samples, representing four major types, fused silica, borosilicate, soda-lime and flint glass (FS, BS, SL and FL), were analysed. Due to their widespread use our study focused mainly on soda-lime glasses, hence the majority, 96 of our glass fragment samples belonged to this type. Within the soda-lime type, float, container, patterned and security glass subtypes (SL/F, SL/C, SL/P, SL/S) were also sampled.

The surface contaminations of the fragments were removed by spectroscopy-grade acetone, followed by a wiping to dryness using Kimwipes tissues. The cleaned fragments were attached to plastic sample holder discs by a double-sided adhesive tape.

LIBS experiments were performed on a J-200 tandem LA/LIBS instrument (Applied Spectra, USA) equipped with a 266 nm, 6 ns Nd:Yag laser source and a six-channel CCD spectrometer with an average spectral resolution of 0.07 nm. LIBS spectra were recorded in the Axiom data acquisition software using 1 μs gate delay and 1 ms integration time, in the wavelength range of 190 to 1040 nm. The energy of laser pulses was 15 mJ (2% RSD), and the light was focused into a 40 μm wide focal point. The ablation chamber was rinsed by a 99.9995% purity argon gas (Messer Ltd., Hungary) flow at 0.5 L/min flowrate. 25 spectra of each samples were recorded (5 repetitions from 5 different locations).

Refractive index (RI) measurements were carried out on 589 nm by the oil immersion method, using a GRIM 3 system (Foster + Freeman, UK). The RI values were determined using temperature-matched calibration curve based on the measurement of 10 glass standards (Locke Scientific, UK). The laser ablation craters on the glass samples were investigated by using a Veeco Dektakt 8 contact profilometer (Vacuum Electronic Equipment Co., USA). The craters were fully mapped by 330 nm lateral and 400 nm vertical stepping resolution.

3. RESULTS AND DISCUSSION

Glass is produced by mixing and melting together the components, thus glass products are usually considered homogenous materials, and a shard may correctly represent the bulk. However, this property is crucial in glass microfragment analysis, thus we investigated the intra-fragment homogeneity of our samples by comparing the 5-5 LIBS spectra collected at different points of the sample. Linear correlation was used as a comparative function that produces a single numerical value (Pearson coefficient) ranging from 1 to 0, representing full similarity and dissimilarity. Ray plots in **Figure 1.**

show the observed intra-fragment spectral variation for some of selected samples. As expected, it was found that there is a reasonably good similarity between the spectra collected from different spots of the same sample (correlation coefficient was greater than 0.95), which indicates a generally good lateral homogeneity.

Figure 1. Intra–fragment compositional variations in different glass types.

We also studied the depth-resolved elemental distribution which revealed typically flat intensity profiles, expect for Sn. The concentration of this element gradually decreases with the depth in float glasses, which is an artifact caused by the production technology. Tin lines were therefore excluded from the spectra during our later investigations involving float glasses.

The laser ablation behaviour of glass fragments was found to be different from sample to sample. This is evidenced by the diagram in **Figure 2.** which indicates a great variety of crater volumes. In most cases, the crater volumes fall between $3 \cdot 10^5$ and $7 \cdot 10^5$ μm^3, but e.g. for container glasses it showed exceptionally high variation. It also has to be added that crater shapes show jagged edges, which is a clear sign of shock/stress-like fracture – as it is customary for glasses also in large pieces. This varying crater volume makes the accurate quantitative analysis and the qualitative discrimination based on concentration data difficult.

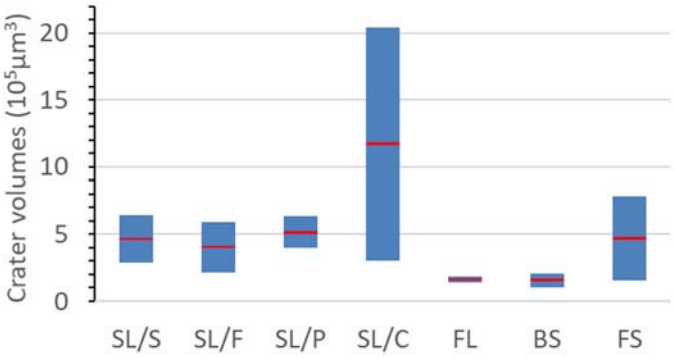

Figure 2. Mean and range values of laser ablation crater volumes for glass types.

The four investigated types of glass samples possess very different elemental composition. For example, fused silica glasses do not contain additives, soda lime glasses have a large Na, K and Ca content, borosilicate glasses contain considerable amount of boron and aluminium, while flint glasses are rich in Ba and Pb. Considering the large variation of compositions between the types, it seems as an easy task to differentiate among the glass types using an element-sensitive analytical technique like LIBS. **Figure 3.**

illustrates the potential of this approach for classification. In this graph, each glass sample is represented as dot placed in the space of their aggregated Ba+Pb, Ca+K and B+Al content. The sample points located close to each other usually belong to the same type group. As it can be noted, the automotive headlight shield glasses behave exceptionally. Although they were expected to be made of borosilicate glass (heat-resistant glass type), but some of them do not contain any boron or aluminium at all, whereas others contain significant amounts of barium and lead in addition to boron and aluminium. Overall, this group is widely scattered. This finding emphasizes that one must not base the discrimination on preconceptions about the composition of glass types.

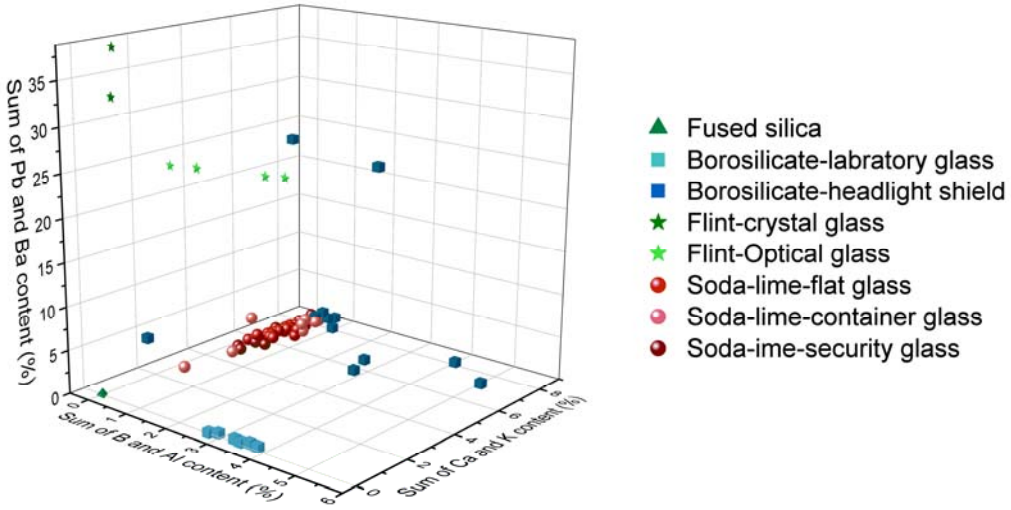

Figure 3. Classification of glass types based on their elemental composition.

Based on the above, we did not use any preliminary chemical information about the glasses during the qualitative discrimination attempts, during which we worked with four subtypes of the soda lime glasses only (SL/F, SL/C, SL/P, SL/S). We tested the accuracy of linear discriminant analysis (LDA), principal component analysis (PCA) and random forest (RF) methods on these data sets for the classification and managed to achieve around 90% of accuracy.

From a chemometric point of view, the identification of individual glass microfragment samples is a more challenging task. For this task, we had to implement a pre-sorting approach too, based on the refractive index in order to have enough "discriminative power" to tell apart individual glass samples. With this combined method, we achieved very satisfying results, which we will disseminate in our poster presentation.

4. CONCLUSIONS

LIBS spectra of numerous glass samples were recorded in this investigation, and a lateral and vertical homogeneity examination was carried out on them. It was found, as expected, that glass samples are generally quite homogenous, which allows the use of LIBS as a microsampling (microprobe) analytical method useful for the discrimination of small glass fragments. We also pointed out to some challenges that are faced when discrimination of glass samples based solely on the elemental concentration information is attempted. These challenges influence the performance of all widely used discrimination techniques, including LIBS. We found that discrimination accuracy is best if it is either based on direct (raw) LIBS spectra, or when LIBS data is combined with refractive index data, in which cases, better than 90% accuracy was achieved.

5. ACKNOWLEDGEMENTS

The financial support received from various sources including the Ministry of Innovation and Technology (through project No. TUDFO/47138-1/2019-ITM FIKP) and the National Research, Development and Innovation Office (through projects No. K_129063, EFOP-3.6.2-16-2017-00005, TKP 2020 Thematic Excellence Program 2020) of Hungary are kindly acknowledged.

6. REFERENCES

[Caddy 2001] B. Caddy: Forensic examination of glass and paint: analysis and interpretation, *Taylor and Francis*, 2001.

[Katz 2016] E. Katz, J. Halámek: Forensic science: a multidisciplinary approach, *Wiley and Sons*, 2016.

[Ramos 2011] D. Ramos, G. Zadora, *Anal. Chim. Acta,* 705 (2011) 207.

[Trejos 2013] T. Trejos, R. Koons, P. Weis, S. Becker, T. Berman, C. Dalpe, M. Duecking, J. Buscaglia, T. Echert-Lumsdon, T. Ernst, C. Hanlon, A. Heydon, K. Mooney, R. Nelson, K. Olsson, I. E. Schenk, C. Palenik, E. C. Pollock, D. Rudell, S. Ryland, A. Tarifa, M. Valadez, A. van Es, V. Zdanowich, J. Almirall, *J. Anal. At. Spectrom.,* 38 (2013) 1270.

[Barnett 2008] C. Barnett, E. Cahoon, J. R. Almirall, *Spectrochim. Acta B*, 63 (2008) 1016.

[El-Deftar 2014] M. M. El-Deftar, N. Speers, S. Eggins, S. Foster, J. Robertson, C. Lennard, *Forensic Sci. Int.*, 241 (2014) 46.

CLASSIFICATION OF PLASTICS USING LIBS AND RAMAN SPECTROSCOPY DATA FUSION

Daniel Holub[1]*, Pavel Pořízka[1,2], Ota Samek[3], Jozef Kaiser[1,2]

[1]Department of Physical Engineering, Faculty of Mechanical Engineering, Brno University of Technology, 616 69 Technická 2896, Brno, Czech Republic
[2]Central European Institute of Technology Brno University of Technology (CEITEC BUT), 612 00, Purkyňova 656/123, Brno, Czech Republic
[3]Department of Biophotonics and Microfluidics, Institute of Scientific Instruments, The Czech Academy of Sciences, 612 64 Královopolská 147, Brno, Czech Republic
**e-mail: 183478@vutbr.cz*

1. INTRODUCTION

Not all materials can be classified using singular spectroscopic methods without tedious pretreatment and data mining. Such materials pose a challenge for usage of spectroscopic methods in automatized industrial processes. Laser Induced Breakdown Spectroscopy (LIBS) gained much attention in recent years thanks to its robustness, low or none material preparation needs and possible usage in remote areas without human presence among other benefits. On the other hand, the Raman spectroscopy method is used regularly in various fields for approximately last 50 years. Its benefits and limitations are well known. Both these methods need little to none sample preparation and can be used remotely. Moreover, these two methods are complementary, because LIBS yields atomic information and Raman spectroscopy provides molecular information. In addition to similar instruments, this duo is a great candidate for combination of acquired data.

In this work, the combination is done via data fusion. This method was already demonstrated by several academic teams and seems to bring better classification results when compared to separately used methods. In work of Hoehse et al. this data fusion was used for classification of inks and pigments. It was demonstrated, that by using LIBS + Raman data fusion, one can recognize similar inks, which form non-recognizable clusters in separate data sets [Hoehse 2012]. Similar results were also provided by Prochazka et al., who used similar data fusion for classification of bacteria [Prochazka 2018].

The aim of this work is to use referenced data fusion method to distinguish spectroscopically challenging material types with as little pretreatment and data mining as possible. For this, several (12) types of plastic were used. Different plastic types were used because of their similar chemical composition and possible industrial utilization. This project should lead to unified way of data treatment for LIBS and Raman spectroscopy data fusion. Now we present results of classification using basic chemometric methods such as PCA and SIMCA. Most important concerns with this type of data fusion are also presented.

2. EXPERIMENTAL

The measurement consisted of LIBS and Raman spectroscopy parts. Samples were chosen from semiproduced materials. All samples except one (PVC) were uncolored. Plastics types are similar to each other chemically due to their chemical composition. All plastics are polymers. They are built by connecting many identical base elements – mers. These mers usually consist of Carbon base and additives. Differences between plastic types are induced by differences between these additives and their connection to base Carbon skeleton.

Raman measurements were done at Institute of Scientific Instruments of Czech Academy of Sciences in Brno. Raman instrument used was Renishaw inVia Raman Spectrometer, Renishaw plc., Wotton-under-Edge, UK. Laser wavelength was 785 nm, objective used had 20x magnification, illumination time was 1 s which was accumulated 10 times for final spectra. Each sample was measured 5 times at 1300 cm^{-1} central Raman shift.

LIBS measurements were done at LIBS laboratory of Department of Physical Engineering of Brno University of Technology. Laboratory system LIBS Discovery was used. Laser wavelength was 532 nm, laser energy was 22 mJ, each spectrum was a result of 5 accumulated shots at the same location. Spectrometer used was EMU Catalina Scientific with an Echelle type grating. Each sample was measured 25 times.

3. RESULTS AND DISCUSSION

3.1. LIBS data analysis

Chemical similarities of different plastic types lead to similar chemical footprint and difficult classification in LIBS. Plastic type classification via LIBS was done several times by various scientific groups. To reach satisfactory accuracy, tedious pretreatment of data mining had to be used. By using Argon atmosphere, line selection and several other data treatments, scientific team from Wuhan (China) reached accuracy over 90% in classification of 11 kinds of plastic [Yu 2014].

Before analysis took place, some data treatment was needed. LIBS spectra were cut to contain only relevant part of wavelength range. Resulting range is 300-800 nm. Lines important for plastic analysis were pinpointed in previous works on plastic identification in LIBS, so these lines were highlighted in our spectra. In attempt to minimize data treatment, this was concluded LIBS data treatment before analysis.

LIBS spectra were then introduced to Principal Component Analysis algorithm. Main goal for this part was to show the need for data fusion. We expect poor classification by LIBS without tedious data treatment. By using first two Principal Components (PCs) more than 95% of data set variance was depicted. Score plot for PC1 and PC2 can be seen in

Figure 1. One of the plastic types is separated from others in the PC space. This is PVC, which was pointed out in the Experiment section as the only colored sample. The difference is highly likely caused by the color additives present in the PVC sample, which are absent in the rest of the samples.

If the data is automatically clustered using k-means clustering, only 3 clusters are formed, which is not surprising. Additional LIBS data analysis is not aim of this work. The expectation that LIBS is not able to properly classify plastic types without complex data treatment was confirmed.

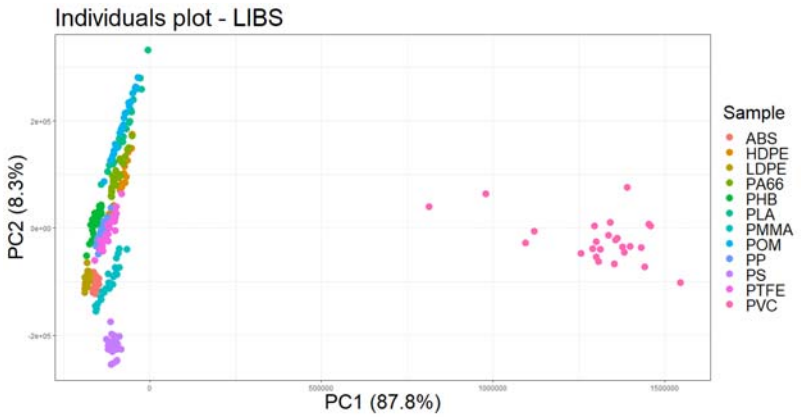

Figure 1. Score plot of separate LIBS measurement.

3.2. Raman spectroscopy data analysis

While LIBS can hardly distinguish plastic types due to similarities in chemical composition, Raman spectroscopy should be more suitable to this task. As plastic types differ in molecular composition, Raman should be able to identify these differences and be more successful in plastic type classification. This was repeatedly confirmed by several papers in past years. For example, in one paper by a scientific team based in Idaho (USA) it was found that 6 types of plastic cound be classified using PCA with an accuracy exceeding 80% [Allen 1999].

Raman spectroscopy data used in this work are of lower resolution in comparison to LIBS data. Before PCA analysis of the data, we tried to pinpoint interesting lines for further usage. This leads us to various papers on Raman spectroscopy of various plastic types. This was needed, because due to molecular differences, no Raman transition was present in every plastic type. Moreover, when the Raman transition was present in multiple plastic types, its Raman shift was different. This leads to different behavior of Raman data in further analysis.

Raman data was then analyzed by PCA in the same way as LIBS data. Again, first two PCs were used to form a scores plot. First two PCs depicted 82.7% of total data variance. Lower percentage of variance depicted by the first two PCs is due to higher number of differences in Raman data of different plastic types. The score plot can be seen in **Figure 2**. It is evident, that the plastic types are more distinguished than in separate LIBS PC space. Again, the colored PVC sample seems farthest from other plastic types. Nevertheless,

using k-means clustering, only 8 clusters were formed, as some of the plastic types cannot be distinguished from each other in this PC space.

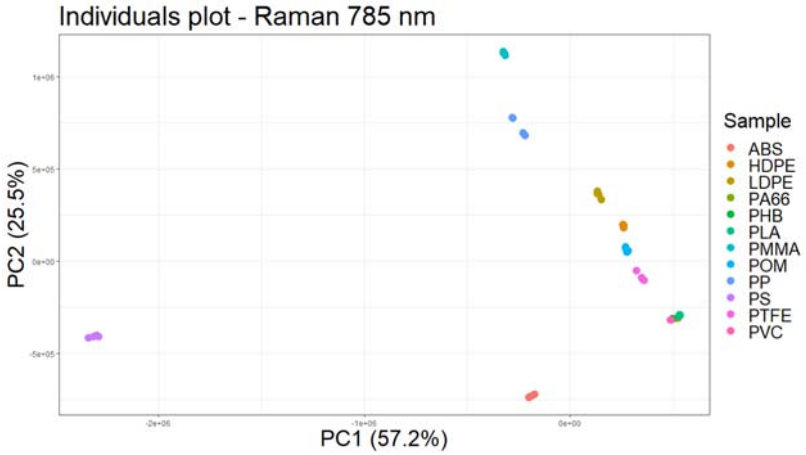

Figure 2. Score plot of separate Raman measurement.

3.3. Fused data analysis

After data fusion, the date set is analyzed by PCA and SIMCA. PCA analysis was done again by analyzing score plot of first two PCs, which depicted 61.4% of data variance. The score plot is in **Figure 3**. It is evident, that data fusion helped with distinction between plastic types in PC space. The data now form 12 separate groups, which is corresponding with the number of plastic types measured. By introducing k-means algorithm, 12 clusters were formed with minimal errors.

To confirm these results, SIMCA algorithm was used. For the training of the algorithm, 35 random pseudo-spectra from every sample were used. The rest of data was used as test set. From 1500 pseudo-spectra, 1370 were correctly classified, the rest was not assigned to any plastic type. This result in accuracy of 91.3%, which is a significant increase in comparison to separately used methods. The results confirmed our expectations.

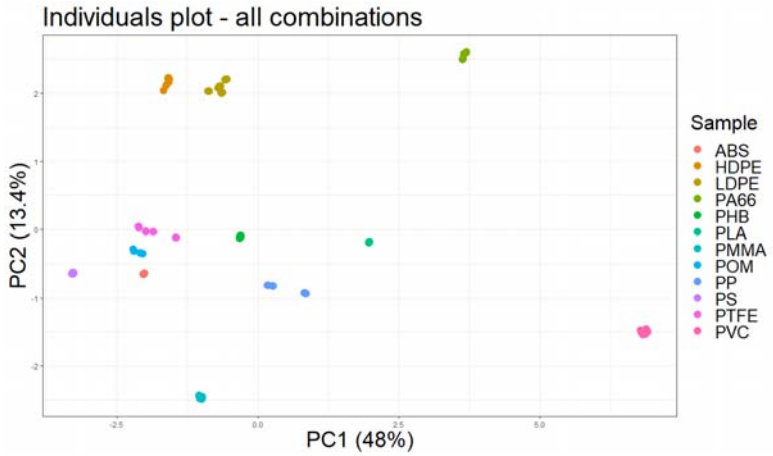

Figure 3. Score plot of fused data sets.

4. CONCLUSIONS

This work was aimed at confirmation of viability of data fusion of LIBS and Raman spectroscopy. 12 different plastic types were chosen as samples. Plastic types classification has also an industrial value. We demonstrated that with minimal data preparation, accuracy of classification using basic methods as PCA and SIMCA increased with usage of fused data. The resulting accuracy using fused data set was 91.3%. This could be used as a stepping stone for automatization of plastic classification.

5. ACKNOWLEDGEMENTS

This research has been financially supported by the Ministry of Education, Youth and Sports of the Czech Republic (MEYS CR) under the project CEITEC 2020 (LQ1601). We acknowledge CzechNanoLab Research Infrastructure supported by MEYS CR (LM2018110) and CEITEC Nano+ project, ID CZ.02.1.01/0.0/0.0/16_013/0001728.

6. REFERENCES

[Hoehse 2012] M. Hoehse, A. Paul, I. Gornushkin, U. Panne, *Anal. Bioanal. Chem.*, 402 (2012) 1443.

[Prochazka 2018] D. Prochazka, O. Samek, M. Mazura, *Spectrochim. Acta B,* 139 (2018) 6.

[Yu 2014] Y. Yu, L. B. Guo, Z. Q. Hao, *Opt. Express*, 22 (2014) 4.

[Allen 1999] V. Allen, J. H. Kalivas, R. G. Rodriguez, *Appl. Spectrosc.*, 53 (2016) 672.

MATRIX EFFECTS IN QUANTITATIVE POLYMER ANALYSIS: A COMPARISON OF ns AND fs LASER SYSTEMS

Lukas Brunnbauer[1], Jhanis Gonzalez[2,3]*, Andreas Limbeck[1]

[1]TU Wien, Institute of Chemical Technologies and Analytics, Getreidemarkt 9/164-I2AC, 1060 Vienna, Austria
[2]Applied Spectra Inc., 950 Riverside Parkway #90, West Sacramento, CA 95605, USA
[3]Lawrence Berkeley National Laboratory, 1 Cyclotron Road, Berkeley, CA 94720, USA
**e-mail: jhanis@appliedspectra.com*

1. INTRODUCTION

As synthetic polymers are becoming more and more important in our daily lives, the need for comprehensive characterization and analysis arises. Besides various physical properties, also the metal content is crucial for many applications. In the food packaging industry, toxic metals must be monitored to avoid migration into the food [Whitt 2013], whereas contaminations of mobile ions in polymers used in the semiconductor industry may cause devices failures [Atkinson 2018]. Conventionally, digestion or combustion protocols with a consecutive liquid ICP-MS or ICP-OES analysis is used to determine the metal content of polymers [Pereira 2011]. As this approach comes with many disadvantages, recently direct-solid sampling techniques such as LIBS have been used for this task. Even though, LIBS can provide many advantages in polymer analysis, obtaining reliable quantitative results is still challenging as matrix-effects occurring during the ablation and excitation of the sample highly influence the signal response. As the use of fs-laser systems has proven to be useful to decrease matrix-effects in LA-ICP-MS analysis compared to ns-laser systems [Koch 2007], in this work we investigate this influence in LIBS analysis. Therefore, a set of in-house prepared polymer standards of 7 different polymer types is analyzed using a ns and a fs LIBS setup and matrix-effects are assessed and compared.

2. EXPERIMENTAL

2.1. Materials

Polymer solutions of seven different polymer types (Polyacrylonitrile (PAN), Polyimide (PI), Poly(methyl methacrylate) (PMMA), Polysulfones (PSU), Polyvinylacetate (PVA), Polyvinylchloride (PVC) and Polyvinylpyrrolidone (PVP) were prepared by dissolving polymer granulates obtained from HP Polymer GmbH (Lenzing, Austria) and Arcos Organics, Geel, Belgium in N-Methyl-2-pyrrolidon (NMP) with p.a. grade quality obtained from Merck (Darmstadt, Germany). NMP standards containing various levels of lithium

were prepared by dissolving Lithium trifluoromethanesulfonate (98%) (Sigma-Aldrich, Buchs, Switzerland) in NMP. Prepared polymer solutions were spiked with the corresponding NMP standards and applied to high purity Si-wafer (10 mm x 10 mm) (Infineon Austria AG, Villach, Austria) via a spin-coating procedure. Samples were cured at 80°C for 12 h to ensure complete evaporation of NMP.

2.2. Instrumentation

LIBS experiments were carried out using a commercially available LIBS J200 system equipped with a Nd:YAG laser operating at 266 nm and a pulse duration in the ns range and a commercially available LIBS J200 Femto iX system equipped with a Yb:YAG laser operating at 1030 nm with a pulse duration in the fs range. In each system, a collection optic was used to collect the light emitted by the laser-induced plasma. Emitted light is transported to an ICCD detection system using optical fibers detecting the Li-emission line at 670.78 nm. Instrumental parameters are summarized in **Table 1**.

LIBS J200 Applied Spectra (West Sacramento, CA)		
Wavelength (nm)	266	1030
Pulse duration	ns	fs
Spot size (µm)	100	
Repetition rate (Hz)	10	
Gate delay (µs)	1	0.1
Accumulated spectra	35	
Measurement spots/sample	6	
Atmosphere	Ar	

Table 1: LIBS measurement parameters

3. RESULTS AND DISCUSSION

The main goal of this work is to investigate the occurrence of matrix-effects during quantitative ns- and fs-LIBS analysis of polymer samples. Therefore, in-house prepared standards of 7 different polymer types were investigated with two different LIBS systems. In a first step, homogeneity of the prepared standards was investigated by assessing Li signal variations over the analyzed area. Different data normalization methods were investigated to improve the quality of the obtained calibration curves (normalization to signal background and normalization to the nominal carbon content). Additionally, the overall quality of the univariate calibration models is assessed and compared between ns- and fs-LIBS. Matrix-effects of different polymer types are observed in different polymer types, as different slopes of the calibration curves. The variation of the obtained slopes was used as a reference value for the occurrence of matrix-effects. If matrix-effects are

reduced, the variation of the obtained slopes of the calibration curves of different polymer types should decrease.

With the different investigated data evaluation strategies, univariate calibration models of adequate quality were obtained for each polymer type and each laser system even though the Li signal response was observed to be highly dependent on the polymer type as well as the employed laser system. Besides PVC showing the highest slope for both laser systems, no systematic trend was observed regarding the signal response between the ns- and fs-LIBS analysis. Additionally, no significant reduction of matrix effects (represented by the variation of the observed slopes of the univariate calibration models) was observed by the use of a fs-LIBS system compared to a ns-LIBS system.

4. CONCLUSIONS

Matrix-effects occurring during quantitative polymer analysis for fs- and ns-LIBS is assessed and compared in this work. No reduction of the severity of matrix-effects was observed for fs-LIBS. The different polymer types showed a highly varying signal response depending not only on the polymer type but also the employed laser system. Therefore, we conclude, that fs-LIBS does not offer any advantages by a reduction of matrix-effects for quantitative polymer analysis compared to ns-LIBS.

5. ACKNOWLEDGMENTS

The author gratefully acknowledges the financial support funded by the Austrian Research Promotion Agency (FFG, Project No. 863947).

6. REFERENCES

[Whitt 2013] M. Whitt, K. Vorst, W. Brown, S. Baker, L. Gorman, *J. Plast. Film Sheeting.*, 29 (2013) 163.

[Atkinson 2018] S. Atkinson, *Seal. Technol.*, 2018 (2018) 5.

[Pereira 2011] J. S. F. Pereira, C. L. Knorr, L. S. F. Pereira, D. P. Moraes, J. N. G. Paniz, E. M. M. Flores, G. Knapp, *J. Anal. At. Spectrom.*, 26 (2011) 1849.

[Koch 2007] J. Koch, D. Günther, *Anal. Bioanal. Chem.*, 387 (2007) 149.

ANALYSIS OF URANIUM-BEARING MATERIALS BY LASER-INDUCED BREAKDOWN SPECTROSCOPY

Dávid J. Palásti[1,2], Patrick Janovszky[1,2], Ádám Bélteki[1], Éva Kovács-Széles[3], Mihály Óvári[3], Csaba Tóbi[3], Zsolt Varga[4], Andrey Berlizov[5], Gábor Galbács[1,2]*

[1]Department of Inorganic and Analytical Chemistry, University of Szeged, 6720 Szeged, Dóm sq. 7, Hungary
[2]Department of Materials Science, Interdisciplinary Excellence Centre, University of Szeged, 6720 Szeged, Dugonics sq. 13, Hungary
[3]Nuclear Security Department, Centre for Energy Research, 1121 Budapest, Konkoly-Thege Miklós way 29-33, Hungary
[4]European Commission, Joint Research Centre, Directorate for Nuclear Safety and Security, Postfach 2340, 76125, Karlsruhe, Germany
[5]International Atomic Energy Agency, Vienna International Centre, 1400 Vienna, Austria
**e-mail: galbx@chem.u-szeged.hu*

1. INTRODUCTION

In recent years, laser-induced breakdown spectroscopy (LIBS) finds more and more applications in the nuclear field. Among the samples for the analysis of which LIBS was successfully tested are reactor structural materials, nuclear fuel, contraband radioactive materials, forensic samples, etc. [Li 2016, Maurya 2020] Although quantitative isotope analysis is not the strong suit of LIBS due to the small isotopic effect of atomic emission spectral lines and their pressure broadening, but with some limitations it is also within reach recently via laser ablation molecular isotope analysis (LAMIS). Similarly to other fields, LIBS was found particularly useful for the qualitative discrimination of sample types, elemental distribution studies and trace analysis [Galbács 2015].

In the present project, commissioned by the International Atomic Energy Agency (IAEA), we investigated the capability of LIBS for the in-field analysis of uranium-bearing materials, more specifically whether or not it can provide quantitative trace analytical results for contaminants in compliance with the ASTM C753-04 standard. Our presentation gives a brief overview of the project's results.

2. EXPERIMENTAL

In order to maintain portability and in-field applicability of the instrumentation, we used a portable LIBS system (LIBScan 25+, Applied Photonics, UK) for spectral data collection and compact (mostly self-developed) devices for sample preparation or ablation control. In accordance with this effort we developed a laser ablation chamber and an electronic chamber ambient gas pressure control unit adapted to the LIBS setup and for the

purposes of the project. Spectral coverage was from the UV to NIR range (240 to 940 nm, with a small gap around 460-470 nm), with a spectral resolution of <0.1 nm. The samples involved in the experiments included the NBL CRM 124 set of reference materials (U_3O_8 matrix); IAEA 874501, IAEA 8747-01 and IAEA 9064-07-01 standards uranium ore concentrates; several uranium-bearing inter-laboratory samples as well as pure, common metals (as targets used in optimization experiments). The powdered samples were pressed into pellets before LIBS analysis. All gases used as ablation ambient gases were of 99.995% grade purity (Messer Hungarogáz, Hungary). All LIBS experiments on uranium-bearing materials were performed in the laboratory of the Nuclear Security Department, Atomic Energy Research Institute (NSD-AERS), whereas experimental planning, optimization experiments and data evaluation was performed at the University of Szeged. Reference compositional measurements on inter-laboratory samples were done also at the (NSD-AERS), using a Thermo Element 2 sector field ICP-MS instrument.

3. RESULTS AND DISCUSSION

Prior to all further works, a selection of prominent spectral lines for the elements included in ASTM C753 was performed, based on theoretical considerations (with priorities on selectivity and sensitivity). We found that analytically the 460 to 800 nm range is the most promising and that most elements in the standard have potentially suitable lines for the analysis in this matrix. We also studied the potential of diminishing spectral interferences from the uranium matrix by using sample dilution [Chinni 2009]. It was found that it is highly adviseable to dilute the samples 100-fold using e.g. spectrographic carbon or other suitable binder/diluent powder.

We carried out experimental testing of several LIBS signal enhancement methodologies that can potentially be applied in the field (e.g. argon gas purge and pressure control, spatial and magnetic plasma confinement, timing optimization, etc.). It was found that gas control is the most reliable and practical enhancement methodology. By using argon gas purging and lower than normal pressure (ca. 100 mbar), a three-fold signal enhancement was achieved. It was also established, that a light collection setup different from the built-in one in the portable LIBS instrument used is needed to fully exploit the signal enhancement methodologies [Palásti 2017].

Several signal calibration and normalization approaches were also theoretically evaluated. It was established that the use of uranium as an internal standard and matrix-matched external calibration are the most practical. Extensive attempts were also made to prepare homogeneous pelletized external samples by mixing metal salts and pure UO_2 powder in order to make calibration standards, but it was not deemed to be reliable.

The analytical performance of the LIBS measurement setup, under optimized conditions was assessed. Calibration plots were constructed for 64 spectral lines of 17 elements, common in both the standard samples and ASTM C753. It was found that most of the spectral lines suffer from interferences from elements outside the focus of the project, therefore only Fe, Zn, K, Mg, Ca, Mn could be properly calibrated (depending on

the sample matrix). Limits of quantitations (LOQs) of 50-100 ppm were achieved, which level is more than adequate for the quantitative analysis of the elements according to ASTM C753, which dictate 200 ppm limits of quantitation or less. The dynamic range of the method was found to be 2-3 orders of magnitude. The signal scatter, which is influenced by many parameters (including laser pulse energy jitter, sample microhomogeneity, matrix composition, etc.), is significant, ca. 10-20 RSD%, with signal normalization, but this is reasonable for portable instrumentation and for compliancy testing [Palásti 2019].

The matrix effect was studied for at least three uranium-bearing matrices (e.g. UO_2, U_3O_8, ammonium-diuranate) and it was found to be significant, as expected. This is primarily caused by the different light absorption of the chemical compounds making up ca. 99% of the samples at the wavelength of the laser, as well as – to a less extent - the density and porosity of the samples. Since plasma characteristics are determined by the matrix (and the gas environment), therefore the influence of the matrix is far from neglectable in the analysis of the trace components. The matrix effect manifested itself in the calibration plots as either different signals for the same analyte concentration (when the plot was linear) and different curvature of the plots (for the same spectral line, in all cases) was found. This finding stresses the importance of matrix-matched calibration.

Quantitative accuracy was tested by analyzing inter-laboratory uranium-bearing samples, using solution-based ICP-MS measurements as reference (after the acid-digestion of the samples). A 20-25% relative inaccuracy was found, which is a fair value considering the factors involved [Galbács 2019].

4. CONCLUSIONS

The LIBS method was generally found to be quite suitable for the quantitative trace analysis of uranium-bearing materials, at the level of detection capabilities and accuracy dictated by ASTM C753-04. The analytical task is fully feasible by portable instrumentation, although some sample preparation (powder dilution) may be needed, but this can potentially also be performed on site.

5. ACKNOWLEDGEMENTS

The financial support received from various sources including the National Research, Development and Innovation Office (through projects No. K_129063, EFOP-3.6.2-16-2017-00005, TKP 2020 Thematic Excellence Program 2020) of Hungary are kindly acknowledged.

6. REFERENCES

[Li 2016] C. Li, C. L. Feng, H. Y. Oderji, G. N. Luo, H. B. Ding, *Front. Phys.*, 11 (2016) 114214.

[Maurya 2020] G. S. Maurya, A. Marín-Roldán, P. Veis, A. K. Pathak, P. Sen, *J. Nucl. Mat.*, 541 (2020) 152417.

[Galbács 2015] G. Galbács, *Anal. Bioanal. Chem*., 407 (2015) 7537.

[Chinni 2009] R. C. Chinni, D. A. Cremers, L. J. Radziemski, M. Bostian, C. Navarro-Northrup, *Appl. Spectrosc.*, 63 (2009) 1238.

[Palásti 2017] D. J. Palásti, É. Kovács-Széles, A. Berlizov, G. Galbács, poster presentation P95, *International Symposium on Analytical and Environmental Problems*, Szeged, Hungary, 2017.

[Palásti 2019] D. J. Palásti, Á. Bélteki, É. Kovács-Széles, A. Berlizov, G. Galbács, poster presentation WP-43, *European Winter Conference on Plasma Spectrochemistry*, Pau, France, 2019.

[Galbács 2019] G. Galbács, D. J. Palásti, A. Metzinger, É.-Kovács Széles, A. Berlizov, oral presentation FT-1, *10th Euro-Mediterranean Symposium on Laser-Induced Breakdown Spectroscopy*, Brno, Czech Republic, 2019.

ON-LINE AND OFF-LINE LIBS DETECTION OF NANOAEROSOLS GENERATED BY ELECTRICAL DISCHARGES

Ádám Bélteki[1], Tira Biros[1], Dávid J. Palásti[1,2], Lajos P. Villy[2,3], Bálint Leits[2,3], Albert Kéri[1,2], Attila Kohut[2,3], Éva Kovács-Széles[4], Tibor Ajtai[3], Zsolt Geretovszky[2,3], Gábor Galbács[1,2]*

[1]Department of Inorganic and Analytical Chemistry, University of Szeged, 6720 Szeged, Dóm sq. 7, Hungary
[2]Department of Materials Science, Interdisciplinary Excellence Centre, University of Szeged, 6720 Szeged, Dugonics sq. 13, Hungary
[3]Department of Optics and Quantum Electronics, University of Szeged, 6720 Szeged, Dóm sq. 9, Hungary
[4] Nuclear Security Department, Centre for Energy Research, 1121 Budapest, Konkoly-Thege Miklós way 29-33, Hungary
**e-mail: galbx@chem.u-szeged.hu*

1. INTRODUCTION

With the increase of the intensity of production and industrial use of engineered nanoparticles comes a growing need for spectroscopic techniques that are capable of monitoring the characteristics of nanoaerosols (nanoparticles distributed in a gaseous medium). Such measurements are equally needed for industrial process control purposes as well as for environmental and health-related studies.

Laser induced breakdown spectroscopy (LIBS) is one of the laser-based spectroscopy techniques available for aerosol analysis. The appeal of LIBS in this field is that it is a robust, easy-to-set-up technique that even can be applied remotely. As it has been demonstrated, it has the potential of providing particle quality and concentration data, if the particle size (mass concentration) is large enough [Diaz 2020, Palásti 2019]. Particles in the micron and sub-micron range has been successfully detected by LIBS, either by on-line or off-line sampling. However, studies in the LIBS literature are very scarce that attempted the detection of nanoaerosols.

In the present work, we investigated the performance of LIBS for the analysis of nanoparticles (NPs) generated by electrical discharges, namely a spark discharge generator (SDG) and an arc discharge generator (ADG). The reason behind choosing these particle sources is that these devices are more and more often considered for industrial scale nanoparticle production in recent years, due to their productivity, energy efficiency, versatility and particle purity [Buonapart-e 2016]. They are also good model aerosol sources, as the particle properties can be relatively easily controlled. We tested both the on-line and off-line methodologies, and worked with not only monometallic, but also binary particles. Collecting detailed compositional information about the produced binary particles can also shed light on some of the particle formation and electrode erosion processes in these discharge generators that are not yet fully understood.

2. EXPERIMENTAL

There are important differences between the operation of the two types of electrical discharge generators. The SDG employs a high voltage, high AC current, oscillating electrical discharge plasma to erode/evaporate the material of two electrodes, whereas the ADG work in the low voltage, low DC current mode and utilizes a molten pool work electrode and a refractory counter electrode. Both generators have an inert gas flowing through their chambers, which cools, quenches the electrode material vapors and helps to form nanoparticles via condensation and aggregation. A quartz/ceramic tube sintering furnace is typically used in these generators for the post-processing of the particles, which helps to obtain uniform size, compact particles. The operating parameters of our SDG and ADG systems can be seen in **Table 1**. In the listed ranges of operating parameters, the particle diameter was 30-40 nm and 80-150 nm for the SDG and ADG, respectively.

Parameter	SDG		ADG	
	monometallic	bimetallic	monometallic	bimetallic
Carrier gas	Ar	Ar	N_2	Ar
Gas flow rate	5 slm		10 slm	
Gas pressure	1015 mbar			
Electrode material	Au - Au	Co - Ag	Cu/W	12, 42, 77 m/m% Sn-Cu alloy/W
Electrode distance	2 mm		~2 mm	
Repetition rate	50 - 250 Hz	100 Hz	continuous	
Impedance	1 Ohm	1 – 9 Ohm	not controlled	
Peak current	~825 A	~165 A	20 – 35 A	30 A

Table 1. The operating parameters of the experimental SDG and ADG systems.

The metallic electrodes used were made of 99.99% purity materials (Kurt J. lesker Co., USA), whereas the Sn-Cu alloy feedstock was prepared from analytical purity materials. For off-line measurements, the particles were collected on a glass fiber filter (Whatman 1822-047 GF/C Glass Microfiber Filter, 1.2 μm pore size, 47 mm diameter), which was later cut to segments and affixed onto microscope slides using double-sided adhesive tape for LIBS analysis. Some filters were dissolved in high purity acids and subjected to ICP-MS analysis (using an Agilent 7700x instrument) in order to obtain reference compositional data. Reference aerosol data were collected using a scanning

mobility particle sizer (TSI, USA) and scanning electron microscopy (Hitachi S-4700, Japan). All gases used were 99.995% purity (Messer Hungarogáz).

LIBS measurements were carried out on an Applied Photonics LIBScan 25+ type portable instrument, using 1064 nm wavelength, 4 ns pulse length and 30 mJ pulse energy settings. In on-line experiments, the repetition rate of the plasma generating laser was set to a low value (ca. 0.25 Hz) thereby ensuring that the content of the chamber is completely renewed by the gas flow between laser shots. The LIBS plasma was observed via two fused silica collimating lenses implemented in two ports located on the sides of the ablation chamber (looking onto the same spot in the chamber in the horizontal direction, with 90° angle between the optical axes of the two lenses). The collected light was coupled into a two-channel fiber-optic CCD spectrometer (AvaSpec-FT2048, Avantes, NL) using solarization resistant optical fibers. The measurement chamber was mounted on a translation stage, which allowed bringing the laser focal spot inside the chamber in front of the light collection lenses. Gating of the spectral data collection was achieved by the internal electronics of the spectrometer, which was triggered by the laser power supply unit and continuously monitored on a digital storage oscilloscope (TDS1002, Tektronix, USA). The gate delay was set to 1 μs and gate width to 2 ms. The double-channel spectrometer allowed the recording of the plasma emission in the 344–888 nm spectral ranges, with resolutions of 0.09 nm and 0.4 nm, respectively.

3. RESULTS AND DISCUSSION

We were particularly interested in the measurement of three aerosol parameters: a.) qualitative detection of the particles, b.) estimation of the particle number concentration (PNC), c.) estimation of particle composition (for binary particles).

3.1. Qualitative detection of nanoparticles

Although we tested both the on-line and off-line sampling methodology and found that the on-line approach only worked with the ADG, for which the particle size and PNC was significantly higher. We found that the on-line detection can only be successful, if the particle mass concentration is above a certain threshold, the value of which depends on the quality of the particles as well as the setup of the LIBS setup. For the metallic particles studied here, this threshold is such that a minimum of 60-70 nm particle diameter and 10^6 cm^{-3} PNC is required.

The qualitative detection of nanoparticles is demonstrated by selected spectra shown in **Figure 1.**; all particles, namely Cu, Au, Sn-Cu, Ag-Co could be detected by LIBS. In the case of binary NPs, the detection of both component elements in all spectra indicated that alloy particles were formed and not alternating monometallic particles.

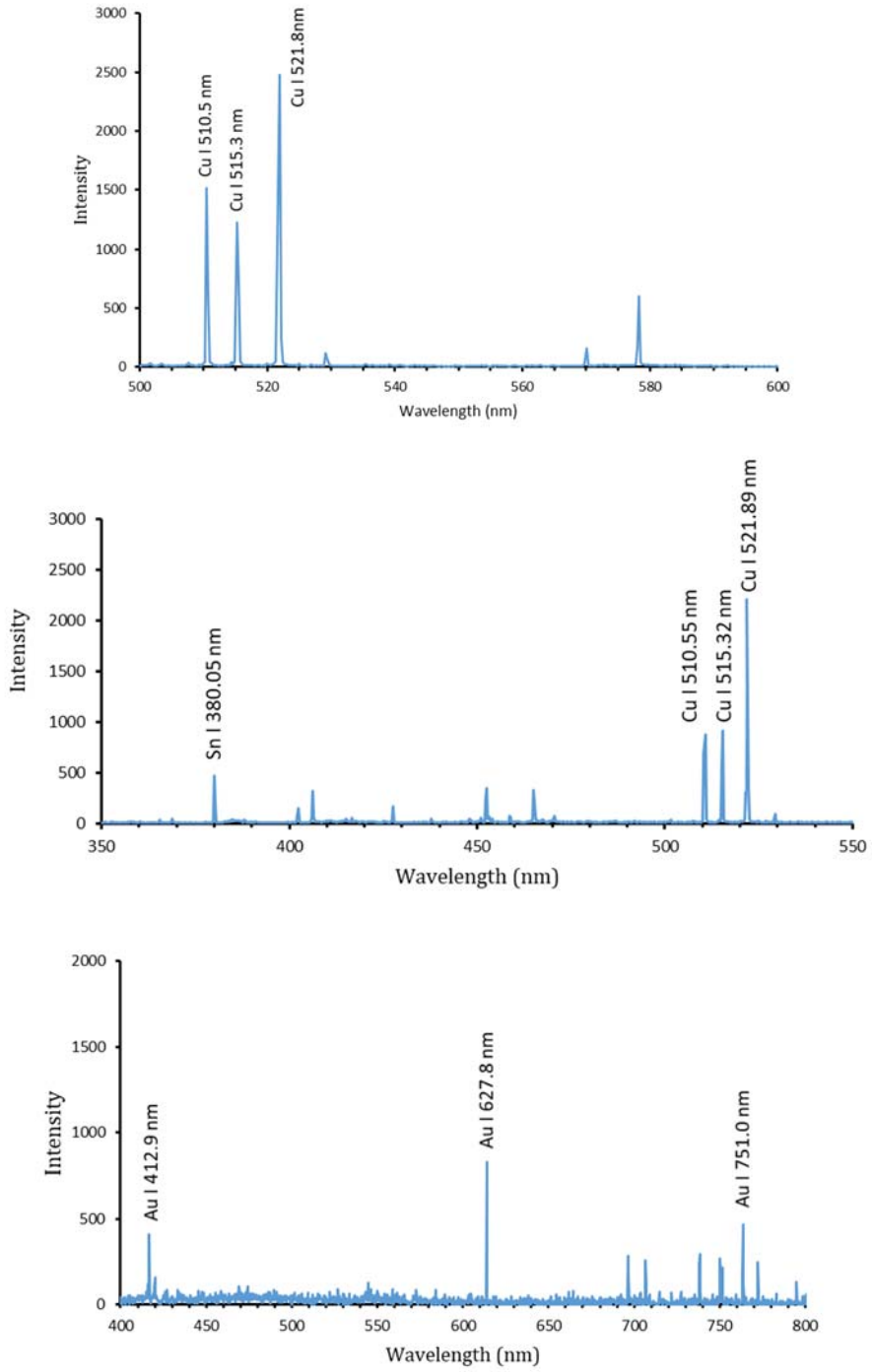

Figure 1. Selected LIBS spectra of some monometallic and binary nanoparticles studied. At the top: on-line detection with ADG; in the middle: on-line detection with ADG; at the bottom: off-line detection with SDG.

3.2. Estimation of the particle number concentration

In on-line mode, and by assuming a constant, calibrated ratio between the number of LIBS particle detection events and the particle number concentration, the latter can be principally estimated based on LIBS data. However, proportionality can be assumed only within a certain concentration range, which is limited at the bottom by the particle mass

concentration detection limit and at the top by a „saturation" of the detection (when the PNC is so high that all laser shots result in a detection). **Figure 2.** illustrates such a proportionality curve for a copper ADG aerosol, where the time-integrated copper signal is shown as a function of PNC. The high signal scatter is a characteristic of ADG generation which has an uneven aerosol mass concentration output due to the strong thermal convection in the discharge chamber. Nevertheless, a reasonable estimate of PNC can be obtained for process control purposes.

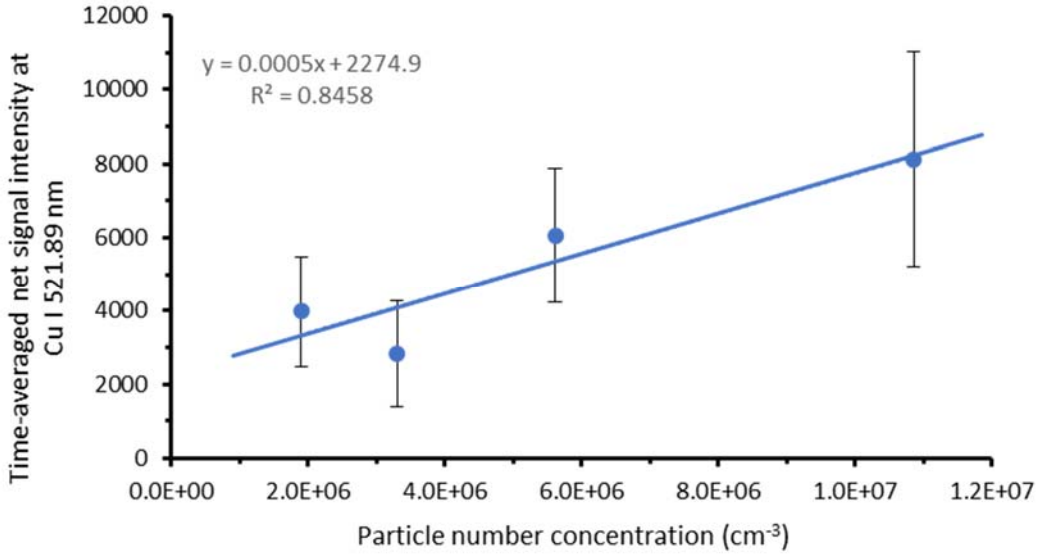

Figure 2. The correlation of the time integrated particle-specific on-line LIBS signal with the particle number concentration (ADG).

The off-line particle detection approach also produces a calibration plot, which shows proportionality between the PNC and the LIBS signal of the particle specific analyte signal, however the proportionality is not necessarily linear. As it is seen in **Figure 3.**, the plot shows a concave character and can be fitted reasonably well with an exponential function. This feature is related to the saturation of the filter on which the particles were collected. In the very low PNC range, the signal linearity holds – as long as there is a sufficient amount of analyte mass in the laser focal spot – as basically it is the filter material which gets ablated, along with some occasional particles. However, as the PNC increases, the particles will start to pile up on the filter (deposited particles will also decrease the effective pore size) and the laser ablation will mostly involve particle material. The LIBS signal in this regime will be determined by the packing density of the particles and above a certain thickness of deposited particles, the correlation between the signal and PNC will not hold. In the range shown in **Figure 3.**, the linear proportionality holds up to about $8.6 \cdot 10^5$ – $1.3 \cdot 10^6$, beyond that the signal increases stronger (filter saturation starts)

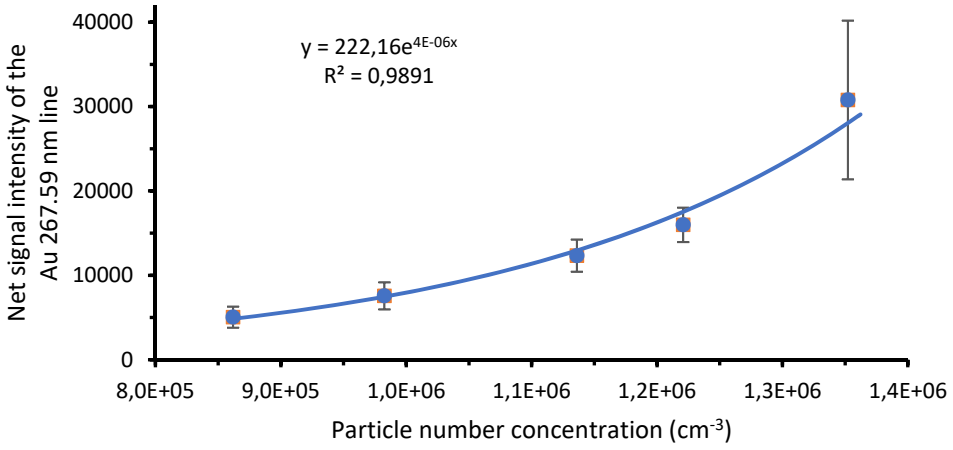

Figure 3. The correlation of the particle specific off-line LIBS signal with the particle number concentration (SDG).

3.3. Estimation of particle composition

In principle, binary particles (e.g. alloys) can be relatively easily produced by electrical discharge generators. For this to be achieved one needs to use different electrode materials (made of the component metals of the alloy) in the SDG, and mixture of metal powder (or alloy molten pool) in the ADG. LIBS in these cases can potentially provide elemental composition data about the particles.

We tested the SDG with a combination of Ag and Co electrodes. The particles were collected on a filter (off-line LIBS) and their reference composition was determined by ICP-MS analysis. As it can be seen in **Figure 4.**, the ratio of the detected LIBS elemental signals correlated reasonably well with the real composition. The signal scatter is large, probably due to the „looseness" of particles on the filter.

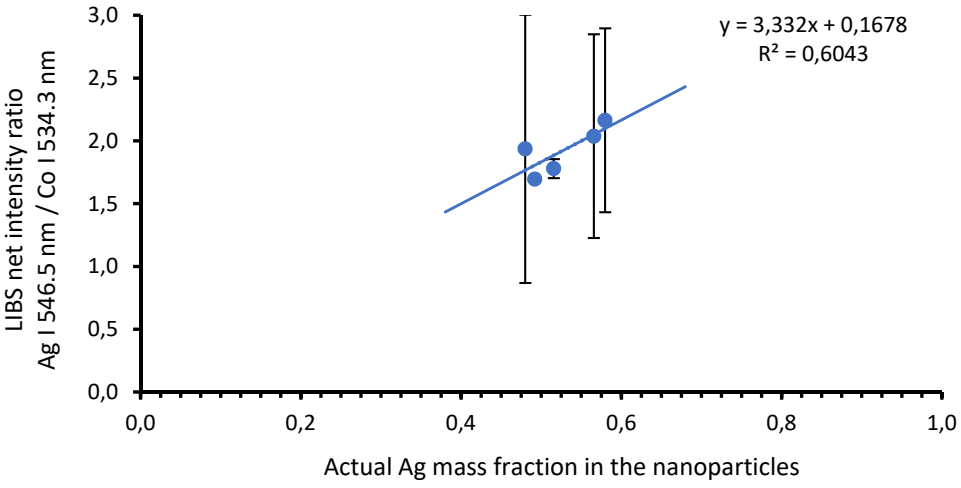

Figure 4. The correlation of the actual (determined by ICP-MS) and off-line LIBS detected particle composition of Ag-Co binary nanoparticles generated in an SDG.

In the on-line ADG experiments, we used a Sn-Cu alloy feedstock (with 12%, 42% and 77% mass fractions of Sn). As can be seen in **Figure 5.**, we found a linear proportionality between the composition of the working electrode and the detected particle composition. This is an important finding, as according to our knowledge, no previous results can be found in the literature on alloy particle production by an ADG. The results also suggest that the mixing in the molten pool fairly efficient and that there is no fractionation of the two metals during NP production, but this still needs to be checked by converting the LIBS intensity data to concentrations.

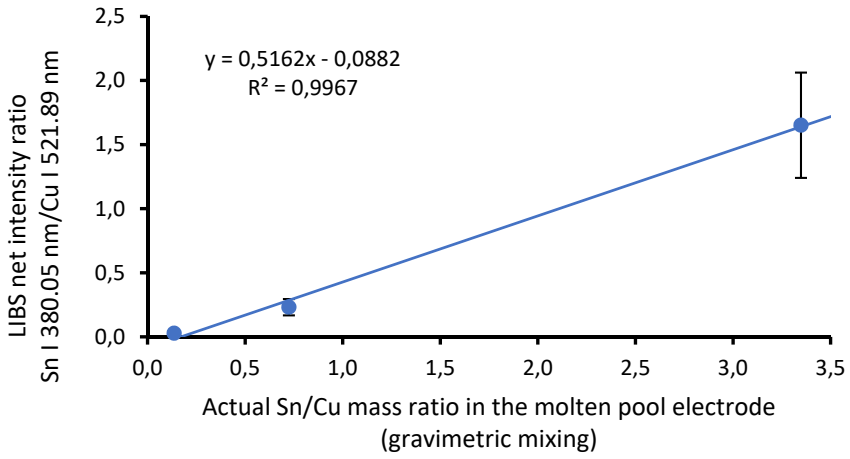

Figure 5. The correlation of the actual (based on gravimetric mixing) and on-line LIBS detected particle composition of Sn-Cu binary nanoparticles generated in an ADG.

4. CONCLUSIONS

Our experiments successfully demonstrated that the on-line and off-line LIBS analysis of nano aerosols is feasible. Electrical discharge generators were employed for the controllable production of the aerosols. It has been shown that particle detection, estimation of particle number concentrations and particle compositions (in the case of binary particles) are all possible. These preliminary results indicate that LIBS has a great potential for the monitoring of the operation of electrical discharge generators, but potentially also other nano aerosol sources.

5. ACKNOWLEDGEMENTS

The authors gratefully acknowledge the financial support from various sources including the National Research, Development and Innovation Office (through projects No. K_129063, EFOP-3.6.2-16-2017-00005 and TKP 2020 Thematic Excellence Programme 2020) of Hungary.

6. REFERENCES

[Diaz 2020] D. Diaz, D. W. Hahn, U. Panne: LIBS for aerosol analysis (Chapter 22) in: Laser-induced breakdown spectroscopy (ed.: J. P. Singh, S. N. Thakur), *Elsevier*, 2020.

[Palásti 2019] D. J. Palásti, A. Metzinger, T. Ajtai, Z. Bozóki, B. Hopp, É. Kovács-Széles, G. Galbács, *Spectrochim. Acta B*, 153 (2019) 34.

[Buonapart-e 2016] https://cordis.europa.eu/project/id/280765/reporting

VENDOR MATERIALS

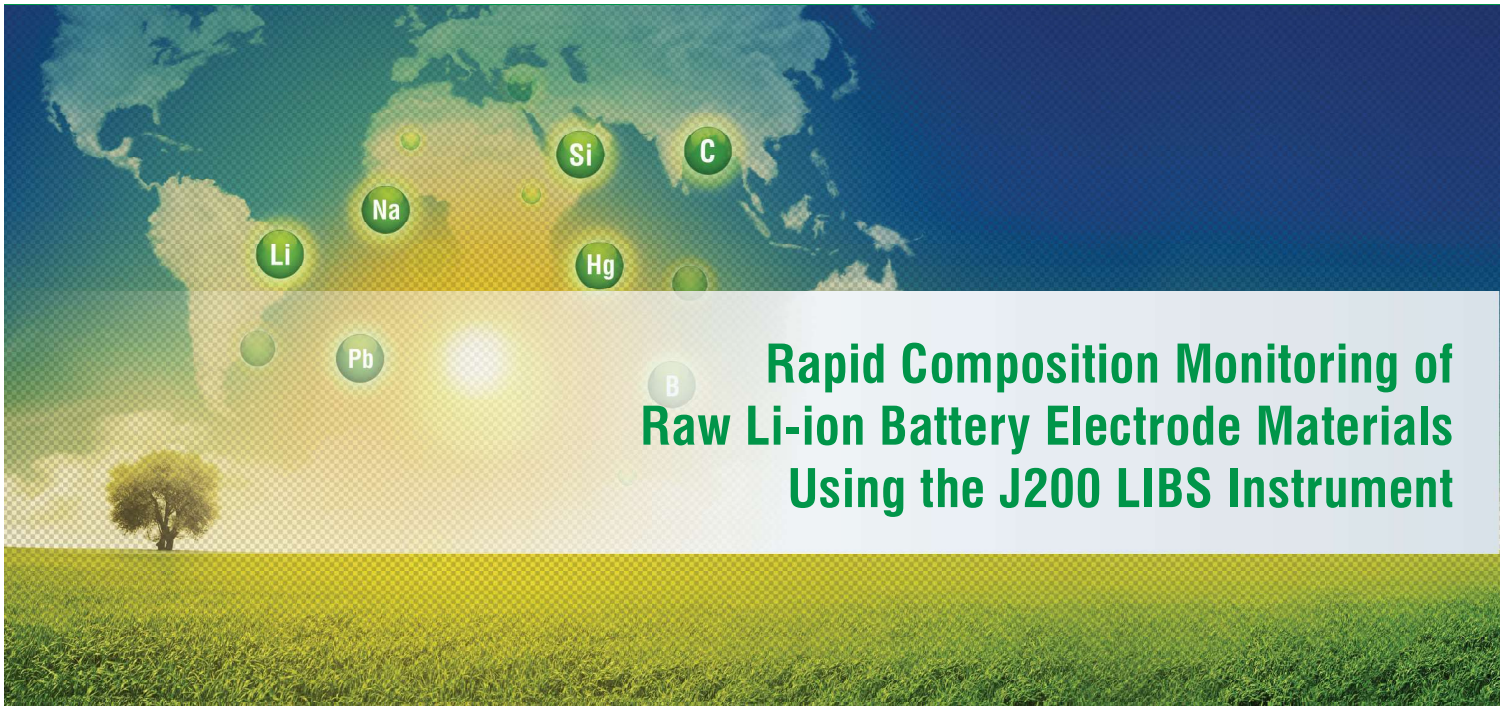

Rapid Composition Monitoring of Raw Li-ion Battery Electrode Materials Using the J200 LIBS Instrument

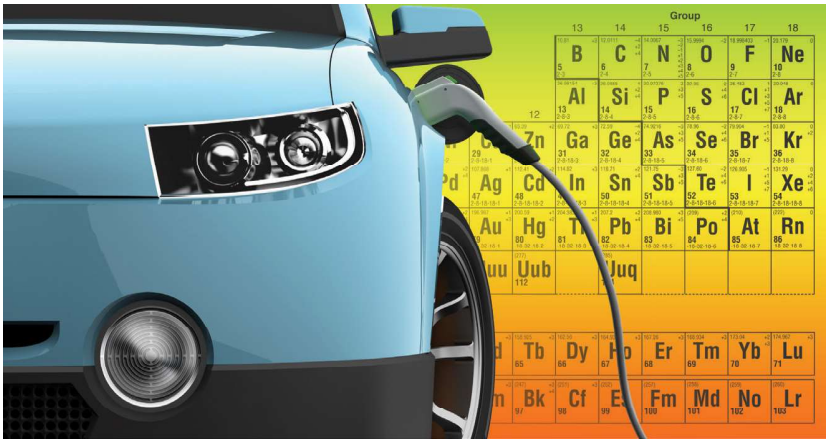

Introduction

Since introduction of the first commercial Li-Ion battery by Sony in the early 1990's, the demand for the Li-ion battery has steadily increased due to growing number of consumer electronic devices that rely on Li-ion batteries for power. In recent years, the demand for the Li-ion battery has soared as its use has exploded in electric and hybrid electric vehicle power applications. The performance specification for the Li-ion battery is significantly more stringent for automotive applications with respect to power density, energy density, cycle life, and reliability. Many electrode chemistries are being assessed to improve Li-ion battery performance.

Maintaining accurate chemistry in the fabricated battery cathode and anode is critical in optimizing battery performance. Monitoring elemental composition of incoming raw materials for the battery electrodes is a vital quality control step to ensure proper battery chemistry in the final products. The techniques that are typically used to analyze these raw materials, such as ICP-OES, are solution-based and require the samples to be digested. These techniques deliver accurate and reliable results, but digestions take time, creates hazardous waste, and may not be suitable for rapid quality control of incoming raw materials.

Monitoring elemental composition of incoming raw materials for battery electrodes is a vital quality control step to ensure proper battery chemistry in final products.

Laser Induced Breakdown Spectroscopy (LIBS) provides real-time analysis of the raw materials for the Li-ion battery electrode in both powder and pressed pellet form. This provides advantages such as, little to no sample preparation, high analysis throughput,

and lower operation cost due to no hazardous waste produced, lower power requirements, and no high vacuum equipment being needed for analysis.

In this work, we highlight the use of LIBS to analyze the bulk composition of raw powders used to fabricate Lithium Nickel Manganese Cobalt Oxide ($LiNiMnCoO_2$) cathodes using Applied Spectra's J200 LIBS instrument. Based on the advanced multivariate calibration, LIBS provides both accurate and precise analytical performance for measured samples with respect to provided ICP-OES cross-reference values.

Operating Parameters

Applied Spectra Inc.'s J200 LIBS Instrument

- 266 nm Nd:YAG laser (ns) and broadband spectrometer controlled using Applied Spectra Axiom Software
- Flex sample chamber with helium or argon gas flow
- Cathode raw materials pressed into pellets
- Laser sampling grid of 12 locations
- LIBS data analyzed with Applied Spectra Data Analysis Software package

Applied Spectra Inc.'s J200 LIBS Instrument

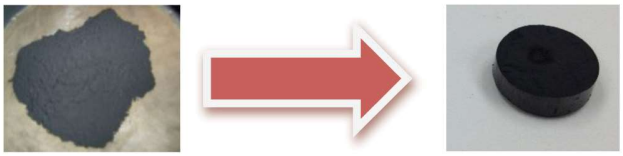

Figure 1. Raw Li-ion Battery materials pressed into pellet form.

Sample Analysis

Raw cathode materials were pressed into pellets and analyzed using the J200 LIBS instrument with a broadband spectrometer. Figure 2 displays a typical spectrum from the raw cathode material.

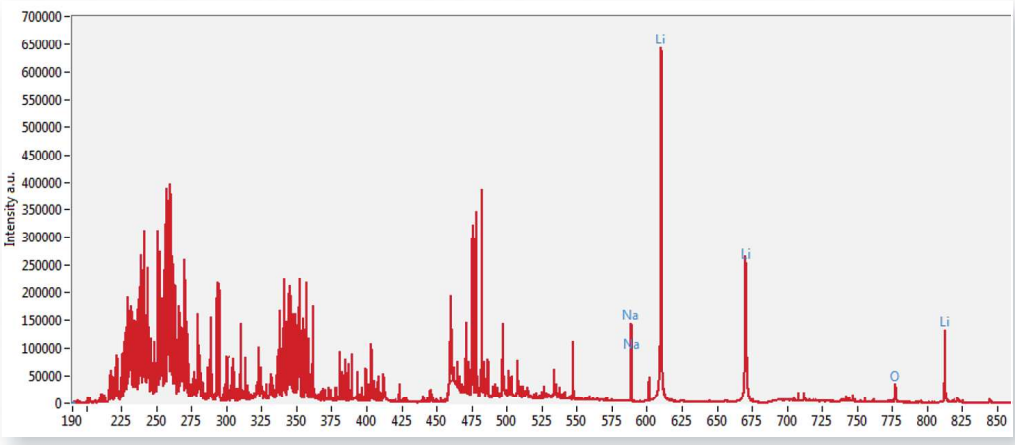

Figure 2. Full LIBS spectrum acquired from the J200 LIBS instrument for raw cathode material.

Applied Spectra, Inc.
46665 Fremont Blvd.
Fremont, CA 94538

Telephone: + 1 510.657.7679
Fax: + 1 510.657.7074
Sales Support: + 1 510.657.7679 x410

LIBS spectra can be complex in nature if the user doesn't have a proper database to help assign atomic lines. Figure 3 shows a few of the atomic lines that were easily identified using the ASI *TruLIBS* database. The analytes of interest for this study were labeled and displayed in Figs. 2 and 3. As seen from the figures, LIBS emission lines associated with main composition of the raw $LiNiMnCoO_2$ cathode material such as Li, Ni, Mn, Co, and O were effectively captured by the J200 LIBS instrument and can be used to quantify the concentration of these elements. Furthermore, the figures show other contaminants in the raw powders such as Fe, Ca and Na that can be also quickly screened. Five raw cathode materials were analyzed to develop the best multivariate calibration method for raw cathode materials. Traditional univariate calibration curves were also assessed using the main atomic line for each analyte in comparison to multivariate calibration curves that utilize each data point from the entire spectrum of each sample.

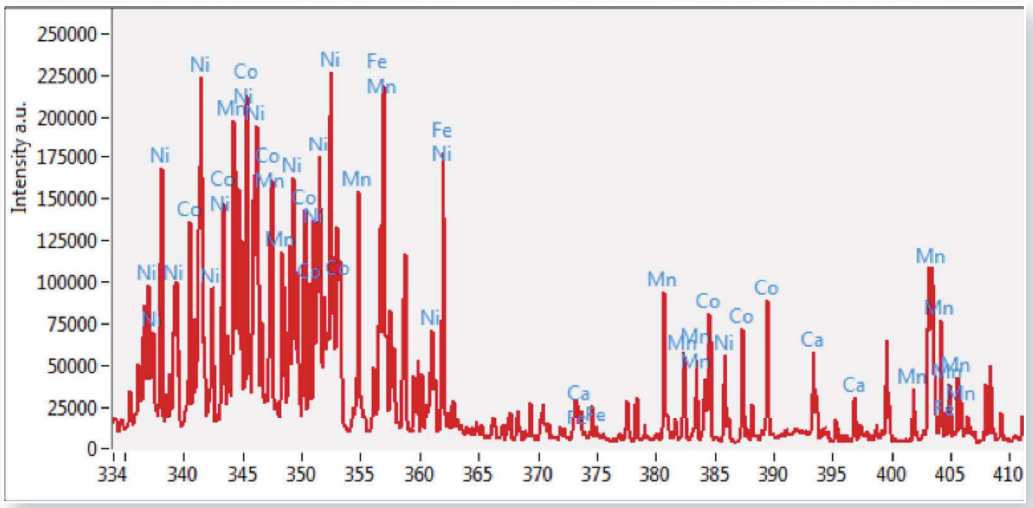

Figure 3. Displays a smaller section of the full LIBS spectrum in order to visually view the Ni, Mn, Co, and Fe atomic lines.

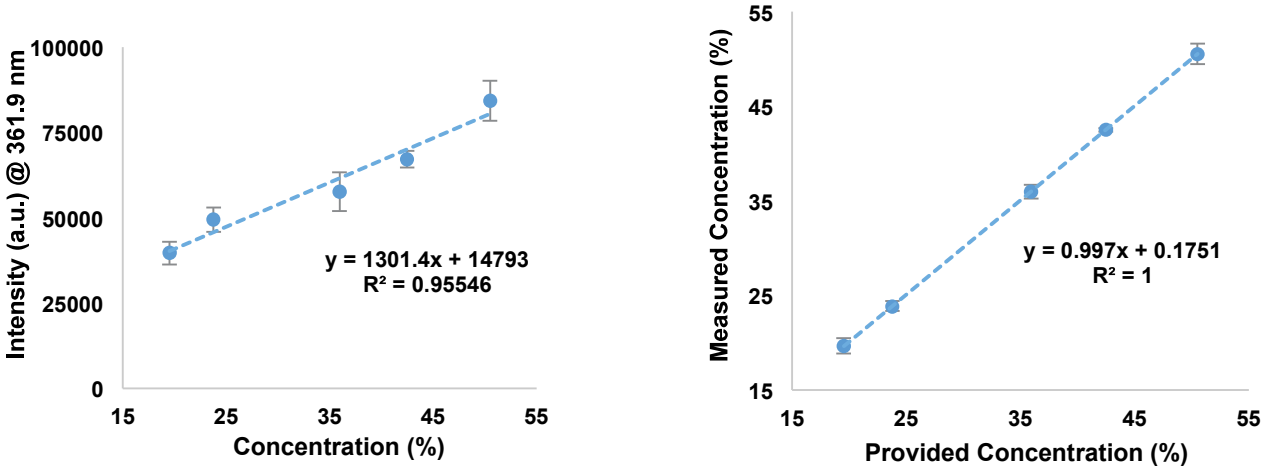

Figure 4. Traditional calibration curve for nickel (integration of Ni peak at 361.9 nm) on the **Left** and multivariate calibration curve for nickel (uses entire spectrum) on the Right

Applied Spectra, Inc.
46665 Fremont Blvd.
Fremont, CA 94538
Telephone: + 1 510.657.7679
Fax: + 1 510.657.7074
Sales Support: + 1 510.657.7679 x410

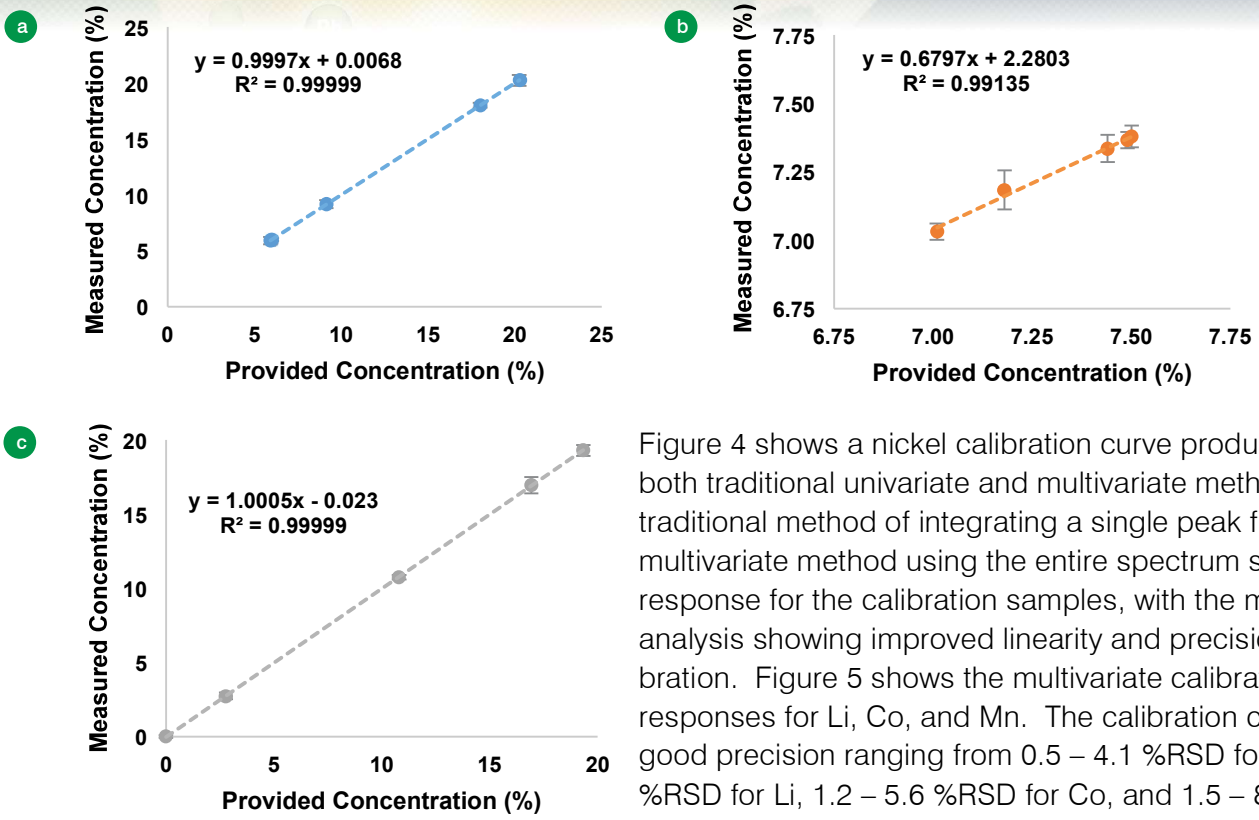

Figure 5. Multivariate calibration curve for **a)** Li, **b)** Co, and **c)** Mn.

Figure 4 shows a nickel calibration curve produced using both traditional univariate and multivariate methods. The traditional method of integrating a single peak for Ni and the multivariate method using the entire spectrum show a linear response for the calibration samples, with the multivariate analysis showing improved linearity and precision of the calibration. Figure 5 shows the multivariate calibration curves responses for Li, Co, and Mn. The calibration curves have good precision ranging from 0.5 – 4.1 %RSD for Ni, 0.4 – 1.0 %RSD for Li, 1.2 – 5.6 %RSD for Co, and 1.5 – 8.1 %RSD for Mn. Two reference samples, also measured by ICP-OES, were tested for Li, Ni, Co, and Mn concentration based on the multivariate calibration aforementioned. Table 1 shows the accuracy and precision of the method for Li, Ni, Co, and Mn. The results show very good precision (≤ 2 % RSDs) and accuracy that is < 3 % Bias for all but one element, which was < 8 % Bias (Li for reference sample 1).

Table 1. Accuracy and precision values of the multivariate calibration method results for two raw material samples.

Reference Sample	Li		Ni		Co		Mn	
	Wt. %	% Bias	Wt. %	% Bias	Wt. %	% Bias	Wt. %	% Bias
1	7.51 ± 0.02	7.9	23.9 ± 0.5	0.5	17.9 ± 0.4	-1.3	17.5 ± 0.3	-1.1
2	7.54 ± 0.04	2.9	42.1 ± 0.2	-0.9	6.07 ± 0.12	1.3	11.1 ± 0.2	2.6

Conclusion

Applied Spectra's J200 LIBS instrument provided quick and effective measurements for understanding the composition of raw cathode materials. In addtion, multivariate analysis showed the ability to remove matrix effects, provided linear calibration curves, and displayed good accuracy and precision in the analyzed samples. This proof of concept study can be easily transferred to a laboratory or factory setting.

Applied Spectra, Inc.
46665 Fremont Blvd.
Fremont, CA 94538

Telephone: + 1 510.657.7679
Fax: + 1 510.657.7074
Sales Support: + 1 510.657.7679 x410

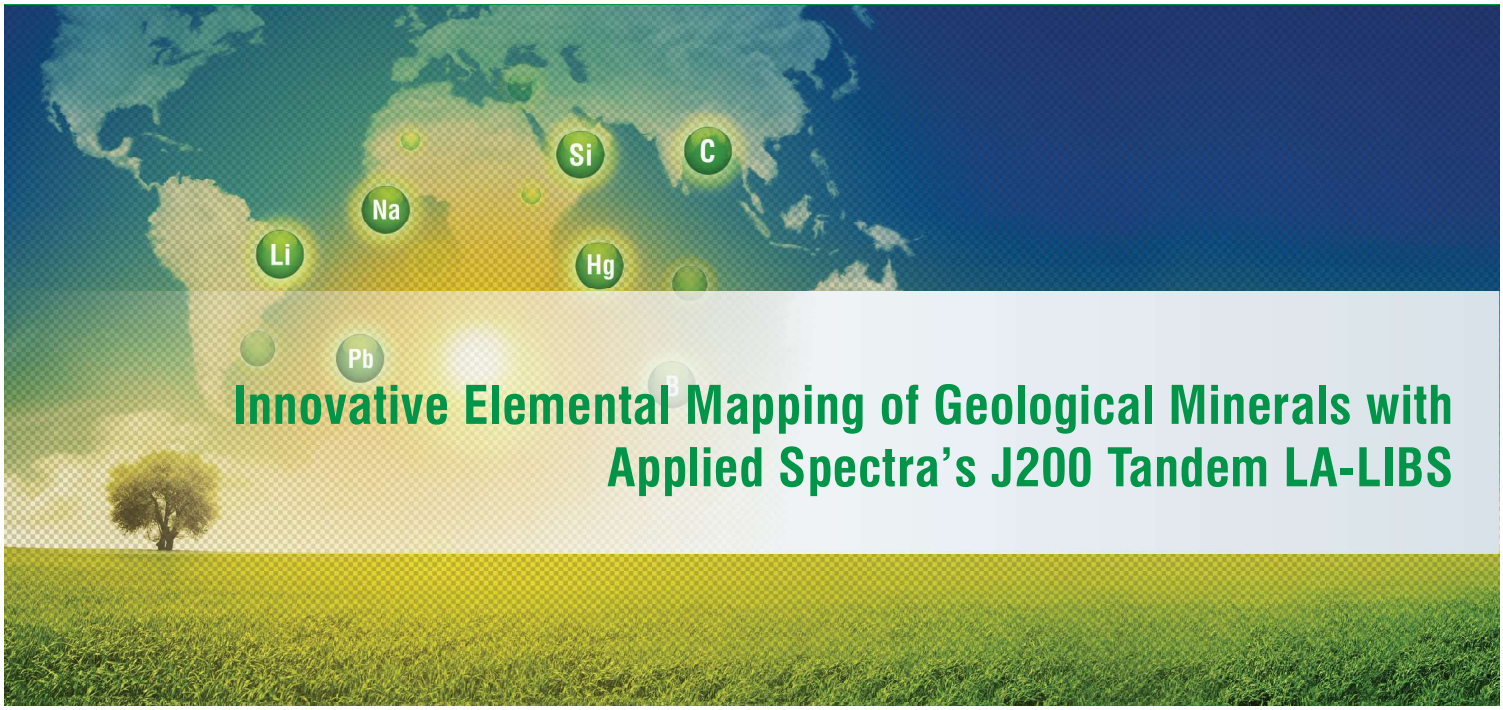

Innovative Elemental Mapping of Geological Minerals with Applied Spectra's J200 Tandem LA-LIBS

Summary

The J200 Tandem LA – LIBS instrument from Applied Spectra, Inc. provides the unique capability of combining the analytical benefits of both LA-ICP-MS (Laser Ablation-Inductively Coupled Plasma-Mass Spectrometry) and LIBS (Laser Induced Breakdown Spectroscopy). Specifically, LIBS can be used for the analysis of H – Pu, which includes non-metals such as H, N, O, and halogens that are difficult or impossible to analyze by a conventional ICP-MS instrument. When coupled with a sensitive ICP-MS instrument, the J200 can perform LA-ICP-MS measurements focusing on trace elemental and isotopic ratio compositions. This tandem instrument, in combination with a Bruker Aurora Elite ICP-MS, expands the dynamic range of analysis from sub-ppb levels with LA-ICP-MS, to % levels with LIBS, while also increasing the elemental coverage to typical ICP-MS elements and lighter, organic, and halogen elements such as H, Ar, He, O, and F detection with LIBS.

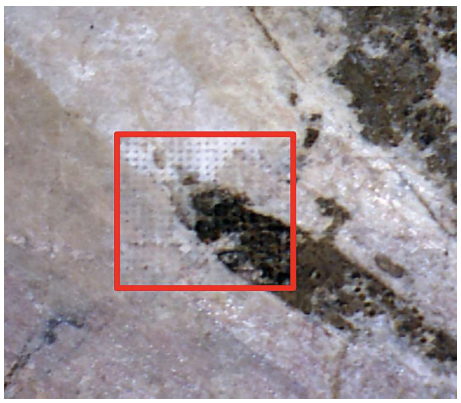

Figure 1. Optical Image of bastnäsite mineral used for LIBS analysis. Tan region = bastnäsite and white region = barite.

To understand the capabilities of the J200 Tandem LA – LIBS instrument in combination with ICP-MS, a rare earth element (REE)-rich mineral was analyzed and the elemental composition over a 16 mm^2 area was mapped using contour plots. The REE-rich sample contains bastnäsite ((Ce, La)CO_3F) and barite ($BaSO_4$), which have very distinct regions as seen in Figure 1.

Operating Parameters

- 213 nm Nd:YAG laser (ns) and an ICCD detector controlled using Applied Spectra Axiom Software
- 85 μm crater diameter (spot size)
- Flex sample chamber with helium gas flow
- Laser sampling grid with a total of 400 locations over a 4 mm x 4 mm area using 50 laser pulses per location
- Applied Spectra Data Analysis Software package

Applied Spectra Inc.'s J200 Tandem LA - LIBS Instrument

Bruker Aurora Elite ICP-MS

- Time resolved "high sensitivity mode" detection
- Peak hopping: $^{49}Ti^+$, $^{65}Cu^+$, $^{66}Zn^+$, $^{137}Ba^+$, $^{139}La^+$, $^{140}Ce^+$, $^{208}Pb^+$, $^{232}Th^+$, and $^{238}U^+$
- Synchronized communication triggering with the J200 Tandem LA – LIBS instrument

Bruker Aurora Elite ICP-MS

Sample Analysis

Rare Earth Element (REE)-Rich Mineral. The mineral sample was used to assess the ability of the J200 tandem instrument in combination with the Bruker Aurora Elite ICP-MS. A 16 mm^2 area was analyzed using a laser spot size of 85 μm (diameter) and spacing of 115 μm between locations.

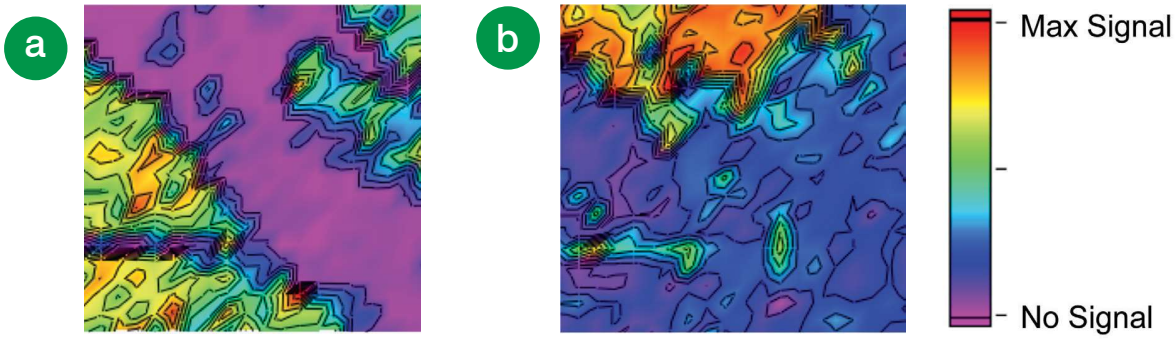

Figure 2. a) Fluorine and **b)** oxygen LIBS intensity maps. The data is a result of 50 laser pulses per location, 85 μm spot size, and 400 locations over a 4 mm x 4 mm area.

Applied Spectra, Inc.
46665 Fremont Blvd.
Fremont, CA 94538

Telephone: + 1 510.657.7679
Fax: + 1 510.657.7074
Sales Support: + 1 510.657.7679 x410

APPLIED SPECTRA
Transforming the way the world does chemistry

Figure 2 displays the LIBS intensity map for F 685.6 nm and O 700.2 nm from the sample. Based on the optical image from Figure 1, the white region of the sample is richer with oxygen than the other regions based on the contour plot in Figure 2. The tan region is richer with fluorine suggesting that these tan areas of the sample are bastnäsite.

The LIBS intensity maps only tell part of the story. Using the unique tandem feature of the J200, LA-ICP-MS data can be obtained simultaneously to complement the LIBS data. Figure 3 displays the intensity maps for the elements that are typically found in barite and bastnäsite minerals. LA-ICP-MS and LIBS together show that the white region is rich in barium and oxygen (aforementioned), which corresponds with barite. The tan region of the sample is high in lanthanum, cerium, and fluorine (aforementioned), which corresponds with the bastnäsite. These contour plots match nicely with the optical image shown in Figure 1.

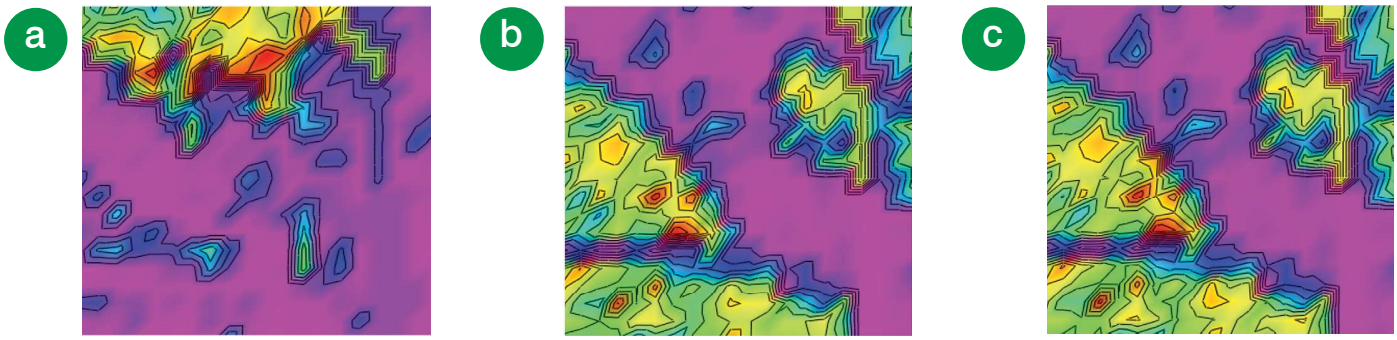

Figure 3. Major elements of the REE-rich sample, **a)** barium, **b)** lanthanum, and **c)** cerium LA-ICP-MS intensity maps.

Figure 4 displays the intensity maps of trace elements from the 16 mm^2 area of the REE-rich mineral sample analyzed. These plots display results from intensities of lead, thorium, uranium, titanium, cobalt, and copper (these elements are typically < 0.1 wt. %). Titanium and copper were found to be mainly associated with the barite mineral (white region). Lead and cobalt were associated with the brown region of the sample. Uranium and thorium were only associated with the bastnäsite. The trace elements detected in this sample match current literature on these types of REE-rich mineral samples.

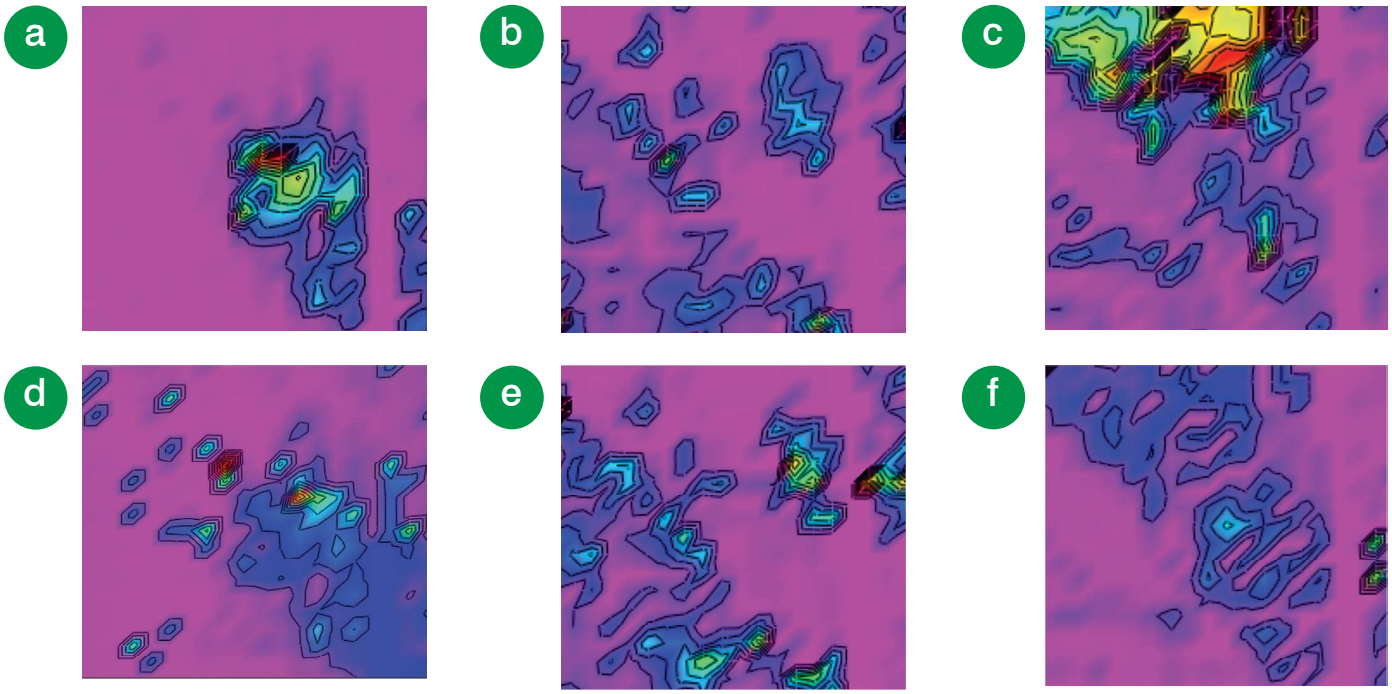

Figure 4. Trace elements of the bastnäsite mineral, **a)** lead, **b)** thorium, **c)** titanium, **d)** cobalt, **e)** uranium, and **f)** copper LA-ICP-MS intensity maps.

Conclusion

LIBS was demonstrated as a means for detecting fluorine and oxygen in REE-rich mineral samples. These are analytes that are difficult or impossible to detect through other atomic spectroscopy techniques. Using the J200 tandem feature to acquire the LIBS data while interfacing the insturment with a sensitive ICP-MS enabled more complete elemental mapping of the investigated mineral. Elemental mapping of the sample using the data analysis software from Applied Spectra allowed for easy integration of the LIBS and LA data to create contour plots as shown in the aforementioned sections. The high sensitivity of the Bruker Aurora Elite ICP-MS was ideal for trace level elemental and isotopic mapping analysis, since LA-ICP-MS often involves very small quantity of sampled mass, especially when high spatial resolution is desired.

Acknowledgements

Applied Spectra would like to thank Bruker for the collaboration and for providing us with an Aurora Elite ICP-MS instrument. Also, we would like to thank the Special Technologies Laboratory for supplying the bastnäsite mineral for testing.

Quantel laser
BY LUMIBIRD

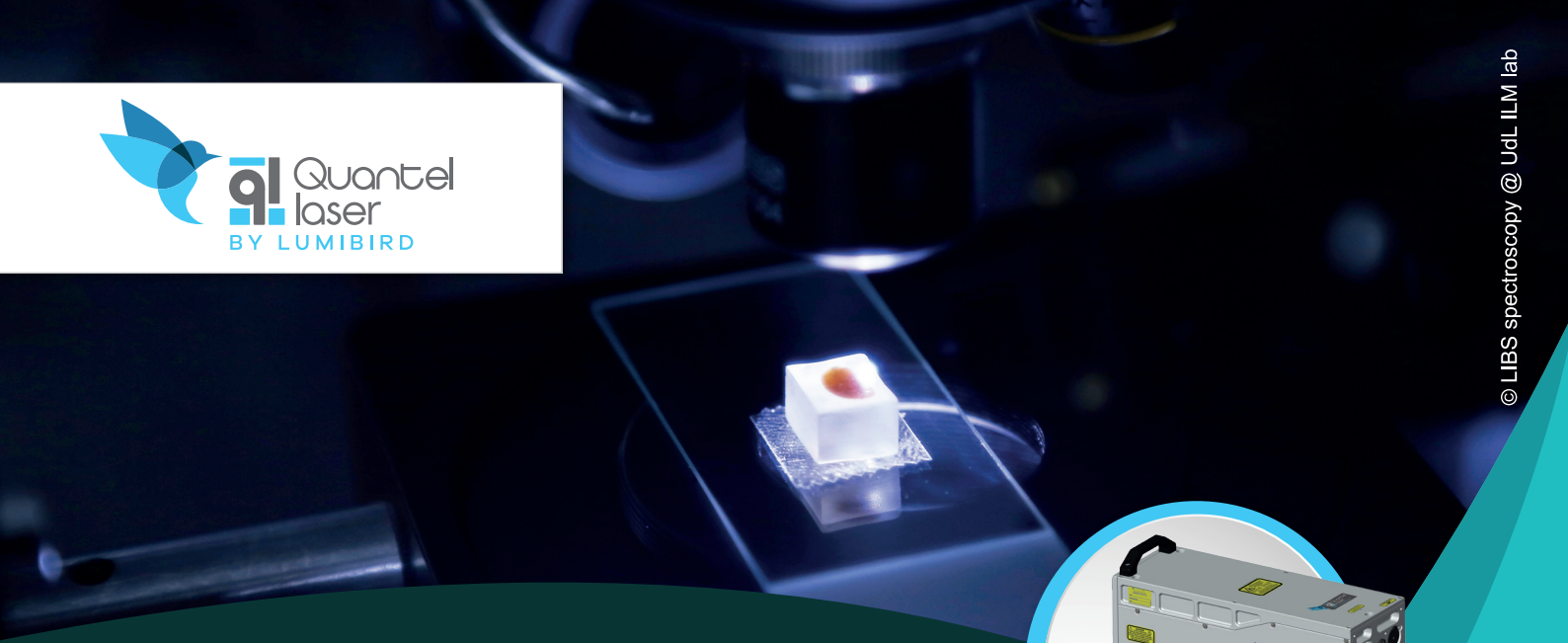

© LIBS spectroscopy @ UdL ILM lab

Q-SMART & ULTRA
Flashlamp-pumped
Nd:YAG

MERION
High power
diode-pumped
Nd:YAG

FALCON & VIRON
Compact diode-pumped
Nd:YAG

PULSED SOLID-STATE LASERS
FOR LIBS APPLICATIONS

- 1064, 532, 355, 266 nm and 1.57 µm available to adapt to all materials
- Portable and rugged lasers for easy integration in LIBS equipment
- High peak power density for facilitating plasma ignition
- Repetition rates from Hz to hundreds of Hz to optimize speed of data acquisition

For more information,
please contact us :
quantel@quantel-laser.com
or visit our web site
www.quantel-laser.com

LUMIBIRD
MORE THAN LASERS

THE SPECIALIST
IN LASER TECHNOLOGIES
www.lumibird.com

Ocean Insight

Application Note

KEYWORDS

- Soils
- Nitrogen, phosphorous and potassium
- Machine learning

TECHNIQUES

- Laser-induced breakdown spectroscopy

APPLICATIONS

- Soil health
- Heavy metals analysis
- Precision agriculture

LIBS for Soil Measurements: Progress and Potential

By Dr. Steve Buckley, Vice President, Product Development and Engineering

Laser-Induced Breakdown Spectroscopy (LIBS) has been investigated for soil measurements for over 20 years. Initial work was largely focused on detection of toxic metals in soils for environmental remediation, while recent work has expanded to include soil nutrients. In this article we discuss some of the most recent work in the context of other methods for soil analysis, and point to future directions and potential for LIBS as a tool for precision agriculture.

I'm always on the hunt for "killer applications" for laser-based spectroscopy, and one of my favorite emerging methods is LIBS. In recent years, LIBS applications have blossomed in diverse areas such as recycling, mining, and metals measurements, among others. Some commonalities among successful applications play to LIBS' unique strengths: optional sample preparation, stand-off detection, mobility/portability, speed, and sensitive light element detection. Although, unlike ICP-MS and some other elemental analysis methods, there is a large "matrix effect" for LIBS that changes the elemental emission based on the underlying material (due to differences in ablation and in-plasma chemistry), we are learning to use analytical methods and machine learning to correct for these changes with sufficient calibration. We've reported earlier that

machine learning methods can be used with LIBS and other spectroscopies to derive material properties, beyond the atomic emission that is the fundamental output of LIBS.[1]

In the five years since the last time we covered applications in soil analysis, a great deal of progress has been made.[2] Some of the progress is around hardware, with compact and portable lasers and spectrometers becoming more available and capable. Another measure of progress has been made due to the proliferation of machine learning tools, which make data analysis both more powerful and more available. We'll touch on both in this article. First, what makes soil analysis a compelling application?

Why Soil Analysis?

Soil analysis has been practiced for more than a century. In his 1960 article "History and Development of Soil Testing," Anderson chronicles the advances in technology through that period, focusing primarily on phosphorous testing, but also considering potassium and nitrogen.[3] He details methods developed for accurate extraction in a variety of soil types, and early evidence (as far back as 1890) of the relationship between soil nutrients and crop yield.

Around the same time, in 1957, David Rice Gardner submitted his Ph.D. thesis to Harvard University, entitled "The National Cooperative Soil Survey of the United States."[4] This was one of the first comprehensive surveys of soil science widely available to agricultural researchers. The post-World War II U.S. economy allowed a dramatic expansion of agricultural extension services at both the federal and state level. An explosion of interest in soil science, as well as herbicides, insecticides, and more productive and disease-resistant strains of crops, have led to dramatic increases in agricultural productivity from the mid-1950s through present day. An example of this is shown in **Figure 1**.

Naturally, soil analysis has evolved since 1960. Common practice over the past decade has been to collect samples in sub-sections of a field. Fifteen to 20 individual samples are collected from random places in a field sub-section of fewer than 20 acres. The soil from that sub-section is mixed. Tests report the pH level in the soil; the plant-available N, P, and K concentrations; Mg, Ca, and in some cases the percent organic matter in the soil; and trace metals. Numerous methods are used in soil testing labs, from colorimetric methods to ICP-MS.

Figure 1: Average corn yields in the United States, from Our World in Data, unmodified.[5]

Recent trends in precision agriculture are for increasingly spatially-precise measurements of plant and soil health, more frequently to provide increasingly localized irrigation, pest control, and fertilization. Rather than a single measurement for a field or even for a 20-acre subplot, many local measurements are performed, perhaps

supplemented by multispectral or hyperspectral imaging to assess plant health. These measurements feed into geospatial information systems on modern tractors and drip irrigation systems, all designed to provide the correct amount of water, pesticides, and nutrients to each part of the field.

LIBS for Soil Monitoring

Much of the early work in LIBS analysis of soils was focused around the detection of trace and heavy metals in soils.[6-7] This followed from investments by the U.S. Department of Defense and U.S. Department of Energy exploring the use of LIBS for toxic metal detection in hazardous waste incinerators, in which the author was one of the participants. This application proved difficult because of a mismatch of detection limit requirements and a lack of analytical precision. For most toxic metals, the LIBS detection limit is between 1-20 ppm in a soil matrix, which is typically at least an order of magnitude higher than the required regulatory detection limit in soils. The changing (and unknown) matrix of soil at each site, and variable grain size of the soil were also cited as potential issues for the measurement.

Over time, applications of LIBS for soil analysis have shifted toward analysis of higher-concentration elements, such as total carbon, as well as nitrogen, phosphorous, and potassium (referred to as NPK), magnesium, and calcium. These elements are at much higher concentration levels in soil than trace toxic metals and are widely used in agronomy for measurement of soil health.

A theme of the more recent work on soil health using LIBS involves classification of the type of soil first, followed by application of a matrix-appropriate calibration. As an example of the ability to positively determine soil type, Yu and coworkers reported in 2016 on the use of soft independent modeling of class analogy (SIMCA) and least-squares support vector machine (LS-SVM) to discriminate between soil types.[8] Seven primary emission lines from Al, Fe, Mg, Ca, Na, K, and Si were selected and used by the chemometric methods to predict soil type. Work with both algorithms revealed that SIMCA had a 90% correct classification rate, while LS-SVM had a 100% correct rate of classification with the training data. Following this, the trained LS-SVM model was applied to a set of eight unknown soil samples, and achieved nearly 100% discrimination. For visualization, **Figure 2** illustrates the scores plot of the first three principal components of a PCA model on the unknown soil spectra.

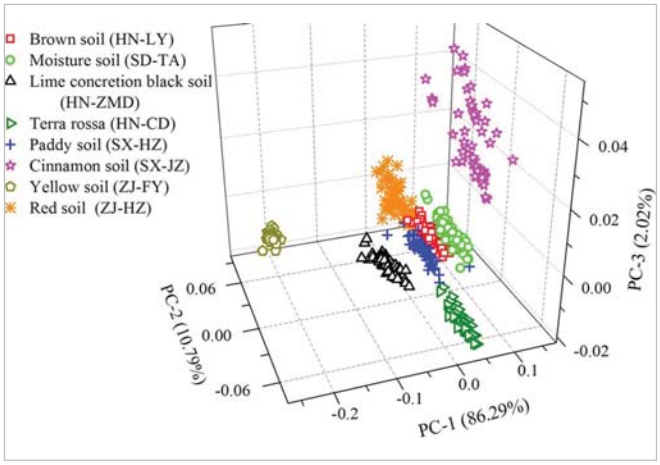

Figure 2: The scores plot from the first three principal components of PCA applied to eight unknown soil samples from different regions of China. From [8], shared under the Creative Commons Attribution 4.0 International License.

This classification work was recently extended by a group from the Institute of Soil Science of the

Chinese Academy of Sciences in Nanjing, P.R.C.[9] They used LIBS along with partial least squares regression, to predict some soil properties, pH, cation exchange capacity (CEC), and soil organic matter (SOM), as well as concentrations of total nitrogen, total phosphorus, total potassium, available phosphorous, and available potassium. The soil property measurements illustrate the ability of LIBS to measure more than simply elemental concentrations. The authors use both the full LIBS spectra and individual spectral lines to predict the soil properties and nutrients.

The authors took 200 soil samples from four different regions, pressed them into pellets, and acquired 75 spectra from each sample using a 5x5 matrix of 25 points. They used 75% of the samples for training and 25% of the samples for validation, following baseline subtraction and a wavelet transform for de-noising.

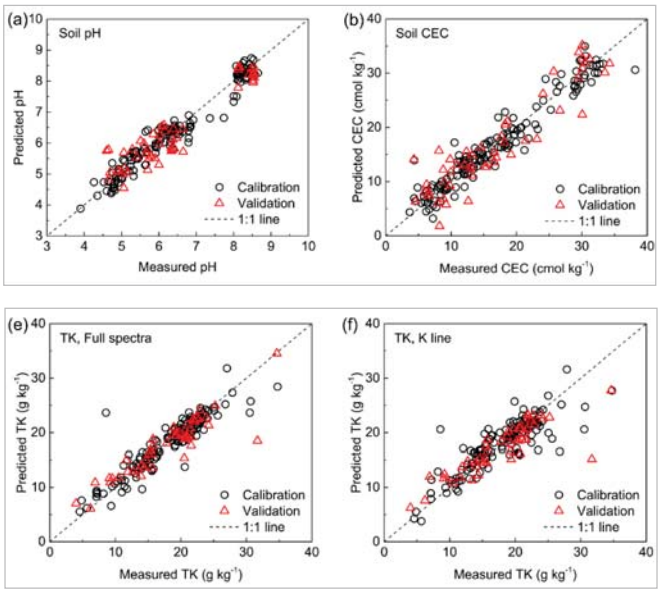

Figure 3: Top: Soil pH and Soil CEC predicted from the entire LIBS spectrum. Bottom: Total K predicted by the entire LIBS spectrum (left) and the K emission line alone (right). Adapted from [9], figures unchanged, shared under the Creative Commons Attribution 4.0 International License.

Figure 3 illustrates a subset of the results. Soil pH and CEC are both a function of the mineral composition of the soil, which influences the pH and "acid-neutralizing capacity" of the soil. Key emission lines related to pH, for example, were shown to be those related to K, Ca, Mg, Al, Si, Fe, and O. Full spectra, rather than individual elemental lines, proved much better at predicting total phosphorous or total potassium. Available phosphorous and available potassium were only weakly predicted. The authors suggest that these results justify application to a larger dataset with more soil types, and development of "simple and convenient" LIBS instruments and algorithms for field use.

The studies above in [8] and [9] show that it is quite possible to use LIBS to determine soil type and to determine NPK and soil properties such as pH. A recent study by Sun, et al. combines these features to predict trace quantities of metals in different soil types, by explicitly concatenating information about the soil type with the spectra vector during the training and validation steps.[10] They then continuously change the adjustable parameters in the model during training, until the relative error of calibration is below a fixed threshold that they set. During the training, data points from spectra with different soil types and the same concentration are randomly exchanged, building a model that is sturdy in the face of experimental fluctuation and general for all soil types. This yields general models.

The authors applied this method to a LIBS data set covering four different soil types, six different concentrations, and with six replicates of each measurement. Preprocessing included picking the best spectral features to include in the model using a scoring criterion. The machine learning

method was a back-propagating neural net with a single hidden layer. Stochastic Gradient Descent iterations were used to train the model.

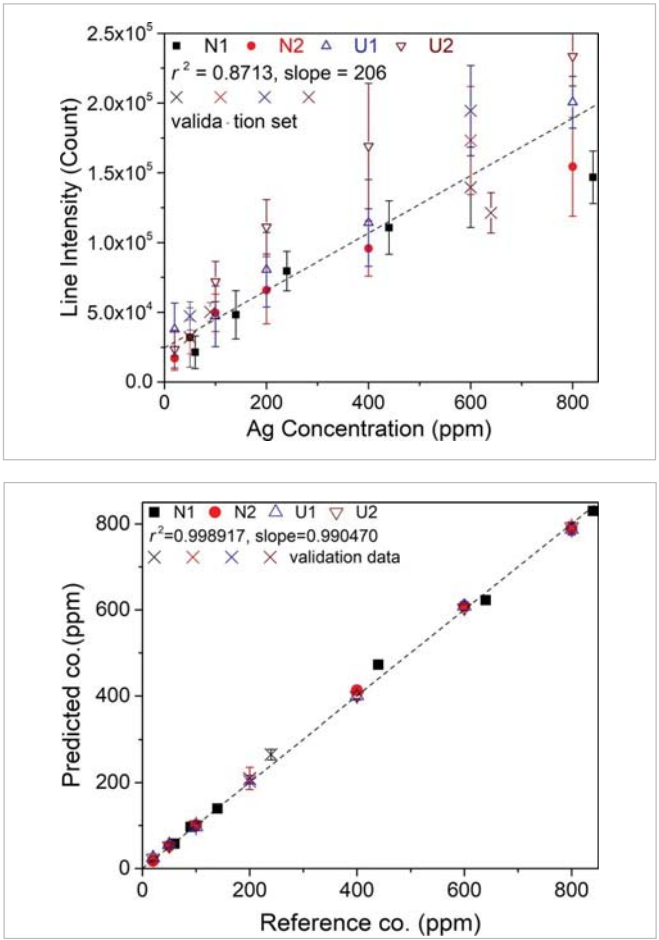

Figure 4: Ag concentration in four different soil matrices as measured (top) by univariate peak integration, and (bottom) using a generalized model for all four matrices, building a model independent of soil type. From [10], shared under the Creative Commons Attribution 4.0 International License.

Figure 4 illustrates the result. Ag was spiked into two standard NIST soils and two collected soils. The univariate curve at the top illustrates the result using standard peak integration analysis on the Ag 328.1 nm neutral line. There is a non-zero y-intercept and significant curvature in the line intensities due to self-absorption, and intensities for the same concentration of Ag may differ by as much as a factor of two. In contrast, the curve at the bottom shows nearly perfect agreement between the predicted concentration and the measured reference concentration using the generalized model.

Prospects for LIBS-based Soil Testing

A few commercial efforts have begun to take root. One company, LogiAg, has spun out a solution called LaserAg that uses LIBS to measure key parameters of soil and foliage, including NPK values. Based in Quebec, Canada, they are employing their LIBS-based solution with local laboratories who have regionally-specific calibrations to accommodate soil types. Calibrations require 500 samples collected from the region with a range of soil types and nutrient values. Once calibrated, customers send samples to the LaserAg lab for analysis.

Also, SciAps is offering their Z300 LIBS handheld analyzer for measurement of total organic carbon in soil. They used 87 soil samples from around the U.S. and Canada to build a calibration for total organic carbon. The R^2 value of the calibration curve they present is 0.8825, with a root mean square error of 0.44% over the range 0-7% organic carbon, indicating that the portable LIBS system may be useful for local checks of carbon content with moderate precision.

The research and commercial results to date clearly indicate the promise for LIBS-based solutions in soil testing. Other portable methods of analysis such as XRF cannot measure light elements such as nitrogen or carbon (the latter also being important in some aspects of

soil analysis). XRF also requires more sample preparation and physical contact with the soil to be measured. The transportable nature of LIBS systems, combined with the stand-off nature of the analysis, makes LIBS a clear possibility for next-generation soil analysis and further evolution toward precision agriculture.

Potentially standing in the path of LIBS adoption for soil analysis are the large number of soil samples that would be required to build a comprehensive database (allowing for the general model to be built), due to matrix effects that need compensation. There is also the large infrastructure of agricultural extension support and testing labs around the world that are familiar with current practices. However, it seems to be only a matter of time before LIBS-based soil analysis gains wider adoption. Stay tuned!

References

1. Buckley, S.G., "Combining Broadband Spectra and Machine Learning to Derive Material Properties," Spectroscopy **32** (10) 2017, pp 26-31.

2. Buckley, S.G., "Down to Earth: Measurements of Geological, Coal, and Soil Samples with LIBS," Spectroscopy **30** (1) 2015, pp 24-31.

3. Anderson, M.S., "History and Development of Soil Testing," J. Agricultural and Food Chemistry **8** (2) 1960, pp 84-87.

4. Reformatted and re-released by the U.S. Department of Agriculture in 1998, retrieved from: https://www.nrcs.usda.gov/Internet/FSE_DOCUMENTS/stelprdb1044424.pdf

5. Retrieved from https://ourworldindata.org/grapher/average-corn-yields-in-the-united-states-1866-2014?time=1866..2014, shared under the Creative Commons Attribution 4.0 International (CC by 4.0) license.

6. Theriault, G.A. Bodensteiner, S., and Lieberman S.H., "A real-time fiber-optic LIBS probe for the in situ delineation of metals in soils," Field Analytical Chemistry and Technology, **2** (2) 1998, pp 117-125.

7. Vadillo, J.M. et al., "Rapid screening method for heavy metals in contaminated soils using LIBS," Quimica Analitica **18** (2) 1999, pp 169-174.

8. Yu, K.-Q. et al., "Laser-Induced Breakdown Spectroscopy Coupled with Multivariate Chemometrics for Variety Discrimination of Soil," Scientific Reports **6**:27574 2016.

9. Xu, X. et al., "Fast and Simultaneous Determination of Soil Properties Using Laser-Induced Breakdown Spectroscopy (LIBS): A Case Study of Typical Farmland Soils in China," Soil Systems **3** (4) 2019, 66.

10. Sun, C. et al., "Machine Learning Allows Calibration Models to Predict Trace Element Concentration in Solids with Generalized LIBS Spectra," Scientific Reports **9**:11363 2019.

Ocean Insight

www.oceaninsight.com

info@oceaninsight.com • **US** +1 727-733-2447

EUROPE +31 26-3190500 • **ASIA** +86 21-6295-6600

102620


UNIVERSITAS SCIENTIARUM SZEGEDIENSIS
SZEGEDI TUDOMANYEGYETEM
VERITAS VIRTUS
LIBERTAS


MAGYAR TUDOMÁNYOS AKADÉMIA
1825


eli
attosecond


SZÉCHENYI 2020
MAGYARORSZÁG KORMÁNYA
Európai Unió
Európai Szociális Alap
BEFEKTETÉS A JÖVŐBE